2016

Crystal Growth And Characterization Of Reduced Early Transition Metal Compounds Grown Via Hydrothermal And Molten Flux Methods

Anthony J. Cortese
University of South Carolina

Crystal Growth and Characterization of Reduced Early Transition Metal Compounds Grown via Hydrothermal and Molten Flux Methods

by

Anthony J. Cortese

Bachelor of Science
University of Pittsburgh, 2010

Submitted in Partial Fulfillment of the Requirements

For the Degree of Doctor of Philosophy in

Chemistry

College of Arts and Sciences

University of South Carolina

2016

Accepted by:

Hans-Conrad zur Loye, Major Professor

Daniel Reger, Committee Member

Linda Shimizu, Committee Member

Harry Ploehn, Committee Member

Lacy Ford, Senior Vice Provost and Dean of Graduate Studies

DEDICATION

to

my mother and father

without whose selfless devotion

and unyielding love

I could not have completed this endeavor.

ACKNOWLEDGEMENTS

I would like to express my deepest gratitude to Hans-Conrad zur Loye. He has been a steadfast source of motivation, leadership, and rigorous academic debate throughout my graduate career.

I would also like to thank the professors who have served as my committee members, Dr. Daniel Reger, Dr. Linda Shimizu, and Dr. Harry Ploehn, who have been crucial to my development as a critically thinking scientist and who have been present for each of my doctoral milestones. I would like to graciously acknowledge Dr. Mark Smith for his unparalleled expertise and countless hours dedicated to the assistance in the structure solution of my materials. Lastly I would like to acknowledge the zur-Loye group, members past and present, who have provided comradery, understanding, and much needed levity in our pursuit of excellence.

Thank you all and may God bless you in your future endeavors.

ABSTRACT

Interest in new and facile ways to prepare early transition metal reduced oxides has recently been increasing. In the past difficult flux techniques involving vacuum furnaces, expensive metal tubing, complicated electrolytic reduction apparatuses, were used to achieve *in situ* reduction of fully oxidized transition metal precursors. Often times these techniques were coupled with use of a difficult flux, such as boric acid, which is hard to remove due to its insolubility in water at room temperature. These limitations can be circumvented in multiple ways, including carefully choosing a redox neutral flux, using evacuated fused silica tubes for reaction vessels, and employing metallic reducing agents such as powered molybdenum, vanadium, or zinc. Virtually no work has been done outside the realm of flux crystal growth. Nevertheless, the hydrothermal method for crystal growth can be employed to yield hybrid materials containing reduced early transition metals.

Through the successful utilization of a two-step hydrothermal method, four oxovanadium(IV) tartrates have been prepared and characterized with three out four having confirmed second harmonic generation activity and one exhibiting spin dimer magnetic behavior. Via a one step hydrothermal method involving an *in situ* reduction, one oxovanadium(IV) phosphate has been prepared and found to exhibit filled channels in two crystallographic directions.

Using the flux method many reduced molybdenum oxides and a related material have been prepared and characterized including the following series: $Na_xLn_{1-x}MoO_4$ *Ln* =

La, Ce, Pr,Nd, Sm, and Eu; $Ln_{\sim 5}Mo_3O_{16}$ *Ln = Ce, Pr, Nd* and *Sm*; and $Ln_5Mo_2O_{12}$ *Ln* = Eu, Tb, Dy, Ho, and Er. Evidence of direct molybdenum to molybdenum bonding was in the $Ln_5Mo_2O_{12}$ series, and all compounds were found to order antiferromagnetically. A related material, $La_{20}Mo_{12}O_{63}Cl_4$, was found to exhibit an optical band gap in the visible region and is the first example of a purely inorganic material that contains molybdenum in a trigonal prismatic coordination environment.

TABLE OF CONTENTS

List of Compounds by Chapter

LIST OF TABLES

LIST OF FIGURES

List of Symbols

°	Degrees
Å	Angstroms
Kα	An emission line that results when an electron transitions to the innermost "K" shell (principal quantum number 1) from a 2p orbital of the second or "L" shell (with principal quantum number 2)
λ	Wavelength
2θ	Total change in angle of an incident X-ray that is diffracted from a sample
Z	Total number of formula units that reside inside a given unit cell
F^2	Structure factor squared
R	Residual factor
R(int)	Merging error, a measure of the precision/reproducibility
R_1	Residual factor for refinement against *F*
wR_2	Residual factor for refinement against F^2
F^2	The structure factor squared
$U_{(eq)}$	One third of the trace of the orthogonalized U_{ij} tensor
U_{ij}	Anisotropic thermal parameter

List of Abbreviations

EDS ..... Energy Dispersive Spectroscopy

en ..... ethylenediamine

EtOH ..... ethanol

fc ..... Field Cooled

IR ..... Fourier Transform Infrared Spectroscopy

MeOH ..... methanol

NLO ..... Nonlinear Optical

PTFE ..... Polytetrafluoroethylene

PXRD ..... Powder X-ray Diffraction

SHG ..... Second Harmonic Generation

SXRD ..... Single Crystal X-ray Diffraction

UV/Vis ..... Ultraviolet/Visible Diffuse Reflectance Spectroscopy

zfc ..... Zero Field Cooled

“Look at a day when you are supremely satisfied at the end. it's not a day when you lounge around doing nothing; it's when you've had everything to do and you've done it.”

– Margaret Thatcher

CHAPTER I

INTRODUCTION

The purpose of this thesis is to educate the reader on the mild hydrothermal and molten flux synthesis of early transition metal hybrids, reduced oxides, and related materials. To accomplish this purpose, the thesis is divided into eight chapters, including this introduction. This introductory chapter will give a brief historical overview and critical analysis of synthetic techniques that have been used in the past to create materials containing reduced early transition metals. A summary of to the techniques used throughout this thesis, hydrothermal and molten flux, will be presented in two parts.

Chapters 2 and 3 focuses on the hydrothermal synthesis of oxovanadium(IV) hybrid materials. Specifically, Chapter 2 will discuss four noncentrosymmetric oxovanadium(IV) tartrates synthesized via a two-step mild hydrothermal method and their optical and magnetic properties. Chapter 3 focuses on an oxovanadium(IV) phosphate material synthesized via a one step hydrothermal method and its optical and magnetic properties. Chapter 4 focuses on a brief period of work involving the molten flux synthesis of a partially reduced niobium compound and its characterization.

Chapters 5 through 7 will discuss the molten flux synthesis and characterization of many lanthanide reduced molybdenum oxides that cluster into three different series along the lanthanide series. This work convincingly demonstrates the effects rare earth cation size and choice of flux can have on structural outcome, and subsequently the magnetic properties of the materials. Specifically, Chapter 5 will discuss a series of sodium lanthanide molybdates, $Na_xLn_{1-x}MoO_4$ *Ln* = La, Ce, Pr, Nd, Sm, and Eu, prepared via a sodium chloride/cesium chloride eutectic. In Chapter 6, a pure cesium chloride flux is used instead of a eutectic, resulting in a different series of lanthanide molybdates, $Ln_{\sim 5}Mo_3O_{16}$ *Ln* = Ce, Pr, Nd, Sm, and Eu, that contain a higher percentage of reduced

molybdenum. Attempts to extend the series in Chapter 6 beyond samarium resulted in the work presented in Chapter 7; a different lanthanide molybdate series, $Ln_5Mo_2O_{12}$ *Ln* = Eu, Dy, Ho, and Er that contains exclusively reduced molybdenum. In Chapter 8, a reduced molybdenum oxide related material, $La_{20}Mo_{12}O_{63}Cl_4$, is presented. This material was found when attempting to extend the series in Chapter 6 beyond cerium to lanthanum. This compound represents a new structure type and is the first example of a purely inorganic oxide material that contains molybdenum in a trigonal prismatic coordination environment.

Historical Methods

Molten flux crystal growth of early transition metals oxides has historically been hampered due to the unique synthetic challenges involved in this type of crystal growth. It is, however, an interesting area of research for the creation of oxides containing unpaired electrons, in particular since early transition metals in reduced oxidation states can potentially lead to interesting electrical and magnetic properties.[1-18]

In the past researchers have reported simple reduced early transition metal oxides such as VO_2, V_2O_3[1, 18, 19], TiO[11], and Ti_2O_3[16], as well as some ternary and higher reduced oxides, including reduced perovskites and bronzes: $SrTiO_{2.5}$[20], $Ba_6Nb_{14}Si_4O_{47}$[14], $Ax NbO_3$(*A*=Sr, Ba), $Ba_3M_5O_{15}$(*M*=Nb, Ta)[8, 13], $A_{0.3}MoO_3$ (*A*=K, Rb, Tl[3, 7], $Cs_{0.33}MoO_3$[4, 5], $K_2Mo_4Nb_3O_{20}$[15], SrV_4O_9,[2] and $Y_5Mo_2O_{12}$[21] using crystal growth approaches that include fused salt electrolysis, chemical vapor transport, and flux methods involving a vacuum furnace.

While these techniques have proven successful they do not represent facile or inexpensive routes to achieve the desired outcome. For example, a fused salt electrolysis

apparatus is an expensive piece of equipment and utilization of this method can result in the formation of bronzes which often exhibit a range of stoichiometry making full characterization and property measurement difficult. The use of chemical vapor transport often entails the sublimation of a material and sometimes requires the use of an additional reactive gas to perform the reaction. This technique does not lend itself to exploratory crystal growth as only a limited number of precursors are suitable. Flux methods that have been used in the past often employed fluxes that are difficult to work with, particularly borates, which are highly viscous and especially difficult to solubilize in water during crystal isolation. Additionally, often times an expensive vacuum furnace needed to be used to ensure an inert environment for the reaction to take place. In examples where a conventional high temperature furnace was used, the reaction vessel had to be welded from within a glove box to preserve an inert atmosphere. Often times this reaction vessel was made from expensive-to-machine and tough-to-weld metals including molybdenum and niobium.[22-27]

New Approaches

The limited number of known oxides containing reduced early transition metals has pushed us to pursue synthetic strategies to prepare such oxides and to explore their physical properties, including magnetism. Our research has resulted in three highly successful approaches including two hydrothermal techniques and one molten flux technique.

Hydrothermal Methods

Our group has had great success employing variations on the hydrothermal method to create compounds that contain transition metals, including vanadium, in a reduced

oxidation state. It is possible to reduce aqueous vanadium(V) species, such as VO_2^{2+}, using organic reducing agents, including oxalic acid, citric acid, ascorbic acid, and tartaric acid to create reduced vanadium(IV) species, such as VO^{2+}.[28-33]

We have recently reported on a convenient two-step hydrothermal method that facilitates the formation of hybrid materials containing metal cations in reduced states. In the case of reactions where the rate of transition metal reduction is slow relative to the crystallization of an unwanted species, the use of the two-step approach is extremely effective for obtaining the desired reduced products. Essentially the reduction step and the product creation step are performed sequentially. In the first step the metal cation is reduced from its fully oxidized state and in the second step, the crystallization of the hybrid material takes place. This is a completely general approach that can be extremely helpful for many reactions where the simultaneous *in-situ* reduction and complex formation does not succeed due to unfavorable kinetics of competing crystallization processes. This method has been very successful for preparing single crystals of hybrid materials containing V^{4+} and U^{4+} including: $A_2[(VO)_2(C_4H_4O_6)(C_4H_2O_6)(H_2O)_2]\bullet(H_2O)_2$ A = Cs, Rb; $K_2[(VO)_2(C_4H_2O_6)_2(H_2O)_2]\bullet(H_2O)_2$; $Na_2[(VO)_2(C_4H_4O_6)(C_4H_2O_6)(H_2O)_7]\bullet(H_2O)_2$; $[H_2en]_4[V_7P_8O_{35}(OH)_6(H_2O)]\cdot 3H_2O$, $Ba_3[(VO)_2(C_2O_4)_5(H_2O)_6](H_2O)_3$, $Cs_2V_3O_8$, $Na_2U_2M(C_2O_4)_6(H_2O)_4$ M = Mn^{2+}, Fe^{2+}, Co^{2+}, and Zn^{2+}; $U_3F_{12}(H_2O)$ $Na_4MU_6F_{30}$ M = Mn^{2+}, Co^{2+}, Ni^{2+}, Cu^{2+}, and Zn^{2+}.[34-39]

Molten Flux Methods

To explore the preparation of reduced oxides at high temperatures, we explored the use of flux crystal growth, a well-known, facile method for the crystal growth of diverse oxides, including reduced ones.[40] In order to successfully grow reduced oxide crystals,

we carefully select alkali metal halides as redox neutral fluxes, which can be utilized as high temperature fluxes in evacuated sealed fused silica reaction vessels, making them excellent candidates for our work. Additionally, most alkali metal halides are inexpensive and readily dissolve in water at room temperature, making crystal isolation rudimentary.

In some situations, to lower reaction temperature, a eutectic melt can be used. In our work a combination of alkali metal halides or alkali/alkaline earth halides has proven effective. By using a eutectic melt, the liquid range of the flux can be extended allowing for optimum conditions for crystallization.

This approach has been highly successful for our group in the preparation of reduced early transition metal oxides including: $La_{20}Mo_{12}O_{63}Cl_4$; $Ln_5Mo_2O_{12}$ *Ln* = Eu, Tb, Dy, Ho, and Er; $Ce_{4.92}Mo_3O_{16}$, $Pr_{4.880(3)}Mo_3O_{16}$, $Nd_{4.910(3)}Mo_3O_{16}$, $Sm_{4.952(3)}Mo_3O_{16}$; $La_{0.516(3)}Na_{0.484(3)}MoO_4$, $Ce_{0.512(2)}Na_{0.488(2)}MoO_4$, $Pr_{0.502(2)}Na_{0.498(2)}MoO_4$, $Nd_{0.501(2)}Na_{0.499(2)}MoO_4$, $Sm_{0.509(2)}Na_{0.491(2)}MoO_4$, and $Eu_{0.603(2)}Na_{0.397(2)}MoO_4$.[35, 41-44]

This method has also yielded several silicate compounds including: $Ba_3Na_{0.32}Nb_6O_{12}(Si_2O_7)_2$[45], and $Ln_4V_{5-x}Zn_xSi_4O_{22}$ (Ln = La, Ce, Pr, and Nd)[46], where silicon is slowly leached via the molten flux from the inner walls of the fused silica vessel in a controlled fashion so as not to degrade the structural integrity of the reaction vessel.

The overall goal in the synthesis of reduced early transition metal compounds is to discover new materials, structure types, and properties in an untapped area of chemistry. My thesis work focused on the hydrothermal and molten flux synthesis of such materials and has resulted in compounds that exhibit unusual magnetic and optical properties, as well as well as several new structure types.

References

(1) G. Andersson. *Acta. Chem. Scand.* **1954**, *8*, 1599-1606.

(2) S. C. Chen; B. Wang; M. Greenblatt. *Inorg. Chem.* **1993**, *32*, 4306-4310.

(3) C. R. Feger; R. P. Ziebarth. *Chem. Mater.* **1995**, *7*, 373-378.

(4) M. Greenblatt. *Chem. Rev.* **1988**, *88*, 31-53.

(5) M. Greenblatt. *Physics and Chemistry of Materials with Low-Dimensional Structures* **1989**, *11*, 1-48.

(6) T. K. Hamasaki, H. Sekine, T. Hasem, M. Kitazawa, H. *J. Phys.: Conf. Ser.* **2009**, *150*, 042047.

(7) B. Hessen; S. A. Sunshine; T. Siegrist; A. T. Fiory; J. V. Waszczak. *Chem. Mater.* **1991**, *3*, 528-534.

(8) B. Hessen; S. A. Sunshine; T. Siegrist; R. Jimenez. *Mater. Res. Bull.* **1991**, *26*, 85-90.

(9) T. Lancaster; P. J. Baker; F. L. Pratt; S. J. Blundell; W. Hayes; D. Prabhakaran. *Phys. Rev. B: Condens. Matter. Mater. Phys.* **2012**, *85*, 184404.

(10) S. O. Mat'aš, A.; K. K. Prokeš, B. *J. Phys.: Conf. Ser.* **2010**, *251*, 012024.

(11) F. J. Morin. *Bell Syst. Tech. J.* **1958**, *37*, 1047-1084.

(12) K. M. Ok; E. O. Chi; P. S. Halasyamani. *Chemical Society Reviews* **2006**, *35*, 710-717.

(13) D. Ridgley; R. Ward. *J. Am. Chem. Soc.* **1955**, *77*, 6132-6136.

(14) D. L. Serra; S.-J. Hwu. *J. Solid State Chem.* **1992**, *101*, 32-40.

(15) P. P. Tsai; J. A. Potenza; M. Greenblatt. *J. Solid State Chem.* **1987**, *69*, 329-335.

(16) L. L. Van Zandt; J. M. Honig; J. B. Goodenough. *J. Appl. Phys.* **1968**, *39*, 594-595.

(17) S. Vasala; H. Saadaoui; E. Morenzoni; O. Chmaissem; T.-S. Chan; J.-M. Chen; Y.-Y. Hsu; H. Yamauchi; M. Karppinen. *Phys. Rev. B: Condens. Matter. Mater. Phys.* **2014**, *89*, 134419.

(18) S. Westman; C. Nordmark. *Acta Chem. Scand.* **1960**, *14*, 465-470.

(19) M. Pouchard; J. C. Launay. *Mater. Res. Bull.* **1973**, *8*, 95-104.

(20) M. Kestigian; J. G. Dickinson; R. Ward. *J. Am. Chem. Soc.* **1957**, *79*, 5598-5601.

(21) C. C. Torardi; C. Fecketter; W. H. McCarroll; F. J. DiSalvo. *J. Solid State Chem.* **1985**, *60*, 332-342.

(22) S. J. Clarke; A. J. Fowkes; A. Harrison; R. M. Ibberson; M. J. Rosseinsky. *Chem. Mater.* **1998**, *10*, 372-384.

(23) O. G. D'yachenko; S. Y. Istomin; A. M. Abakumov; E. V. Antipov. *Inorg. Mater.* **2000**, *36*, 247-259.

(24) M. J. Geselbracht; L. D. Noailles; L. T. Ngo; J. H. Pikul. *Chem. Mater.* **2004**, *16*, 1153-1159.

(25) S. Y. Istomin; G. Svensson; O. G. D'yachenko; W. Holm; E. V. Antipov. *J. Solid State Chem.* **1998**, *141*, 514-521.

(26) P. Mahjoor; S. E. Latturner. *Inorg. Chem.* **2010**, *49*, 4486-4490.

(27) T. Siegrist; R. J. Cava; J. J. Krajewski. *Mater. Res. Bull.* **1997**, *32*, 881-887.

(28) C. K. Blakely; S. R. Bruno; V. V. Poltavets. *Inorg. Chem.* **2011**, *50*, 6696-6700.

(29) T. Kiss; P. Buglyó; D. Sanna; G. Micera; P. Decock; D. Dewaele. *Inorg. Chim. Acta* **1995**, *239*, 145-153.

(30) M. J. Polinski; J. N. Cross; E. M. Villa; J. Lin; E. V. Alekseev; W. Depmeier; T. E. Albrecht-Schmitt. *Inorg. Chem.* **2013**, *52*, 8099-8105.

(31) C. F. Tsang; A. Manthiram. *J. Mater. Chem.* **1997**, *7*, 1003-1006.

(32) C. F. Tsang; J. Kim; A. Manthiram. *J. Mater. Chem.* **1998**, *8*, 425-428.

(33) J. Yeon; A. S. Sefat; T. T. Tran; P. S. Halasyamani; H.-C. zur Loye. *Inorg. Chem.* **2013**, *52*, 6179-6186.

(34) D. Abeysinghe; M. D. Smith; J. Yeon; G. Morrison; H.-C. zur Loye. *Cryst. Growth & Des.* **2014**, *14*, 4749-4758.

(35) A. J. Cortese; B. Wilkins; M. D. Smith; J. Yeon; G. Morrison; T. T. Tran; P. S. Halasyamani; H.-C. zur Loye. *Inorg. Chem.* **2015**, *54*, 4011-4020.

(36) J. Yeon; M. D. Smith; A. S. Sefat; H.-C. zur Loye. *Inorg. Chem.* **2013**, *52*, 2199-2207.

(37) J. Yeon; A. S. Sefat; T. T. Tran; P. S. Halasyamani; H.-C. zur Loye. *Inorg. Chem.* **2013**, *52*, 6179-6186.

(38) J. Yeon; M. D. Smith; A. S. Sefat; T. T. Tran; P. S. Halasyamani; H.-C. zur Loye. *Inorg. Chem.* **2013**, *52*, 8303-8305.

(39) J. Yeon; M. D. Smith; J. Tapp; A. Möller; H.-C. zur Loye. *J. Am. Chem. Soc.* **2014**, *136*, 3955-3963.

(40) D. E. Bugaris; H.-C. zur Loye. *Angew. Chem. Int. Ed.* **2012**, *51*, 3780-3811.

(41) A. J. Cortese; D. Abeysinghe; M. D. Smith; H.-C. zur loye. *J. Solid State Chem.* **(submitted)**,

(42) A. J. Cortese; D. Abeysinghe; B. Wilkins; M. D. Smith; H.-C. zur Loye. *Cryst. Growth Des.* **(submitted)**,

(43) A. J. Cortese; B. Wilkins; M. D. Smith; G. Morrison; H.-C. zur loye. *Solid State Sciences* **2015**, *48*, 133-140.

(44) A. J. Cortese; D. abeysinghe; B. Wilkins; M. D. Smith; G. Morrison; H.-C. zur Loye. *Inorg. Chem.* **2015**, *54*, 11875-11882.

(45) A. J. Cortese; B. Wilkins; M. D. Smith; G. Morrison; H.-C. zur Loye. *Solid State Sciences* **2015**, *48*, 7-12.

(46) D. Abeysinghe; M. D. Smith; J. Yeon; G. Morrison; H.-C. zur Loye. *Inorg. Chem.* **2016**, *55*, 1821-1830.

CHAPTER II

CRYSTAL GROWTH OF FOUR OXOVANADIUM(IV) TARTRATES PREPARED VIA A MILD HYDROTHERMAL METHOD: OBSERVATION OF SPIN-DIMER BEHAVIOR AND SECOND HARMONIC GENERATION*

*Adapted with permission from Cortese, A. J.; Wilkins, B.; Smith, M. D.; Yeon, J.; Morrison, G.; Tran, T. T.; Halasyamani, P. S.; zur Loye, H.-C. *Inorg. Chem.* **2015**, *54(8)*, 4011-4020.

Abstract

Four new oxovanadium(IV) tartrates, $A_2[(VO)_2(C_4H_4O_6)(C_4H_2O_6)(H_2O)_2]\bullet(H_2O)_2$ A = Cs, **2.1**, Rb, **2.2**; $K_2[(VO)_2(C_4H_2O_6)_2(H_2O)_2]\bullet(H_2O)_2$, **2.3**; and $Na_2[(VO)_2(C_4H_4O_6)(C_4H_2O_6)(H_2O)_7]\bullet(H_2O)_2$, **2.4** were prepared utilizing a two-step, mild hydrothermal route involving L-(+)-tartaric acid as the reducing agent. All four compounds were structurally characterized by single crystal and powder X-ray diffraction methods and were found to crystallize in the noncentrosymmetric orthorhombic space groups $P2_12_12_1$ for **2.1**, **2.2**, and **2.4** and $C222_1$ for **2.3**. The temperature dependence of the magnetic susceptibility of these compounds was measured and **2.1**, **2.2**, and **2.4** were found to be paramagnetic down to 2K while **2.3** was found to exhibit spin dimer behavior. Compounds **2.1**, **2.2**, and **2.3** were found to be second harmonic generation active. All compounds were further characterized by IR and UV-Vis spectroscopy.

Introduction

Vanadium containing compounds have been investigated for a variety of applications, including as magnetic materials,[1-4] for catalysts,[5-8] as cathode materials,[9-12] and as ion exchange materials.[13, 14] In these applications the vanadium oxidation state can range from fully oxidized, as in some oxidation catalysts, to reduced, as in some lithium battery cathode materials. Overall, the oxidation state chemistry of vanadium is rich and includes the +5, +4, +3, and +2 oxidation states, where color is often used to distinguish and confirm the oxidation states of vanadium species. In an aqueous environment, vanadium can exist in oxidation states ranging from +2 to +5 with colors ranging from yellow (V^{5+}), blue (V^{4+}), green (V^{3+}), and lilac (V^{2+}).[15-21] It is possible to reduce aqueous vanadium species using organic reducing agents, where the combination of organic

reagent and temperature determine the final vanadium oxidation state. While harsher conditions, such as sulfuric acid catalyzed zinc reduction under inert atmosphere, are needed to create V^{2+} in aqueous solutions, many simple organic acids, including oxalic acid, citric acid, ascorbic acid, and tartaric acid can be used to create V^{4+} in solution.[20, 21] One such acid, tartaric acid, has the ability to perform the reduction of vanadium from +5 to +4 in air under mild hydrothermal conditions. With both carboxyl and hydroxyl functional groups and a flexible carbon backbone, tartaric acid is an attractive candidate as a ligand for vanadium containing hybrid materials owing to the variety of chelating motifs that can be adopted. A few vanadium – tartrate hybrid materials are known, including $[Sr(VO)((\pm)\text{-}C_4H_2O_6)(H_2O)_3]_2$,[22] $A_4[(VO)(C_4H_2O_6)]_2 \bullet xH_2O$ A = Cs, Rb,[23] $Na_4[V_4O_8((\pm)\text{-}C_4H_2O_6)_2] \bullet (H_2O)_{12}$,[24] and $(N(CH_2CH_3)_4)[V_4O_8(D\text{-}C_4H_2O_6)_2] \bullet (H_2O)_6$.[24]

We have recently reported on a convenient two-step hydrothermal method that facilitates the formation of hybrid materials containing metal cations in reduced states.[21, 25] In the case of reactions where the rate of vanadium reduction is slow relative to the crystallization of an unwanted species, either V^{5+} containing complexes or mixed ligand complexes, the use of the two-step approach is extremely effective for obtaining the desired V^{4+} products. Essentially the reduction step and the product creation step are performed sequentially. In the first step the vanadium cation is reduced from +5 to +4 and in the second step, the crystallization of the hybrid material takes place. This is a completely general approach that can be extremely helpful for many reactions where the simultaneous *in-situ* reduction and complex formation does not succeed due to unfavorable kinetics of competing crystallization processes.

To create the title compounds, $A_2[(VO)_2(C_4H_4O_6)(C_4H_2O_6)(H_2O)_2]\bullet(H_2O)_2$ A = Cs, Rb and $K_2[(VO)_2(C_4H_2O_6)_2(H_2O)_2]\bullet(H_2O)_2$, we used this two step approach and sequentially performed the vanadium reduction step and the crystallization of the vanadium - L-(+)-tartaric acid containing product step. To create $Na_2[(VO)_2(C_4H_4O_6)(C_4H_2O_6)(H_2O)_7]\bullet(H_2O)_2$, a slow evaporation method was employed. The use of enantiomerically pure tartaric acid in the syntheses to create tartaric acid containing products will, by default, create enantiomerically pure chiral materials. Consequently, the four title compounds are all chiral and, therefore, non-centrosymmetric, which is one of the requirements for materials to display Second Harmonic Generation (SHG). Compounds crystallizing in noncentrosymmetric space groups are capable of exhibiting interesting nonlinear optical properties including piezoelectricity, pyroelectricity, circular dichroism, and SHG.[26] The title compounds all crystallize in noncentrosymmetric orthorhombic space groups allowing for the measurement of their SHG response.

Using the two-step reduction method we have successfully synthesized four new chiral oxovanadium(IV) tartrates in good yield. Herein we report the synthesis, structural characterization, magnetic properties, and SHG response of these compounds.

Experimental Details

Reagents.

V_2O_5 (99.6% min., Alfa Aesar), L-(+)-$C_4H_6O_6$ (99%, Alfa Aesar), CsCl (99%, Alfa Aesar), Cs_2CO_3 (99%, Alfa Aesar), RbCl (99%, Alfa Aesar). Rb_2CO_3 (99%, Alfa Aesar), KCl (Certified A.C.S., Fisher) K_2CO_3 (Certified A.C.S., Fisher), NaCl (Certified

A.C.S., Fisher), Na_2CO_3 (Certified A.C.S., Fisher), methanol (Certified A.C.S., BDH), and ethanol (USP Spec, Decon Labs, Inc.) were used as received.

Hydrothermal Syntheses.

Synthesis of $Cs_2[(VO)_2(C_4H_4O_6)(C_4H_2O_6)(H_2O)_2]\bullet(H_2O)_2$, ***2.1***

Purple colored single crystals of $Cs_2[(VO)_2(C_4H_4O_6)(C_4H_2O_6)(H_2O)_2]\bullet(H_2O)_2$, **2.1**, were grown via a two step hydrothermal route. In the first step, 1 mmol of V_2O_5, 4 mmol of L-(+)-$C_4H_6O_6$, and 4 mL of H_2O were placed in a PTFE autoclave. The autoclave was placed inside a programmable oven and heated to 160°C at a rate of 10°C/min, held for 4 hours, and cooled to room temperature by turning off the oven. The resulting blue solution was reacted with 2 mmol of Cs_2CO_3 and 3 mmol of CsCl and added to a thick walled PTFE capped Pyrex tube. The tube was placed inside a programmable oven and heated to 90°C at a rate of 10°C/min, held for 48 hours, and cooled to room temperature at a rate of 0.1°C/min. The mother liquor was decanted yielding a phase pure product in approximately 85% yield based on V_2O_5. **Figure 2.1** shows an optical image of **2.1**. **Figure 2.2** shows a powder X-Ray diffraction pattern (PXRD) of ground crystals demonstrating the phase purity of the product crystals.

Synthesis of $Rb_2[(VO)_2(C_4H_4O_6)(C_4H_2O_6)(H_2O)_2]\bullet(H_2O)_2$, ***2.2***

Purple colored single crystals of $Rb_2[(VO)_2(C_4H_4O_6)(C_4H_2O_6)(H_2O)_2]\bullet(H_2O)_2$, **2.2**, were grown via a two step hydrothermal route. In the first step, 1 mmol of V_2O_5, 4 mmol of L-(+)-$C_4H_6O_6$, and 4 mL of H_2O were placed in a PTFE autoclave. The autoclave was placed inside a programmable oven and heated to 160°C at a rate of 10°C/min, held for 4 hours, and cooled to room temperature by turning off the oven. The resulting blue solution was reacted with 2 mmol of Rb_2CO_3, 3 mmol of RbCl, and 2.7 mL

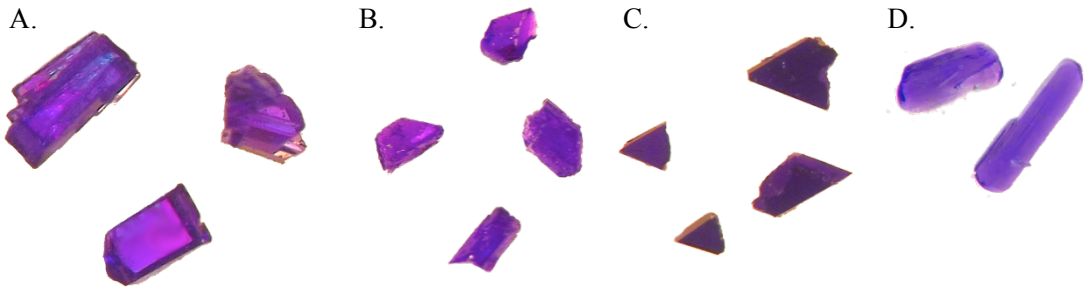

Figure 2.1 Optical image of single crystals of A. **2.1**; B. **2.2**; C. **2.3**; and D. **2.4** Crystals are approximately 0.75 mm in length.

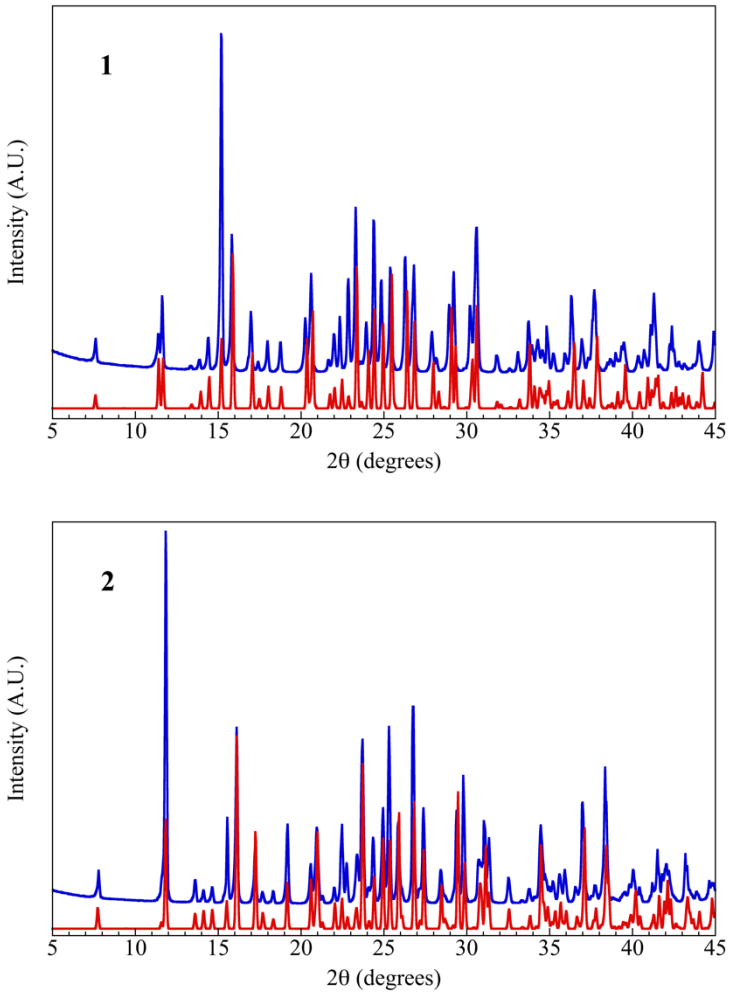

Figure 2.2 PXRD patterns of compound **2.1**, pane 1; and compound **2.2**, pane 2. Experimental diffraction is shown in blue. The calculated pattern is shown in red.

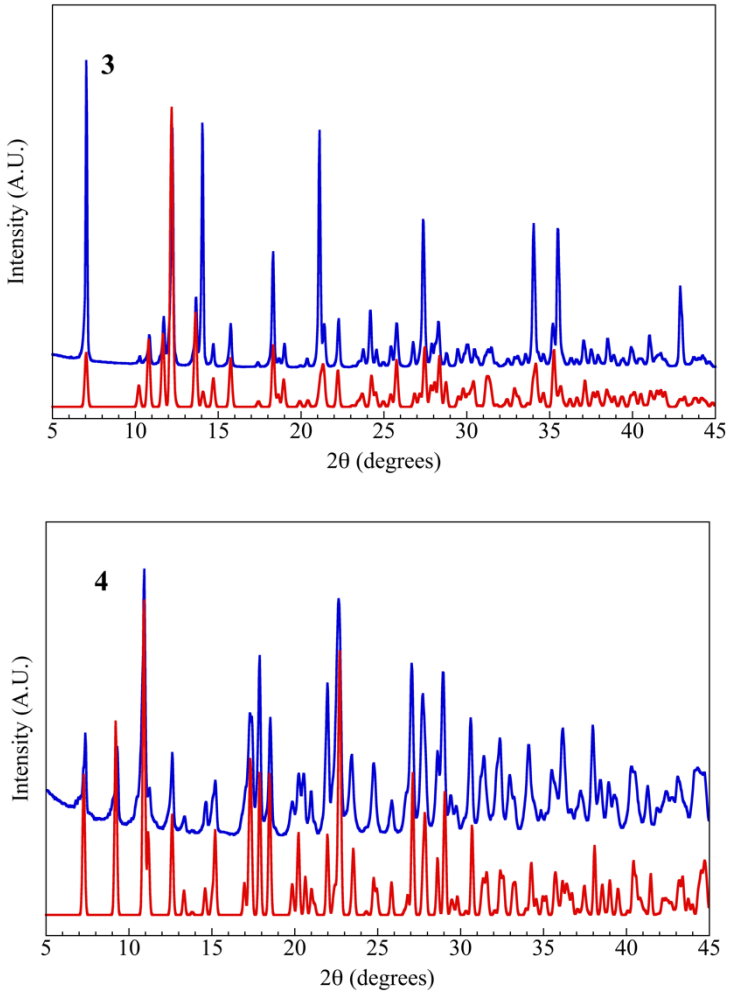

Figure 2.2 (cont.) PXRD patterns of compound **2.3**, pane 3; and compound **2.4**, pane 4. Experimental diffraction is shown in blue. The calculated pattern is shown in red.

ethanol and added to a thick walled PTFE capped Pyrex tube. The tube was placed inside a programmable oven and heated to 90°C at a rate of 10°C/min, held for 48 hours, and cooled to room temperature at a rate of 0.1°C/min. The mother liquor was decanted yielding a phase pure product in approximately 80% yield based on V_2O_5. **Figure 2.1** shows an optical image of **2.2**. **Figure 2.2** shows a powder X-Ray diffraction pattern (PXRD) of ground crystals demonstrating the phase purity of the product crystals.

Synthesis of $K_2[(VO)_2(C_4H_2O_6)_2(H_2O)_2]\bullet(H_2O)_2$, ***2.3***

Purple colored single crystals of $K_2[(VO)_2(C_4H_2O_6)_2(H_2O)_2]\bullet(H_2O)_2$, **2.3**, were grown via a two step hydrothermal route. In the first step, 1 mmol of V_2O_5, 4 mmol of L-(+)-$C_4H_6O_6$, and 4 mL of H_2O were placed in a PTFE autoclave. The autoclave was placed inside a programmable oven and heated to 160°C at a rate of 10°C/min, held for 4 hours, and cooled to room temperature by turning off the oven. The resulting blue solution was reacted with 2 mmol of K_2CO_3, 3 mmol of KCl, and 1 mL methanol and added to a thick walled PTFE capped Pyrex tube. The tube was placed inside a programmable oven and heated to 90°C at a rate of 10°C/min, held for 48 hours, and cooled to room temperature at a rate of 0.1°C/min. The mother liquor was decanted yielding a phase pure product in approximately 75% yield based on V_2O_5. **Figure 2.1** shows an optical image of **2.3**. **Figure 2.2** shows a powder X-Ray diffraction pattern (PXRD) of ground crystals demonstrating the phase purity of the product crystals.

Synthesis of $Na_2[(VO)_2(C_4H_4O_6)(C_4H_2O_6)(H_2O)_7]\bullet(H_2O)_2$, ***2.4***

Blue colored single crystals of $Na_2[(VO)_2(C_4H_4O_6)(C_4H_2O_6)(H_2O)_7]\bullet(H_2O)_2$, **2.4**, were grown via a one step hydrothermal technique followed by slow evaporation. In the first step, 1 mmol of V_2O_5, 4 mmol of L-(+)-$C_4H_6O_6$, and 4 mL of H_2O were placed in a

PTFE autoclave. The autoclave was placed inside a programmable oven and heated to 160°C at a rate of 10°C/min, held for 4 hours, and cooled to room temperature by turning off the oven. The resulting blue solution was reacted with 2 mmol of Na_2CO_3 and 3 mmol of NaCl and added to a thick walled pyrex tube. The solution was allowed to evaporate very slowly at room temperature for 120 days. The mother liquor was decanted yielding a phase pure product in approximately 30% yield based on V_2O_5. **Figure 2.1** shows an optical image of **2.4**. **Figure 2.2** shows a powder X-Ray diffraction pattern (PXRD) of ground crystals demonstrating the phase purity of the product crystals.

Single Crystal X-ray Diffraction (SXRD).

X-ray intensity data from deep violet rectangular plates of **2.1** and **2.2**, a purple hexagonal plate of **2.3**, and a purple needle of **2.4** were collected at 100(2) K using a Bruker SMART APEX diffractometer (Mo Kα radiation, λ = 0.71073 Å).[27] The raw area detector frames were reduced and corrected for absorption effects using the SAINT+ and SADABS programs.[27] Final unit cell parameters were determined by least-squares refinement of reflections from the data set. Direct methods structure solution, difference Fourier calculations and full-matrix least –squares refinements against F^2 were performed with SHELXS and SHELXL-2013/4[28] using OLEX2.[29]

Compounds **2.1** and **2.2** are isostructural and crystallize in the orthorhombic space group $P2_12_12_1$ as determined by the pattern of systematic absences in the intensity data and by structure solution. The asymmetric unit consists of two cesium atoms, two VO^{2+} units, two differently protonated tartrate ligands, and several coordinated and non-coordinated water molecules. One tartrate ligand (C1-C4, O1-O6) is deprotonated only at the carboxylate groups, giving it a charge of -2. The second independent tartrate ligand

(C5-C8, O7-O12) is fully deprotonated at both carboxylate groups and both hydroxyl groups, giving it a charge of -4. The state of protonation of the two independent tartrate ligands was determined by: (a) clear presence or absence of reasonably refinable hydrogen atoms in the Fourier difference map, enabled by the very high crystal quality of the material, (b) analysis of the hydrogen bonding environments of each candidate oxygen atom, and (c) longer bond distances from the hydroxyl oxygen atoms to vanadium. All non-hydrogen atoms were refined with anisotropic displacement parameters. Hydrogen atoms bonded to carbon were located in difference maps before being placed in geometrically idealized positions and included as riding atoms. The hydroxyl and water hydrogen atoms were located in difference maps and refined isotropically, with *d*(O-H) distances restrained to 0.84(2) Å. The absolute structure (Flack) parameters refined to 0.015(14) and 0.015(5) for **2.1** and **2.2**, respectively, confirming the enantiopurity of the materials and that the correct absolute structure was refined.

Compound **2.3** crystallizes in the orthorhombic space group $C222_1$ as determined uniquely by the pattern of systematic absences in the intensity data. The asymmetric unit consists of two vanadium atoms, three potassium atoms, two of which are located on two-fold axes of rotation, two singly protonated tartrate anions, and several water molecules. Potassium atoms K1 and K3 are located on C_2 axes. K3 is disordered over two sites on the C_2 axis, with occupancies K3A/K3B = 0.69(2)/0.31(2) (constrained to sum to unity). Several disordered and fractionally occupied oxygen atoms of water molecules were located in the vicinity of potassium atoms K2 and K3. The oxygens numbered O15-O17 are within reasonable distances to be considered bonded to K2 and K3. O15 was modeled

with two sites, O16 with three sites and O17 with two sites. Occupancies of O15A/B and O16A/B/C were constrained to unity. O17A/B occupancies were refined freely. Four additional peaks, O1S-O4S are distant enough from potassium to be considered non-coordinated interstitial water molecules. Their occupancies were also refined freely. Non-hydrogen atoms were refined with anisotropic displacement parameters except for disordered oxygen atoms (isotropic). Hydrogen atoms bonded to carbon were placed in geometrically idealized positions and included as riding atoms. The two hydroxyl hydrogen atoms of the tartrate ligands (H3A and H10A) were located in difference maps and refined isotropically with their O-H distances restrained to d(O-H) = 0.84(2) Å. After the final refinement cycle, the absolute structure (Flack) parameter was 0.01(2), confirming the enantiopurity of the material and that the correct absolute structure was refined.

Compound **2.4** crystallizes in the orthorhombic space group $P2_12_12_1$ as determined by the pattern of systematic absences in the intensity data. The asymmetric unit consists of two sodium atoms, two VO^{2+} units, two differently protonated tartrate ligands, seven coordinated water molecules and two non-coordinated water molecules. One tartrate ligand (C1-C4, O1-O6) is deprotonated only at the carboxylate groups, giving it a charge of -2. The second independent tartrate ligand (C5-C8, O7-O12) is fully deprotonated (both carboxylate groups and both hydroxyl groups), giving it a charge of -4. The state of protonation of the two independent tartrate ligands was determined by: (a) clear presence or absence of hydrogen atoms in the Fourier difference map, (b) analysis of the hydrogen bonding environments of each candidate oxygen atom, and (c) longer bond distances from the protonated hydroxyl oxygen atoms to vanadium

compared to the deprotonated hydroxyl V-O distances. All non-hydrogen atoms were refined with anisotropic displacement parameters except where noted below. Hydrogen atoms bonded to carbon were placed in geometrically idealized positions and included as riding atoms. The hydroxyl and water hydrogen atoms were located in difference maps. Most were refined isotropically with *d*(O-H) distances restrained to 0.84(2) Å. Those bonded to O18 and O21 were located, their distances adjusted to give *d*(O-H) = 0.84 Å and subsequently refined as riding atoms with $U_{iso,H} = 1.5U_{eq,O}$. One non-coordinated water (O23) is disordered over two sites and was refined isotropically with the total site population constrained to sum to unity. The absolute structure (Flack) parameter refined to 0.025(7), confirming the enantiopurity of the material and that the correct absolute structure was refined.

Crystallographic data, selected interatomic distances, select hydrogen bonding distances, and atomic coordinates are listed in **Tables 2.1 - 2.4**. Crystallographic information may be obtained for compounds **2.1** – **2.4** by accessing the Cambridge Crystallographic Data Centre (CCDC) with the following CCDC numbers: compound **2.1**: #993881, compound **2.2**: #993882, compound **2.3**: #993883, and compound **2.4**: #1061468.

Bond valence sums[30, 31] for vanadium were calculated for all four structures and found to be between 4.09 and 4.17,[32] confirming the oxidation state of V as +4 and being consistent with the compositions obtained by single crystal X-ray diffraction.

Powder X-ray diffraction (PXRD).

Powder X-ray diffraction data were collected on a Rigaku D/Max-2100 powder X-ray diffractometer using Cu Kα radiation. The step scan covered the angular range 5-

Table 2.1 Crystal data and structure refinements for compounds **2.1** and **2.2**.

	2.1	**2.2**
Empirical formula	$C_8H_{14}Cs_2O_{18}V_2$	$C_8H_{14}Rb_2O_{18}V_2$
Formula weight	765.89	671.01
Temperature	100(2) K	100(2) K
Wavelength	0.71073 Å	0.71073 Å
Crystal system	orthorhombic	orthorhombic
Space group	$P2_12_12_1$	$P2_12_12_1$
Unit cell dimensions	a = 8.0320(6) Å	a = 7.9061(8) Å
	b = 10.4016(8) Å	b = 10.2647(11) Å
	c = 23.3623(17) Å	c = 22.814(2) Å
	α = 90°	α = 90°
	β = 90°	β = 90°
	γ = 90°	γ = 90°
Volume	1951.8(3) Å^3	1851.5(3) Å^3
Z	4	4
Density (calculated)	2.61 mg/m^3	2.41 mg/m^3
Absorption coefficient	4.7 mm^{-1}	6.3 mm^{-1}
F(000)	1448.0	1304.0
Crystal size	0.1 × 0.08 × 0.05 mm^3	0.24 × 0.22 × 0.2 mm^3
2θ range for data collected	3.48 to 55.36°	3.58 to 55.82°
Index ranges	$-10 \le h \le 10$	$-10 \le h \le 10$
	$-13 \le k \le 13$	$-13 \le k \le 13$
	$-30 \le l \le 30$	$-30 \le l \le 30$
Reflections collected	29398	26955
Ind. reflections	4570[R(int) = 0.0437]	4431[R(int) = 0.0466]
Data / restraints / parameters	4570 / 11 / 311	4431 / 11 / 309
Goodness-of-fit on F^2	1.060	1.050
Final R indices [I>2sigma(I)]	R_1 = 0.0210	R_1 = 0.0238
	wR_2 = 0.0478	wR_2 = 0.0527
R indices (all data)	R_1 = 0.0223	R_1 = 0.0270
	wR_2 = 0.0487	wR_2 = 0.0543
Flack parameter	0.015(14)	-0.015(5)
Largest diff. peak and hole	1.00 and −0.42 e$^-$ × Å^{-3}	0.67 and −0.32 e$^-$ × Å^{-3}

Table 2.1 (cont.) Crystal data and structure refinements for compounds **2.3** and **2.4**.

	2.3	**2.4**
Empirical formula	$C_8H_{13.91}K_2O_{17.96}V_2$	$C_8H_{24}Na_2O_{23}V_2$
Formula weight	577.54	636.13
Temperature	100(2) K	100(2) K
Wavelength	0.71073 Å	0.71073 Å
Crystal system	orthorhombic	orthorhombic
Space group	$C222_1$	$P2_12_12_1$
Unit cell dimensions	a = 8.4341(13) Å	a = 8.5931(5) Å
	b = 17.331(3) Å	b = 10.4332(6) Å
	c = 25.140(4) Å	c = 24.2289(13) Å
	α = 90°	α = 90°
	β = 90°	β = 90°
	γ = 90°	γ = 90°
Volume	3670.5(10) Å^3	2172.2(2) Å^3
Z	8	4
Density (calculated)	2.090 mg/m^3	1.945 mg/m^3
Absorption coefficient	1.566 mm^{-1}	1.010 mm^{-1}
F(000)	2317.0	1296.0
Crystal size	0.22 × 0.15 × 0.1 mm^3	0.32 × 0.2 × 0.06 mm^3
2θ range for data collected	3.24 to 50.226°	3.362 to 55.898°
Index ranges	$-10 \le h \le 10$	$-11 \le h \le 11$
	$-20 \le k \le 20$	$-13 \le k \le 13$
	$-30 \le l \le 30$	$-31 \le l \le 31$
Reflections collected	20299	43999
Ind. reflections	3291[R(int) = 0.0833]	5225[R(int) = 0.0647]
Data / restraints / parameters	3291 / 3 / 296	5225 / 20 / 374
Goodness-of-fit on F^2	0.922	1.173
Final R indices [I>2sigma(I)]	R_1 = 0.0339	R_1 = 0.0398
	wR_2 = 0.0616	wR_2 = 0.0877
R indices (all data)	R_1 = 0.0409	R_1 = 0.0415
	wR_2 = 0.0638	wR_2 = 0.0883
Flack parameter	0.01(2)	0.025(7)
Largest diff. peak and hole	0.46 and −0.31 e$^-$ × Å^{-3}	0.87 and −0.53 e$^-$ × Å^{-3}

Table 2.2 Selected interatomic distances (Å) for compounds **2.1** and **2.2**.

2.1							
Cs(1)^{8}–O(2)^{1}	3.197(2)	Cs(1)^{8}–O(17)^{1}	3.753(3)	Cs(2)^{7}–O(16)^{6}	3.082(2)	V(1)–O(14)	1.606(2)
Cs(1)^{4}–O(6)^{2}	3.013(2)	Cs(2)–O(1)	3.159(2)	Cs(2)–O(17)	3.266(3)	V(2)–O(4)	2.216(2)
Cs(1)^{9}–O(8)^{3}	3.157(2)	Cs(2)^{4}–O(3)^{2}	3.071(2)	Cs(2)^{4}–O(18)^{2}	3.456(3)	V(2)–O(5)	2.010(2)
Cs(1)^{2}–O(11)^{4}	3.124(2)	Cs(2)^{4}–O(6)^{2}	3.449(3)	V(1)–O(1)	2.010(2)	V(2)–O(10)	1.969(2)
Cs(1)^{2}–O(12)^{4}	3.193(2)	Cs(2)^{2}–O(12)^{4}	3.131(2)	V(1)–O(3)	2.269(3)	V(2)–O(11)	1.991(2)
Cs(1)–O(13)	3.539(3)	Cs(2)^{4}–O(13)^{2}	3.599(3)	V(1)–O(7)	1.987(2)	V(2)–O(15)	2.074(3)
Cs(1)–O(14)	3.019(2)	Cs(2)–O(14)	3.206(3)	V(1)–O(9)	1.952(2)	V(2)–O(16)	1.608(3)
Cs(1)^{10}–O(16)^{5}	3.019(2)	Cs(2)^{7}–O(15)^{6}	3.408(3)	V(1)–O(13)	2.043(3)		
2.2							
Rb(1)^{8}–O(2)^{1}	3.125(2)	Rb(1)^{8}–O(17)^{1}	3.539(2)	Rb(2)^{7}–O(16)^{6}	2.954(2)	V(1)–O(14)	1.607(2)
Rb(1)^{4}–O(6)^{2}	2.896(2)	Rb(2)–O(1)	2.997(2)	Rb(2)–O(17)	3.168(3)	V(2)–O(4)	2.200(2)
Rb(1)^{9}–O(8)^{3}	3.030(2)	Rb(2)^{4}–O(3)^{2}	2.983(2)	Rb(2)^{4}–O(18)^{2}	3.357(2)	V(2)–O(5)	2.001(2)
Rb(1)^{2}–O(11)^{4}	3.044(2)	Rb(2)^{4}–O(6)^{2}	3.357(3)	V(1)–O(1)	2.018(2)	V(2)–O(10)	1.964(2)
Rb(1)^{2}–O(12)^{4}	2.986(2)	Rb(2)^{2}–O(12)^{4}	2.999(2)	V(1)–O(3)	2.275(2)	V(2)–O(11)	1.987(2)
Rb(1)–O(13)	3.452(2)	Rb(2)^{4}–O(13)^{2}	3.513(2)	V(1)–O(7)	1.988(2)	V(2)–O(15)	2.083(2)
Rb(1)–O(14)	2.870(2)	Rb(2)–O(14)	3.063(2)	V(1)–O(9)	1.948(2)	V(2)–O(16)	1.616(2)
Rb(1)^{10}–O(16)^{5}	2.863(2)	Rb(2)^{7}–O(15)^{6}	3.244(2)	V(1)–O(13)	2.043(2)		

[1] 1+X, +Y, +Z [2] 1−X, −1/2+Y, 1/2−Z [3] 2−X, 1/2+Y, 1/2−Z [4] 1−X, 1/2+Y, 1/2−Z [5] 3/2−X, 1−Y, −1/2+Z
[6] 1/2−X, 1−Y, −1/2+Z [7] 1/2−X, 1−Y, 1/2+Z [8] −1+X, +Y, +Z [9] 2−X, −1/2+Y, 1/2−Z [10] 3/2−X, 1−Y, 1/2+Z

Table 2.2 (cont.) Selected interatomic distances (Å) for **2.3** and **2.4**.

2.3							
K(1)[8]–O(2)[2]	2.680(4)	K(2)–O(14)	2.894(4)	K(3A)–O(17D)[7]	3.13(2)	V(1)–O(9)	1.989(4)
K(1)[9]–O(8)[4]	3.245(5)	K(2)–O(15A)	2.906(13)	K(3B)–O(10)[7]	2.721(4)	V(1)[1]–O(12)[1]	1.954(4)
K(1)–O(11)[1]	2.806(4)	K(2)–O(15B)	2.727(16)	K(3B)–O(16A)	2.886(15)	V(1)–O(13)	1.589(4)
K(1)–O(13)[1]	2.812(4)	K(2)[6]–O(16A)[6]	2.830(13)	K(3B)–O(16B)[7]	2.509(17)	V(2)–O(4)	1.970(4)
K(2)[8]–O(6)[3]	2.706(5)	K(2)–O(16B)	3.049(17)	K(3B)–O(16C)[7]	2.419(17)	V(2)–O(5)	1.955(4)
K(2)[9]–O(8)[4]	2.802(4)	K(3A)–O(10)[7]	2.696(9)	K(3B)–O(17D)[7]	2.70(2)	V(2)–O(7)	1.977(4)
K(2)–O(9)	3.141(4)	K(3A)–O(14)[7]	2.696(9)	K(3B)–O(17E)[7]	2.75(2)	V(2)–O(9)	1.933(4)
K(2)–O(10)	2.949(5)	K(3A)–O(16A)[7]	2.842(14)	V(1)–O(1)	2.024(4)	V(2)–O(14)	1.596(4)
K(2)–O(11)	2.726(4)	K(3A)–O(16B)[7]	2.594(17)	V(1)–O(3)	2.326(4)		
K(2)–O(13)	2.988(4)	K(3A)–O(16C)[7]	2.648(17)	V(1)–O(4)	2.052(4)		

[1] +X, 1−Y, −Z; [2] −1/2+X, 3/2−Y, −Z; [3] −1/2+X, −1/2+Y, +Z; [4] −1+X, +Y, +Z; [5] −1+X, 1−Y, −Z; [6] −X, +Y, 1/2−Z; [7] 1−X, +Y, 1/2−Z; [8] 1/2+X, ½+Y, +Z; [9] 1+X, +Y, +Z

2.4							
Na(1)–O(5)	2.608(4)	Na(2)[1]–O(2)[3]	2.492(4)	V(1)–O(1)	2.026(3)	V(2)–O(5)	2.011(3)
Na(1)–O(6)	2.651(4)	Na(2)[3]–O(7)[1]	2.772(4)	V(1)–O(3)	2.252(3)	V(2)–O(10)	1.941(3)
Na(1)[3]–O(8)[1]	2.254(4)	Na(2)[3]–O(8)[1]	2.528(4)	V(1)–O(7)	1.965(3)	V(2)–O(11)	1.992(3)
Na(1)–O(17)	2.326(4)	Na(2)–O(15)	2.450(4)	V(1)–O(9)	1.947(3)	V(2)–O(15)	1.607(3)
Na(1)–O(18)	2.388(4)	Na(2)–O(19)	2.423(5)	V(1)–O(13)	1.599(3)	V(2)–O(16)	2.029(3)
Na(1)–O(19)	2.428(5)	Na(2)–O(20)	2.416(4)	V(1)–O(14)	2.064(4)		
Na(1)[4]–O(21)[2]	2.788(5)	Na(2)–O(21)	2.514(5)	V(2)–O(4)	2.359(3)		

[1] 1−X, −1/2+Y, 1/2−Z; [2] −1−X, +Y, +Z; [3] 1−X, 1/2+Y, 1/2−Z; [4] 1+X, +Y, +Z

Table 2.3. Hydrogen Bond distances (Å and °) for **2.1** and **2.2**.

D – H · · · A	d(D – H)	d(H · · · A)	d(D · · · A)	(D – H · · · A)°
		2.1		
O(3) – H(3A) · · · O(10)	0.84(2)	1.82(2)	2.644(3)	169(6)
O(4) – H(4A) · · · O(8)[1]	0.825(19)	1.73(2)	2.535(3)	164(5)
O(13) – H(13A) · · · O(17)[2]	0.823(19)	1.90(2)	2.720(4)	173(5)
O(13) – H(13B) · · · O(9)[2]	0.818(19)	1.74(2)	2.559(3)	179(6)
O(15) – H(15A) · · · O(12)[3]	0.792(18)	1.931(19)	2.719(4)	173(5)
O(15) – H(15B) · · · O(18)[1]	0.795(18)	1.915(19)	2.708(4)	175(5)
O(17) – H(17A) · · · O(2)	0.846(19)	2.31(3)	3.088(4)	153(4)
O(17) – H(17B) · · · O(2)[4]	0.815(19)	2.00(3)	2.750(4)	153(4)
O(18) – H(18A) · · · O(10)	0.819(19)	2.06(2)	2.860(4)	166(4)
O(18) – H(18B) · · · O(5)[5]	0.827(18)	1.985(19)	2.809(3)	174(4)
		2.2		
O(3) – H(3A) · · · O(10)	0.828(19)	1.87(2)	2.677(3)	165(5)
O(4) – H(4A) · · · O(8)[1]	0.815(19)	1.74(2)	2.540(3)	165(4)
O(13) – H(13A) · · · O(17)[2]	0.817(19)	1.89(2)	2.703(3)	176(4)
O(13) – H(13B) · · · O(9)[2]	0.824(19)	1.722(19)	2.543(3)	175(4)
O(15) – H(15A) · · · O(12)[3]	0.820(19)	1.882(19)	2.685(3)	166(4)
O(15) – H(15B) · · · O(18)[1]	0.827(18)	1.888(19)	2.709(3)	171(4)
O(17) – H(17A) · · · O(2)	0.842(19)	2.26(3)	3.012(3)	148(4)
O(17) – H(17B) · · · O(2)[4]	0.814(19)	2.01(2)	2.784(3)	159(4)
O(18) – H(18A) · · · O(10)	0.805(18)	2.03(2)	2.824(3)	168(4)
O(18) – H(18B) · · · O(5)[5]	0.832(18)	1.916(18)	2.748(3)	179(4)

[1] −1+X, +Y, +Z [2] 1−X, 1/2+Y, 1/2−Z [3] −1/2+X, 1/2−Y, 1−Z [4] −X, −1/2+Y, 1/2−Z [5] 1/2+X, 3/2−Y, 1−Z

Table 2.3 (cont.) Hydrogen Bond distances (Å and °) for **2.3**.

D – H · · · A	d(D – H)	d(H · · · A)	d(D · · · A)	(D – H · · · A)°
		2.3		
O(3) – H(3A) · · · O(1)[1]	0.83(3)	1.82(3)	2.655(5)	176(6)
O(10) – H(10A) · · · O(17E)	0.82(3)	2.03(5)	2.64(2)	131(6)
O(10) – H(10A) · · · O(3S_a)	0.82(3)	1.90(4)	2.71(2)	173(6)
O(10) – H(10A) · · · O(4S_a)	0.82(3)	2.15(5)	2.85(3)	144(6)

[1] 1/2+X, 3/2−Y, −Z

Table 2.3 (cont.) Hydrogen Bond distances (Å and °) for **2.4.**

D – H · · · A	d(D – H)	d(H · · · A)	d(D · · · A)	(D – H · · · A)°
		2.4		
O(3) – H(3A) · · · O(22)	0.81(3)	1.80(3)	2.608(5)	172(7)
O(4) – H(4A) · · · O(9)	0.83(3)	1.86(4)	2.640(4)	157(8)
O(14) – H(14A) · · · O(13)[1]	0.82(3)	2.07(5)	2.749(5)	140(6)
O(14) – H(14A) · · · O(23B)[2]	0.82(3)	2.22(5)	2.832(13)	131(6)
O(14) – H(14B) · · · O(12)[3]	0.84(3)	1.79(3)	2.608(5)	167(6)
O(16) – H(16A) · · · O(10)[4]	0.84(3)	1.72(3)	2.547(5)	167(7)
O(16) – H(16B) · · · O(22)[4]	0.84(3)	2.06(4)	2.864(5)	160(8)
O(17) – H(17A) · · · O(2)[5]	0.82(3)	1.96(3)	2.749(5)	161(6)
O(17) – H(17B) · · · O(11)[2]	0.82(3)	2.12(3)	2.893(5)	157(5)
O(18) – H(18A) · · · O(23A)[3]	0.84	2.06	2.773(7)	142.6
O(18) – H(18A) · · · O(23B)[3]	0.84	2.19	2.920(13)	145.3
O(18) – H(18B) · · · O(1)[6]	0.84	2.12	2.913(5)	157.9
O(19) – H(19A) · · · O(4)[2]	0.83(3)	2.07(4)	2.838(5)	154(7)
O(19) – H(19B) · · · O(23A)[7]	0.84(3)	2.09(4)	2.897(7)	159(7)
O(20) – H(20B) · · · O(18)[8]	0.83(3)	2.00(4)	2.794(6)	161(7)
O(21) – H(21A) · · · O(23B)	0.84	2.06	2.873(13)	164.3
O(22) – H(22A) · · · O(6)[5]	0.83(3)	1.97(3)	2.778(5)	165(5)
O(22) – H(22B) · · · O(17)	0.82(3)	1.92(3)	2.702(5)	160(6)
O(23A) – H(23A) · · · O(20)	0.85(3)	1.88(3)	2.707(7)	161(6)
O(23A) – H(23B) · · · O(9)[9]	0.84(3)	1.95(3)	2.755(6)	160(6)

[1] −1/2+X, 3/2−Y, −Z [2] 1−X, 1/2+Y, 1/2−Z [3] −1+X, +Y, +Z [4] 1−X, −1/2+Y, 1/2−Z [5] −X, 1/2+Y, 1/2−Z;
[6] 1/2−X, 1−Y, 1/2+Z; [7] 1/2+X, 3/2−Y, 1−Z; [8] 1/2+X, 3/2−Y, 1−Z; [9]3/2−X, 1−Y, 1/2+Z

Table 2.4 Atomic coordinates ($\times 10^4$) and equivalent isotropic displacement parameters ($Å^2 \times 10^3$) for compound **2.1**. $U_{(eq)}$ is defined as one third of the trace of the orthogonalized U_{ij} tensor.

2.1									
Atom	*x*	*y*	*z*	$U_{(eq)}$	Atom	*x*	*y*	*z*	$U_{(eq)}$
Cs1	9034.3(2)	6165.4(2)	1273.36(9)	11.96(5)	O12	4717(3)	1509(2)	4151.3(11)	12.6(5)
Cs2	3620.5(2)	3927.4(2)	1233.72(10)	14.04(5)	O13	6518(3)	7259(2)	2417.6(11)	14.2(5)
V1	5967.1(7)	5404.3(6)	2635.0(2)	8.91(12)	O14	6634(3)	4773(2)	2051.1(10)	14.2(5)
V2	3099.8(7)	4926.1(5)	4687.8(3)	9.56(12)	O15	598(3)	4862(3)	4905.3(12)	17.1(6)
O1	3617(3)	5621(2)	2355.9(10)	11.5(5)	O16	3718(3)	4848(2)	5341.3(11)	16.5(6)
O2	1083(3)	6446(2)	2440.0(11)	15.6(5)	O17	740(4)	3537(2)	2204.8(12)	18.7(6)
O3	4650(3)	6463(2)	3353.8(11)	10.6(5)	O18	8118(3)	6347(3)	4481.8(11)	15.7(5)
O4	1904(3)	5283(2)	3847.7(10)	9.8(5)	C1	2509(4)	6261(3)	2626.2(14)	11.7(7)
O5	2910(3)	6848(2)	4626.7(10)	12.9(5)	C2	3008(4)	6851(3)	3195.2(14)	10.6(7)
O6	2250(4)	8611(2)	4145.2(11)	20.8(6)	C3	1795(4)	6602(3)	3684.7(15)	10.0(7)
O7	7957(3)	5318(2)	3138.6(10)	11.8(5)	C4	2319(4)	7443(3)	4187.6(15)	12.5(7)
O8	9322(3)	3922(2)	3697.4(10)	13.6(5)	C5	8050(4)	4293(3)	3447.1(14)	10.2(7)
O9	5292(3)	3926(2)	3094.2(10)	10.7(5)	C6	6446(4)	3518(3)	3506.5(14)	9.7(7)
O10	5164(3)	4915(2)	4233.7(11)	10.1(5)	C7	5781(4)	3663(3)	4125.2(14)	9.3(7)
O11	3073(3)	3084(2)	4456.9(10)	11.9(5)	C8	4445(4)	2660(3)	4244.5(15)	9.7(7)

Table 2.4 (cont.) Atomic coordinates ($\times 10^4$) and equivalent isotropic displacement parameters ($Å^2 \times 10^3$) for compound **2.2**. $U_{(eq)}$ is defined as one third of the trace of the orthogonalized U_{ij} tensor.

2.2									
Atom	*x*	*y*	*z*	$U_{(eq)}$	Atom	*x*	*y*	*z*	$U_{(eq)}$
Rb1	9010.3(4)	6121.2(3)	1261.55(12)	11.96(7)	O12	4572(3)	1450.1(19)	4126.0(9)	12.4(5)
Rb2	3709.9(4)	3985.6(3)	1253.11(13)	14.71(7)	O13	6624(3)	7288(2)	2415(1)	14.4(5)
V1	6037.9(7)	5409.9(5)	2631.0(2)	8.69(10)	O14	6700(3)	4793(2)	2025.6(9)	13.9(4)
V2	3077.1(7)	4915.9(5)	4724.5(2)	9.44(10)	O15	518(3)	4962(2)	4939.2(10)	16.8(5)
O1	3649(3)	5634.6(19)	2337.1(9)	10.8(4)	O16	3639(3)	4810(2)	5404.0(9)	15.4(5)
O2	1081(3)	6486(2)	2416.7(9)	14.1(4)	O17	702(3)	3624(2)	2156.1(11)	18.2(5)
O3	4691(3)	6493.7(19)	3365.0(9)	10.1(4)	O18	8099(3)	6432(2)	4419.7(10)	15.1(5)
O4	1922(3)	5288(2)	3863.2(8)	10.4(4)	C1	2523(4)	6277(3)	2613.9(13)	10.8(6)
O5	2966(3)	6857.2(19)	4654.9(9)	12.7(4)	C2	3026(4)	6884(3)	3196.8(12)	9.6(6)
O6	2250(3)	8656(2)	4174(1)	19.9(5)	C3	1784(4)	6616(3)	3694.2(13)	9.5(5)
O7	8059(3)	5253(2)	3144.2(9)	12.5(4)	C4	2342(4)	7473(3)	4210.5(13)	11.6(6)
O8	9391(3)	3803(2)	3709.9(9)	13.3(4)	C5	8112(4)	4211(3)	3460.8(12)	11.0(6)
O9	5310(3)	3915(2)	3092.8(9)	10.1(4)	C6	6461(4)	3465(3)	3517.3(13)	10.5(6)
O10	5185(2)	4877(2)	4269.4(9)	9.8(4)	C7	5763(4)	3604(3)	4147.5(12)	9.5(6)
O11	2981(3)	3064(2)	4473.7(9)	12.2(4)	C8	4348(4)	2613(3)	4245.9(12)	9.3(6)

Table 2.4 (cont.) Atomic coordinates ($\times 10^4$) and equivalent isotropic displacement parameters ($Å^2 \times 10^3$) for compound **2.3**. $U_{(eq)}$ is defined as one third of the trace of the orthogonalized U_{ij} tensor.

2.3									
Atom	*x*	*y*	*z*	$U_{(eq)}$	Atom	*x*	*y*	*z*	$U_{(eq)}$
V1	2953.1(12)	6481.1(6)	555.6(4)	12.3(2)	O15A	-550(16)	6363(6)	2034(8)	44(4)
V2	4511.3(12)	6364.7(6)	1627.8(4)	16.4(3)	O15B	-230(20)	6449(10)	1830(12)	30(7)
K1	-361(2)	5000	0	16.5(4)	O16A	1655(17)	4748(9)	2636(5)	29(4)
K2	1147.4(15)	5084.1(8)	1547.4(5)	20.4(3)	O16B	2050(20)	4367(11)	2613(7)	42(5)
K3A	5000	4758(6)	2500	23.1(14)	O16C	2340(20)	3962(10)	2620(6)	25(5)
K3B	5000	4458(9)	2500	23.1(14)	O17D	3070(20)	3214(11)	2542(7)	55(5)
O1	2385(4)	7459(2)	157.2(14)	14.4(10)	O17E	5170(20)	3059(11)	1985(8)	55(8)
O2	2855(4)	8725(2)	83.7(16)	18.8(10)	C1	3168(7)	8092(4)	270(2)	15.2(14)
O3	5223(5)	7243(2)	582.3(16)	15.2(9)	C2	4464(7)	7974(3)	681(2)	15.2(14)
O4	3109(5)	7093(2)	1252.5(14)	15.0(9)	C3	3741(7)	7857(3)	1239(2)	17.2(14)
O5	5552(5)	7318(2)	1855.3(15)	20.3(10)	C4	4988(8)	7955(4)	1661(2)	20.4(15)
O6	5458(6)	8598(3)	1787.2(16)	31.9(12)	C5	6805(7)	5323(4)	1236(3)	21.4(15)
O7	6581(5)	5830(2)	1610.3(17)	21.4(10)	C6	5402(7)	5205(3)	860(2)	15.0(14)
O8	8030(5)	4959(3)	1172.2(18)	31.8(12)	C7	4766(7)	4378(3)	920(2)	14.3(14)
O9	4202(5)	5746(2)	996.3(15)	13.2(10)	C8	3435(7)	4230(3)	519(2)	11.6(13)
O10	4234(5)	4294(3)	1454.6(16)	21.0(11)	O1S_a	4000(20)	2522(11)	1132(8)	85(5)
O11	2034(5)	4354(2)	633.8(15)	16.4(10)	O2S_a	2930(20)	2635(12)	2620(7)	85(5)
O12	3941(5)	3984(2)	70.4(15)	15.2(10)	O3S_a	3720(30)	2820(14)	1775(10)	85(5)
O13	1216(5)	6132(2)	603.2(15)	16.2(9)	O4S_a	4760(40)	2668(16)	1507(13)	85(5)
O14	3491(5)	6003(2)	2101.1(15)	22.4(11)					

Table 2.4 (cont.) Atomic coordinates ($\times 10^4$) and equivalent isotropic displacement parameters ($Å^2 \times 10^3$) for compound **2.4**. $U_{(eq)}$ is defined as one third of the trace of the orthogonalized U_{ij} tensor.

2.4									
Atom	*x*	*y*	*z*	$U_{(eq)}$	Atom	*x*	*y*	*z*	$U_{(eq)}$
V1	2677.6(9)	6747.6(7)	657.0(3)	10.66(16)	O15	7047(4)	6051(3)	2979.1(13)	16.5(7)
V2	6087.4(9)	5501.6(7)	2461.4(3)	10.80(16)	O16	6240(4)	3611(3)	2649.7(14)	16.1(7)
Na1	2589(3)	5949(2)	3719.5(8)	26.6(5)	O17	1098(4)	7579(3)	3332.2(14)	16.2(7)
Na2	6822(2)	6074.7(19)	3987.1(8)	17.8(4)	O18	1833(5)	6387(4)	4649.0(15)	29.4(9)
O1	1969(4)	4897(3)	628.2(13)	14.2(7)	O19	4628(5)	7514(4)	3882.6(18)	26.8(9)
O2	1506(4)	3026(3)	1037.8(13)	13.8(7)	O20	6235(5)	6140(4)	4961.7(16)	27.1(9)
O3	1901(4)	6220(3)	1515.0(13)	9.9(6)	O21	9493(5)	5180(4)	3814.1(19)	33(1)
O4	4437(4)	4614(3)	1783.8(13)	11.1(6)	C1	1711(5)	4203(4)	1055.3(18)	11.2(9)
O5	3911(4)	5566(3)	2764.9(12)	13.0(6)	C2	1652(5)	4882(4)	1612.2(18)	9.5(8)
O6	1529(4)	4738(3)	2834.1(13)	15.1(7)	C3	2921(5)	4363(4)	1996.1(17)	9.8(8)
O7	3321(4)	8425(3)	946.5(14)	15.1(7)	C4	2750(5)	4921(4)	2578.7(18)	12.1(8)
O8	5463(4)	9563(3)	1102.1(14)	16.1(7)	C5	4816(5)	8535(4)	1030.2(18)	11.6(9)
O9	4692(4)	6226(3)	948.6(13)	10.9(6)	C6	5723(5)	7277(4)	1013.7(18)	11.0(9)
O10	5784(4)	7015(3)	2007.9(13)	11.1(6)	C7	6725(5)	7115(4)	1532.2(18)	10.2(8)
O11	7632(4)	5102(3)	1873.1(13)	14.1(6)	C8	7731(5)	5915(4)	1471.7(19)	12.4(9)
O12	8568(4)	5739(3)	1067.2(14)	16.6(7)	O22	613(4)	7750(3)	2233.0(14)	16.6(7)
O13	3025(4)	6861(3)	10.6(13)	18.0(7)	O23A	9224(6)	5632(5)	5239(2)	17.9(15)
O14	446(4)	7478(4)	674.3(15)	19.0(7)	O23B	9272(14)	4715(12)	4980(5)	25(4)

45° 2θ in steps of 0.04°. No impurities were observed and the calculated and experimental PXRD patterns are in excellent agreement. See **Figure 2.2**.

Energy-Dispersive Spectroscopy (EDS).

Elemental analysis was performed on the single crystals using a TESCAN Vega-3 SBU scanning electron microscope (SEM) with EDS capabilities. The crystals were mounted on carbon tape and analyzed using a 20 kV accelerating voltage and an accumulation time of 1 minute. As a qualitative measure, EDS confirmed the presence of each reported element in the title compounds.

Fourier Transform Infrared Spectroscopy (IR).

IR spectra of ground crystals of **2.1**, **2.2**, **2.3**, and **2.4** were recorded on a PerkinElmer Spectrum 100 FT-IR spectrometer fitted with an ATR accessory in the range of 650-4000 cm^{-1}.

UV/Vis Diffuse Reflectance Spectroscopy (UV/Vis).

UV/Vis diffuse reflectance spectroscopy data of ground crystals of **2.1**, **2.2**, **2.3**, and **2.4** were obtained using a PerkinElmer Lambda 35 UV-Vis scanning spectrophotometer equipped with an integrating sphere accessory in the range of 200-900 nm. Reflectance data were transformed to absorbance via the Kubelka-Munk function.

Magnetic Susceptibility.

The magnetic susceptibility of **2.1**, **2.2**, **2.3**, and **2.4** were measured using a Quantum Design MPMS SQUID VSM Evercool magnetometer. The zero-field cooled magnetic susceptibility was measured as a function of temperature between 2-300K in an

applied field of 1000 Oe. The measured magnetic data were corrected for shape and radial offset effects using methods reported by Morrison et. al.[33]

Second Harmonic Generation (SHG).

Powder SHG measurements were performed on a modified Kurtz nonlinear-optical (NLO) system using a pulsed Nd:YAG laser with a wavelength of 1064 nm. Comparisons with known SHG materials were made using ground crystalline α-SiO_2. A detailed description of the equipment and methodology has been published elsewhere.[26, 34]

Results and Discussion

Synthesis.

A number of organic acids, such as tartaric acid, are known to reduce many transition elements under mild hydrothermal conditions and can be used as one route to obtain V^{4+} solution species *in situ*.[21, 25, 35] Separating the reduction step from the crystallization step has shown to be helpful in eliminating the formation of undesired V(V) species over desired V(IV) containing products.[25] In addition, simple alcohols such as methanol and ethanol can be added to reactions to increase yields via decreased product solubility in solution without incorporation of the alcohol into the product. Crystals of **2.1**, **2.2**, and **2.3** were obtained via such a two-step hydrothermal method to avoid precipitation of alkali tartrates, which tend to crystallize much faster than the time it takes to reduce the vanadium from 5+ to 4+. To achieve formation of **2.1**, **2.2**, and **2.3**, the V(IV) precursor solution was created in the first step by reacting V_2O_5 with L-(+)-tartaric acid at 160°C for four hours. The resultant blue solution was then used as the V(IV) source material for the second step in which it was reacted with a combination of

ACl and A_2CO_3 A = Cs, Rb, K at only 90°C. Initial yields of **2.2** and **2.3** were quite low; however, the addition of ethanol and methanol in step two to reduce the solubility of the dissolved reagents caused the yield to increase to approximately 80%. The use of ethanol or methanol to aid in the crystallization of **2.1** resulted in the formation of a blue powder impurity instead of phase pure crystals. However, even in the absence of additional alcohols, plentiful, well faceted violet crystals of **2.1** were obtained with a yield of approximately 75%. Attempts to crystallize a sodium compound via the same method were unsuccessful and did not yield single crystals. Slow evaporation of a sodium reaction solution over the course of 120 days produced **2.4** with a yield of approximately 30%. Crystals of **2.1**, **2.2**, **2.3**, and **2.4** were isolated by decanting the mother liquor and collecting the crystals by filtration.

Structure.

Compounds **2.1** and **2.2** are isostructural and crystallize in the chiral, orthorhombic space group $P2_12_12_1$ and exhibit a three-dimensional crystal structure consisting of distorted VO_6 octahedra and irregular AO_9/AO_{10} (A = Cs, Rb) polyhedra linked via bridging tartrate ligands that are partially deprotonated and an extensive hydrogen bonding network. Previous studies have found the protonation pattern of tartaric acid in V(IV) solutions to be pH dependent.[36, 37] The extended structure of **2.1** and **2.2** viewed along the *a*-axis is shown in **Figure 2.3**. V(1) and V(2) are located in highly distorted VO_6 octahedra with four equatorial V-O bonds of roughly the same length, one exceptionally long V-O axial bond, and one exceptionally short V-O bond. Four out of six oxygens bonded to V(1), O1, O3, O7, and O9, originate from two bidentate tartrate ligands; one, O13, from a monodentate water; and one, O14, from a bridging oxygen

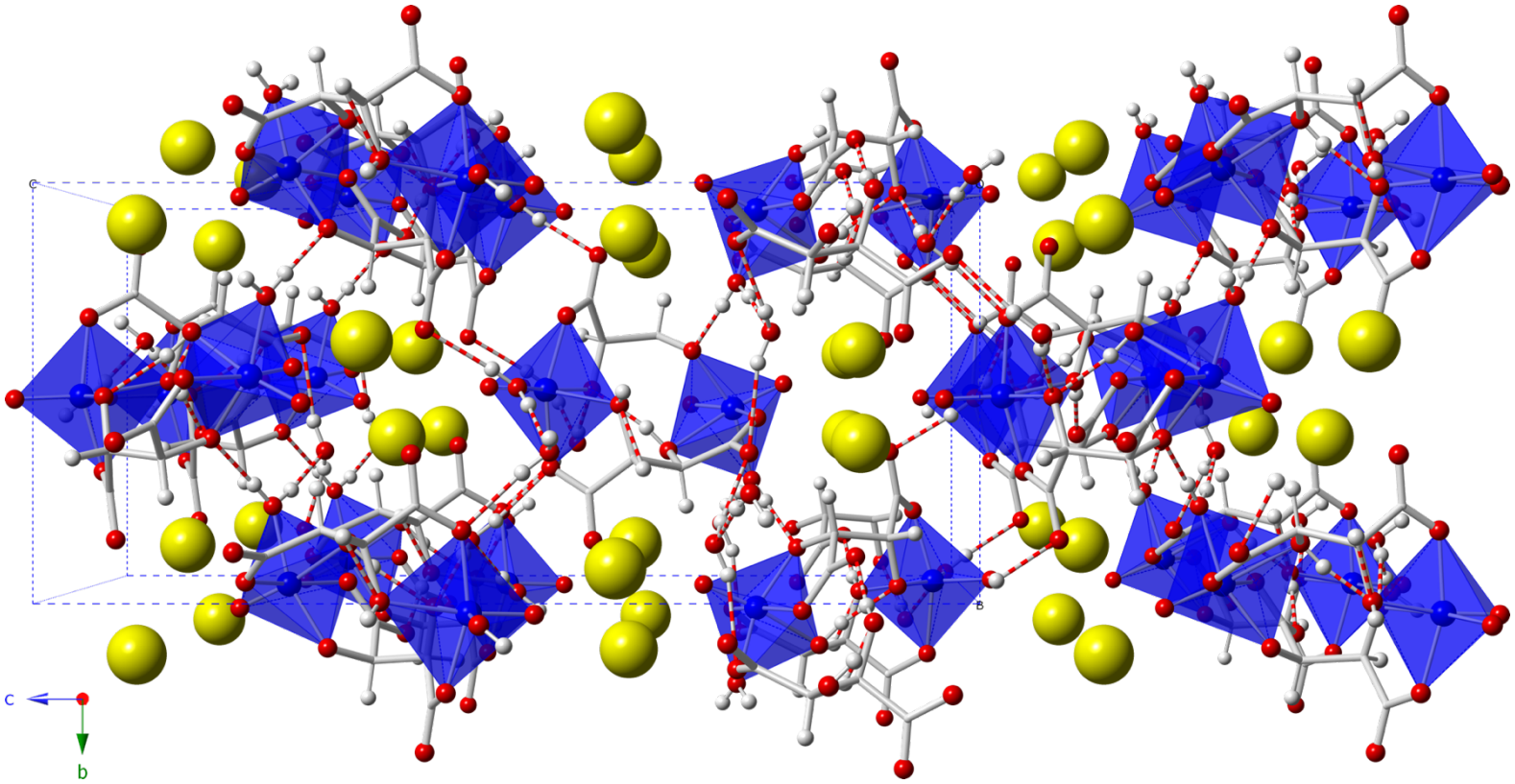

Figure 2.3 Compounds **2.1** and **2.2** viewed down the *a* axis. Blue, grey, red, white, and yellow represent vanadium, carbon, oxygen, hydrogen, and Cs/Rb, respectively. Hydrogen bonds are shown as dashed red and white cylinders.

(oxo) atom. Four out of six oxygens bonded to V(2), O4, O5, O10, and O11, originate from two bidentate tartrate ligands; one, O15, from a monodentate water; and one, O16, from a bridging oxygen (oxo) atom. The V-O bond distances of V(1) and V(2) range from 1.606(2) Å – 2.279(5) Å. The bidentate tartrate ligands connect the two VO_6 distorted octahedra into the dimeric unit shown in **Figure 2.4**. These dimeric units are connected to each other via Cs or Rb cations to create the extended structure shown in **Figure 2.3**. The structure contains two types of alkali cations, A(1) and A(2), (A = Cs, Rb), which are located in 9 and 10 coordinated irregular polyhedra, respectively. The Cs(1)-O and Rb(1)-O distances range from 3.013(2) Å – 3.753(3) Å and 2.863(2) Å – 3.539(2) Å, respectively. The Cs(2)-O and Rb(2)-O distances range from 3.071(2) Å – 3.599(3) Å and 2.954(2) Å – 3.513(2) Å, respectively. One water molecule is coordinated to A(1) and two water molecules are coordinated to A(2). All hydrogen atoms could be located on these water molecules and were refined freely. These water molecules and hydroxyl groups on the tartrate ligands give rise to an extensive hydrogen bonding network shown in **Figure 2.3**, with hydrogen bond distances ranging from 1.722(19) Å – 2.31(3) Å. Select hydrogen bond distances are given in **Table 2.3**.

Compound **2.3** crystallizes in the orthorhombic space group $C222_1$ and exhibits a three dimensional structure consisting of VO_6 distorted octahedra, VO_5 square pyramids, and KO_7/KO_8 irregular polyhedra linked via bridging tartrate ligands that are fully deprotonated. The extended structure of **2.3** viewed down the *a*-axis is shown in **Figure 2.5**. The difference in the protonation pattern of **2.3** accounts for the structural change when compared to **2.1** and **2.2**, which contain tartrate ligands that are only partially deprotonated. V(1) and V(2) are located in VO_6 distorted octahedra and VO_5 square

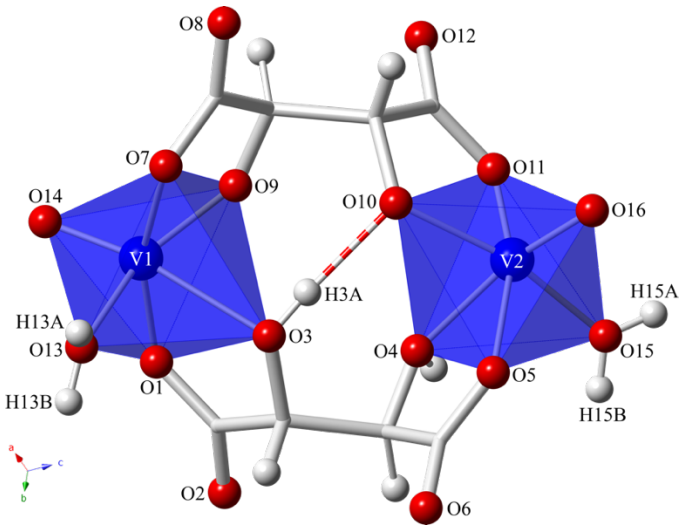

Figure 2.4 V_2O_{12} dimer of compounds **2.1** and **2.2**. The intracluster hydrogen bond is shown as a dashed red and white cylinder.

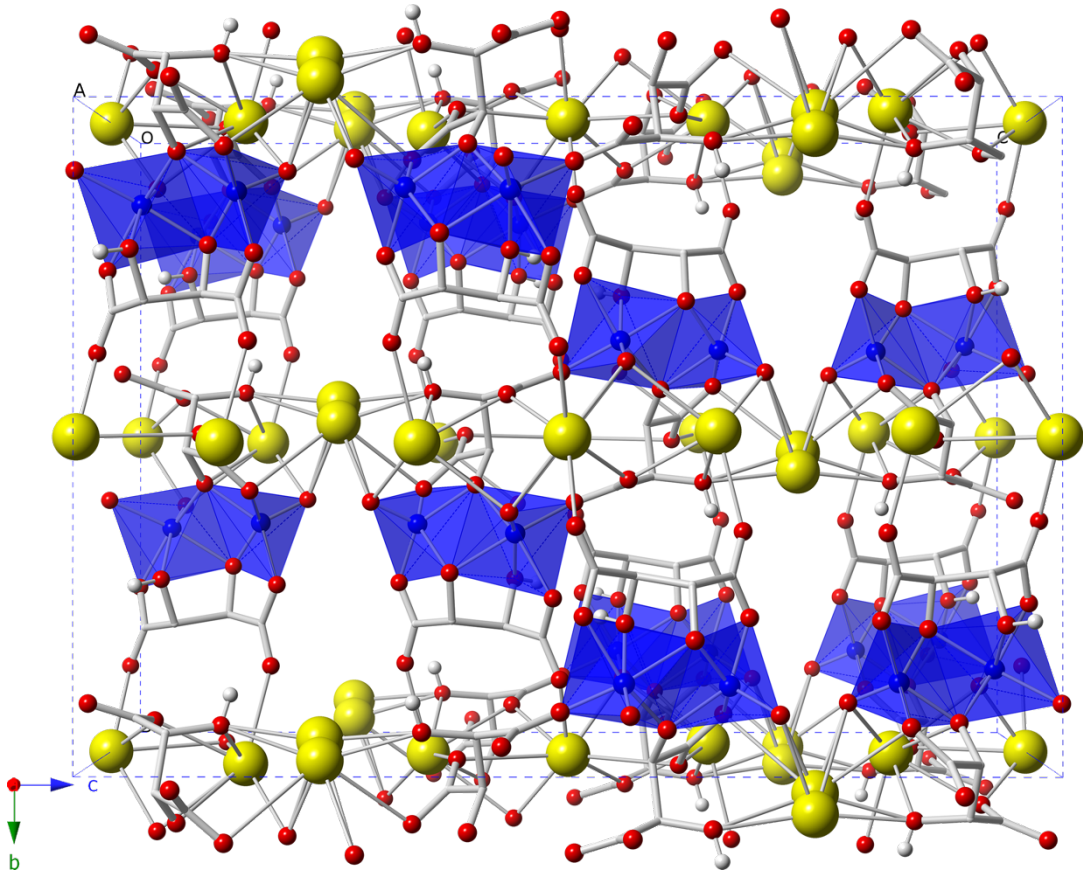

Figure 2.5 Compound **2.3** viewed in the *bc* plane. Disordered K3A/K3B cations join double layer K/VO/tartrate slabs into a 3D framework. Blue, grey, red, white, and yellow represent vanadium, carbon, oxygen, hydrogen, and potassium, respectively. Interstitial waters reside in the cavities and are omitted for clarity.

pyramids. These polyhedra share an edge, forming unusual edge sharing V_2O_9 dimers. Five out of six oxygens bonded to V(1), O1, O3, O4, O9, and O12, originate from a tridentate and two monodentate tartrate ligands, respectively, and one, O13, from a bridging oxygen (oxo) atom. Four out of five oxygens bonded to V(2), O4, O5, O7, and O9, originate from two bidentate tartrate ligands and one, O14, from a bridging oxygen (oxo) atom. The V-O bond distances on V(1) and V(2) range from 1.589(4) Å – 2.326(4) Å and 1.596(4) Å – 1.977(4)Å, respectively. V(1) and V(2) polyhedra and bridging tartrate ligands form clusters shown in **Figure 2.6**. These clusters are connected via three types of potassium atoms, K1, K2, and K3A/B, which are located in 8 and two 7 coordinate polyhedra, respectively. K1-O and K2-O distances range from 2.680(4) Å – 3.245(5) Å and 2.706(5) Å – 3.184 Å, respectively. K3 is disordered over two sites with partial occupancies of 0.69(2) and 0.31(2) for K3A and K3B, respectively. K3A/B-O distances range from 2.419(17) Å – 3.13(2) Å. Disordered water molecules, O15 – O17, and tartrate ligands are coordinated to these potassium atoms. Hydrogen atoms could not be located on the disordered water molecules. Additional disordered water molecules, O1S – O4s, are located within cavities formed by the linkage of $K_2(VO)_2(C_4H_2O_6)_2$ clusters into a layer, that is shown in **Figure 2.7**. These layers are connected by K1 into double layer slabs that are further connected via K3A/B to form the overall extended structure.

Compound **2.4** crystallizes in the orthorhombic space group $P2_12_12_1$ and exhibits a three dimensional structure consisting of VO_6 distorted octahedra and irregular NaO_7 polyhedra linked via bridging tartrate ligands, bridging waters, and an extensive hydrogen bonding network. The extended structure of **2.4** viewed along the *a*-axis is

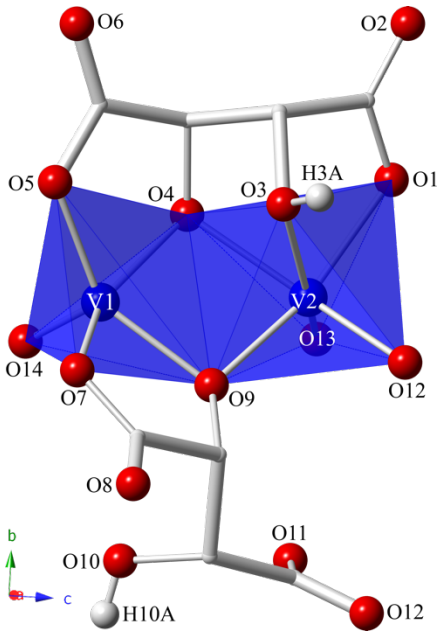

Figure 2.6 V_2O_9 dimer of compound **2.3**.

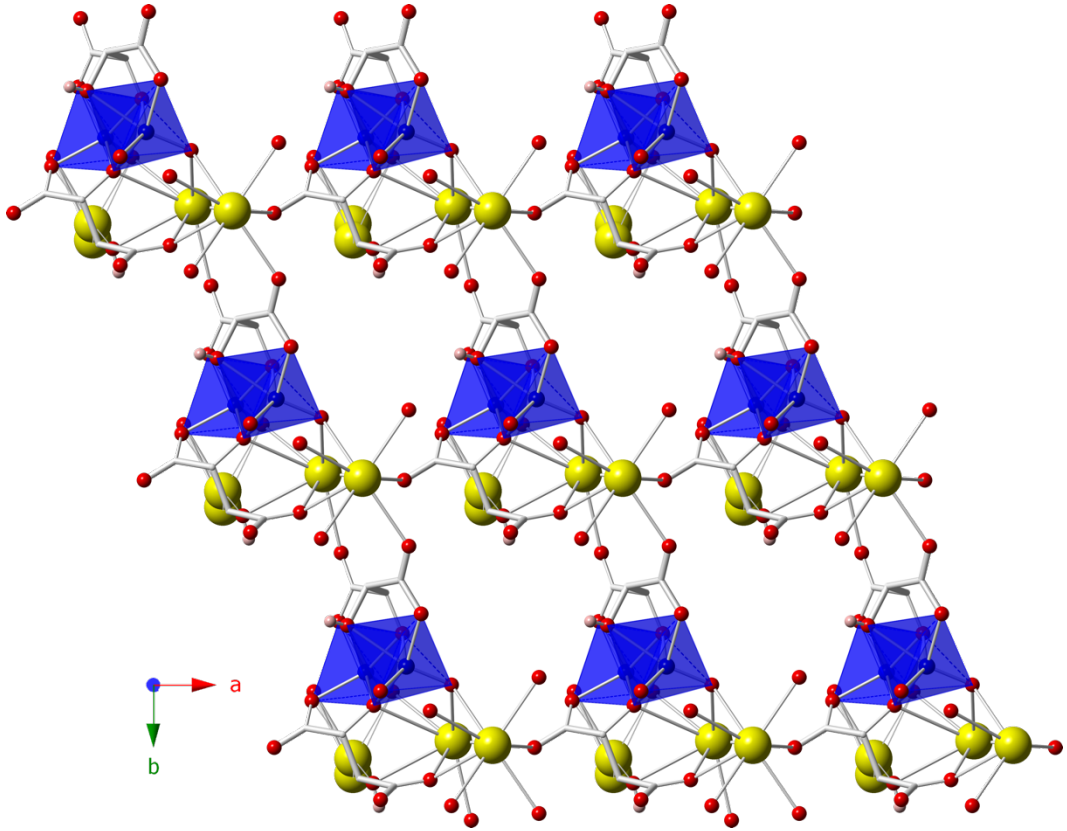

Figure 2.7 $K_2(VO)_2(C_4H_2O_6)_2$ cluster interconnectivity of compound **2.3** viewed in the *ab* plane. Blue, grey, red, white, and yellow represent vanadium, carbon, oxygen, hydrogen, and potassium, respectively. Interstitial waters reside in the cavities formed and are omitted for clarity.

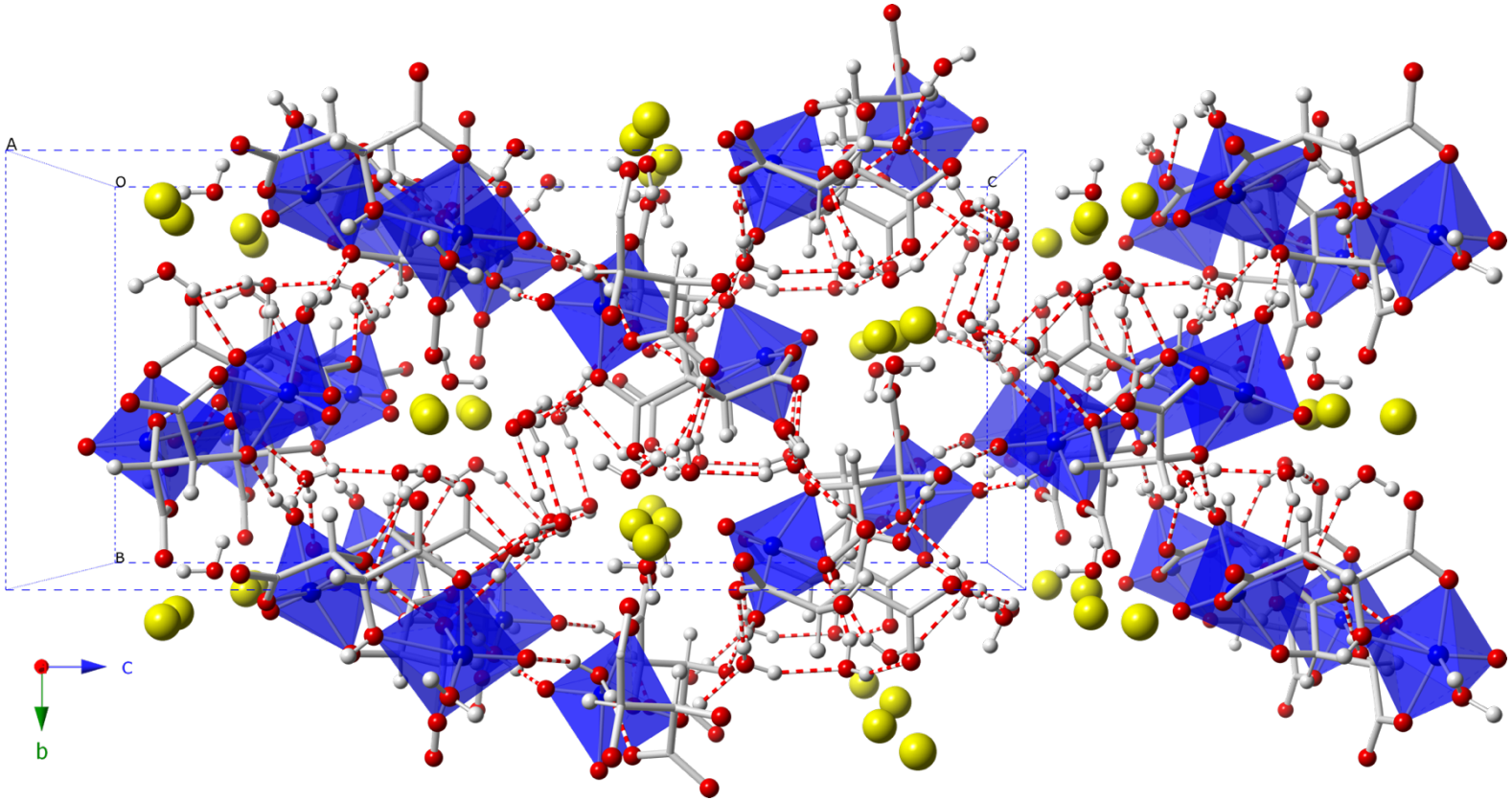

Figure 2.8 Compound **2.4** viewed down the *a* axis. Blue, grey, red, white, and yellow represent vanadium, carbon, oxygen, hydrogen, and Cs/Rb, respectively. Hydrogen bonds are shown as dashed red and white cylinders.

shown in **Figure 2.8**. V(1) and V(2) are located in distorted VO_6 octahedra. Four out of six oxygens bonded to V(1), O1, O3, O7, and O9, originate from two bidentate tartrate ligands, one, O14, from a monodentate water; and one, O13, from a bridging oxygen (oxo) atom. Four out of six oxygens bonded to V(2), O4, O5, O10, and O11, originate from two bidentate tartrate ligands; one, O16, from a monodentate water; and one, O15, from a bridging oxygen (oxo) atom. The V-O bond distances of V(1) and V(2) range from 1.599(3) Å – 2.359(3) Å. The bidentate tartrate ligands connect the two VO_6 distorted octahedra into a dimeric unit similar to dimer observed in **2.1** and **2.2**. These dimeric units are connected to each other via Na cations, water, and an extensive hydrogen bonding network to create the extended structure shown in **Figure 2.8**. The structure contains two types of alkali cations, Na(1) and Na(2), which are located in 7 coordinated irregular polyhedra. The Na(1)-O and Na(2)-O distances range from 2.254(4) Å – 2.788(5) Å and 2.416(4) Å – 2.772(4) Å, respectively. Four water molecules are coordinated to Na(1) and three water molecules are coordinated to Na(2). All hydrogen atoms could be located on these water molecules and were refined freely. These water molecules and hydroxyl groups on the tartrate ligands give rise to an extensive hydrogen bonding network shown in **Figure 2.8**, with hydrogen bond distances ranging from 1.80(3) Å – 2.22(5) Å. Select hydrogen bond distances are given in **Table 2.3**.

Fourier Transform Infrared Spectroscopy (IR).

The IR spectra for **2.1**, **2.2**, **2.3**, and **2.4** are shown in **Figure 2.9**, were collected between 650 – 4000 cm^{-1}. The broad band observed in the 3200 – 3600 cm^{-1} region is characteristic for O-H vibrations of water molecules and hydroxyl groups. The presence of tartrate groups produces vibrations of C-O, C-C, C-O-O. The expected bending mode

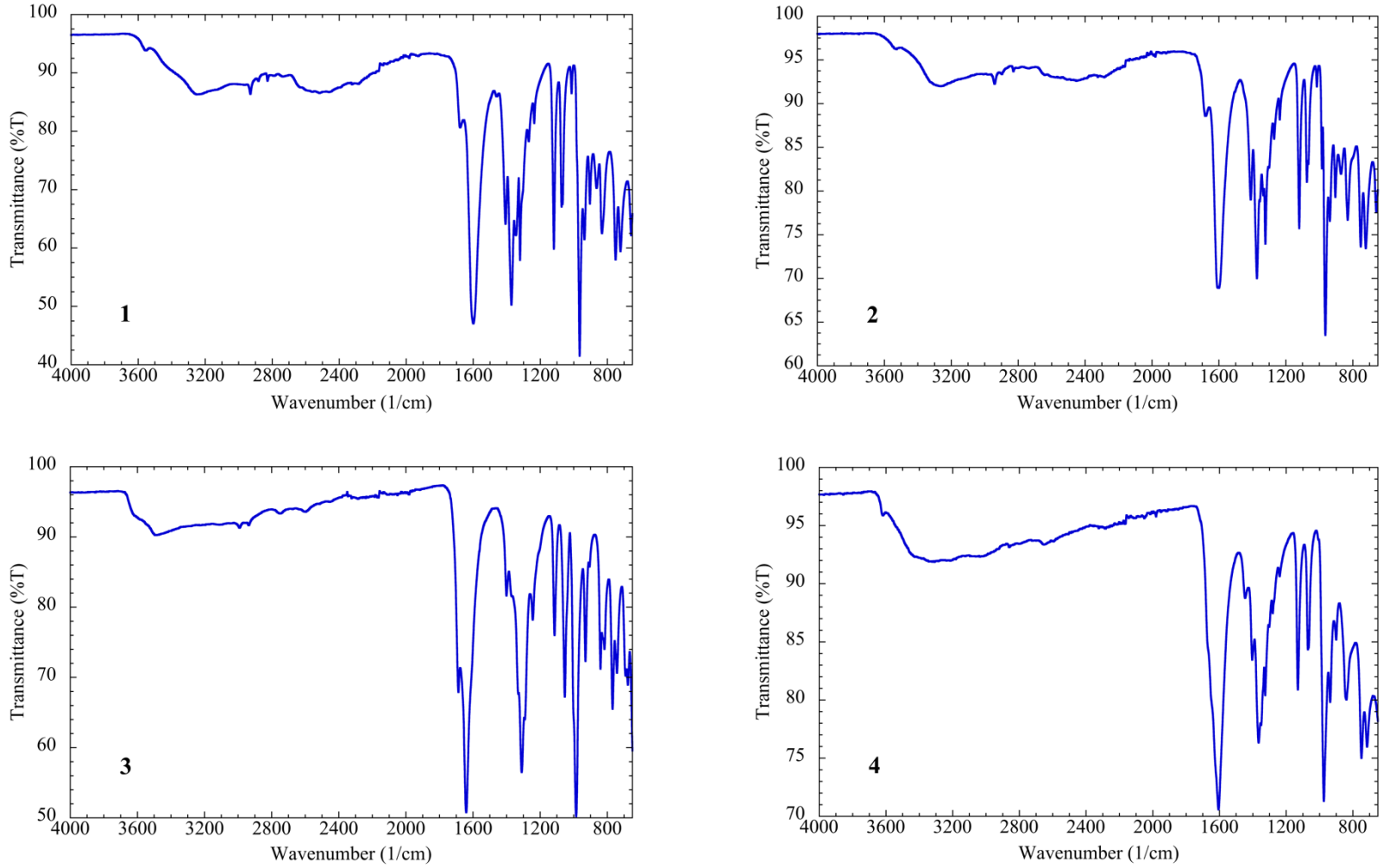

Figure 2.9 IR spectra of compound **2.1**, pane 1; compound **2.2**, pane 2; compound **2.3**, pane 3; and compound **2.4**, pane 4.

of water at around 1600 cm^{-1} overlaps with the intense C-O stretching mode of the tartrate group. The bands in the region of 1200 – 1450 cm^{-1} are attributed to the symmetric stretching modes of the tartrate C-O bonds and the remainder of the bands observed below 1000 cm^{-1} can be assigned to V-O, C-C and C-O-O vibrational modes.[20, 21, 38-40]

UV/Vis Diffuse Reflectance Spectroscopy (UV/Vis) and Magnetism.

UV/Vis absorbance data shown in **Figure 2.10** were collected using ground crystals of **2.1**, **2.2**, **2.3**, and **2.4**. Vanadium in the +4 oxidation state has a d^1 electron configuration and a transition from the $^2T_{2g}$ ground state to the ^2E_g excited state is expected. Three absorption maxima are observed for each compound approximately located at 375 nm, 550 nm, and 775 nm and can be assigned to $d_{xy} \rightarrow d_z2$, $d_{xy} \rightarrow d_x2_{-y}2$, and $d_{xy} \rightarrow d_{xz}/d_{yz}$ transitions, respectively.[41, 42] The unpaired electrons in **2.1**, **2.2**, **2.3**, and **2.4** can be observed in magnetic susceptibility measurements. The temperature dependences of the magnetic susceptibilities of **2.1**, **2.2**, **2.3**, and **2.4** measured in an applied field of 1000 Oe, are shown in **Figure 2.11**. In **2.1**, **2.2**, and **2.4** the distorted VO_6 octahedra are separated by the bridging tartrate ligands and, due to the long V-V separation, no magnetic coupling is expected or observed. Down to 2K, the data do not reveal any long-range magnetic order and follow the Curie-Weiss (C-W) law as expected for simple paramagnetic species. The magnetic moments calculated from the inverse susceptibilities are 1.71 μ_B, 1.72 μ_B, and 1.75 μ_B for **2.1**, **2.2**, and **2.4** respectively, which are in good agreement with the expected value of 1.73 μ_B for a $3d^1$ spin-only system.[43] The magnetic property of **2.3**, however, is quite different from the other members, as expected considering its crystal structure in which edge-shared V_2O_9 dimers are present.

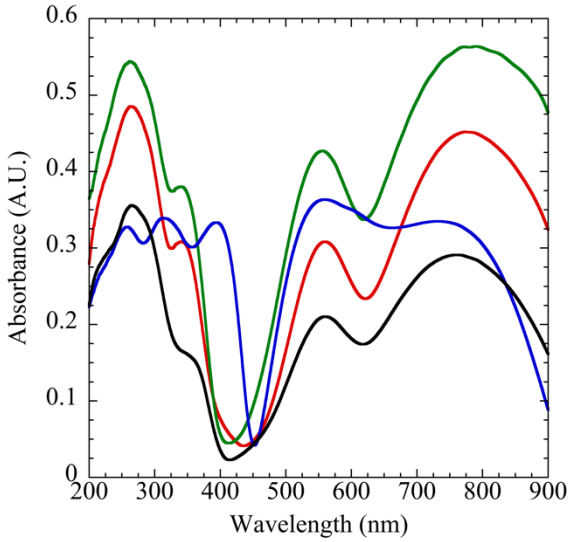

Figure 2.10 UV/Vis data for compound **2.1**, compound **2.2**, compound **2.3**, and compound **2.4** shown in red, green, and blue, respectively. Three absorption maxima are observed for each compound approximately located at 375 nm, 550 nm, and 775 nm and can be assigned to $d_{xy} \rightarrow d_z2$, $d_{xy} \rightarrow d_x2_{-y}2$, and $d_{xy} \rightarrow d_{xz}/d_{yz}$ transitions, respectively.

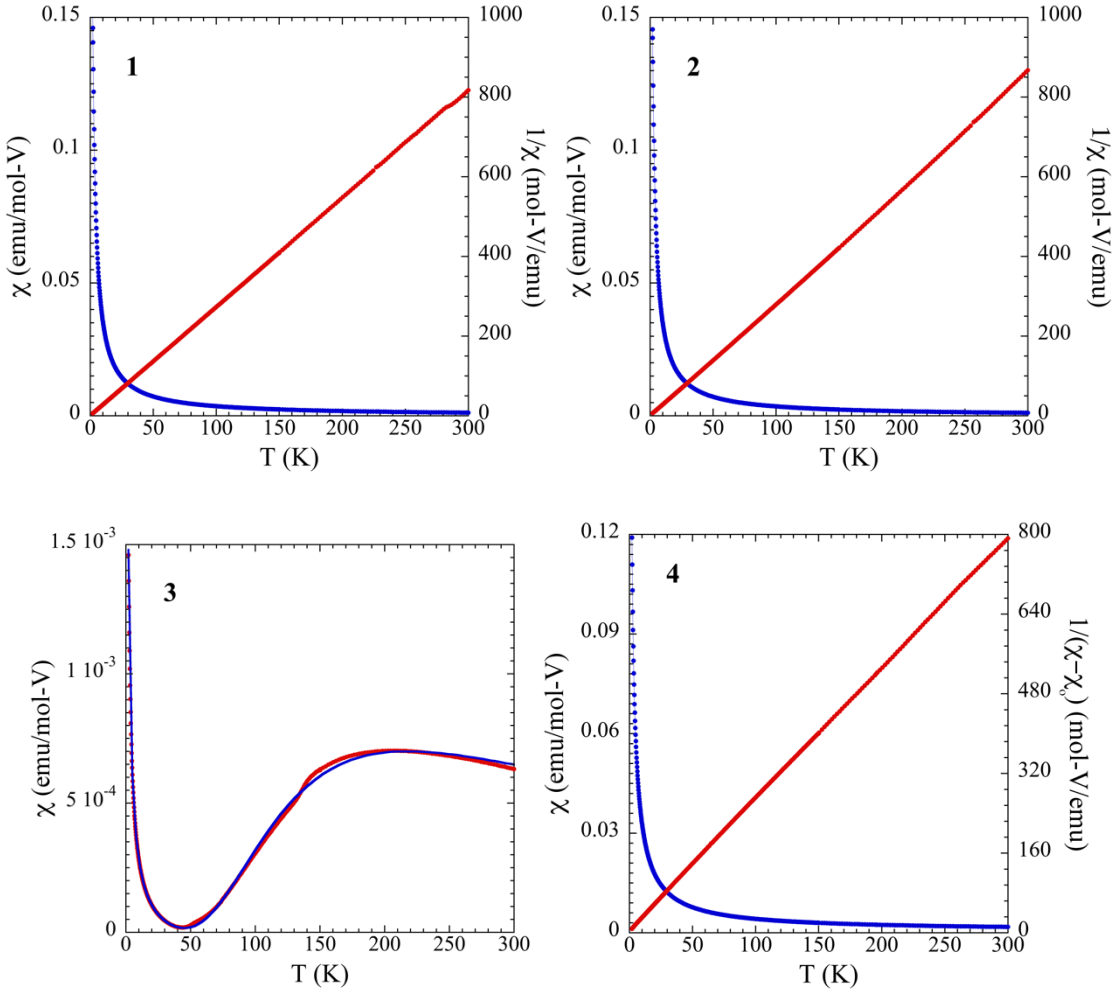

Figure 2.11 Magnetic susceptibility plots of compound **2.1**, pane 1; compound **2.2**, pane 2; compound **2.3**, pane 3; and compound **2.4**, pane 4. χ and 1/χ are shown in blue and red, respectively, for compound **2.1**, compound **2.2**, and compound **2.4**. For compound **2.3**, χ and a fit to the data using the Bleaney-Bowers equation for isolated dimers are shown in blue and red, respectively.

Since there was no significant difference between zfc and fc data, only zfc data is shown for the purpose of discussion. The broad maximum in the susceptibility data observed at approximately 180 K, is indicative of spin coupling within the vanadium dimers in this compound, whereas the sharp increase at low temperature is likely due to the presence of a small amount of a paramagnetic impurity. Considering the crystal structure of **2.3**, one would expect that the magnetic interactions between the V^{4+} ions within the dimer would dominate the magnetic data and that magnetic coupling between dimers, due to their long physical separation, would not be observed. Such a spin ½ dimer system is perhaps the simplest low-dimensional magnetic system exhibiting a spin-gap between the ground and excited states.[44-46] In order to better understand the magnetism of **2.3**, we modeled the magnetic susceptibility data using the modified Bleaney-Bowers equation,[47-49] which can be written as

$$\chi_M = \frac{N_A \mu_B^2 g^2}{k_B T\left(3+E^{-2J/k_B T}\right)} + \frac{C}{T-\theta} + \chi_{TIP} \qquad (1)$$

where N_A, g, μ_B, k_B, and *J* are Avogadro's number, g-factor, Bohr-magneton, Boltzmann constant, and the intradimer exchange coupling constant, respectively. The second C-W term corrects for contributions from trace amount of impurities that are sometimes observed in the very low temperature regime, and χ_{TIP} is the temperature-independent paramagnetic susceptibility. The best fit generated values of g = 1.89, J/k_B = -177 K, and $\chi_{TIP} = -7.65 \times 10^{-5}$ emu/mol. The negative J value implied an antiferromagnetic interaction within the dimers, which is expected based on the dimer bridging angles (V-O-V) of 100.0(2) and 96.7(2). The magnetic property of **2.3** appears well described by the isolated spin-half dimer model.

Second Harmonic Generation (SHG).

All materials that crystallize in one of the noncentrosymmetric crystal classes, except 432, may exhibit SHG behavior. Although **2.1**, **2.2**, **2.3**, and **2.4** belong to this class, only very weak behavior was observed for **2.1**, **2.2**, and **2.3**; most likely due to fact that these compound exhibit only a very small dipole moment. The spherical-like coordination environments of the alkali cations and opposing orientation of polar axial V-O bonds in VO_6 polyhedra of the dimers account for the small magnitude of the dipole moment. Large SHG efficiency is typically correlated with large dipole moments.[50-52] All compounds exhibit non-phase-matching behavior with an SHG efficiency of approximately 1x α-SiO_2, shown in **Figure 2.12**. Compound **2.4** could not be tested due insufficient sample size and the impracticality of creating more given the time it takes to crystallize **2.4**.

Conclusion

We have successfully synthesized and characterized four new oxovanadium(IV) tartrate hybrid compounds, $A_2[(VO)_2(C_4H_4O_6)(C_4H_2O_6)(H_2O)_2]\bullet(H_2O)_2$ A = Cs, Rb; $K_2[(VO)_2(C_4H_2O_6)_2(H_2O)_2]\bullet(H_2O)_2$; and $Na_2[(VO)_2(C_4H_4O_6)(C_4H_2O_6)(H_2O)_7]\bullet(H_2O)_2$, utilizing a two step, mild hydrothermal technique and slow evaporation. Vanadium in these structures is in the +4 oxidation state. By varying the size of the alkali cation three different structure types can be formed. Structures **2.1**, **2.2**, and **2.4** formed for A = Cs, Rb, and Na and have dimers with long V-V vanadium distances and exhibit simple paramagnetic behavior, while structure **2.3**, which forms for A= K, contains isolated dimers with short V-V separations that give rise to spin dimer behavior due to antiferromagnetic coupling between the V^{4+} ions.

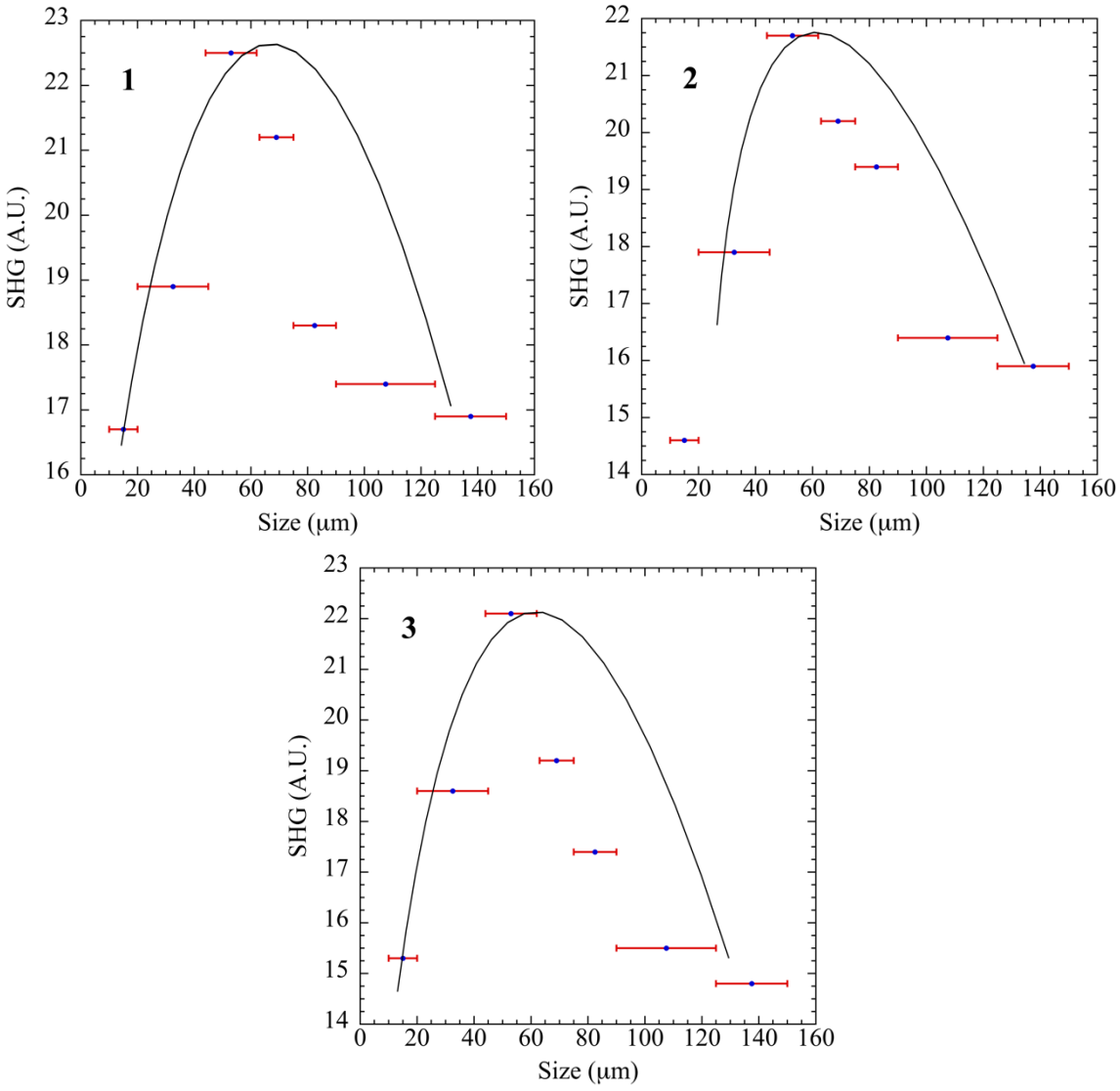

Figure 2.12 Size dependent SHG response of compound **2.1**, pane 1; compound **2.2**, pane 2; and compound **2.3**, pane 3. Uncertainty is shown as red error bars. Black curves were added to help guide the eye when interpreting the behavior.

Acknowledgement

Financial support for this work was provided by the National Science Foundation under DMR-1301757 and is gratefully acknowledged. Support for magnetic measurements was provided by a grant from the U.S. Department of Energy, Office of Basic Energy Studies, Materials Sciences and Engineering Division under DE-SC-0001061 and is gratefully acknowledged.

References

(1) Djerdj, I.; Cao, M.; Rocquefelte, X.; Ćerný, R.; Jagličić, Z.; Arčon, D.; Potočnik, A.; Gozzo, F.; Niederberger, M. *Chem. Mater.* **2009**, *21*, 3356-3369.

(2) Marino, N.; Lloret, F.; Julve, M.; Doyle, R. P. *Dalton Trans.* **2011**, *40*, 12248-12256.

(3) Yan, B.; Luo, J.; Dube, P.; Sefat, A. S.; Greedan, J. E.; Maggard, P. A. *Inorg. Chem.* **2006**, *45*, 5109-5118.

(4) Yan, B.; Maggard, P. A. *Inorg. Chem.* **2007**, *46*, 6640-6646.

(5) Park, D. H.; Cheng, C.-F.; He, H.; Klinowski, J. *J. Mater. Chem.* **1997**, *7*, 159-162.

(6) Santamaría-González, J.; Luque-Zambrana, J.; Mérida-Robles, J.; Maireles-Torres, P.; Rodríguez-Castellón, E.; Jiménez-López, A. *Catalysis* **2000**, *68*, 67-73.

(7) Scheurell, K.; Hoppe, E.; Brzezinka, K.-W.; Kemnitz, E. *J. Mater. Chem.* **2004**, *14*, 2560-2568.

(8) Taufiq-Yap, Y. H.; Rownaghi, A. A.; Hussein, M. Z.; Irmawati, R. *Catal. Lett.* **2007**, *119*, 64-71.

(9) Chernova, N. A.; Roppolo, M.; Dillon, A. C.; Whittingham, M. S. *J. Mater. Chem.* **2009**, *19*, 2526-2552.

(10) Koffer, J. H.; Olshansky, J. H.; Smith, M. D.; Hernandez, K. J.; Zeller, M.; Ferrence, G. M.; Schrier, J.; Norquist, A. J. *Cryst. Growth Des.* **2013**, *13*, 4504-4511.

(11) Pralong, V.; Caignaert, V.; Raveau, B. *J. Mater. Chem.* **2011**, *21*, 12188-12201.

(12) Whittingham, M. S. *Chem. Rev.* **2004**, *104*, 4271-4302.

(13) Tengku Azmi, T. S. M.; Yusoff, A. R. M.; Abdul Karim, K. J. *Chromatographia* **2010**, *72*, 141-144.

(14) Zhang, X.-M.; Tong, M.-L.; Lee, H. K.; Chen, X.-M. *J. Solid State Chem.* **2001**, *160*, 118-122.

(15) Blakely, C. K.; Bruno, S. R.; Poltavets, V. V. *Inorg. Chem.* **2011**, *50*, 6696-6700.

(16) Kiss, T.; Buglyó, P.; Sanna, D.; Micera, G.; Decock, P.; Dewaele, D. *Inorg. Chim. Acta* **1995**, *239*, 145-153.

(17) Polinski, M. J.; Cross, J. N.; Villa, E. M.; Lin, J.; Alekseev, E. V.; Depmeier, W.; Albrecht-Schmitt, T. E. *Inorg. Chem.* **2013**, *52*, 8099-8105.

(18) Tsang, C. F.; Manthiram, A. *J. Mater. Chem.* **1997**, *7*, 1003-1006.

(19) Tsang, C. F.; Kim, J.; Manthiram, A. *J. Mater. Chem.* **1998**, *8*, 425-428.

(20) Yeon, J.; Smith, M. D.; Sefat, A. S.; zur Loye, H.-C. *Inorg. Chem.* **2013**, *52*, 2199-2207.

(21) Yeon, J.; Sefat, A. S.; Tran, T. T.; Halasyamani, P. S.; zur Loye, H.-C. *Inorg. Chem.* **2013**, *52*, 6179-6186.

(22) García-Jaca, J.; Pizarro, J. L.; Larramendi, J. I. R.; Lezama, L.; Arriortua, M. I.; Rojo, T. *J. Mater. Chem.* **1995**, *5*, 277-283.

(23) Wrobleski, J. T.; Thompson, M. R. *Inorg. Chim. Acta* **1988**, *150*, 269-277.

(24) Schwendt, P.; Tracey, A. S.; Tatiersky, J.; Gáliková, J.; Žák, Z. *Inorg. Chem.* **2007**, *46*, 3971-3983.

(25) Abeysinghe, D.; Smith, M. D.; Yeon, J.; Morrison, G.; zur Loye, H.-C. *Cryst. Growth Des.* **2014**, *14*, 4749-4758.

(26) Ok, K. M.; Chi, E. O.; Halasyamani, P. S. *Chem. Soc. Rev.* **2006**, *35*, 710-717.

(27) SMART Version 5.630, SAINT+ Version 6.45 and SADABS Version 2.10. Bruker Analytical X-ray Systems, Inc., Madison, Wisconsin, USA, 2003.

(28) Sheldrick, G. M. *Acta Crystallogr., Sect. A: Found. Crystallogr.* **2008**, *64*, 112-122.

(29) Dolomanov, O. V.; Bourhis, L. J.; Gildea, R. J.; Howard, J. A. K.; Puschmann, H. *J. Appl. Crystallogr.* **2009**, *42*, 339-341.

(30) Brese, N. E.; O'Keeffe, M. *Acta Crystallogr., Sect. B: Struct. Crystallogr. Cryst. Chem.* **1991**, *47*, 192-197.

(31) Brown, I. D.; Altermatt, D. *Acta Crystallogr., Sect. B: Struct. Crystallogr. Cryst. Chem.* **1985**, *41*, 244-247.

(32) Compound 1, V1: 4.14 V2: 4.09; Compound 2, V1: 4.12 V2: 4.09; Compound 3, V1: 4.14 V2: 4.16; Compound 4, V1: 4.17 V2: 4.10.

(33) Morrison, G.; zur Loye, H.-C. *J. Solid State Chem.* **2015**, *221*, 334-337.

(34) Kurtz, S. K.; Perry, T. T. *J. Appl. Phys.* **1968**, *39*, 3798-3813.

(35) Hamdouni, M.; Walha, S.; Kabadou, A.; Duhayon, C.; Sutter, J.-P. *Cryst. Growth Des.* **2013**, *13*, 5100-5106.

(36) Dyachkova, T. A.; Glebov, A. N.; Budnikov, G. K.; Tarasov, O. Y.; Sal-nikov, Y. I. *Koord. Khim.* **1990**, *16*, 1227-1229.

(37) Glebov, A. N.; Sal'nikov, Y. I.; Tarasov, O. Y. *Koord. Khim.* **1988**, *45*, 655-660.

(38) Davis, J. M. *J. Chem. Educ.* **1968**, *45*, 473.

(39) Deacon, G. B.; Phillips, R. J. *Coord. Chem. Rev.* **1980**, *33*, 227-250.

(40) Frederickson Jr., L. D.; Hausen, D. M. *Anal. Chem.* **1963**, *35*, 818-827.

(41) Ballhausen, C. J.; Gray, H. B. *Inorg. Chem.* **1962**, *1*, 111-122.

(42) Kumar, P.; Gupta, M.; Lal, K. M. *Asian J. Phys.* **1995**, *4*, 205-206.

(43) Blundell, S. *Magnetism in Condensed Matter*; Oxford University Press: Oxford, 2001.

(44) Camara, I. S.; Gautier, R.; Le Fur, E.; Trombe, J.-C.; J., G.; Ghorayeb, A. M.; Stepanov, A. *Phys. Rev. B: Condens. Matter Mater. Phys.* **2010**, *81*, 184433.

(45) Isobe, M.; Ueda, Y. *J. Phys. Soc. Jpn.* **1996**, *65*, 3142-3145.

(46) Mur, J.; Darriet, J. *C. R. Acad. Sci., Ser. II: Mec., Phys., Chim., Sci. Terre Univers* **1985**, *300*, 599-602.

(47) Bleaney, B.; Bowers, K. D.; Ingram, D. J. E. *Proc. R. Soc. London, Ser. A* **1955**, *228*, 147-157.

(48) Kahn, O. *Molecular Magnetism*; VCH Publishers: New York, 1993.

(49) Lahti, P. M. *Magnetic Properties of Organic Materials*; Marcel Dekker, Inc.: New York, 1999; pp 558.

(50) Kim, S.-H.; Yeon, J.; Halasyamani, P. S. *Chem. Mater.* **2009**, *21*, 5335-5342.

(51) Nguyen, S. D.; Yeon, J.; Kim, S.-H.; Halasyamani, P. S. *J. Am. Chem. Soc.* **2011**, *133*, 12422-12425.

(52) Yeon, J.; Kim, S.-H.; Nguyen, S. D.; Lee, H.; Halasyamani, P. S. *Inorg. Chem.* **2012**, *51*, 2662-2668.

CHAPTER III

CRYSTAL GROWTH, STRUCTURE, AND PROPERTIES, OF A NEW OXOVANDIUM(IV) PHOSPHATE MATERIAL, $[H_2EN]_4[V_7P_8O_{35}(OH)_6(H_2O)]\cdot 3H_2O$ PREPARED VIA A MILD ONE STEP HYDROTHERMAL METHOD*

*Cortese, A. J.; Smith, M. D.; zur Loye, H.-C. *CrystEngComm.* **2016**. *Submitted*.

Abstract

One new oxovanadium(IV) phosphate material, $[H_2en]_4[V_7P_8O_{35}(OH)_6(H_2O)]\cdot 3H_2O$ was prepared utilizing a one step, mild hydrothermal route involving ethylenediamine as the reducing agent. The compound was structurally characterized by single crystal and powder X-ray diffraction methods and found to crystallize in the monoclinic space group *C*2/*c*. The temperature dependence of the magnetic susceptibility of was measured and found to be paramagnetic down to 2K. The compound was further characterized by IR and UV/Vis spectroscopies.

Introduction

Vanadium containing compounds have been investigated for a variety of applications, including as magnetic materials[1-4], for catalysts[5-8], and as cathode materials[9-12]. In these applications the oxidation state of vanadium can range from fully oxidized to reduced. The chemistry of vanadium is rich with many accessible oxidation states including, +5, +4, +3, and +2, where color can be utilized to distinguish and confirm the oxidation states of vanadium species. In an aqueous solution, vanadium can exist from +2 to +5 with colors ranging from yellow (V^{5+}), blue (V^{4+}), green (V^{3+}), and lilac (V^{2+}).[13-18] It is possible to reduce aqueous vanadium species using organic reducing agents, where the combination of organic reagent and temperature determine the final vanadium oxidation state. We have recently reported on a convenient two-step hydrothermal method that facilitates the formation of hybrid materials containing metal cations in reduced states.[19-24] In the case of those reactions, the rate of metal reduction is slow relative to the crystallization of an unwanted species, and the use of the two-step approach is extremely effective for obtaining the desired reduced products.

To create the title compound, $[H_2en]_4[V_7P_8O_{35}(OH)_6(H_2O)]\cdot 3H_2O$, we wanted to explore use of more soluble vanadium precursors and stronger reducing agents to perform a one step reaction involving an *in situ* reduction followed by product crystallization. To that end, reactions were devised using ethylenediamine, a well known, strong reducing agent.[25] Ethylenediamine has also been shown to be an effective templating agent for porous structures, often residing in channels as protonated ions.[26, 27] Concentrated phosphoric acid can be used to help solubilize vanadium precursors and as a source of phosphate ligands for the formation of a three dimensional inorganic framework. Several oxovanadium(IV) phosphates have been prepared using similar methods, including $(C_2H_{10}N_2)_4[H_2Ni(H_2O)_2(VO)_8(OH)_4(PO_4)_8]$[28], $(C_2H_8N_2)[(VO)(VOH)(PO(OH)_3)](PO_4)_2$[29], $(C_2H_{10}N_2)(C_2H_9N_2)_2[(VO)_4(PO_4)_4(H_2O)]$[30], and $(C_2H_{10}N_2)[(HVO_3)(HVO_2)(PO_4)]$.[31] Herein we report the synthesis, structural characterization, optical spectroscopy, and magnetic properties of the title compound.

Experimental details

Reagents.

$NaVO_3$ (96%, Alfa Aesar), 85% H_3PO_4 (ACS grade, Fisher), and ethylenediamine (en) (99% min, Sigma-Aldrich) were used as received.

Hydrothermal Synthesis.

Synthesis of $[C_2H_{10}N_2]_4[V_7P_8O_{35}(OH)_6(H_2O)]\cdot 3H_2O$, ***3.1***

Bright blue single crystals of $[C_2H_{10}N_2]_4[V_7P_8O_{35}(OH)_6(H_2O)]\cdot 3H_2O$, $C_2H_{10}N_2 = H_2en^{2+}$, were grown via a one step hydrothermal route. In a fume hood, 3 mmol of $NaVO_3$, 1 mL of 85% H_3PO_4, 2.4 mL of H_2O, and 1 mL of ethylenediamine were placed

in a thick walled pyrex tube and sealed with a polytetrafluoroethylene (PTFE) stopper. The tube was placed inside a programmable oven and heated to 170°C at a rate of 10°C/min, held for 5 days, and slowly cooled to room temperature at a rate of 0.1°C/min. The mother liquor was decanted yielding a phase pure product in approximately 82% yield based on V_2O_5. A powder X-Ray diffraction pattern (PXRD) of ground crystals demonstrates the phase purity of the product crystals. (See **Figure 3.1**.)

Single Crystal X-ray Diffraction (SXRD).

X-ray intensity data from a bright blue crystal were collected at 100(2) K using a Bruker D8 QUEST diffractometer equipped with a PHOTON 100 CMOS area detector and an Incoatec microfocus source (Mo Kα radiation, λ = 0.71073 Å).[32] The raw area detector frames were reduced and corrected for absorption effects using the SAINT+ and SADABS programs.[32] Final unit cell parameters were determined by least-squares refinement of 9951 reflections from the data set. Direct methods structure solution, difference Fourier calculations and full-matrix least –squares refinements against F^2 were performed with SHELXL-2014 using OLEX2.[33]

The compound crystallizes in the monoclinic system. The pattern of systematic absences in the intensity data was consistent with the space groups *Cc* and *C*2/*c*. The centrosymmetric group *C*2/*c* was confirmed by structure solution. The complex asymmetric unit consists of 3.5 vanadium atoms, four phosphorus atoms, 17 oxo oxygen atoms, three hydroxyl groups (O5, O17, O20), a disordered set of oxygen atoms bonded to V4 which were modeled as 0.5 oxo oxygen atoms and 0.5 water molecules, one interstitial water (O23), half of another interstitial water located on a crystallographic two-fold axis of rotation (O24), one complete ethylenediammonium (H_2en^{2+}) cation

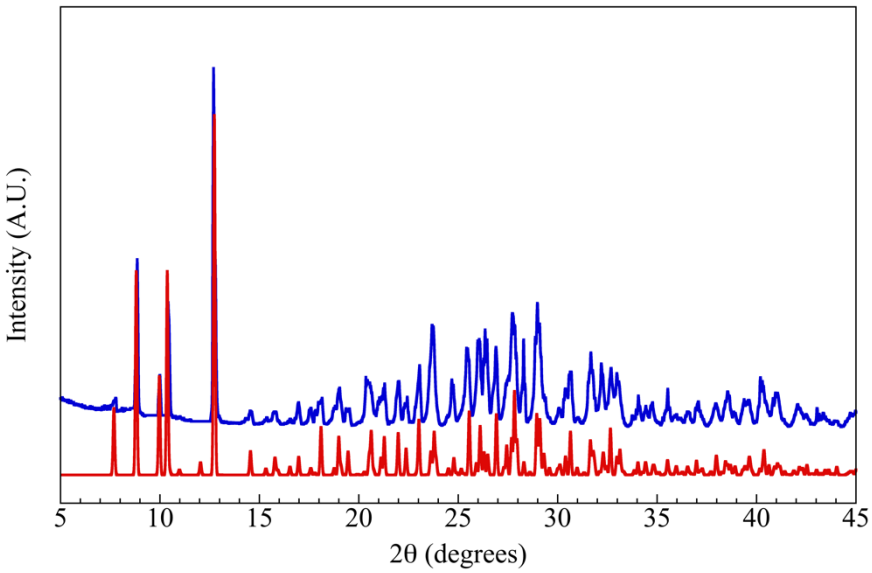

Figure 3.1 PXRD patterns of compound **3.1**. Experimental diffraction is shown in blue. The calculated pattern is shown in red.

(C1,C2,N1,N2), and half each of two additional H_2en^{2+} cations, one located on an inversion center (C3,N3) and one located on a two-fold axis of rotation (C4,N4). There is crystallographically imposed two-fold disorder of the pseudo-octahedral $V(O)O_4(H_2O)$ grouping (V4) as follows. Vanadium V4 is disordered across an inversion center and only half is present per asymmetric unit. Initial refinements with V4 located on the inversion center resulted in a highly elongated displacement parameter (U_3/U_1 = 15.6); displacing the V4 position just off the center (0.14 Å) gave an acceptably spherical ellipsoid (U_3/U_1 = 3.5). The inversion symmetry also imposes disorder on the atoms coordinated axially to V4: O21 (V4-O21 = 1.604(7) Å) and water molecule O22 (V4-O22 = 2.320(7) Å), but does not disorder the equatorial oxygen atoms O16 and O18, which are consistent with inversion symmetry. V4, O21 and O22 were refined with fixed occupancy values of 0.5; the nearly superimposed O21/O22 atoms were assigned common displacement parameters. Identical 50/50 oxo/water scrambling was observed upon trial refinements in the acentric space group *Cc*, which lacks inversion symmetry, and therefore *C*2/*c* was retained as the proper space group. All non-hydrogen atoms were refined with anisotropic displacement parameters. Hydrogen atoms bonded to carbon and nitrogen (H_2en^{2+} hydrogens) were located in difference maps before being included as riding atoms with refined isotropic displacement parameters. Water and hydroxyl hydrogen atoms were located in difference maps and refined isotropically. All O-H distances were restrained to be approximately equal using a SHELX SADI restraint. The largest residual electron density peak in the final difference map is 0.50 $e^-/Å^3$, located 0.76 Å from C4. Crystallographic data, selected interatomic distances, and select hydrogen bonding

distances are listed in **Tables 3.1 – 3.3**. The Cambridge Crystallographic Data Centre (CCDC) number is #1452074.

Powder X-ray diffraction (PXRD).

Powder X-ray diffraction data were collected on a Rigaku D/Max-2100 powder X-ray diffractometer using Cu Kα radiation. The step scan covered the angular range 5-45° 2θ in steps of 0.04°. No impurities were observed and the calculated and experimental PXRD patterns are in excellent agreement (See **Figure 3.1**).

Energy-Dispersive Spectroscopy (EDS).

Elemental analysis was performed on the single crystals using a TESCAN Vega-3 SBU scanning electron microscope (SEM) with EDS capabilities. The crystals were mounted on carbon tape and analyzed using a 20 kV accelerating voltage and an accumulation time of 1 minute. As a qualitative measure, EDS confirmed the presence of each reported element in the title compounds.

Infrared Spectroscopy (IR).

The IR spectrum of ground crystals of compound **3.1** was recorded on a PerkinElmer Spectrum 100 FT-IR spectrometer fitted with an ATR accessory in the range of 650-4000 cm^{-1}.

UV-vis Diffuse Reflectance Spectroscopy (UV/Vis).

UV-Vis diffuse reflectance spectroscopy data of ground crystals of compound **3.1** was obtained using a PerkinElmer Lambda 35 UV-Vis scanning spectrophotometer equipped with an integrating sphere accessory in the range of 200-900 nm. Reflectance data were transformed to absorbance via the Kubelka-Munk function.[34]

Table 3.1 Crystal data and structure refinements for compound **3.1**.

	3.1
Empirical formula	$C_8H_{54}N_8O_{45}P_8V_7$
Formula weight	1586.93
Temperature	100(2)
Wavelength	0.71073 Å
Crystal system	monoclinic
Space group	*C*2/*c*
Unit cell dimensions	a = 20.6241(9) Å b = 9.9553(5) Å c = 23.6628(11) Å α = 90° β = 101.1608(16)° γ = 90°
Volume	4766.5(4) Å^3
Z	4
Denisty (calculated)	2.211 mg/m^3
Absorption coefficient	1.714 mm^{-1}
F(000)	3196.0
Crystal size	0.16 × 0.12 × 0.10 mm^3
2θ range for data collected	4.56 to 56.624°
Index ranges	−27 ≤ h ≤ 27 −13 ≤ k ≤ 13 −31 ≤ l ≤ 31
Reflections collected	85805
Ind. reflections	5938[R(int) = 0.0400]
Data / restraints / parameters	5938 / 21 / 408
Goodness-of-fit on F^2	1.050
Final R indices [I>2sigma(I)]	R_1 = 0.0217 wR_2 = 0.0534
R indices (all data)	R_1 = 0.0262 wR_2 = 0.0554
Largest diff. peak and hole	0.50 and −0.43 e$^-$×Å^{-3}

Table 3.2 Selected bond lengths [Å] for compound **3.1**.

3.1							
V(1)−O(1)	1.5870(12)	V(2)−O(9)	2.0111(12)	V(4)−O(18)	1.984(9)	P(2)−O(17)	1.5565(13)
V(1)−O(2)	1.9700(11)	V(3)−O(10)	1.5916(12)	V(4)−O(21)	1.863(7)	P(3)−O(3)	1.5410(12)
V(1)−O(3)	1.9834(12)	V(3)−O(11)	1.9408(12)	V(4)−O(22)	2.070(7)	P(3)−O(9)	1.5391(12)
V(1)−O(4)	1.9788(11)	V(3)−O(12)	1.9970(12)	P(1)−O(2)	1.5437(11)	P(3)−O(12)	1.5296(12)
V(1)−O(5)	1.9748(11)	V(3)−O(13)	1.9820(11)	P(1)−O(4)	1.5349(12)	P(3)−O(18)	1.5304(12)
V(2)−O(5)	1.9778(12)	V(3)−O(14)	2.0170(11)	P(1)−O(7)	1.5457(12)	P(4)−O(13)	1.5337(12)
V(2)−O(6)	1.5918(12)	V(4)−O(16)	2.071(8)	P(2)−O(8)	1.5224(12)	P(4)−O(14)	1.5272(12)
V(2)−O(7)	1.9735(12)	V(4)−O(16)	1.955(9)	P(2)−O(11)	1.5103(12)	P(4)−O(19)	1.5196(12)
V(2)–O(8)	1.9955(12)	V(4)–O(18)	1.965(9)	P(2)–O(16)	1.5396(14)	P(4)−O(20)	1.5766(12)

Table 3.3 Hydrogen bonds [Å and °] for compound **3.1**

3.1							
H(5)−O(2)	1.974(18)	H(23B)−O(19)	2.04(2)	H(2A)−O(15)	1.91	H(3B)−O(19)	1.96
H(17)−O(19)	1.698(19)	H(24)−O(23)	1.953(19)	H(2B)−O(14)	1.99	H(3C)−O(7)	2.01
H(20)−O(15)	1.71(3)	H(1A)−O(3)	1.93	H(2C)−O(16)	2.46	H(4A)−O(9)	1.98
H(22A)−O(7)	2.10(2)	H(1B)−O(16)	2.01	H(2C)−O(21)	2.43	H(4B)−O(15)	1.93
H(22B)−O(13)	1.96(2)	H(1B)−O(17)	2.48	H(2C)−O(22)	2.40	H(4C)−O(24)	1.89
H(23A)–O(6)	2.37(2)	H(1C)−O(20)	1.98	H(3A)−O(12)	2.23		

Magnetic Susceptibility.

The magnetic susceptibility of compound **3.1** was measured using a Quantum Design MPMS SQUID VSM Evercool magnetometer. The zero-field cooled magnetic susceptibility was measured as a function of temperature between 2-300K in an applied field of 1000 Oe. The measured magnetic data were corrected for shape and radial offset effects using methods reported by Morrison et. al.[35]

Results and Discussion

Synthesis.

A number of reduced oxovanadium(IV) phosphate materials have been synthesized under acidic mild hydrothermal conditions using ethylenediamine as an *in situ* reducing agent and templating agent. Crystals of compound **3.1** were obtained via such a method. Initial reactions using vanadium(V) oxide as a vanadium source resulted in an amorphous brown powder. Reactions using sodium metavanadate resulted in single crystals of compound **3.1**, most likely due to the superior solubility of sodium metavanadate at elevated temperatures when compared with vanadium(V) oxide. An increased dwell time was found to dramatically improve the product yield, with dwells of 5 days yielding a phase pure product in approximately 82% yield.

Structure.

Compound **3.1** crystallizes in the monoclinic space group *C*2/*c* and exhibits a porous three-dimensional crystal structure consisting of distorted $VO_4(OH)$ and VO_5 square pyramids linked via bridging phosphate ligands that form 2D sheets which are linked via $VO_5(H_2O)$ octahedra. Channels that form in the (010) and (101) directions are

filled with hydrogen bonded interstitial waters and H_2en^{2+} ions. The extended structure of compound **3.1** viewed down the *b*-axis and (101) direction is shown in **Figures 3.2** and **3.3**. V(1) and V(2) are located in distorted $VO_4(OH)$ square pyramids with four equatorial V-O bonds of roughly the same length and one exceptionally short V-O axial bond. Three out of five oxygens bonded to V(1), O2, O3, and O4, originate from bridging phosphate ligands; one, O5, from a bridging hydroxide; and one, O1, is a monodentate oxo atom. Three out of five oxygens bonded to V(2), O7, O8, and O9, originate from bridging phosphate ligands; one, O5, from a bridging hydroxide; and one, O6, is a monodentate oxo atom. The V-O bond distances of V(1) and V(2) range from 1.5870(12) Å – 2.0111(12) Å. Polyhedral representations of V(1) and V(2) are shown in **Figure 3.4**. V(3) is located in a distorted VO_5 distorted square pyramid with four equatorial V-O bonds of roughly the same length and one exceptionally short V-O axial bond. Four out of five oxygens bonded to V(3), O(11), O(12), O(13), and O(14), originate from bridging phosphate ligands. The remaining oxygen, O(10), is a monodentate oxo atom. V(4) is located in a distorted $VO_5(OH)$ octahedron with four equatorial V-O bonds of roughly the same length and one exceptionally long and one exceptionally short V-O axial bond. Four out of six oxygens bonded to V(4), two O(16) and two O(18), originate from bridging phosphate ligands; one, O(22), from a monodentate water; and one, O21, is a monodentate oxo atom. Polyhedral representations of V(3) and V(4) are shown in **Figure 3.5**. Channels that form in the (010) and (101) directions are filled with interstitial waters and H_2en^{2+} ions that are held by hydrogen bonds with distances ranging from 1.722(19) Å – 2.31(3) Å. V(1), V(2), and V(3) form 2D sheets via bridging phosphate ligands shown in **Figure 3.6**. Select hydrogen bond distances are given in Table 3. Bond valence

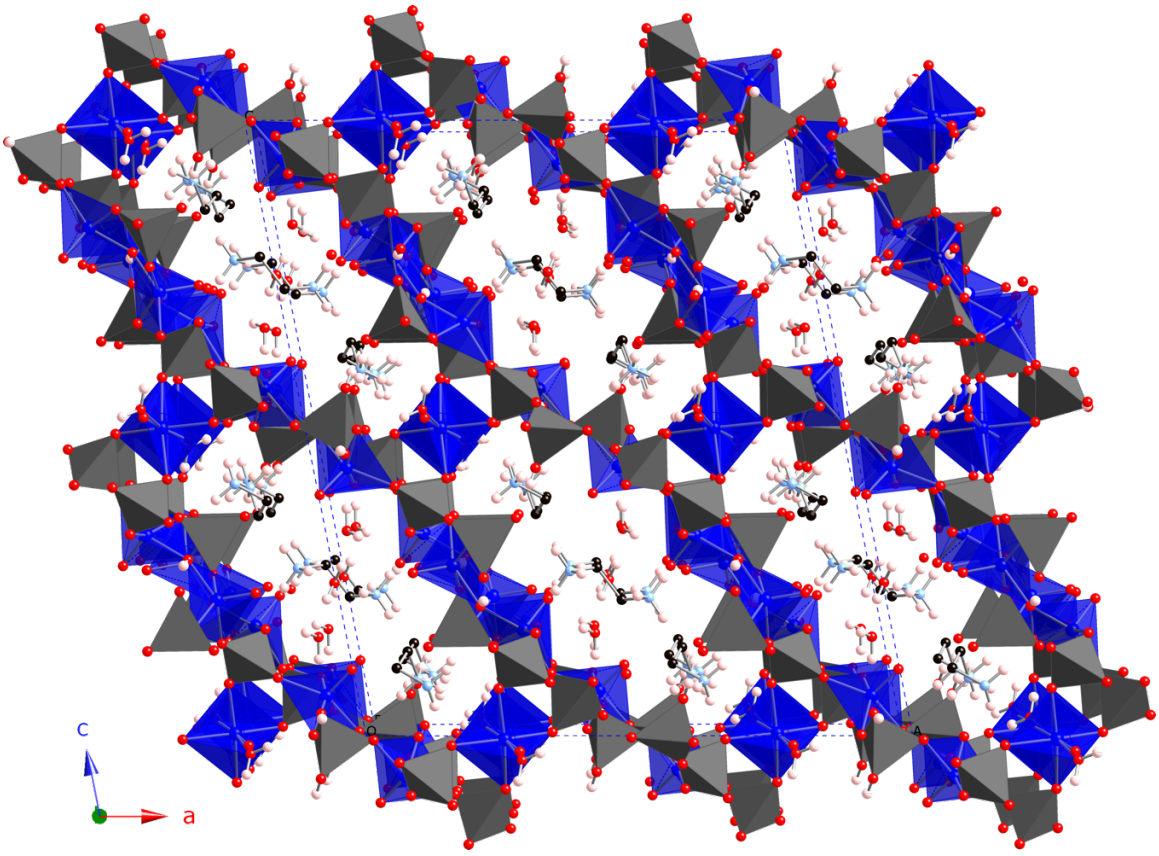

Figure 3.2 Compound **3.1** viewed down the *b*-axis. Interstitial waters and ethylenediamonium cations reside in the channels. V, P, O, N, C, H shown in blue, grey, red, light blue, black, and white, respectively.

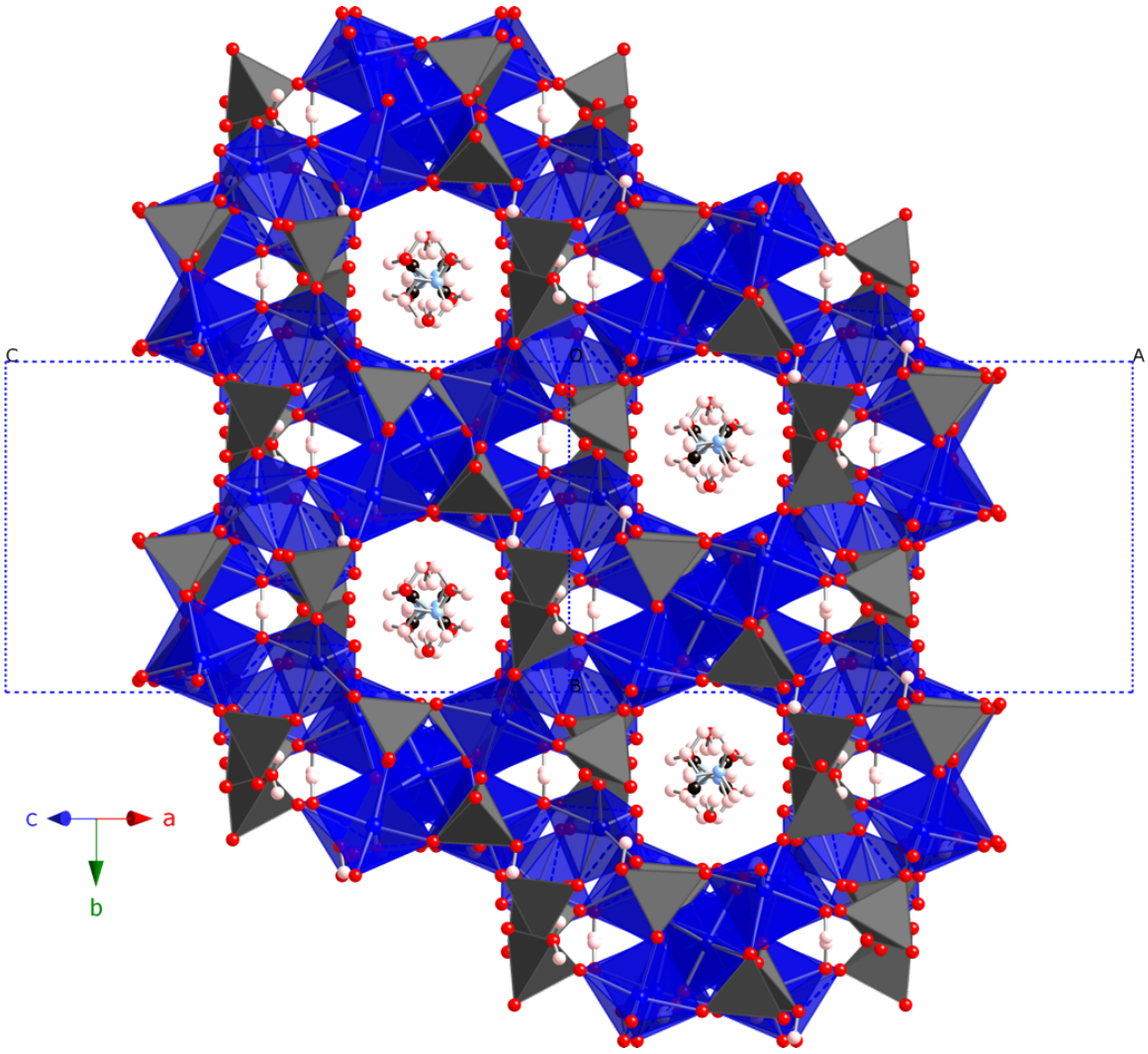

Figure 3.3 Compound **3.1** viewed down the (101) direction. Interstitial water and ethylenediamonium cations reside in the channels. V, P, O, N, C, H shown in blue, grey, red, light blue, black, and white, respectively.

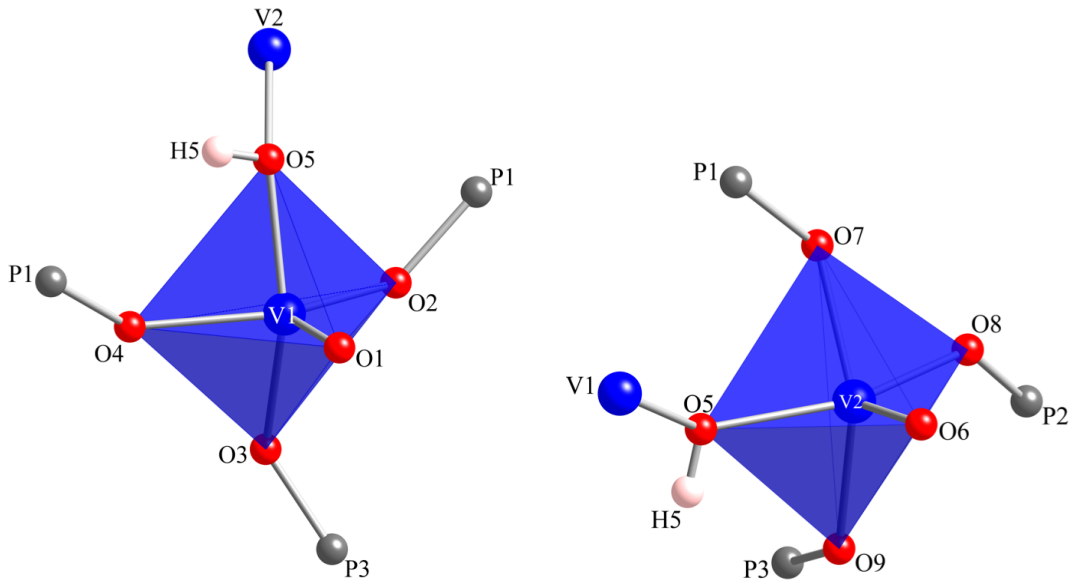

Figure 3.4 Polyhedral representations of V(1) and V(1).

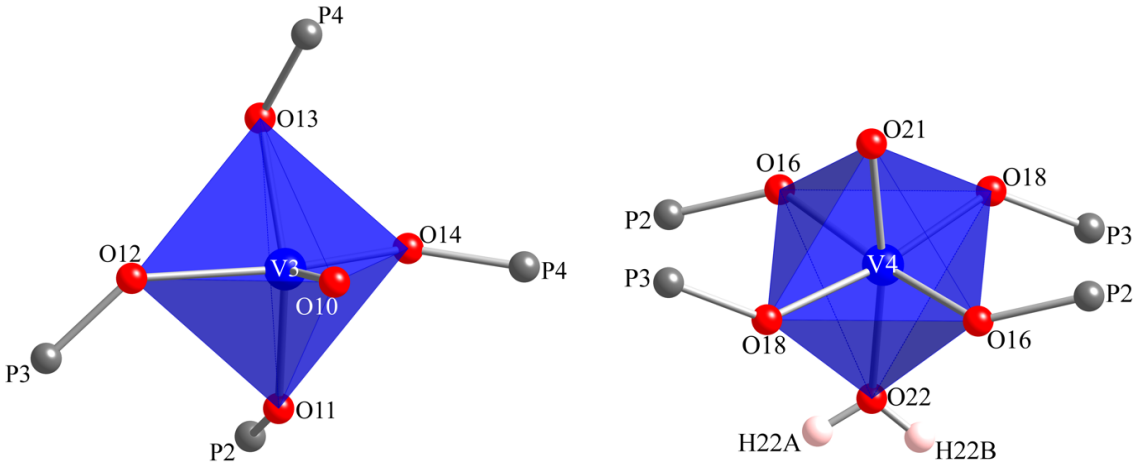

Figure 3.5 Polyhedral representations of V(3) and V(4).

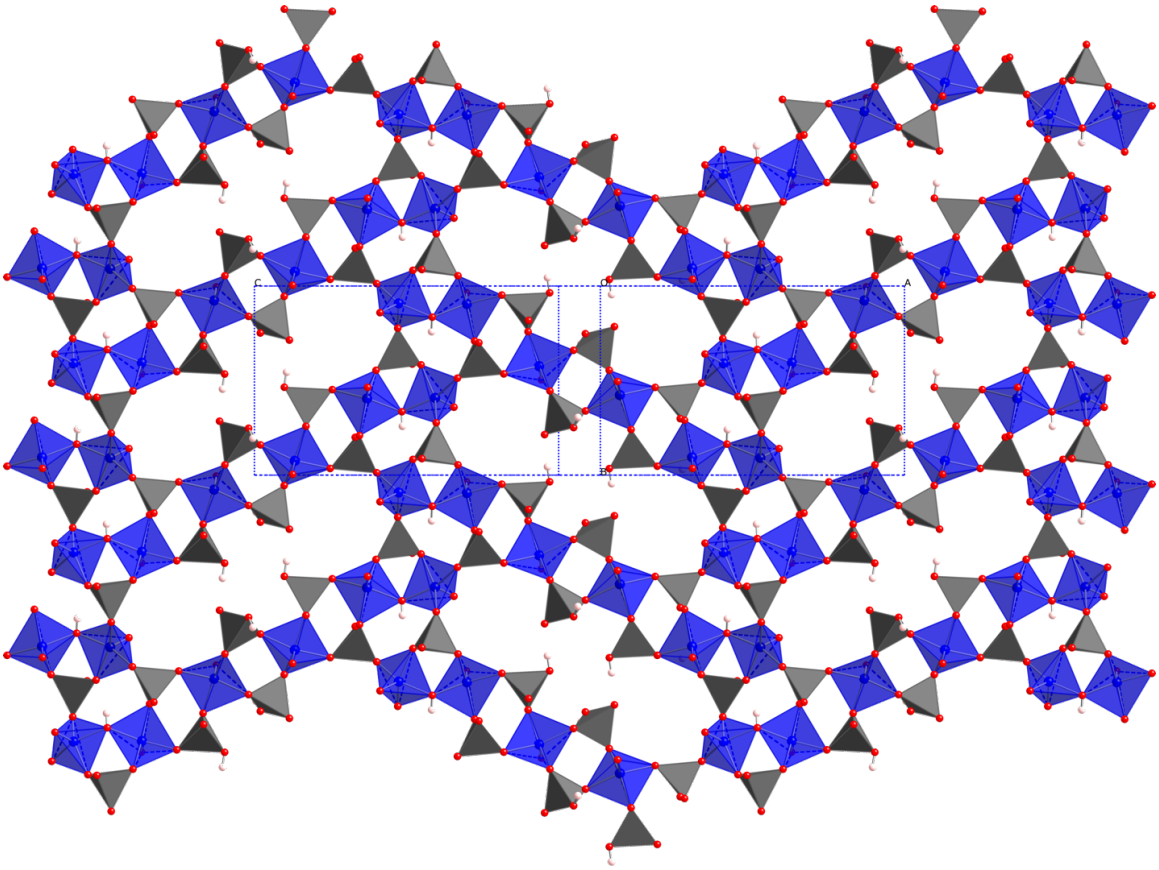

Figure 3.6 2D sheets formed by the connectivity of V(1), V(2), V(3), and phosphate ligands. V, P, O, N, C, H shown in blue, grey, red, light blue, black, and white, respectively.

sums for each vanadium site were calculated found to be 4.07 for V(1), 3.98 for V(2), 4.02 for V(3), and 4.15 for V(4),[36, 37] confirming the oxidation state of V as +4 and being consistent with the compositions obtained by single crystal X-ray diffraction.

Infrared Spectroscopy (IR).

The IR spectrum for compound **3.1** which is shown in **Figure 3.7**, was collected between 650 – 4000 cm^{-1}. The broad band observed in the 3200 – 3600 cm^{-1} region is characteristic for O-H vibrations of water molecules and hydroxyl groups. The presence of phosphate groups produces P-O vibrations. The expected bending mode of water at around 1600 cm^{-1} is observed. Bands between 1600 cm^{-1} and 100 cm^{-1} are attributed to bending and stretching modes of ethylenediamine.[38] The intense band around 1000 cm^{-1} is attributed to the asymmetric stretching and bending modes of the phosphate P-O bonds.[39]

UV-vis Diffuse Reflectance Spectroscopy (UV/Vis).

UV-Vis absorbance data shown in **Figure 3.8** was collected using ground crystals of compound **3.1**. Vanadium in the +4 oxidation state has a d^1 electron configuration and a transition from the $^2T_{2g}$ ground state to the ^2E_g excited state is expected. Three absorption maxima are observed for each compound approximately located at 401 nm, 627 nm, and 775 nm and can be assigned to $d_{xy} \rightarrow d_{z^2}$, $d_{xy} \rightarrow d_{x^2-y^2}$, and $d_{xy} \rightarrow d_{xz}/d_{yz}$ transitions, respectively.[40, 41]

Magnetism.

The unpaired electrons in compound **3.1** can be observed in magnetic susceptibility measurements. The temperature dependences of the magnetic

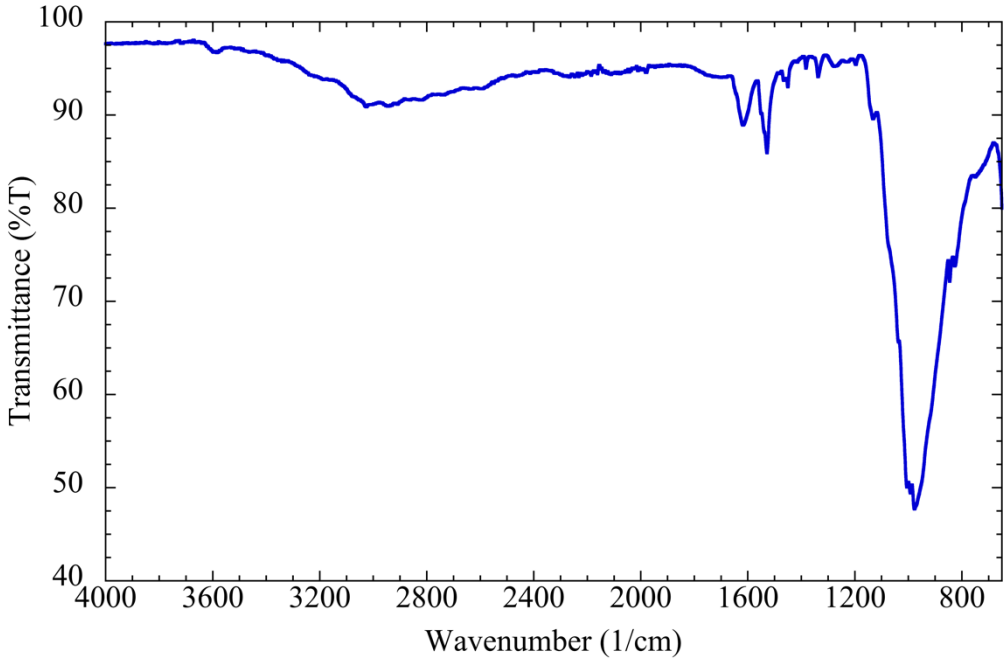

Figure 3.7 IR spectrum of compound **3.1**.

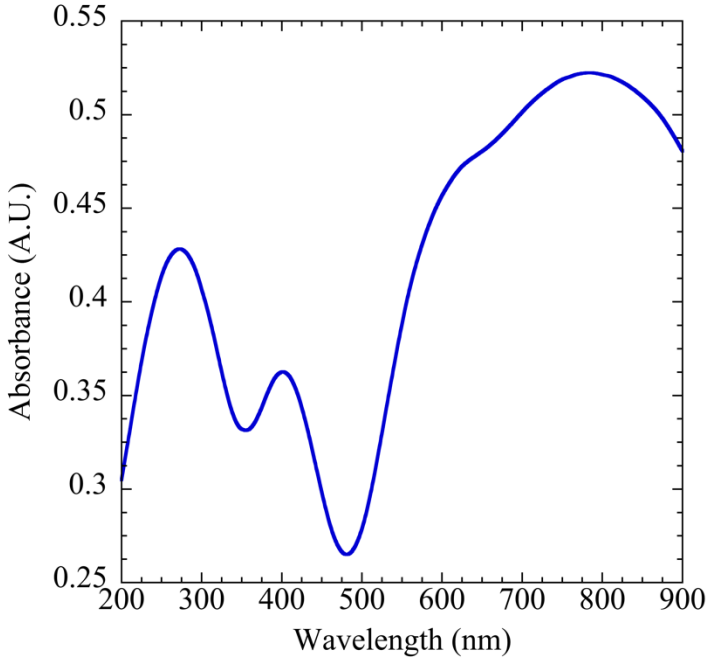

Figure 3.8 UV/Vis absorbance spectrum of compound **3.1**.

susceptibilities measured in an applied field of 1000 Oe, are shown in **Figure 3.9**. As the vanadium polyhedra are separated by bridging phosphate ligands, due to the long V-V separation, no magnetic coupling is expected or observed. Down to 2K, the data do not reveal any long-range magnetic order and follow the Curie-Weiss (C-W) law as expected for simple paramagnetic species. The magnetic moment calculated from the inverse susceptibility is 1.72 μ_B, which is in good agreement with the expected value of 1.73 μ_B for a $3d^1$ spin-only system.[42]

Conclusion

We have successfully synthesized and characterized the new oxovanadium(IV) phosphate material, $[H_2en]_4[V_7P_8O_{35}(OH)_6(H_2O)]\cdot 3H_2O$ utilizing a one step, mild hydrothermal technique. Vanadium in this structures is in the +4 oxidation state. The structure exhibits phosphate bridged vanadium(IV) polyhedra and exhibits simple paramagnetic behavior due to long V-V distances.

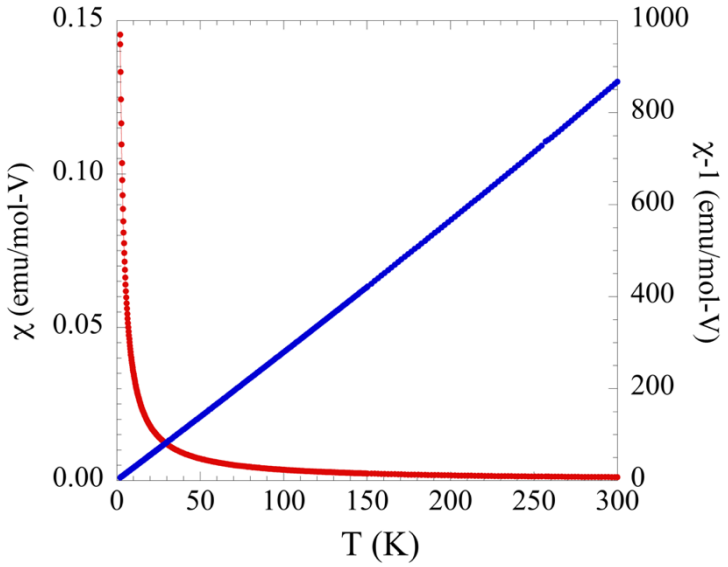

Figure 3.9 Magnetic susceptibility plot of **3.1**. χ and $1/\chi$ are shown in blue and red.

ACKNOWLEDGEMENT

Financial support for this work was provided by the National Science Foundation under DMR-1301757 and is gratefully acknowledged.

References

(1) I. Djerdj; M. Cao; X. Rocquefelte; R. Ćerný; Z. Jagličić; D. Arčon; A. Potočnik; F. Gozzo; M. Niederberger. *Chem. Mater.* **2009**, *21*, 3356-3369.

(2) N. Marino; F. Lloret; M. Julve; R. P. Doyle. *Dalton Trans.* **2011**, *40*, 12248-12256.

(3) B. Yan; J. Luo; P. Dube; A. S. Sefat; J. E. Greedan; P. A. Maggard. *Inorg. Chem.* **2006**, *45*, 5109-5118.

(4) B. Yan; P. A. Maggard. *Inorg. Chem.* **2007**, *46*, 6640-6646.

(5) D. H. Park; C.-F. Cheng; H. He; J. Klinowski. *J Mater. Chem.* **1997**, *7*, 159-162.

(6) J. Santamaría-González; J. Luque-Zambrana; J. Mérida-Robles; P. Maireles-Torres; E. Rodríguez-Castellón; A. Jiménez-López. *Catalysis* **2000**, *68*, 67-73.

(7) K. Scheurell; E. Hoppe; K.-W. Brzezinka; E. Kemnitz. *J. Mater. Chem.* **2004**, *14*, 2560-2568.

(8) Y. H. Taufiq-Yap; A. A. Rownaghi; M. Z. Hussein; R. Irmawati. *Catal. Lett.* **2007**, *119*, 64-71.

(9) N. A. Chernova; M. Roppolo; A. C. Dillon; M. S. Whittingham. *J. Mater. Chem.* **2009**, *19*, 2526-2552.

(10) J. H. Koffer; J. H. Olshansky; M. D. Smith; K. J. Hernandez; M. Zeller; G. M. Ferrence; J. Schrier; A. J. Norquist. *Cryst. Growth Des.* **2013**, *13*, 4504-4511.

(11) V. Pralong; V. Caignaert; B. Raveau. *J. Mater Chem.* **2011**, *21*, 12188-12201.

(12) M. S. Whittingham. *Chem Rev.* **2004**, *104*, 4271-4302.

(13) C. K. Blakely; S. R. Bruno; V. V. Poltavets. *Inorg. Chem.* **2011**, *50*, 6696-6700.

(14) T. Kiss; P. Buglyó; D. Sanna; G. Micera; P. Decock; D. Dewaele. *Inorg. Chim. Acta* **1995**, *239*, 145-153.

(15) M. J. Polinski; J. N. Cross; E. M. Villa; J. Lin; E. V. Alekseev; W. Depmeier; T. E. Albrecht-Schmitt. *Inorg. Chem.* **2013**, *52*, 8099-8105.

(16) C. F. Tsang; A. Manthiram. *J. Mater. Chem.* **1997**, *7*, 1003-1006.

(17) C. F. Tsang; J. Kim; A. Manthiram. *J. Mater. Chem.* **1998**, *8*, 425-428.

(18) J. Yeon; A. S. Sefat; T. T. Tran; P. S. Halasyamani; H.-C. zur Loye. *Inorg. Chem.* **2013**, *52*, 6179-6186.

(19) D. Abeysinghe; M. D. Smith; J. Yeon; G. Morrison; H.-C. zur Loye. *Cryst. Growth & Des.* **2014**, *14*, 4749-4758.

(20) A. J. Cortese; B. Wilkins; M. D. Smith; J. Yeon; G. Morrison; T. T. Tran; P. S. Halasyamani; H.-C. zur Loye. *Inorg. Chem.* **2015**, *54*, 4011-4020.

(21) J. Yeon; M. D. Smith; A. S. Sefat; H.-C. zur Loye. *Inorg. Chem.* **2013**, *52*, 2199-2207.

(22) J. Yeon; M. D. Smith; A. S. Sefat; T. T. Tran; P. S. Halasyamani; H.-C. zur Loye. *Inorg. Chem.* **2013**, *52*, 8303-8305.

(23) J. Yeon; M. D. Smith; J. Tapp; A. Möller; H.-C. zur Loye. *J. Am. Chem. Soc.* **2014**, *136*, 3955-3963.

(24) J. Yeon; M. D. Smith; J. Tapp; A. Möller; H.-C. zur Loye. *Inorg. Chem.* **2014**, *53*, 6289-6298.

(25) A. J. Vaškelis, J. Norkus, E. Chemija. *Chemija* **1995**, *N 3*, 291-307.

(26) Q. Banghua; N. Xiaomin; L. Dongguo; Z. Huagui. *Chem. Lett.* **2008**, *37*, 336-337.

(27) V. T. Yilmaz; S. Demir; C. Kazak; W. T. A. Harrison. *Solid State Sciences* **2005**, *7*, 1247-1255.

(28) F.-W. Yin; C.-D. Peng; Y.-S. Li; T.-T. Zhuang; Q.-X. Zeng; Z.-H. Yuan. *Z. Anorg. Allg. Chem.* **2013**, *639*, 543-547.

(29) Q. Z. Huang; Y. Q. Feng; Z. H. Meng; H. Z. Shi. *Russ. J. Coord. Chem.* **2010**, *36*, 572-578.

(30) Y.-L. Niu; J.-Y. Ji. Huaxue Yanjiu Yu Yingyong **2007**, *19*, 543-546.

(31) J.-X. Chen; C.-X. Wei; Z.-C. Zhang; Y.-B. Huang; T.-Y. Lan; Z.-S. Li; W.-J. Zhang. *Inorg. Chim. Acta* **2006**, *359*, 3396-3404.

(32) APEX2 Version 2014.9-0, SAINT+ Version 8.34A and SADABS Version 2014/4. Bruker Analytical X-ray Systems.

(33) O. V. Dolomanov; L. J. Bourhis; R. J. Gildea; J. A. K. Howard; H. Puschmann. *Journal of Applied Crystallography* **2009**, *42*, 339-341.

(34) P. Kubelka; F. Munk. *Zeit. Für Tekn. Physik* **1931**, *12*, 593.

(35) G. Morrison; H.-C. zur Loye. *J. Solid State Chem.* **2015**, *221*, 334-337.

(36) N. E. Brese; M. O'Keeffe. *Acta Crystallogr., Sect. B: Struct. Crystallogr. Cryst. Chem.* **1991**, *47*, 192-197.

(37) I. D. Brown; D. Altermatt. *Acta Crystallogr., Sect. B: Struct. Crystallogr. Cryst. Chem.* **1985**, *41*, 244-247.

(38) A. L. Smith. **1982**,

(39) W. Jastrzębski; M. Sitarz; M. Rokita; K. Bułat. *Spectrochim. Acta, Part A* **2011**, *79*, 722-727.

(40) C. J. Ballhausen; H. B. Gray. *Inorg. Chem.* **1962**, *1*, 111-122.

(41) P. Kumar; M. Gupta; K. M. Lal. *Asian J. Phys.* **1995**, *4*, 205-206.

(42) Blundell, S. *Magnetism in Condensed Matter*; 2001.

CHAPTER IV

SINGLE CRYSTAL GROWTH AND CHARACTERIZATION OF THE REDUCED BARIUM SODIUM SILICONIOBATE, $Ba_3Na_{0.32}Nb_6O_{12}(Si_2O_7)_2$*

*Adapted with permission from Cortese, A. J.; Wilkins, B.; Smith, M. D.; Morrison, G.; zur Loye, H.-C. *Solid State Sci.* **2015**, *48*, 7-12.

Abstract

Single crystals of $Ba_3Na_{0.32}Nb_6O_{12}(Si_2O_7)_2$, **4.1**, were grown for the first time. The use of an alkali/alkaline earth eutectic flux facilitated the crystal growth. **4.1**, a mixed valent Nb(V)/Nb(IV) compound, crystallizes in the noncentrosymmetric hexagonal space group *P*-62*m* with a = 8.9998(10) Å and c = 7.8119(17) Å. The temperature dependence of the magnetic susceptibility was measured and found to be paramagnetic across the entire 2-300 K temperature range measured. Although noncentrosymmetric, **4.1** was not found to be second harmonic generation active. **4.1** was further characterized by IR and UV/Vis spectroscopies.

Introduction

The investigation of complex oxides containing early transition metals in reduced oxidation states remains a relatively unexplored area in materials science due to the difficulty of preparing such materials. Interest in these materials arises from the expectation that the different coordination environments of these early transition metal oxides can promote the formation of new structure types. In addition, the introduction of *d*-electrons, the number of which scales with the degree of reduction, coupled with the extended *d*-orbitals typical for early transition metal oxides, can lead to interesting physical properties including magnetism and/or metallic conductivity.[1-3]

A limited number of complex reduced niobium oxides have been synthesized, typically via methods that have involved extreme temperatures and/or the use of specialized equipment and techniques for the exclusion of oxygen from the reaction environment.[4, 5, 6] The most common approach has relied on the use of sealed niobium or tantalum tubes to exclude oxygen from the reaction mixture.[7-9] An attractive alternative

to metal tubes is the use of fused silica tubes filled with a redox stable flux containing the reagents plus a reducing agent. A number of papers describe such an approach[4, 10] that, while attractive in theory, does not always succeed in practice. For example, the attempt by Shannon and Katz to prepare a reduced niobate containing Nb(IV) utilizing BaO, Nb_2O_5, Nb metal, and a BaF_2 mineralizer reacted in a sealed, evacuated fused silica tube, resulted in the Nb(V) containing Belkovite-type structure, $Ba_3Nb_6O_{12}(Si_2O_7)_2$.[11] This outcome may well have been a result of the kinetically slow reduction of Nb(V) to Nb(IV) using the high melting point metallic niobium reducing agent. Limited reactant/reducing agent contact does not favor fast kinetics and allows other processes that result in the formation of complex oxides containing fully oxidized niobium to take place first. The use of a molten (at the reaction temperature) reducing agent can overcome this limitation.

The utilization of molten fluxes is well known as one of the most effective approaches for crystal growth because it lowers the reaction temperature and allows for the dissolution of a wide range of elements and precursors.[12] Careful selection of flux to assure redox stability is an important factor to consider when attempting the preparation of reduced species. Alkali metal chlorides fall into that category and the combined use of such fluxes with a molten reducing agent has enabled our group to prepare a variety of reduced oxides. Specifically the use of molten zinc metal as a reducing agent has been very effective. The operating temperatures for halide fluxes range from 600 to 1100°C, which makes zinc, with its relatively low melting point of 419°C, an attractive reducing agent that will be liquid/gaseous under the reaction conditions.

Using an alkali/alkaline earth halide eutectic melt, we successfully crystallized **4.1**, a partially reduced siliconiobate, that contains a small amount of Nb(IV). Herein we detail the crystal growth, structure, magnetic and optical properties of the Belkovite-type **4.1**.

Experimental Details

Reagents.

$BaCl_2 \cdot 2H_2O$ (Alfa Aesar, 99+%), NaCl (Fisher, ACS grade), and $NaNbO_3$ (Strem Chemicals, 99.9%) were dried at 260°C for a minimum of 24 hours before use. Zinc powder (Alfa Aesar, 99.9%) was used as received.

Flux Synthesis.

Synthesis of $Ba_3Na_{0.32}Nb_6O_{12}(Si_2O_7)_2$, ***4.1***

Single crystals of **4.1** were grown out of a molten barium chloride/sodium chloride eutectic flux. In a typical procedure, 1.5 mmol of $NaNbO_3$ (dried at 260°C for 24 hours), 2 mmol of Zn powder, and a 10x excess by weight of $BaCl_2$/NaCl (dried at 260°C for 24 hours) were placed in a 8'' long fused silica tube of ½'' diameter. The tube was evacuated via a vacuum manifold to a pressure of 10^{-4} torr and flame sealed. The tube was heated in a programmable furnace to 1050°C at a rate of 15°C/min, held for 48 hours, and then cooled to 550°C at a rate of 6°C/hr. At this point the furnace was shut off and allowed to cool to room temperature. The chloride flux was dissolved in water aided by sonication. Residual zinc powder was removed via sonication of the product in dilute HCl. The crystals were isolated via vacuum filtration yielding a phase pure product in approximately 75% yield based on $NaNbO_3$. **Figure 4.1** shows an optical image and a

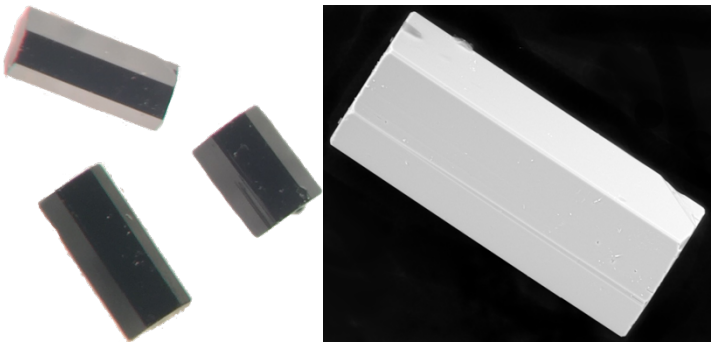

Figure 4.1 Optical image of compound **4.1** grown out of a barium chloride/sodium chloride melt and SEM image of compound **4.1**.

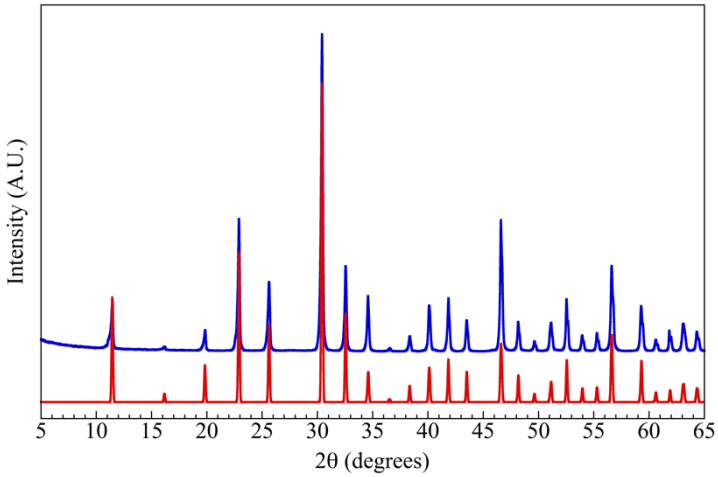

Figure 4.2 PXRD pattern of compound **4.1**. Experimental diffraction is shown in blue. The calculated pattern is shown in red.

scanning electron microscopy (SEM) image of the crystals. **Figure 4.2** shows a powder X-ray diffraction pattern (PXRD) of ground crystals, demonstrating the phase purity of the product crystals.

Energy-Dispersive Spectroscopy (EDS).

Elemental analysis was performed on the single crystals using a TESCAN Vega-3 SBU SEM with EDS capabilities. The crystals were mounted on carbon tape and analyzed using a 20 kV accelerating voltage and an accumulation time of 1 minute. As a qualitative measure, EDS confirmed the presence of each reported element in the title compound.

Single Crystal X-ray Diffraction (SXRD).

X-ray intensity data from a dark blue hexagonal rod crystal were collected at 294(2) K using a Bruker SMART APEX diffractometer (Mo Kα radiation, λ = 0.71073 Å). [13] Larger crystals appear lustrous black, but are blue in color when thinner. The raw area detector data frames were reduced and corrected for absorption effects with the SAINT+ and SADABS programs.[13] Final unit cell parameters were determined by least-squares refinement of 6599 reflections from the data set. An initial structural model was obtained with direct methods. Subsequent difference Fourier calculations and full-matrix least-squares refinement against F^2 were performed with SHELXL-2014[14] using the ShelXle interface.[15]

The compound crystallizes in the hexagonal system. No pattern of systematic absences was observed in the intensity data, leaving 16 possible space group choices. The non-centrosymmetric group *P*-62*m* (No. 189) was eventually confirmed by structure solution and by reference to previously published data. There are nine atomic positions in

the asymmetric unit: one barium atom, one niobium atom, one silicon atom, five oxygen atoms and one partially occupied position modeled as sodium. Barium Ba(1) and oxygen O(3) are located on site 3*g*, and O(4) on site 3*f*, both with *m*2*m* site symmetry. Nb(1) and O(2) are located on a mirror plane (site 6*i*, ..*m* site symmetry). Si(1) is located on a three-fold axis (site 4*h*, 3.. site symmetry), oxygen O(1) is on a general position, and O(5) is located on site 2*c*, with -6.. site symmetry. After location and normal refinement of atoms of the $Ba_3Nb_6Si_4O_{26}$ framework described above, a residual electron density peak of magnitude 2.95 e-/Å^3 was observed in the difference map. This peak occupied a chemically sensible location in a cavity bounded by seven oxygen atoms within a range of 2.55 - 3.04 Å. The next largest residual electron density peak was 0.83 e-/Å^3. The peak was refined as a fractionally occupied sodium atom originating from the reaction flux, as indicated by elemental analysis (EDS) data. The two shortest distances of 2.55 Å suggest this atom is not barium. Including this atom in the refinement reduced the *R*-factors from *R*1/*wR*2 = 0.0213 / 0.0472 to 0.0193/0.0394 (all data) and flattened the difference map. All atoms were refined with anisotropic displacement parameters except for the partially occupied sodium. No deviation from full site occupancy was observed for Ba(1), Nb(1) or Si(1). The final absolute structure (Flack) parameter refined to 0.42(2), and the structural model was refined as an inversion twin with this value as the minor twin fraction. Crystallographic data, equivalent atomic positions, and selected interatomic distances are listed in Tables **4.1 – 4.3**. The Cambridge Crystallographic Data Centre (CCDC) number is: #1452140. The Inorganic Crystal Structure Database (ICSD) number is: #429258.

Table 4.1 Crystal data and structure refinements for compound **4.1**.

	4.1
Empirical formula	$Ba_3Na_{0.32}Nb_6O_{26}Si_4$
Formula weight	1505.25
Temperature	294(2) K
Wavelength	0.71073 Å
Crystal system	hexagonal
Space group	*P*-62*m*
Unit cell dimensions	a = 8.9998(10) Å b = 8.9998(10) Å c = 7.8119(17) Å α = 90° β = 90° γ = 120°
Volume	547.96(17) $Å^3$
Z	1
Denisty (calculated)	4.561 mg/m^3
Absorption coefficient	8.660 mm^{-1}
F(000)	682.0
Crystal size	0.12 × 0.08 × 0.08 mm^3
2θ range for data collected	2.607 to 35.427°
Index ranges	−14 ≤ h ≤ 14 −13 ≤ k ≤14 −12 ≤ l ≤ 11
Reflections collected	15798
Ind. reflections	953[R(int) = 0.0321]
Data / restraints / parameters	953 / 0 / 44
Goodness-of-fit on F^2	1.179
Final R indices [I>2sigma(I)]	R_1 = 0.0189 wR_2 = 0.0381
R indices (all data)	R_1 = 0.0193 wR_2 = 0.0382
Flack parameter	0.42(2)
Largest diff. peak and hole	0.813 and −1.105 $e^- \times Å^{-3}$

Table 4.2 Selected interatomic distances (Å) for compound **4.1**.

4.1			
Ba(1)^{15}–O(1)$^{1-4}$ x 4	2.864(3)	Si(1)^{17}–O(5)	1.6025(16)
Ba(1)–O(2)^{5} x 2	2.865(4)	Si(1)–O(1)^{13,14} x 3	1.622(3)
Ba(1)^{12}–O(1)$^{6-9}$ x 4	2.984(3)	Na(1)–O(2)^{17} x 2	2.550(19)
Nb(1)^{10}–O(2)^{11,12} x 2	1.9352(12)	Na(1)^{16}–O(5)^{18,19} x 2	2.819(10)
Nb(1)^{17}–O(4)	1.9385(12)	Na(1)^{11}–O(4)^{7,10} x 2	3.054(19)
Nb(1)^{5}–O(3)	2.0027(8)	Na(1)–O(4)	3.10(3)
Nb(1)^{15}–O(1)^{1,3} x 2	2.041(3)		

^{1} −X+Y, −X, +Z ^{2} +Y, +X, −Z+1 ^{3} +X, +Y, +Z ^{4} −X+Y, −X, −Z+1
^{5} +X, +Y, −Z+1 ^{6} −X+1, −X+Y, −Z+1 ^{7} −Y+1, X−Y, +Z
^{8} −X+1, −X+Y, +Z ^{9} −Y+1, X−Y, −Z+1 ^{10} −X+Y+1, −X, +Z
^{11} −Y, X−Y−1, +Z ^{12} −X+Y+1, −X+1, Z ^{13} −X+Y, −X+1, +Z
^{14} −Y+1, X−Y+1, +Z ^{15}−Y, X−Y, +Z ^{16} +X, Y+1, +Z ^{17} +X, +Y, −Z
^{18} +X, Y−1, +Z ^{19} Y, X, −Z

Table 4.3 Atomic Coordinates and equivalent isotropic displacement parameters U_{eq} for compound **4.1**. U_{eq} is defined as one third of the trace of the orthogonalized U_{ij} tensor.

	Occupancy	*x*	*y*	*z*	U_{eq}
Ba(1)	1	0.6006(1)	0	½	0.011(1)
Nb(1)	1	0.2376(1)	0	0.2440(1)	0.015(1)
Si(1)	1	⅓	⅔	0.2051(2)	0.007(1)
O(1)	1	0.1815(3)	0.4881(3)	0.2838(3)	0.011(1)
O(2)	1	0.8194(4)	0	0.2336(4)	0.010(1)
O(3)	1	0.2259(6)	0	½	0.013(1)
O(4)	1	0.2768(6)	0	0	0.012(1)
O(5)	1	⅓	⅔	0	0.018(1)
Na(1)	0.107	0.6210(30)	0	0	0.010(7)

Powder X-ray Diffraction (PXRD).

PXRD data were collected on a Rigaku D/Max-2100 powder X-ray diffractometer using Cu Kα radiation. The step scan covered the angular range 5-65° 2θ in steps of 0.04°. No impurities were observed and the experimental and calculated PXRD patterns are in excellent agreement (see **Figure 4.2**).

UV/Vis Diffuse Reflectance Spectroscopy (UV/Vis).

UV/Vis diffuse reflectance spectroscopy data of ground crystals were obtained using a PerkinElmer Lambda 35 UV-Vis scanning spectrophotometer equipped with an integrating sphere accessory in the range of 200-900 nm. Reflectance data were transformed to absorbance via the Kubelka-Munk function.[16]

Fourier Transform Infrared Spectroscopy (IR).

An IR spectrum of ground crystals was recorded on a PerkinElmer Spectrum 100 FT-IR spectrometer fitted with an ATR accessory in the range of 650-4000 cm^{-1}.

Magnetic Susceptibility.

The magnetic susceptibility was measured using a Quantum Design MPMS 3 SQUID magnetometer. The zero-field cooled magnetic susceptibility was measured as a function of temperature between 2-300K in an applied field of 1000 Oe. The measured magnetic data were corrected for shape and radial offset effects using the method reported by Morrison et al.[17]

Second Harmonic Generation (SHG).

Powder SHG measurements were performed on a modified Kurtz nonlinear-optical (NLO) system using a pulsed Nd:YAG laser with a wavelength of 1064 nm. A comparison with a known SHG material was made using ground crystalline α-SiO_2. A

detailed description of the equipment and methodology has been published elsewhere.[18, 19]

Results and discussion

Synthesis.

Crystals of **4.1** were grown out of a chloride flux, which are known to be redox stable solvents suitable for the crystal growth of reduced oxides.[20-22] In this work a $BaCl_2$/NaCl eutectic flux was used to ensure a long liquid range and, furthermore, to function as a source of barium and sodium ions during the crystallization process. Excluding potential oxidizing species, such as oxygen or water, from the reaction is crucial to promote a reducing environment. For this reason the reaction was performed in an evacuated sealed fused silica tube and all reagents except for the zinc powder were dried for 24 hours in an oven at 260°C to exclude water from the reaction. At a dwell temperature of 1050°C, the zinc metal is above its boiling point of 907°C and generates a vapor pressure significant enough to establish a uniform reducing atmosphere within the tube, but not so great as to rupture the fused silica tube.

At elevated temperatures Group 5 oxides are known to attack fused silica and, in this regard, $NaNbO_3$ serves as a mineralizer for silicon, which is leached from the interior walls of the fused silica tube. It was found that the addition of dry, powdered SiO_2 as a more finely divided source of silicon in fact worsened the yield and crystal quality of the product. We postulate that the slow dissolution of silicon from the interior wall of the fused silica tube allows for a more controlled crystallization, which results in a phase pure sample. The PXRD pattern of the ground crystals, shown in **Figure 4.2**, is in excellent agreement with the powder pattern calculated from single crystal data,

confirming the phase purity of the sample. Attempts to crystallize compositions with higher sodium content were unsuccessful.

Structure.

The structure of **4.1** is based on the Belkovite structure type which exhibits a three dimensional crystal structure consisting of corner- or edged-sharing BaO_{10}, NbO_6, and SiO_4 polyhedra that form a siliconiobate framework with barium cations residing within large cavities of the framework.[11] This structure is similar to the known hexagonal tungsten bronzes, which contain a framework of corner-sharing tungsten polyhedra with alkali cations residing in channels within the structure.[23] In **4.1**, additional smaller cavities exist in the framework that cannot accommodate a large barium cation and are unoccupied in the fully oxidized structure. In **4.1**, fractionally occupied NaO_7 polyhedra reside in these smaller cavities. The barium and sodium cavities stack in an alternating AB sequence down the *c* axis and are easily distinguished when viewing the structure along the *c* axis, as shown in **Figure 4.3**. By doping in positive charge in the form of Na^+, we are able to partially reduce the Nb(V) to Nb(IV). As sodium is significantly smaller than barium, its presence does not significantly alter the unit cell parameters, which are consistent with those of the fully oxidized structure.[11, 24] Ba(1) is located in a ten coordinate distorted pentagonal prism, shown in **Figure 4.4**, with Ba-O distances between 2.864 Å – 3.122 Å. Ba(1) shares edges with itself, Si(1), and Nb(1) through O(1) and O(2). Ba(1) also shares a corner with the fractionally occupied Na(1) through O(2). Nb(1) is located in a six coordinate distorted octahedron, shown in **Figure 4.5**, with Nb-O distances between 1.935 Å – 2.041 Å. Nb(1) shares corners with itself through O(2) forming Nb_3O_{15} trimeric clusters, shown in **Figure 4.6**, and with itself through O(4)

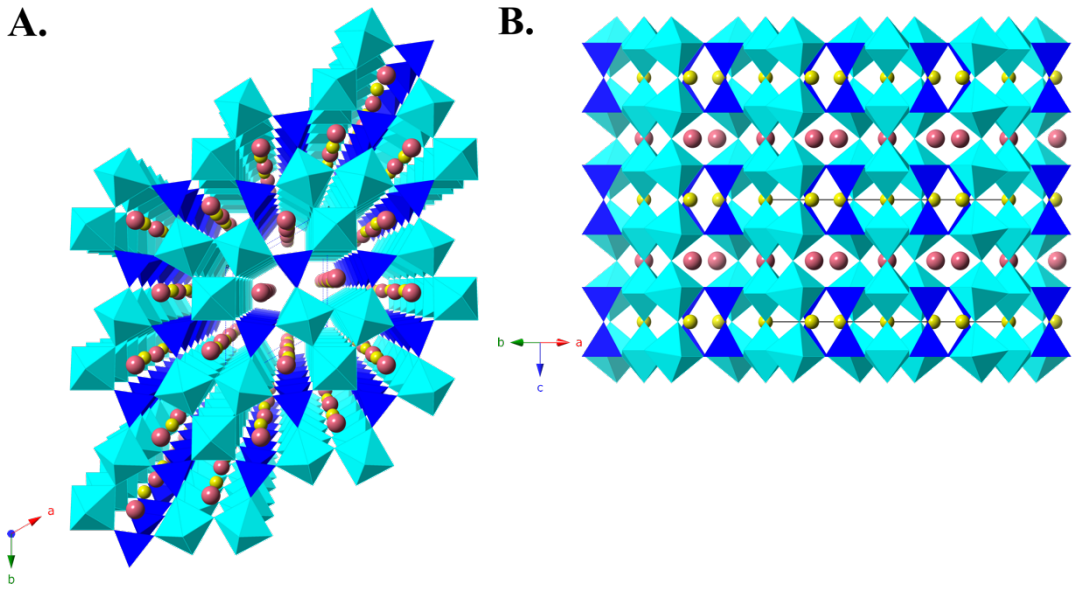

Figure 4.3 A. Compound **4.1** viewed down the *c* axis. B. Compound **4.1** viewed along the *c* axis. Ba, Na, Nb, Si, and O shown in pink, yellow, cyan, blue, and red, respectively. Fractional Na shown in full occupancy in figure for clarity. Unit cell shown as black solid line.

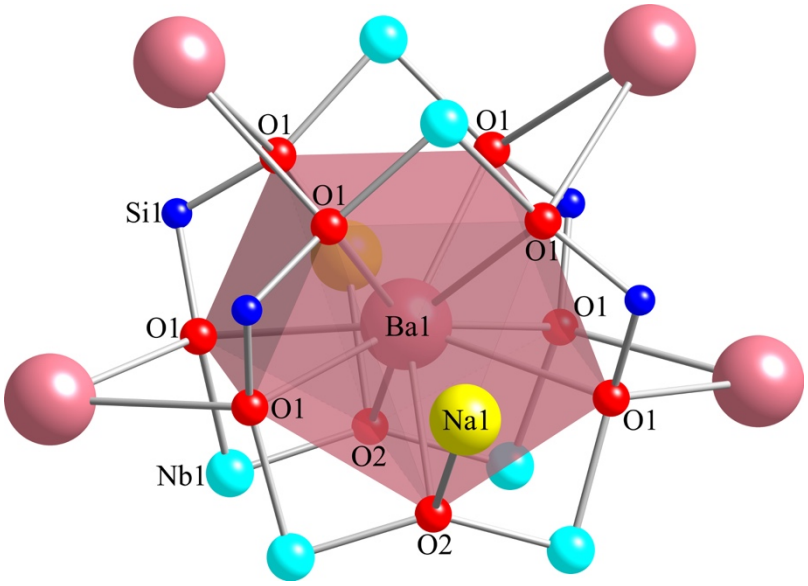

Figure 4.4 Local coordination environment of Ba(1). Ba, Na, Nb, Si, and O shown in pink, yellow, cyan, blue, and red, respectively.

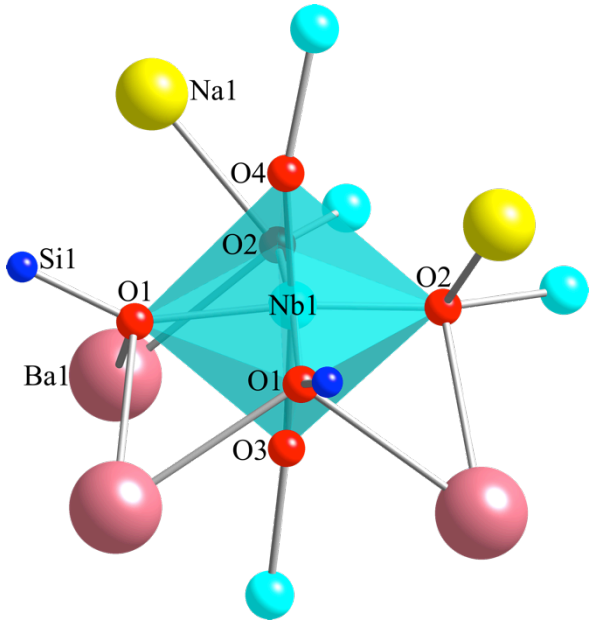

Figure 4.5 Local coordination environment of Nb(1). Ba, Na, Nb, Si, and O shown in pink, yellow, cyan, blue, and red, respectively.

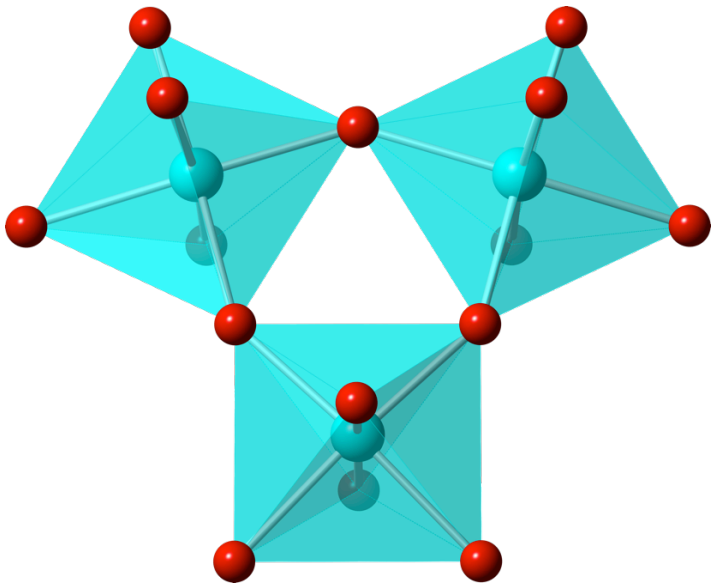

Figure 4.6 Nb_3O_{15} trimeric cluster. Nb and O shown in cyan and red, respectively.

forming columns of trimeric clusters, shown in **Figure 4.7**. These trimeric columns are linked via Si(1) with corner sharing through O(1). Nb(1) also shares a corner with fractionally occupied Na(1) through O(2). Si(1) is located in a four coordinate tetrahedral coordination environment with Si-O distances ranging from 1.603 Å – 1.622 Å. Si(1) shares a corner with itself through O(5) forming pyrosilicate groups, shown in **Figure 4.8**. $Si(1)O_4$ tetrahedra share an edge with Ba(1) and Nb(1) through O(1) and corner shares with fractionally occupied Na(1). Na(1) is fractionally occupied in a seven coordinate irregular coordination environment, shown in **Figure 4.9**, with Na-O distances ranging from 2.550 Å – 3.103 Å. The $Na(1)O_7$ polyhedron shares corners with Ba(1), Nb(1), and Si(1) through O(2), O(4), and O(5), respectively, and edges with Nb(1) through O(2) and O(4). Na(1) resides in cavities that are empty in the fully oxidized parent compound $Ba_3Nb_6O_{12}(Si_2O_7)_2$. As a consequence of this sodium doping, a small but not negligible amount of the niobium in **4.1** must be reduced from +5 to +4. The blue color of the compound provides evidence for this, as previously reported mixed $Nb^{+4/+5}$ compounds are often blue. Based on the chemical composition of the title compound, the average oxidation state for niobium is +4.94 with 94.67% Nb(V) and 5.33% Nb(IV).

UV/Vis Diffuse Reflectance Spectroscopy (UV/Vis).

UV/Vis absorbance data shown in **Figure 4.10** were collected using ground crystals. The absorption edge is clearly observed in the UV region, and the band gap estimated by the onset of the absorption edge is approximately 3.4 eV, indicating insulating behavior for the siliconiobate. A broad absorbance ranging from 900 nm – 400 nm is observed, with a maximum at 882 nm and shoulders at approximately 560 nm and

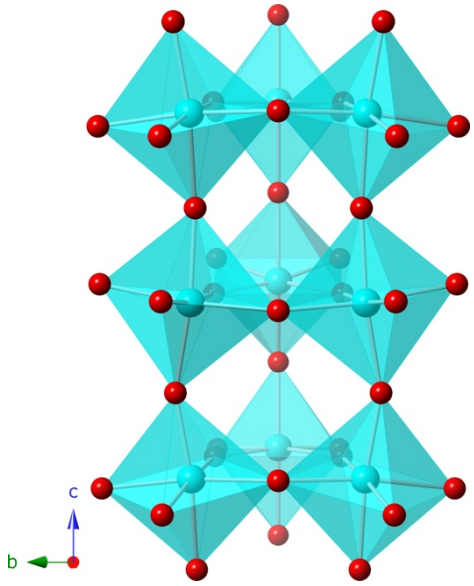

Figure 4.7 Column of stacked Nb_3O_{15} trimeric clusters. Nb and O shown in cyan and red, respectively.

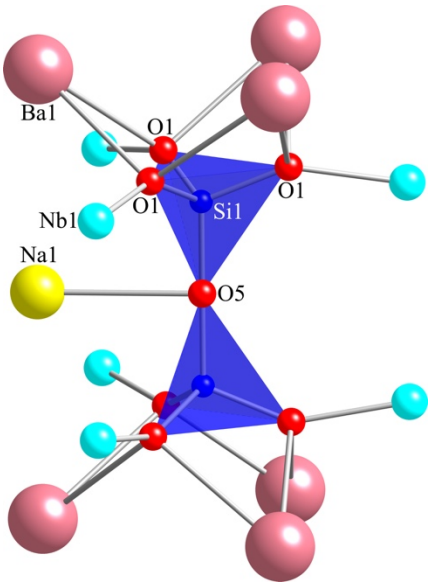

Figure 4.8 Local coordination environment of $Si(1)_2O_7$ pyrosilicate group. Ba, Na, Nb, Si, and O shown in pink, yellow, cyan, blue, and red, respectively.

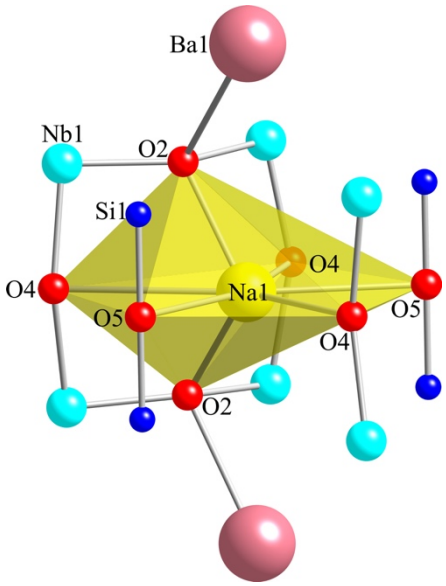

Figure 4.9 Local coordination environment of Na(1). Ba, Na, Nb, Si, and O shown in pink, yellow, cyan, blue, and red, respectively.

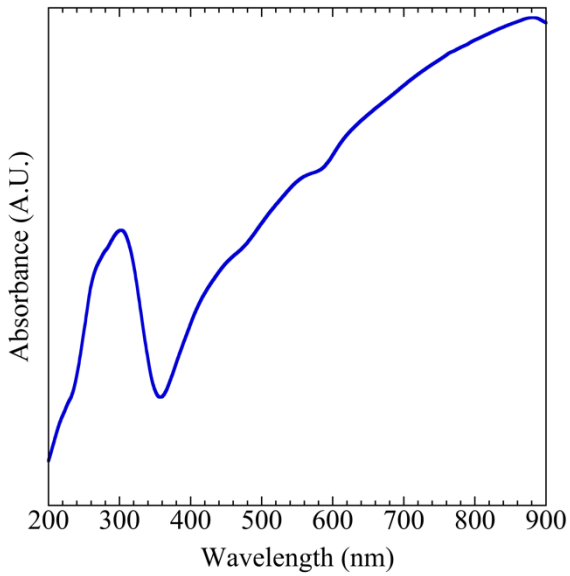

Figure 4.10 UV/Vis absorbance spectrum for compound **4.1**.

450 nm, that is consistent with the presence of Nb(IV) based on reports in the literature describing the UV/Vis absorption of niobium(IV) containing compounds.[25]

Fourier Transform Infrared Spectroscopy (IR).

The IR spectrum, which is shown in **Figure 4.11**, was collected between 650 – 4000 cm^{-1}. The bands between 1200 cm^{-1} – 850 cm^{-1} correspond to asymmetric Si – O – Si stretching modes and symmetric and asymmetric stretching modes of SiO_3.[26] The band observed at 736 cm^{-1} corresponds to the NbO_6 symmetric stretching mode.[26]

Magnetic Susceptibility.

The unpaired electrons in **4.1** can be observed in magnetic susceptibility measurements. The temperature dependence of the magnetic susceptibility of **4.1** measured in an applied field of 1000 Oe is shown in **Figure 4.12**. In **4.1** the amount of Nb(IV) is small and is therefore magnetically dilute, thus no magnetic coupling is expected or observed. Down to 2K, the data do not reveal any long-range magnetic order and follow the Curie-Weiss (C-W) law as expected for simple paramagnetic species. The magnetic moment calculated from the inverse susceptibilities is 1.75 μ_B/mol Nb(IV), which is in good agreement with the expected spin only value for **4.1** of 1.73 μ_B/mol Nb(IV).[27]

Second Harmonic Generation (SHG).

Although **4.1** belongs to the noncentrosymmetric space group *P*-62*m*, no detectable SHG response was observed when measuring a ground polycrystalline sample.

Conclusion

We successfully synthesized a new barium sodium siliconiobate, $Ba_3Na_{0.32}Nb_6O_{12}(Si_2O_7)_2$ via a molten salt flux technique and characterized its structure

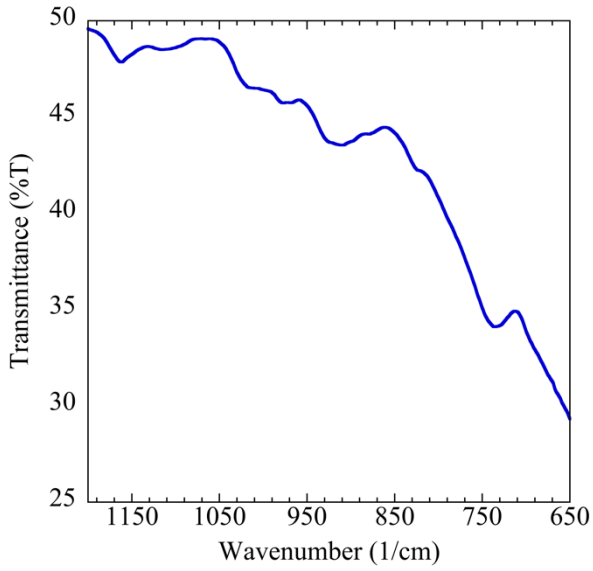

Figure 4.11 IR spectrum of compound **4.1**.

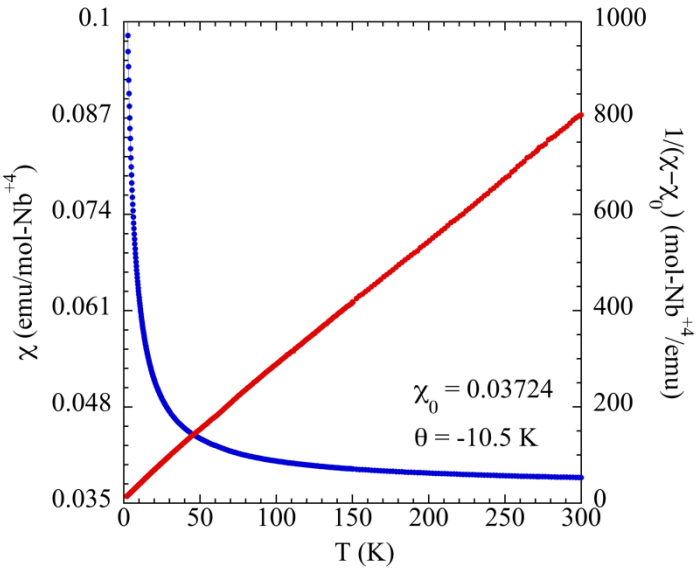

Figure 4.12 Magnetic susceptibility plot for compound **4.1**. χ and $1/\chi - \chi_0$ are shown in blue and red, respectively.

and physical properties. By utilizing a flux containing sodium we were able to fractionally dope sodium into cavities that remain empty in the fully oxidized parent compound, $Ba_3Nb_6O_{12}(Si_2O_7)_2$. Niobium in this structure is slightly reduced with an average oxidation state of +4.94 and a Nb(IV) content of 5.33%. As a result of the diluteness of the Nb(IV) in the compound, only simple paramagnetic behavior is observed. The agreement of the experimental and theoretical magnetic moments confirms the presence and quantity of Nb(IV) in the structure.

Acknowledgement

Financial support for this work was provided by the National Science Foundation under DMR-1301757 and is gratefully acknowledged. Powder SHG measurements were performed at the University of Houston by T. Thao Tran of the P. Shiv Halasyamani Group and are gratefully acknowledged.

References

(1) M. J. Geselbracht; T. J. Richardson; A. M. Stacy. Nature. 345 (6273) (1990) 324-326.

(2) H. Kusumoto; K. Narita; J. Umeda. Kotai Butsuri. (1967) 3-11.

(3) G. J. Hill; R. H. Martin. Phys. Lett. A. (1968) 34-35.

(4) O. G. D'yachenko; S. Y. Istomin; A. M. Abakumov; E. V. Antipov. Inorg. Mater. 36 (3) (2000) 247-259.

(5) T. McQueen; Q. Xu; E. N. Andersen; H. W. Zandbergen; R. J. Cava. J. Solid State Chem. 180 (10) (2007) 2864-2870.

(6) J. Köhler; G. Svensson; A. Simon. Angew. Chem. Int. Edi. 31 (11) (1992) 1437-1456.

(7) S. Y. Istomin; O. G. D'yachenko; E. V. Antipov; G. Svensson. Mater. Res. Bull. 32 (4) (1997) 421-430.

(8) S. Y. Istomin; O. G. D'yachenko; E. V. Antipov; G. Svensson; B. Lundqvist. Mater. Res. Bull. 33 (8) (1998) 1251-1256.

(9) S. Y. Istomin; G. Svensson; O. G. D'yachenko; W. Holm; E. V. Antipov. J. Solid State Chem. 141 (2) (1998) 514-521.

(10) N. Kumada; N. Kinomiura. J. Solid State Chem. 147 (2) (1999) 671-675.

(11) J. Shannon; L. Katz. Acta Crystallogr., Sect. B: Struct. Crystallogr. Cryst. Chem. 26 (2) (1970) 105-109.

(12) D. E. Bugaris; H.-C. zur-Loye. Angew. Chem., Int. Ed. 51 (16) (2012) 3780-3811.

(13) SMART Version 5.630, SAINT+ Version 6.45 and SADABS Version 2.10. Bruker Analytical X-ray Systems, Inc., Madison, Wisconsin, USA, 2003.

(14) G. M. Sheldrick. Acta Crystallogr., Sect. A: Found. Crystallogr. 64 (1) (2008) 112-122.

(15) C. B. Hübschle; G. M. Sheldrick; B. Dittrich. J. Appl. Cryst. 44 (6) (2011) 1281-1284.

(16) P. Kubelka; F. Z. Munk. Tech. Phys. 12 (1931) 593-601.

(17) G. Morrison; H.-C. zur Loye. J. Solid State Chem. 221 (2015) 334-337.

(18) S. K. Kurtz; T. T. Perry. J. Appl. Phys. 39 (8) (1968) 3798-3813.

(19) K. M. Ok; E. O. Chi; P. S. Halasyamani. Chem. Soc. Rev. 35 (8) (2006) 710-717.

(20) P. Mahjoor; S. E. Latturner. Inorg. Chem. 49 (10) (2010) 4486-4490.

(21) P. Mahjoor; S. E. Latturner. Philos. Mag. 92 (19-21) (2012) 2582-2595.

(22) M. P. Rogge; J. H. Caldwell; D. R. Ingram; C. E. Green; M. J. Geselbracht; T. Siegrist. J Solid State Chem. 141 (2) (1998) 338-342.

(23) L. Khilborg; A. Hussain. Mater. Res. Bull. 14 (1979) 667-674.

(24) J. Choisnet; N. Nguyen; D. Groult; B. Raveau. Mater. Res. Bull. 11 (1976) 887-894.

(24) H. Mizoguchi; M. Orita; M. Hirano; S. Fujitsu; T. Takeuchi; H. Hosono. Appl. Phys. Lett. 80 (2002) 4732-4734.

(25) J. Choisnet; N. Nguyen; B. Raveau; M. Gabelica-Robert; P. Tarte. J. Solid State Chem. 26 (1) (1978) 83-95.

(26) Blundell, S. *Magnetism in Condensed Matter*; Oxford University Press: Oxford, UK, 2001.

CHAPTER V

SINGLE CRYSTAL GROWTH AND CHARACTERIZATION OF $NA_xLN_{1-x}MoO_4$, *LN* = LA, CE, PR, ND, SM, AND EU (X = 0.397 – 0.499)*

*Cortese, A. J.; Abeysinghe, D.; Smith, M. D.; zur Loye, H.-C. *J. Solid State Chem.* **2016** *Submitted.*

Abstract

Single crystals of $La_{0.516(3)}Na_{0.484(3)}MoO_4$, $Ce_{0.512(2)}Na_{0.488(2)}MoO_4$, $Pr_{0.502(2)}Na_{0.498(2)}MoO_4$, $Nd_{0.501(2)}Na_{0.499(2)}MoO_4$, $Sm_{0.509(2)}Na_{0.491(2)}MoO_4$, and $Eu_{0.603(2)}Na_{0.397(2)}MoO_4$ were grown for the first time out of an alkali/alkaline earth eutectic flux. All compounds crystallize in the tetragonal space group $I4_1/a$. UV/Vis measurements indicate insulating behavior for all compounds except $Eu_{0.603(2)}Na_{0.397(2)}MoO_4$. The temperature dependence of the magnetic susceptibility was measured for all compounds and found to be paramagnetic across the entire 2 – 300 K temperature range measured.

Introduction

Crystal growth of compounds containing early transition metals in reduced oxidation states is an emerging area of materials chemistry that has historically been hampered due to the unique synthetic challenges involved in this type of crystal growth. It is, however, an interesting area of research for the creation of oxides containing unpaired electrons, in particular since early transition metals in reduced oxidation states can potentially lead to interesting electrical and magnetic properties. Historically, researchers have reported simple reduced early transition metal oxides such as VO_2, V_2O_3[1-3], TiO[4], and Ti_2O_3[5], as well as some ternary and higher reduced oxides, including reduced perovskites and bronzes: $SrTiO_{2.5}$[6], $Ba_6Nb_{14}Si_4O_{47}$[7], $AxNbO_3$(A=Sr, Ba)[8, 9], $Ba_3M_5O_{15}$(M=Nb, Ta)[10, 11], $A_{0.3}MoO_3$ (A=K, Rb, Tl)[12, 13], $Cs_{0.33}MoO_3$[14], $K_2Mo_4Nb_3O_{20}$[15], and SrV_4O_9[16] using crystal growth approaches that include fused salt electrolysis, chemical vapor transport, hydrothermal, and flux methods.

The limited number of known oxides containing reduced early transition metals has pushed us to pursue synthetic strategies to prepare such oxides and to explore their physical properties, including magnetism. One approach, a two step-hydrothermal method, has been very successful for preparing single crystals of hybrid materials containing V^{4+} and U^{4+}[17-23]. To explore the preparation of reduced oxides, we explored the use of flux crystal growth, a well-known, facile method for the crystal growth of a diverse oxides, including reduced ones[24]. In order to successfully grow reduced oxide crystals, we carefully selected alkali metal halides as redox neutral fluxes, which can be utilized as high temperature fluxes in sealed reaction vessels, making them excellent candidates for our work. Most compounds reported in the literature were prepared using niobium, tantalum or fused silica sealed tubes[10, 25-30].

Our approach is based on the *in situ* reduction of early transition cations using a metal reductant, such as Mo, W, V, or Zn combined with eutectic alkali halide melts in an evacuated sealed fused silica tube. This method has been used by us very successfully for the preparation of reduced oxides containing Nb^{4+}, Mo^{4+}, Mo^{5+}, V^{3+}, V^{4+}, and Eu^{2+}[31-36].

Recently we reported the synthesis and characterization of several potassium doped europium molybdates containing $Mo^{5+/6+}$ and $Eu^{2+/3+}$[32]. In order to fully explore the phase space of these structures we attempted to prepare sodium doped molybdates using analogous reaction conditions, which has resulted in the six title compounds: $La_{0.516(3)}Na_{0.484(3)}MoO_4$, $Ce_{0.512(2)}Na_{0.488(2)}MoO_4$, $Pr_{0.502(2)}Na_{0.498(2)}MoO_4$, $Nd_{0.50}Na_{0.50}MoO_4$, $Sm_{0.509(2)}Na_{0.491(2)}MoO_4$, and $Eu_{0.603(2)}Na_{0.397(2)}MoO_4$. All six compositions crystallize in the scheelite structure ($CaWO_4/ABO_4$), which consists of corner sharing 8-coordinate *A* and 4-coordinate *B* sites.

To characterize the structure and the oxidation states of the metals within the flux grown single crystals, a combination of single crystal X-ray diffraction, bond valence sum calculations and magnetic susceptibility measurements were employed. Herein, we report the synthesis, crystal structure and physical property characterization of $La_{0.516(3)}Na_{0.484(3)}MoO_4$, $Ce_{0.512(2)}Na_{0.488(2)}MoO_4$, $Pr_{0.502(2)}Na_{0.498(2)}MoO_4$, $Nd_{0.501(2)}Na_{0.499(2)}MoO_4$, $Sm_{0.509(2)}Na_{0.491(2)}MoO_4$, and $Eu_{0.603(2)}Na_{0.397(2)}MoO_4$.

Experimental details

Reagents.

MoO_3 (99.95%, Alfa Aesar), Mo metal (99.9%, ~250 mesh, Alfa Aesar) and CeO_2 (99.99%, Alfa Aesar) were used as received. NaCl (ACS grade, Fisher) and CsCl (99.9%, Alfa Aesar) were dried prior to synthesis for 24 hours at 260 °C in an oven. La_2O_3 (99.99%, Alfa Aesar), Nd_2O_3 (99.99%, Alfa Aesar), Sm_2O_3 (99.99%, Alfa Aesar), and Eu_2O_3 (99.99%, Alfa Aesar) were activated at 1000 °C for 12 hours in a furnace before use. Pr_6O_{11} (Alfa Aesar, 99.9%) was reduced to Pr_2O_3 under 4%H_2/96%N_2 at 800 °C for 12 hours before use.

Flux Synthesis.

Synthesis of $La_{0.516(3)}Na_{0.484(3)}MoO_4$, ***5.1***; $Ce_{0.512(2)}Na_{0.488(2)}MoO_4$, ***5.2***; $Pr_{0.502(2)}Na_{0.498(2)}MoO_4$, ***5.3***; $Nd_{0.501(2)}Na_{0.499(2)}MoO_4$, ***5.4***; $Sm_{0.509(2)}Na_{0.491(2)}MoO_4$, ***5.5***; *and* $Eu_{0.603(2)}Na_{0.397(2)}MoO_4$, ***5.6***

Single crystals of the title compounds were grown in vacuum sealed fused silica tubes out of a NaCl/CsCl eutectic melt. As detailed in **Table 5.1**, the respective amounts of reagents were placed in a fused silica tube, evacuated to a pressure of ~10^{-4} torr, and flame sealed. The title compounds were obtained by heating the mixture at a rate of 10

°C/min to a temperature of 825 °C, dwelling for 24 hours and cooling the mixture to 450 °C at a rate of 6 °C/hr. Single crystals were isolated via vacuum filtration by dissolving the remaining flux in water aided by gentle sonication. As shown in **Figure 5.1**, the powder X-ray diffraction patterns (PXRD) of the ground crystals match the patterns calculated using the single crystal structural data.

Energy-Dispersive Spectroscopy (EDS).

Elemental analysis was performed on all reported single crystals using a TESCAN Vega-3 SBU scanning electron microscope (SEM) with EDS capabilities. The crystals were mounted on carbon tape and analyzed using a 20 kV accelerating voltage and an accumulation time of 1 minute. As a qualitative measure, EDS confirmed the presence of each reported element in the title compounds.

Single crystal X-ray Diffraction (SXRD).

X-ray intensity data from crystals of **5.1** – **5.6** were collected at 296(2) K using a Bruker SMART APEX diffractometer (Mo $K\alpha$ radiation, λ = 0.71073 Å)[37]. The data collection covered 100% of reciprocal space to $2\theta_{max}$ 65.1 – 75.6°, with an average reflection redundancy of 5.6 – 13.4 and R_{int} = 0.0179 – 0.0377 after absorption correction. The raw area detector data frames were reduced and corrected for absorption effects with the SAINT+ and SADABS programs[37]. Final unit cell parameters were determined by least-squares refinement of 298 – 444 independent reflections from the data sets. Atomic coordinates of the common $CaWO_4$ structure type were used as an initial structural model. Subsequent difference Fourier calculations and full-matrix least-squares refinement against F^2 were performed with SHELXL-2013/4[38] using the ShelXle interface[39].

Table 5.1 Respective amounts of reagents and flux used in each reaction and their respective products obtained with crystal morphologies.

Reagents (mmol)	Reducing agent (mmol)	Flux (g)	Product	Crystal Morphology
MoO_3:La_2O_3 2:1	Mo 0.5	CsCl:NaCl 2.25:0.5	$La_{0.516(3)}Na_{0.484(3)}MoO_4$	black tetragonal bipyramids
MoO_3:CeO_2 2:1	Mo 0.5	CsCl:NaCl 2.25:0.5	$Ce_{0.512(2)}Na_{0.488(2)}MoO_4$	black tetragonal bipyramids
MoO_3:Pr_2O_3 2:1	Mo 0.5	CsCl:NaCl 2.25:0.5	$Pr_{0.502(2)}Na_{0.498(2)}MoO_4$	grey tetragonal bipyramids
MoO_3:Nd_2O_3 2:1	Mo 0.5	CsCl:NaCl 2.25:0.5	$Nd_{0.501(2)}Na_{0.499(2)}MoO_4$	purple tetragonal bipyramids
MoO_3:Sm_2O_3 2:1	Mo 0.5	CsCl:NaCl 2.25:0.5	$Sm_{0.509(2)}Na_{0.491(2)}MoO_4$	black tetragonal bipyramids
MoO_3:Eu_2O_3 2:1	Mo 0.5	CsCl:NaCl 2.25:0.5	$Eu_{0.603(2)}Na_{0.397(2)}MoO_4$	black tetragonal bipyramids

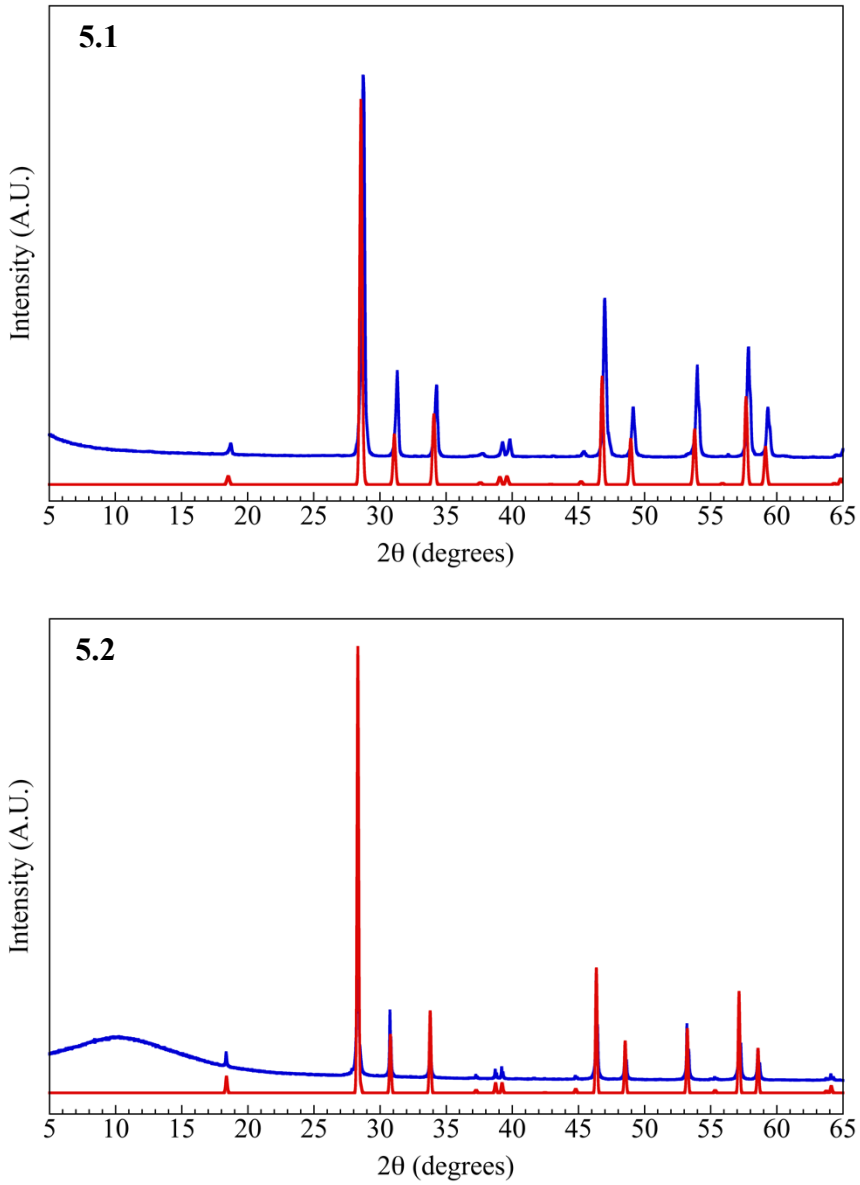

Figure 5.1 Experimental (blue) and calculated (red) powder X-ray diffraction patterns for compounds **5.1** and **5.2**.

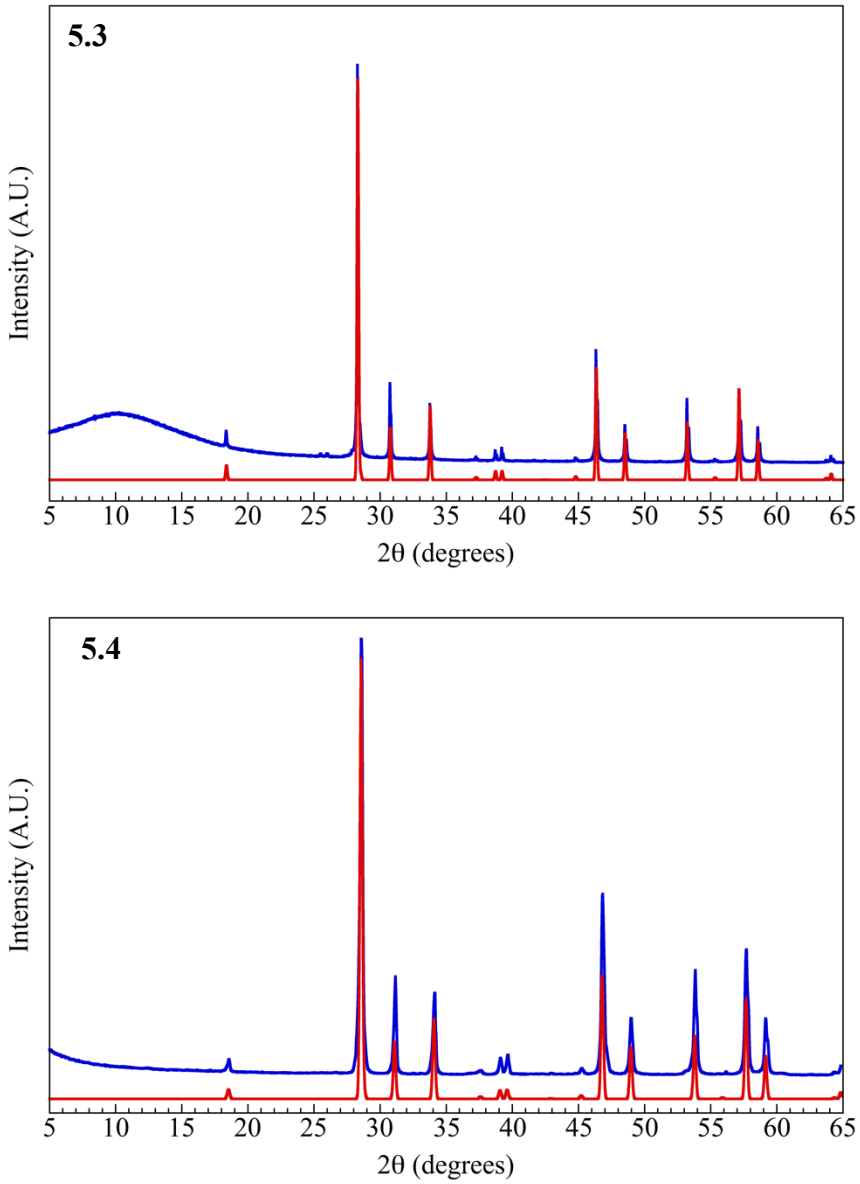

Figure 5.1 (cont.) Experimental (blue) and calculated (red) powder X-ray diffraction patterns for compounds **5.3** and **5.4**.

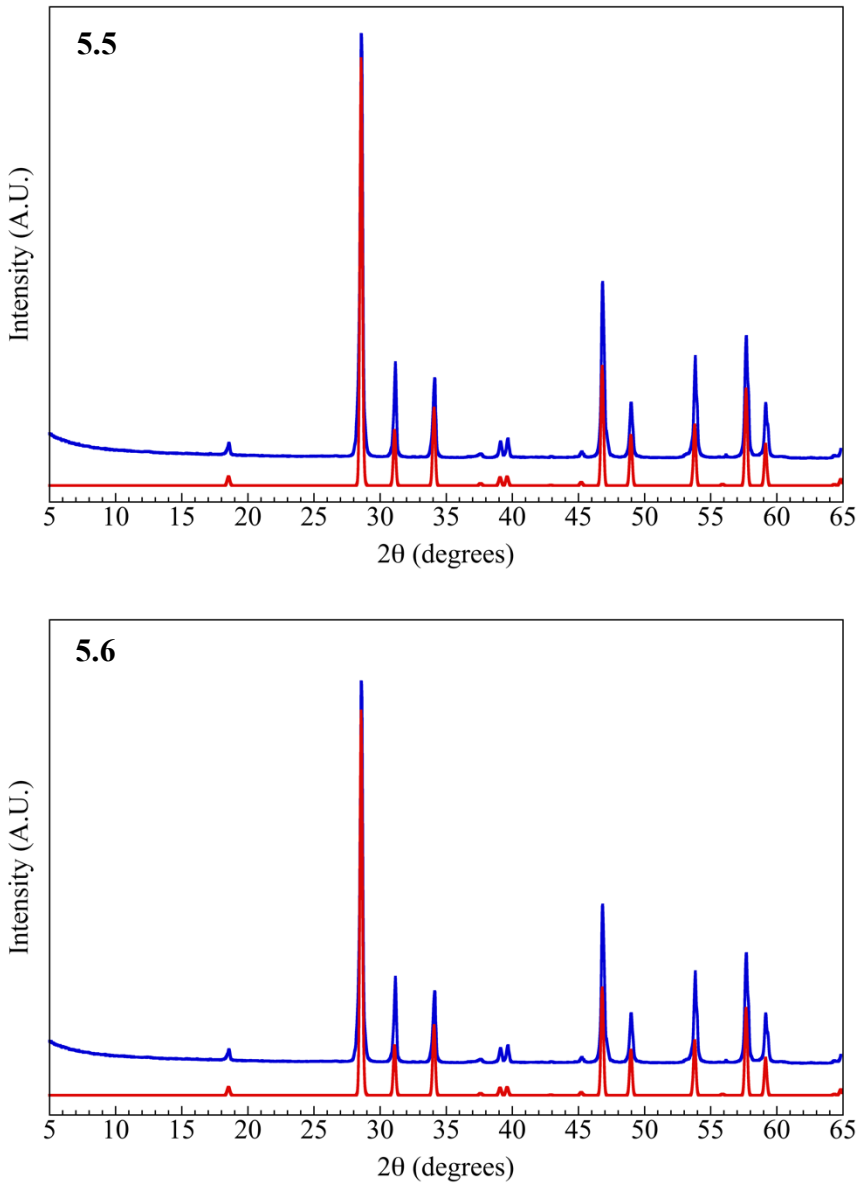

Figure 5.1 (cont.) Experimental (blue) and calculated (red) powder X-ray diffraction patterns for compounds **5.5** and **5.6**.

All title compounds crystallize in the tetragonal system. The space group $I4_1/a$ (No. 88, origin choice 2) was determined uniquely by the pattern of systematic absences in the intensity data. The compound adopts the scheelite ($CaWO_4$) structure type. The asymmetric unit consists of three atomic positions: one mixed *Ln*/Na position (site 4*b*, -4.. site symmetry), one Mo atom (site 4*a*, -4.. site symmetry) and one oxygen atom (general position, site 16*f*). The 4*b* site is occupied by a mixture of *Ln* and Na based on trial refinements. The total site occupancy of the mixed *Ln*/Na site was constrained to sum to unity. The atomic ratio refined to *Ln*/Na = 0.516(3)/0.484(3) for La, 0.512(2)/0.488(2) for Ce, 0.502(2)/0.498(2) for Pr, 0.501(2)/0.499(2) for Nd, 0.509(2)/0.491(2) for Sm, and 0.603(2)/0.397(2), for Eu. All atoms were refined with anisotropic displacement parameters. No significant deviation from unity occupancy was observed for the Mo or O atoms. Final atomic coordinates were standardized with Structure Tidy[40-42]. Crystallographic data, atomic coordinates and isotropic displacement parameters, and selected interatomic distances are listed in **Tables 5.2 – 5.4**. Cambridge Crystallographic Data Centre (CCDC) numbers are as follows: compound **5.1**: #1452142, compound **5.2**: #1452143, compound **5.3**: #1452144, compound **5.4**: #1452145, compound **5.5**: #1452146, and compound **5.6**: #1452147. Inorganic Crystal Structure database numbers are as follows: compound **5.1**: #430108, compound **5.2**: #430110, compound **5.3**: #430106, compound **5.4**: #430107, compound **5.5**: #430111, and compound **5.6**: #430109.

Powder X-ray Diffraction (PXRD).

Powder X-ray diffraction data were collected on either a Rigaku D/Max-2100 or Ultima(IV) powder X-ray diffractometer using Cu K*α radiation.* The step-scan covered

Table 5.2 Crystal data and structure refinements for compounds **5.1** and **5.2**.

	5.1	**5.2**
Empirical formula	$La_{0.516(3)}Na_{0.484(3)}MoO_4$	$Ce_{0.512(2)}Na_{0.488(2)}MoO_4$
Formula weight	242.74	242.90
Temperature	296(2) K	296(2) K
Wavelength	0.71073 Å	0.70173 Å
Crystal system	tetragonal	tetragonal
Space group	$I4_1/a$	$I4_1/a$
Unit cell dimensions	a = 5.3414(2) Å	a = 5.3173(2) Å
	b = 5.3414(2) Å	b = 5.3173(2) Å
	c = 11.7393(6) Å	c = 11.6652(6) Å
	$\alpha = 90°$	$\alpha = 90°$
	$\beta = 90°$	$\beta = 90°$
	$\gamma = 90°$	$\gamma = 90°$
Volume	334.93(3) $Å^3$	329.82(3)
Z	4	4
Denisty (calculated)	4.814 mg/m^3	4.892 mg/m^3
Absorption coefficient	10.214 mm^{-1}	10.757 mm^{-1}
F(000)	435.0	436.0
Crystal size	0.10 × 0.08 × 0.05 mm^3	0.08 × 0.06 × 0.05 mm^3
2θ range for data collected	4.192 to 32.565°	4.212 to 37.802°
Index ranges	$-7 \le h \le 8$	$-9 \le h \le 9$
	$-8 \le k \le 8$	$-9 \le k \le 9$
	$-17 \le l \le 17$	$-20 \le l \le 20$
Reflections collected	4161	5910
Ind. reflections	310[R(int) = 0.0179]	444[R(int) = 0.0377]
Data / restraints / parameters	310 / 0 / 16	444 / 0 / 16
Goodness-of-fit on F^2	1.396	1.224
Final R indices [I>2sigma(I)]	R_1 = 0.0271	R_1 = 0.0222
	wR_2 = 0.0434	wR_2 = 0.0439
R indices (all data)	R_1 = 0.0289	R_1 = 0.0313
	wR_2 = 0.0440	wR_2 = 0.0473
Largest diff. peak and hole	0.392 and −0.460 $e^-×Å^{-3}$	0.892 and −1.288 $e^-×Å^{-3}$

Table 5.2 Crystal data and structure refinements for compounds **5.3** and **5.4**.

	5.3	**5.4**
Empirical formula	$Pr_{0.502(2)}Na_{0.498(2)}MoO_4$	$Nd_{0.501(2)}Na_{0.499(2)}MoO_4$
Formula weight	242.07	243.68
Temperature	296(2) K	296(2) K
Wavelength	0.71073 Å	0.70173 Å
Crystal system	tetragonal	tetragonal
Space group	$I4_1/a$	$I4_1/a$
Unit cell dimensions	a = 5.30090(15) Å	a = 5.2854(2) Å
	b = 5.30090(15) Å	b = 5.2854(2) Å
	c = 11.6089(7) Å	c = 11.5675(6) Å
	$\alpha = 90°$	$\alpha = 90°$
	$\beta = 90°$	$\beta = 90°$
	$\gamma = 90°$	$\gamma = 90°$
Volume	326.20(3) $Å^3$	323.14(3)
Z	4	4
Denisty (calculated)	4.929 mg/m^3	5.009 mg/m^3
Absorption coefficient	11.227 mm^{-1}	11.822 mm^{-1}
F(000)	436.0	438.0
Crystal size	0.07 × 0.05 × 0.04 mm^3	0.10 × 0.08 × 0.05 mm^3
2θ range for data collected	4.226 to 35.015°	4.239 to 35.040°
Index ranges	$-8 \le h \le 8$	$-8 \le h \le 8$
	$-6 \le k \le 8$	$-8 \le k \le 7$
	$-18 \le l \le 18$	$-18 \le l \le 18$
Reflections collected	2053	4184
Ind. reflections	366[R(int) = 0.0253]	362[R(int) = 0.0260]
Data / restraints / parameters	366 / 0 / 16	362 / 0 / 16
Goodness-of-fit on F^2	1.042	1.118
Final R indices [I>2sigma(I)]	R_1 = 0.0195	R_1 = 0.0185
	wR_2 = 0.0491	wR_2 = 0.0474
R indices (all data)	R_1 = 0.0309	R_1 = 0.0224
	wR_2 = 0.0540	wR_2 = 0.0498
Largest diff. peak and hole	0.886 and −0.584 $e^-×Å^{-3}$	0.948 and −0.782 $e^-×Å^{-3}$

Table 5.2 Crystal data and structure refinements for compounds **5.5** and **5.6**.

	5.5	**5.6**
Empirical formula	$Sm_{0.509(2)}Na_{0.491(2)}MoO_4$	$Eu_{0.603(2)}Na_{0.397(2)}MoO_4$
Formula weight	247.79	242.90
Temperature	296(2) K	296(2) K
Wavelength	0.70173 Å	0.70173 Å
Crystal system	tetragonal	tetragonal
Space group	$I4_1/a$	$I4_1/a$
Unit cell dimensions	a = 5.2560(2) Å	a = 5.2797(2) Å
	b = 5.2560(2) Å	b = 5.2797(2) Å
	c = 11.4921(6) Å	c = 11.5869(6) Å
	$\alpha = 90°$	$\alpha = 90°$
	$\beta = 90°$	$\beta = 90°$
	$\gamma = 90°$	$\gamma = 90°$
Volume	317.48(3)	322.99(3)
Z	4	4
Denisty (calculated)	5.184 mg/m^3	5.361 mg/m^3
Absorption coefficient	13.255 mm^{-1}	15.429 mm^{-1}
F(000)	444.0	465.0
Crystal size	0.10 × 0.08 × 0.07 mm^3	0.08 × 0.06 × 0.06 mm^3
2θ range for data collected	4.264 to 35.106°	4.242 to 32.604°
Index ranges	$-7 \le h \le 8$	$-7 \le h \le 8$
	$-8 \le k \le 8$	$-8 \le k \le 7$
	$-18 \le l \le 18$	$-17 \le l \le 17$
Reflections collected	4133	3773
Ind. reflections	358[R(int) = 0.0247]	298[R(int) = 0.0200]
Data / restraints / parameters	358 / 0 / 16	298 / 0 / 16
Goodness-of-fit on F^2	1.212	1.158
Final R indices [I>2sigma(I)]	R_1 = 0.0252	R_1 = 0.0161
	wR_2 = 0.0664	wR_2 = 0.0334
R indices (all data)	R_1 = 0.0312	R_1 = 0.0230
	wR_2 = 0.0713	wR_2 = 0.0353
Largest diff. peak and hole	0.750 and −2.233 e$^-$×Å^{-3}	0.311 and −0.429 e$^-$×Å^{-3}

Table 5.3 Selected interatomic distances (Å) for compounds **5.1** – **5.6**

		5.1			
La(1) – O(1) x 4	2.525(2)	La(1) – O(1) x 4	2.561(2)	Mo(1) – O(1) x 4	1.771(2)
		5.2			
Ce(1) – O(1) x 4	2.5058(14)	Ce(1) – O(1) x 4	2.5419(14)	Mo(1) – O(1) x 4	1.7729(14)
		5.3			
Pr(1) – O(1) x 4	2.4943(15)	Pr(1) – O(1) x 4	2.5288(15)	Mo(1) – O(1) x 4	1.7722(15)
		5.4			
Nd(1) – O(1) x 4	2.4842(13)	Nd(1) – O(1) x 4	2.5146(13)	Mo(1) – O(1) x 4	1.7746(13)
		5.5			
Sm(1) – O(1) x 4	2.4664(15)	Sm(1) – O(1) x 4	2.4909(15)	Mo(1) – O(1) x 4	1.7742(14)
		5.6			
Eu(1) – O(1) x 4	2.4905(17)	Eu(1) – O(1) x 4	2.5108(16)	Mo(1) – O(1) x 4	1.7709(16)

Table 5.4 Atomic coordinates and isotropic displacement parameters ($Å^2$ x10^3) for compounds **5.1** – **5.3**.

5.1					
	Occupancy	*x*	*y*	*z*	$U_{(eq)}$
La(1)	0.516(3)	0	¼	0.6250	12(1)
Na(1)	0.484(3)	0	¼	0.6250	12(1)
Mo(1)	1	0	¼	0.6250	10(1)
O(1)	1	0.2388(4)	0.1087(4)	0.0424(2)	15(1)

5.2					
	Occupancy	*x*	*y*	*z*	$U_{(eq)}$
Ce(1)	0.512(2)	0	¼	0.6250	10(1)
Na(1)	0.488(2)	0	¼	0.6250	10(1)
Mo(1)	1	0	¼	0.6250	9(1)
O(1)	1	0.1427(2)	0.0101(3)	0.2081(1)	15(1)

5.3					
	Occupancy	*x*	*y*	*z*	$U_{(eq)}$
Pr(1)	0.502(2)	0	¼	0.6250	12(1)
Na(1)	0.498(2)	0	¼	0.6250	12(1)
Mo(1)	1	0	¼	0.6250	12(1)
O(1)	1	0.1440(3)	0.0098(3)	0.2084(1)	18(1)

Table 5.4 (cont.) Atomic coordinates and isotropic displacement parameters ($Å^2$ x10^3) for compounds **5.4** – **5.6**.

5.4					
	Occupancy	*x*	*y*	*z*	$U_{(eq)}$
Nd(1)	0.501(2)	0	¼	0.6250	11(1)
Na(1)	0.499(2)	0	¼	0.6250	11(1)
Mo(1)	1	0	¼	0.1250	11(1)
O(1)	1	0.2407(2)	0.1043(2)	0.413(1)	18(1)

5.5					
	Occupancy	*x*	*y*	*z*	$U_{(eq)}$
Sm(1)	0.509(2)	0	¼	0.6250	12(1)
Na(1)	0.491(2)	0	¼	0.6250	12(1)
Mo(1)	1	0	¼	0.1250	12(1)
O(1)	1	0.2418(3)	0.1025(3)	0.0410(1)	19(1)

5.6					
	Occupancy	*x*	*y*	*z*	$U_{(eq)}$
Eu(1)	0.603(2)	0	¼	0.6250	12(1)
Na(1)	0.397(2)	0	¼	0.6250	12(1)
Mo(1)	1	0	¼	0.1250	13(1)
O(1)	1	0.1458(2)	0.0095(3)	0.2082(2)	19(1)

the angular range 5 – 65° 2θ in steps of 0.04°. The calculated and experimental PXRD patterns are in excellent agreement (see **Figure 5.1**).

UV-vis Diffuse Reflectance Spectroscopy (UV/Vis).

UV–vis diffuse reflectance spectroscopy data of the powder samples of the reported materials were obtained using a Perkin-Elmer Lambda 35 UV–vis scanning spectrophotometer equipped with an integrating sphere in the range of 200 – 900 nm.

Magnetic Susceptibility.

The magnetic susceptibility of the reported materials was measured using a Quantum Design MPMS SQUID magnetometer. The zero-field cooled magnetic susceptibility was measured as a function of temperature between 2 and 300 K in an applied field of 1000 Oe. The measured magnetic moment was corrected for shape and radial offset effects using the methods reported by Morrison et al.[43], which determines the correction factors by comparing the moments observed from DC and VSM scans at a single temperature, 30 K.

Results and Discussion

Synthesis.

The flux technique was employed to synthesize the bipyramidal single crystals of the title compounds. Although the flux technique is widely utilized for crystal growth, not all fluxes are appropriate for the synthesis of reduced oxides because many of them do not facilitate the necessary redox neutral environment required at elevated reaction temperatures where crystal growth takes place. Alkali metal chlorides, which are redox neutral and shown to dissolve a wide variety of elements, can be used for this purpose. A NaCl/CsCl eutectic flux was used to ensure a long liquid range, lower the melting point

of the flux, and function as a source or sodium ions during the crystallization process. By selecting CsCl, we could reasonably expect to exclude cesium cations from product crystals while still lowering the melting point of the flux. Reactions using a NaCl/KCl eutectic resulted in multiple phases present in the product. Mo powder was used as the reducing agent in an attempt to reduce Mo(VI) to Mo(V) *in situ*. This approach worked well for **5.6**, but was less effective for the remaining title compounds. However, in the case of **5.2**, the Mo powder did prove to be an effective reducing agent for the reduction of Ce(IV) in CeO_2 to Ce(III) in the product crystal. Interestingly, in the case of **5.6**, the Mo powder did not reduce Eu(III) from Eu_2O_3 to Eu(II) in the product crystal. All products formed in yields approximately between 65% - and 80% based on Ln_2O_3 or CeO_2

Structure.

The title compounds crystallize in the tetragonal space group $I4_1/a$ adopting the sheelite ($CaWO_4$) structure and they exhibit a three dimensional structure consisting of MoO_4 tetrahedra and Na/LnO_8 polyhedra. A representation of the three-dimensional structure along the *a*- axis is shown in **Figure 5.2**. Each Na/LnO_8 polyhedron corner shares with eight adjacent MoO_4 polyhedra. Mo atoms are located in regular tetrahedra with Mo(1) – O bond distances ranging from 1.7709 Å –1 .7746 Å. The eight coordinate Na/*Ln* cations form a distorted eight coordinate polyhedron with Na/*Ln* – O bond distances ranging from 2.466 Å – 2.561 Å. Bond valance sum[44, 45] (BVS) calculations, assuming Mo(VI), for Mo in each compound were found to be 5.77 for compound **5.1**, 5.74 for compound **5.2**, 5.76 for compound **5.3**, 5.72 for compound **5.4**, 5.73 for compound **5.5**, and 5.78 for compound **5.6**.

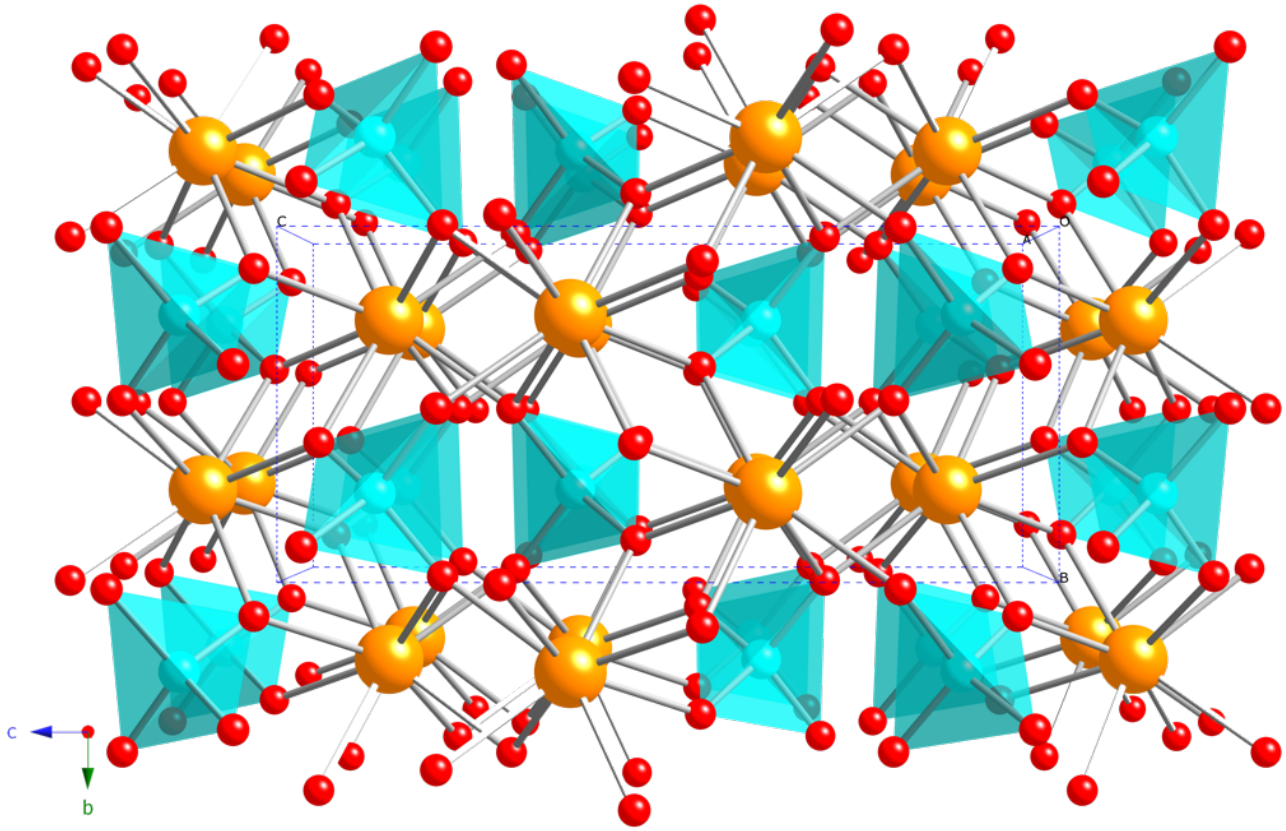

Figure 5.2 The 3D structure along the *a* axis. The MoO_4 polyhedra, *Ln*/Na positions, and O spheres are shown in cyan, orange, and red, respectively.

UV-vis Diffuse Reflectance Spectroscopy (UV/Vis).

The UV-vis diffuse reflectance data were collected on the ground crystals of the title compounds and were converted to absorbance via the Kubelka-Munk function and shown in **Figure 5.3**. The data for compounds **5.1** – **5.5** show strong absorption edges clustered approximately around 3.5 eV, indicating insulating behavior. For compound **5.4** characteristic *f-f* transitions are observed between 550 – 900 nm.

Magnetic Susceptibility.

Unpaired *d* electrons from MoO_4 units and unpaired *f* electrons from the lanthanide cations are expected to contribute to the magnetic moment of the compounds and can be observed in magnetic susceptibility measurements. The temperature dependence of the magnetic susceptibilities of compounds **5.1** – **5.6** were measured in an applied field of 1000 Oe and are shown in **Figure 5.4**. As the amount of Mo^{5+} is very small for all compounds, no magnetic coupling is expected or observed for molybdenum. The ratios of Mo^{5+} to Mo^{6+} are listed in **Table 5.5**. As the lanthanide sites are spatially far apart, no magnetic coupling is expected or observed. Down to 2K, for each compound, the data do not reveal any long range magnetic order. Above 150 K the data for compounds **5.1** – **5.4** obey the Currie–Weiss (C-W) law and experimental magnetic moments can be determined. The theoretical and experimental magnetic moments for compounds **5.1** – **5.4** are collected in **Table 5.5** and are in good agreement. It is well known that samples containing Sm^{3+} and Eu^{3+} do not follow the C-W law[46], and hence, to determine the experimental magnetic moment of compounds **5.5** and **5.6** , χT vs T plots were prepared and are shown in **Figure 5.4**. The magnetic moments of compounds **5.5**

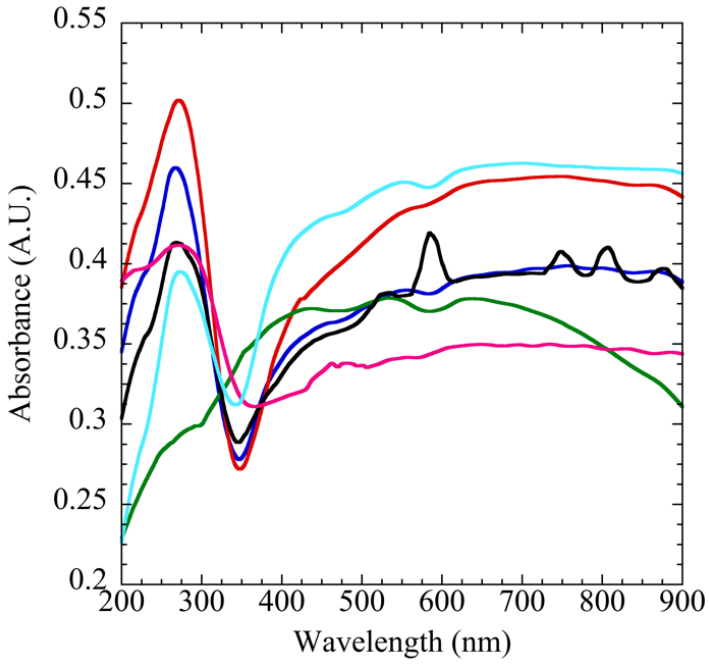

Figure 5.3 UV-vis diffuse reflectance spectroscopy data for compound **5.1** (cyan), compound **5.2** (red), compound **5.3** (pink), compound **5.4** (black), compound **5.5** (blue), and compound **5.6** (green).

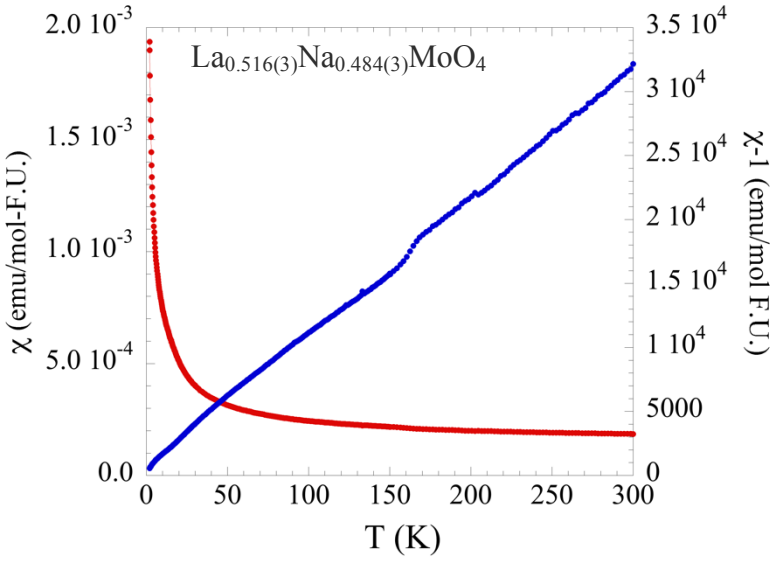

Figure 5.4 Magnetic susceptibility plot for compound **5.1**. χ and $1/\chi$ are shown in red and blue, respectively.

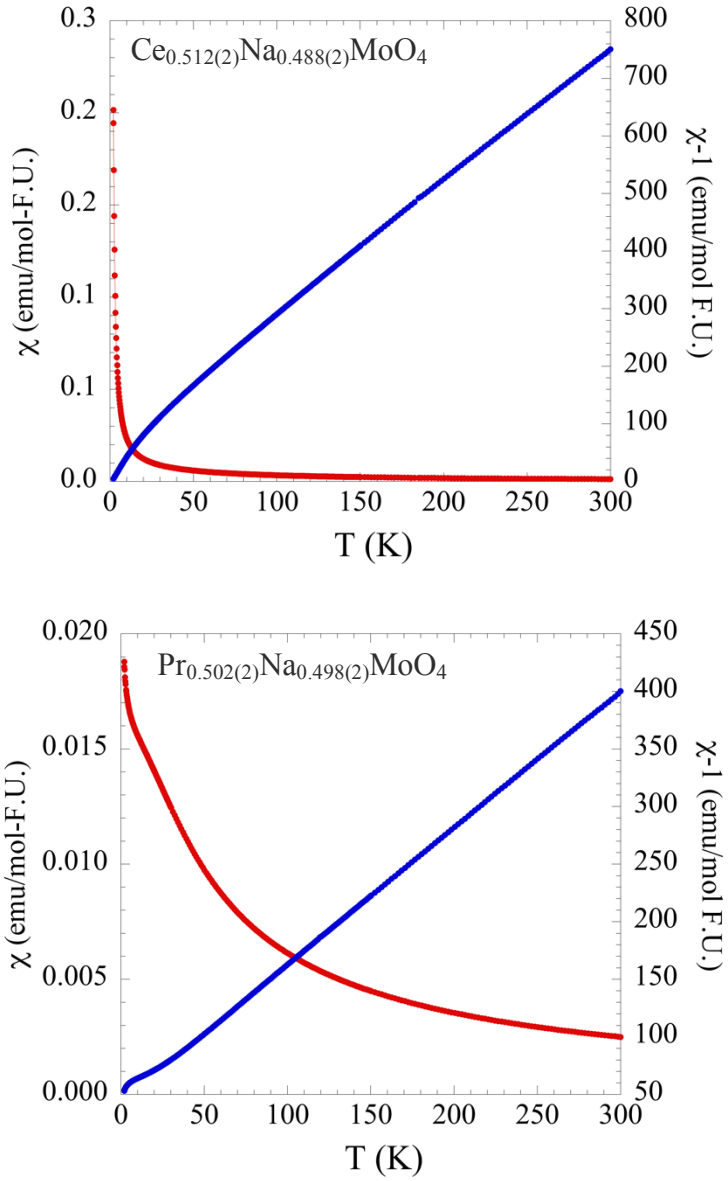

Figure 5.4 (cont.) Magnetic susceptibility plots for compounds **5.2** and **5.3**. χ and $1/\chi$ are shown in red and blue, respectively.

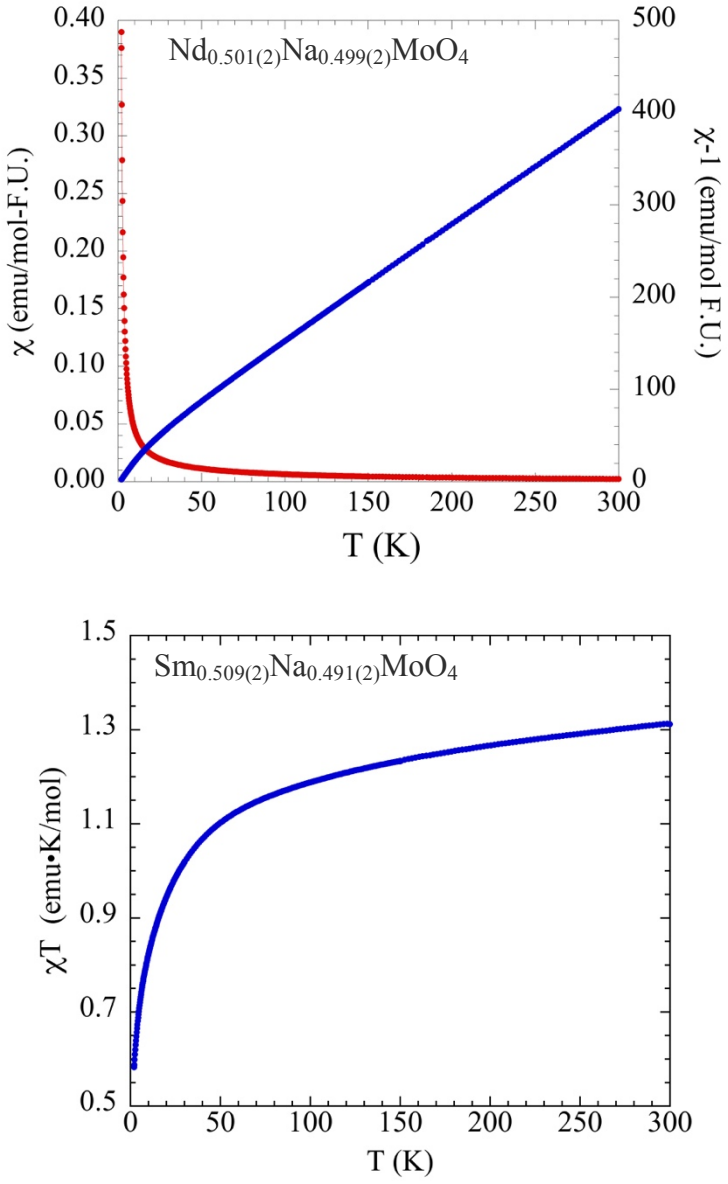

Figure 5.4 (cont.) Magnetic susceptibility plots for compounds **5.4** and **5.5**. χ and $1/\chi$ are shown in red and blue, respectively. For **5.5** a χT plot is shown, as it does not obey the C-W law.

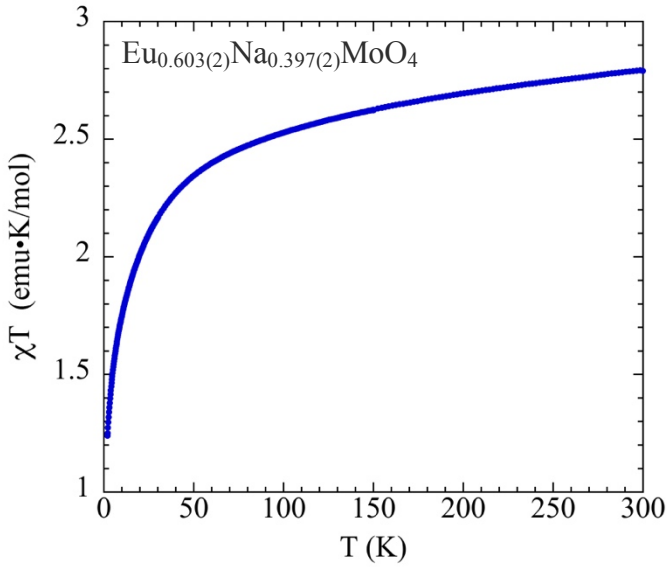

Figure 5.4 (cont.) Magnetic susceptibility plots for compound **5.5**. A χT plot is shown, as it does not obey the C-W law.

Table 5.5 Magnetic data for compounds **5.1** – **5.6**. For compounds **5.5** and **5.6** the calculated moment was taken from a plot of $\underline{\chi T}$ as the compound does not obey the C-W law. The ratios of Mo^{5+} to Mo^{6+} are also tabulated.

Compound	μ_B theoretical	μ_B experimental	Mo(V):Mo(VI)
5.1	0.31	0.28	0.032 : 0.968
5.2	1.84	1.88	0.024 : 0.976
5.3	2.54	2.59	0.004 : 0.996
5.4	2.56	2.53	0.002 : 0.998
5.5	1.26	1.31	0.018 : 0.982
5.6	2.75	2.79	0.206 : 0.794

and **5.6** at 300 K are in good agreement with the theoretical 300 K values and are listed in **Table 5.5**.

Conclusion

We successfully synthesized $La_{0.516(3)}Na_{0.484(3)}MoO_4$, $Ce_{0.512(2)}Na_{0.488(2)}MoO_4$, $Pr_{0.502(2)}Na_{0.498(2)}MoO_4$, $Nd_{0.501(2)}Na_{0.499(2)}MoO_4$, $Sm_{0.509(2)}Na_{0.491(2)}MoO_4$, and $Eu_{0.603(2)}Na_{0.397(2)}MoO_4$. Mo powder was found to be an effective reducing agent in the case of $Ce_{0.512(2)}Na_{0.488(2)}MoO_4$, reducing Ce(IV) to Ce(III) and in the case of $Eu_{0.603(2)}Na_{0.397(2)}MoO_4$, reducing Mo(VI) to Mo(V). As a result of the diluteness of the Mo^{5+} in the title compounds, only simple paramagnetic behavior is observed. The agreement of the experimental and theoretical magnetic moments confirms the stoichiometric ratio of Na/*Ln* in the title compounds.

Acknowledgement

Financial support for this work was provided by the National Science Foundation under DMR-1301757 and is gratefully acknowledged.

References

(1) G. Andersson. *Acta. Chem. Scand.* **1954**, *8*, 1599-1606.

(2) M. Pouchard; J. C. Launay. *Mater. Res. Bull.* **1973**, *8*, 95-104.

(3) S. Westman; C. Nordmark. *Acta. Chem. Scand.* **1960**, *14*, 465-470.

(4) F. J. Morin. *Bell Syst. Tech. J.* **1958**, *37*, 1047-1084.

(5) L. L. V. Zandt; J. M. Honig; J. B. Goodneough. *J. Appl. Phys.* **1968**, *39*, 594-595.

(6) M. Kestigian; J. G. Dickinson; R. Ward. *J. Am. Chem. Soc.* **1957**, *79*, 5598-5601.

(7) D. L. Serra; S.-J. Hwu. *J. Solid State Chem.* **1992**, *101*, 32-40.

(8) B. Hessen; S. A. Sunshine; T. Siegrist; R. Jimenez. *Mater. Res. Bull.* **1991**, *26*, 85-90.

(9) D. Ridgley; R. Ward. *J. Am. Chem. Soc.* **1955**, *77*, 6132-6136.

(10) C. R. Feger; R. P. Ziebarth. *Chem. Mater.* **1995**, *7*, 373-378.

(11) B. Hessen; S. A. Sunshine; T. Siegrist; A. T. Fiory; J. V. Waszczak. *Chem. Mater.* **1991**, *3*, 528-534.

(12) M. Greenblatt. *Chem. Rev.* **1988**, *88*, 31-53.

(13) M. Greenblatt. *Physics and Chemistry of Materials with Low-Dimensional Structures* **1989**, *11*, 1-48.

(14) P. P. Tsai; J. A. Potenza; M. Greenblatt. *J. Solid State Chem.* **1987**, *69*, 329-335.

(15) S. C. Chen; B. Wang; M. Greenblatt. *Inorg. Chem.* **1993**, *32*, 4306-4310.

(16) Y. Oka; T. Yao; N. Yamamoto; M. Ueda; S. Maegawa. *J. Solid State Chem.* **2000**, *149*, 414-418.

(17) D. Abeysinghe; M. D. Smith; J. Yeon; G. Morrison; H.-C. zur Loye. *Cryst. Growth Des.* **2014**, *14*, 4749-4758.

(18) A. J. Cortese; B. Wilkins; M. D. Smith; J. Yeon; G. Morrison; T. T. Tran; P. S. Halasyamani; H.-C. Z. Loye. *Inorg. Chem.* **2015**, *54*, 4011-4020.

(19) J. Yeon; M. D. Smith; A. S. Sefat; H.-C. zur Loye. *Inorg. Chem.* **2013**, *52*, 2199-2207.

(20) J. Yeon; M. D. Smith; A. S. Sefat; T. T. Tran; P. S. Halasyamani; H.-C. zur Loye. *Inorg. Chem.* **2013**, *52*, 8303-8305.

(21) J. Yeon; M. D. Smith; J. Tapp; A. Moller; H.-C. zur Loye. *J. Am. Chem. Soc.* **2014**, *136*, 3955-3963.

(22) J. Yeon; A. S. Sefat; T. T. Tran; P. S. Halasyamani; H.-C. zur Loye. *Inorg. Chem.* **2013**, *52*, 6179-6186.

(23) J. Yeon; J. B. Felder; M. D. Smith; G. Morrison; H.-C. Z. Loye. *CrystEngComm* **2015**, *17*, 8428-8440.

(24) D. E. Bugaris; H.-C. zur Loye. *Angew. Chem. Int. Ed.* **2012**, *51*, 3780-3811.

(25) S. J. Clarke; A. J. Fowkes; A. Harrison; R. M. Ibberson; M. J. Rosseinsky. *Chem. Mater.* **1998**, *10*, 372-384.

(26) O. G. D'yachenko; S. Y. Istomin; A. M. Abakumov; E. V. Antipov. *Inorg. Mater.* **2000**, *36*, 247-259.

(27) M. J. Geselbracht; L. D. Noailles; L. T. Ngo; J. H. Pikul. *Chem. Mater.* **2004**, *16*, 1153-1159.

(28) S. Y. Istomin; G. Svensson; O. G. D'yachenko; W. Holm; E. V. Antipov. *J. Solid State Chem.* **1998**, *141*, 514-521.

(29) P. Mahjoor; S. E. Latturner. *Inorg. Chem.* **2010**, *49*, 4486-4490.

(30) T. Siegrist; R. J. Cava; J. J. Krajewski. *Mater. Res. Bull.* **1997**, *32*, 881-887.

(31) A. J. Cortese; D. Abeysinghe; B. Wilkins; M. D. Smith; H.-C. Z. Loye. *Cryst. Growth Des.* **(submitted)**,

(32) D. Abeysinghe; B. Gerke; G. Morrison; C. H. Hsieh; M. D. Smith; R. Pöttgen; T. M. Makris; H.-C. zur Loye. *Journal of Solid State Chemistry* **2015**, *229*, 173-180.

(33) A. J. Cortese; D. Abeysinghe; B. Wilkins; M. D. Smith; G. Morrison; H.-C. zur Loye. *Inorg. Chem.* **2015**, *54*, 11875-11882.

(34) A. J. Cortese; B. Wilkins; M. D. Smith; G. Morrison; H.-C. zur Loye. *Solid State Sciences* **2015**, *48*, 133-140.

(35) A. J. Cortese; B. Wilkins; M. D. Smith; G. Morrison; H.-C. zur Loye. *Solid State Sciences* **2015**, *48*, 7-12.

(36) D. Abeysinghe; M. D. Smith; J. Yeon; G. Morrison; H.-C. Z. Loye. *Inorg. Chem.* **2016**,

(37) SMART Version 5.631, SAINT+ Version 6.45 and SADABS Version 2.10. Bruker Analytical X-ray Systems, Inc., Madison, Wisconsin, USA, 2003.

(38) G. M. Sheldrick. *Acta Crystallogr. A* **2008**, *64*, 112-122.

(39) C. B. Hubschle; G. M. Sheldrick; B. Dittrich. *J. Appl. Crystallogr.* **2011**, *44*, 1281-1284.

(40) L. M. Gelato; E. Parthe. *J. Appl. Crystallogr.* **1987**, *20*, 139-143.

(41) S. Z. Hu; E. Parthe. *Chin. J. Struct. Chem.* **2004**, *23*, 1150-1160.

(42) E. Parthe; L. M. Gelato. *Acta Crystallogr.* **1984**, *A40*, 169-183.

(43) G. Morrison; H.-C. zur Loye. *J. Solid State Chem.* **2015**, *221*, 334-337.

(44) N. E. Brese; M. O'Keeffe. *Acta Crystallogr. B* **1991**, *47*, 192-197.

(45) I. D. Brown; D. Altermatt. *Acta Crystallogr. B* **1985**, *41*, 244-247.

(46) Blundell, S. *Magnetism in Condensed Matter*; **2001**.

Chapter VI

Oxygen Anion Solubility as a Factor in Molten Flux Crystal Growth, Synthesis and Characterization of Four New Reduced Lanthanide Molybdenum Oxides: $Ce_{4.918(3)}Mo_3O_{16}$, $Pr_{4.880(3)}Mo_3O_{16}$, $Nd_{4.910(3)}Mo_3O_{16}$, and $Sm_{4.952(3)}Mo_3O_{16}$*

*Cortese, A. J.; Abeysinghe, D.; Wilkins, B.; Smith, M. D.; Rassolov, V.; zur Loye, H.-C. *Cryst. Growth Des.* **2016** *Submitted*.

Abstract

Four new reduced lanthanide molybdenum oxides containing mixed valent $Mo(V/VI)O_4$ tetrahedra were prepared in single crystal form by utilizing a high temperature molten salt flux synthesis involving an *in situ* reduction step. Calculations support the experimentally observed result that large alkali metal cations like cesium are superior compared to the smaller alkali metal cations like sodium in solvating O^{2-} to facilitate oxide crystal growth in halide melts. All four compounds were structurally characterized by single crystal and powder X-ray diffraction methods and were found to crystallize in the cubic space group *Pn*-3*n*. The temperature dependence of the magnetic susceptibility of these compounds was measured and all were found to exhibit simple paramagnetism.

Introduction

Oxides containing transition metals in reduced oxidation states have attracted great interest due to the potential for exhibiting interesting and, sometimes, unique electronic and magnetic properties.[1-19] To explore the preparation of new reduced oxides, we have focused on systems that contain reduced early transition metals, such as vanadium(IV), molybdenum(IV), and molybdenum(V).[20-27] The presence of extended *d* orbitals in these systems allows for better orbital overlap between magnetically active transition metal centers and improves the chance of magnetic interaction.

We recently reported the synthesis of $Ln_5Mo_2O_{12}$ (*Ln* = Eu, Tb, Dy, Ho, and Er), a group of reduced Mo(IV/V) lanthanide molybdenum oxides containing rutile-like chains of edge sharing $MoO_2O_{4/2}$ octahedra.[24] Attempts to extend this series of compounds to the left of europium in the lanthanide family resulted in black opaque crystals of the title

compounds, which are structurally related to the previously reported compounds, $Nd_5Mo_3O_{16}$ and $Pr_5Mo_3O_{16}$, which are transparent violet and yellow, respectively.[28, 29] It was reported that the molybdenum oxide underwent partial reduction in air, reducing some of the Mo^{6+} of the starting material to Mo^{5+}; however, crystals obtained via this route always contained excess oxygen, requiring the oxygen content of the composition to be adjusted to $Ln_5Mo_3O_{16+\delta}$ ($\delta \sim 0.5$).[30-32] To avoid the incorporation of excess oxygen into the crystals, reactions can be performed in sealed, evacuated silica tubes to exclude atmospheric oxygen and to maintain an inert atmosphere in which the reduction of Mo^{6+} can take place.

The use of molten fluxes is well known as one of the most effective approaches for crystal growth because it lowers the reaction temperature and allows for the dissolution of a wide range of elements and precursors.[33] Careful selection of an ideal flux, ensuring redox neutrality, is an important factor to consider when attempting to prepare oxides containing reduced species. Alkali metal chlorides fall into this category, and when coupled with a metallic reducing agent have been shown to facilitate the *in situ* reduction of early transition metals.[22, 24-26]

An essential requirement for the crystal growth of oxides from high temperature solutions is the ability of the flux to solvate O^{2-} in order to make O^{2-} available for the build up of single crystals, starting with the initial nucleus that formed in the melt. It is well known that some fluxes, hydroxides for example, have exceptional ability to solvate O^{2-} and, in fact, can contain a very high, and controllable, concentration of O^{2-}.[33] Halide fluxes, in contrast, would appear less suited to solvating O^{2-}, however, they are in fact well established for use in the growth of diverse oxide crystals.[22, 24-26, 34-36] In our work,

we have explored the use of halide fluxes for the preparation of reduced oxides, as they are redox neutral, and have observed empirically that the larger alkali metal cations, like cesium, are superior compared to the smaller alkali metal cations, like sodium, in facilitating oxide crystal growth. To better understand this observation, we have turned to BLYP Density Functional Theory (DFT) calculations to model the solvation of O^{2-} in halide fluxes and to explain the superior performance of the larger alkali metals for the crystal growth of reduced oxides.

Using a halide melt containing the Cs, the largest practical alkali metal, we successfully crystallized $Ce_{4.92}Mo_3O_{16}$, $Pr_{4.880(3)}Mo_3O_{16}$, $Nd_{4.910(3)}Mo_3O_{16}$, and $Sm_{4.952(3)}Mo_3O_{16}$, a series of partially reduced lanthanide molybdenum oxides that contain appreciable amounts of Mo^{5+}. Herein we report their crystal growth, structures and magnetic properties, and the calculations establishing the difference in the solubility of O^{2-} in different alkali metal halide fluxes.

Experimental Details

Reagents.

CsCl (Alfa Aesar, 99+%) was dried at 260 °C for a minimum of 24 hours before use and stored in an oven kept at 260 °C. Nd_2O_3 (Acros Organics, 99.9%) and Sm_2O_3 (Alfa Aesar, 99.99%) were activated in air at 1000°C for 12 hours before use and stored in a vacuum desiccator. Pr_6O_{11} (Alfa Aesar, 99.9%) was reduced to Pr_2O_3 under $4\%H_2/96\%N_2$ at 800 °C for 12 hours before use. CeO_2 (Alfa Aesar, 99.99%), MoO_3 (Alfa Aesar, 99.95%), and Mo powder ~ 250 mesh (Alfa Aesar, 99.9%) were used as received.

Molten Flux Synthesis.

Synthesis of $Ce_{4.918(3)}Mo_3O_{16}$, ***6.1****; $Pr_{4.880(3)}Mo_3O_{16}$,* ***6.2****; $Nd_{4.910(3)}Mo_3O_{16}$,* ***6.3****, and $Sm_{4.952(3)}Mo_3O_{16}$,* ***6.4***

Single crystals of $Ce_{4.918(3)}Mo_3O_{16}$, **6.1**; $Pr_{4.880(3)}Mo_3O_{16}$, **6.2**; $Nd_{4.910(3)}Mo_3O_{16}$, **6.3**; and $Sm_{4.952(3)}Mo_3O_{16}$, **6.4** were grown out of a molten cesium chloride flux. In a typical procedure 2 mmol MoO_3, 0.5 mmol Mo powder, 1 mmol of Ln_2O_3 (*Ln* = Pr, Nd, or Sm) or 2 mmol of CeO_2, and a 10x excess by weight of CsCl (dried at 260 °C for 24 hours) were placed in a 8'' long fused silica tube of ½'' diameter. The tube was evacuated via a vacuum manifold to a pressure of 10^{-4} torr and flame sealed with a methane/oxygen torch. The tube was heated in a programmable furnace to 900 °C at a rate of 15 °C/min, held for 48 hours, and then cooled to 450 °C at a rate of 6 °C/hr. At this point the furnace was shut off and allowed to cool to room temperature. The chloride flux was dissolved in water aided by sonication. Crystals were isolated via vacuum filtration yielding a phase pure product in 67 – 73% yield based on rare earth. **Figure 6.1** shows an optical image and a scanning electron microscopy (SEM) image of **6.2**, which is representative of all crystals of the title compounds. **Figure 6.2** shows powder X-ray diffraction patterns (PXRD) of ground crystals, demonstrating the phase purity of the product crystals.

Single crystal X-ray diffraction (SXRD).

Crystals of all compounds formed as opaque black cubes. X-ray intensity data for all crystals were collected at 298(2) K using a Bruker D8 QUEST diffractometer equipped with a PHOTON 100 CMOS area detector and an Incoatec microfocus source

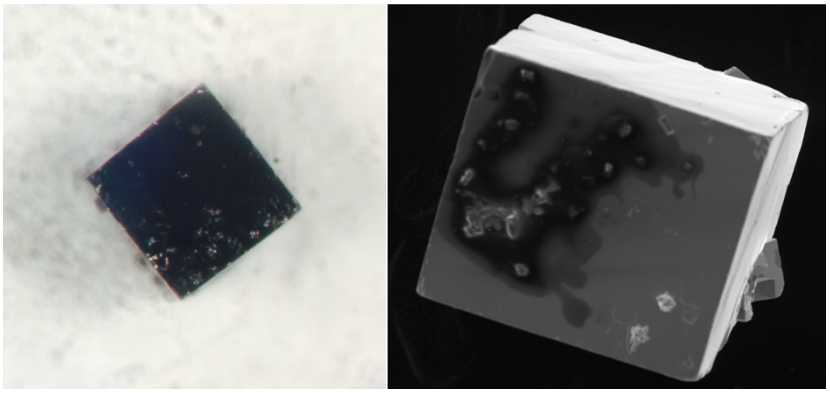

Figure 6.1 Optical image of $Pr_{4.880(3)}Mo_3O_{16}$ grown out of a cesium chloride melt and SEM image of $Pr_{4.880(3)}Mo_3O_{16}$. The optical image and SEM image are representative of the title compounds.

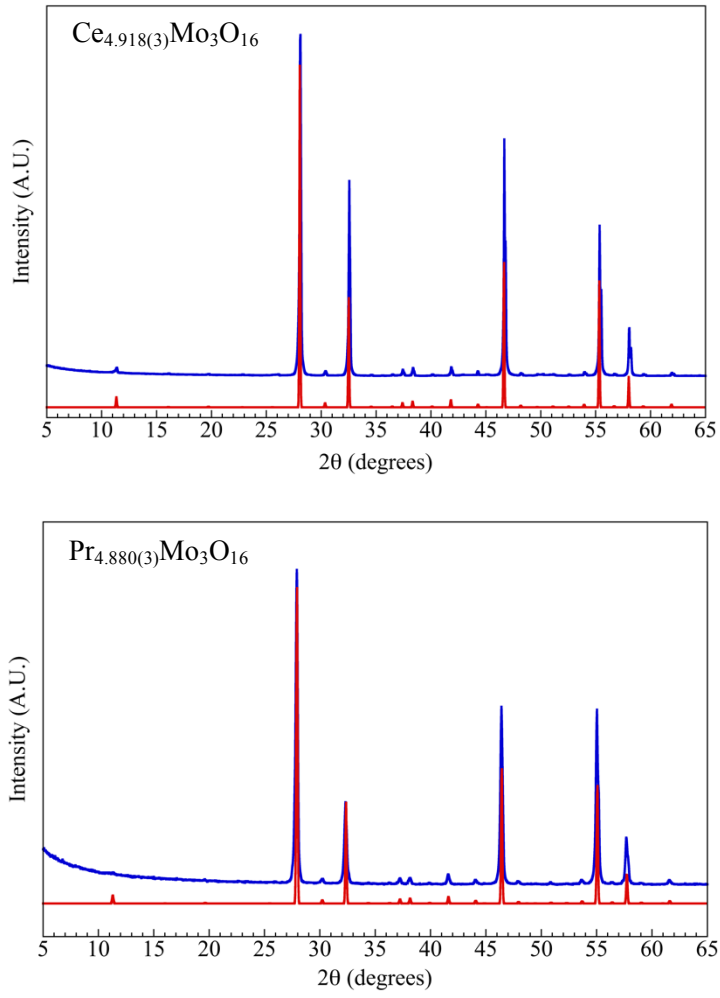

Figure 6.2 PXRD patterns of compound **6.1** and compound **6.2**. Experimental diffraction is shown in blue. The calculated pattern is shown in red.

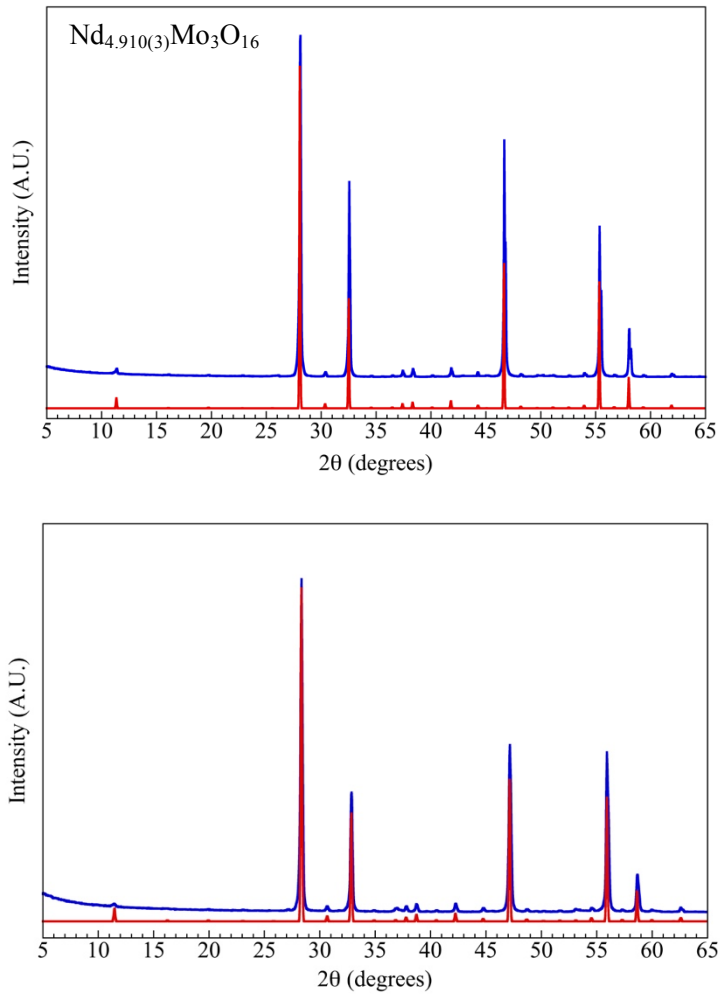

Figure 6.2 PXRD patterns of compound **6.3** and compound **6.4**. Experimental diffraction is shown in blue. The calculated pattern is shown in red.

(Mo Kα radiation, λ = 0.71073 Å).[37] The data collections each covered 100% of reciprocal space to at least $2\theta_{max}$ = 70º (65° for *Ln* = Nd), with average reflection redundancies of at least 15. The raw area detector data frames were reduced and corrected for absorption effects using the SAINT+ and SADABS programs.[37] Final unit cell parameters were determined by least-squares refinement of large sets of strong reflections taken from the data sets. An initial structural model was taken from the literature. Subsequent difference Fourier calculations and full-matrix least-squares refinement against F^2 were performed with SHELXL-2014 using the ShelXle interface.[38]

The compounds crystallize in the cubic system. The space group *Pn*-3*n* (No. 222, origin choice #2) was uniquely determined by the pattern of systematic absences in the intensity data for each crystal. The compounds are isostructural with $Nd_5Mo_3O_{16}$. The asymmetric unit consists of five atoms: two *Ln* atoms (*Ln*1 on Wyckoff site 12e, site symmetry 4.., *Ln*2 on site 8c, site symmetry .-3.), one molybdenum atom (Mo1, site 12d, site symmetry -4..), and two oxygen atoms (O1 on a general position, site 48i, O2 on site 16f, site symmetry .3.). All atoms were refined with anisotropic displacement parameters. For all compounds, a small deviation from full site occupancy was consistently observed at the 8c *Ln*2 site. Lanthanide cation partial occupancies and disorder on this site has been reported previously in this structure type. In each case the largest negative electron density concentration (difference map hole) was located near the *Ln*2 site. Free refinement of the *Ln*2 site occupancy factor (sof) for each dataset gave 0.960(2) for Ce, 0.940(2) for Pr, 0.955(2) for Nd, and 0.976(2) for Sm, resulting in modest but significant R-value and residual difference map improvements. Before *Ln*2(sof) refinements, *R*1/*wR*2 values and difference map features for *Ln* = Ce were: 0.0206 / 0.0487 and Δρ+/-

= +1.45 / -2.06 e-/Å^3, with the hole located 0.36 Å from Ce2. After *Ln*2(sof) refinement, *R*1/*wR*2 values and difference map extrema were 0.0193 / 0.0478 and +1.18 / -0.87 e-/Å^3, respectively. For *Ln* = Pr, these parameters are *R*1/*wR*2 = 0.0298 / 0.0588 before and 0.0249 / 0.0577 after refinement and, and Δρ+/- = +1.62 / -2.78 e-/Å^3 before refinement (largest hole located 0.34 Å from Pr2) and +0.92 / -0.98 e-/Å^3 after refinement. For *Ln* = Nd, these parameters are: *R*1/*wR*2 = 0.0210 / 0.537 before and 0.0205 / 0.0534 after refinement, and Δρ+/- = +0.98 / -1.62 e-/Å^3 before refinement (largest hole located 0.33 A from Nd2) and +0.75 / -1.04 e-/Å^3 after refinement. For *Ln* = Sm, *R*1/*wR*2 = 0.0215 / 0.0583 and Δρ+/- = +0.76 / -1.17 e-/Å3 (hole located 0.51 Å from Sm2) before refinement and *R*1/*wR*2 = 0.0202 / 0.0529 and Δρ+/- = +0.77 / -0.89 e-/Å3 after *Ln*2(sof) refinement. The sof values for the *Ln*1, molybdenum and both oxygen sites refined to full occupancy within experimental error in each case. No evidence for disordered or split positions near the *Ln*2 or any other site was observed in difference maps from our datasets, as was reported previously. Crystallographic data, atomic coordinates, and selected interatomic distances for all compounds are listed in **Tables 6.1** – **6.3**. Cambridge Crystallographic Data Centre (CCDC) numbers are as follows: compound **6.1**: #1451391, compound **6.2**: #1451392, compound **6.3**: #1451393, and compound **6.4**: #1451394. Inorganic Crystal Structure database numbers are as follows: compound **6.1**: #430113, compound **6.2**: #430112, compound **6.3**: #429276, and compound **6.4**: #429277.

Powder X-ray diffraction (PXRD).

PXRD data were collected on a Rigaku D/Max-2100 powder X-ray diffractometer using Cu Kα radiation. The step scan covered the angular range 5-65° 2θ in steps of

Table 6.1 Crystal data and structure refinements for compounds **6.1** and **6.2**.

	6.1	**6.2**
Empirical formula	$Ce_{4.92}Mo_3O_{16}$	$Pr_{4.88}Mo_3O_{16}$
Formula weight	1233.21	1231.46
Temperature	298(2) K	298(2) K
Wavelength	0.71073 Å	0.71073 Å
Crystal system	cubic	cubic
Space group	*Pn*-3*n*	*Pn*-3*n*
Unit cell dimensions	a = 11.1281(3) Å	a = 11.0494(13) Å
	b = 11.1281(3) Å	b = 11.0494(13) Å
	c = 11.1281(3) Å	c = 11.0494(13) Å
	$\alpha = 90°$	$\alpha = 90°$
	$\beta = 90°$	$\beta = 90°$
	$\gamma = 90°$	$\gamma = 90°$
Volume	1378.04(11) $Å^3$	1349.0(5) $Å^3$
Z	4	4
Density (calculated)	5.94 mg/m^3	6.06 mg/m^3
Absorption coefficient	18.615 mm^{-1}	20.042 mm^{-1}
F(000)	2157.0	2168.0
Crystal size	0.14 × 0.12 × 0.1 mm^3	0.06 × 0.04 × 0.04 mm^3
2θ range for data collected	2.58 to 40.23°	2.61 to 35.00°
Index ranges	$-20 \le h \le 19$	$-11 \le h \le 17$
	$-20 \le k \le 20$	$-17 \le k \le 17$
	$-20 \le l \le 19$	$-17 \le l \le 16$
Reflections collected	36143	12671
Ind. reflections	738[R(int) = 0.0438]	509[R(int) = 0.0470]
Data / restraints / parameters	738 / 0 / 22	509 / 0 / 22
Goodness-of-fit on F^2	1.143	1.089
Final R indices [I>2sigma(I)]	R_1 = 0.0193	R_1 = 0.0249
	wR_2 = 0.0375	wR_2 = 0.0459
R indices (all data)	R_1 = 0.0338	R_1 = 0.0431
	wR_2 = 0.0478	wR_2 = 0.0577
Largest diff. peak and hole	1.18 and −0.87 $e^- \times Å^{-3}$	0.92 and −0.99 $e^- \times Å^{-3}$

Table 6.1 (cont.) Crystal data and structure refinements for compounds **6.3** and **6.4**.

	6.3	**6.4**
Empirical formula	$Nd_{4.91}Mo_3O_{16}$	$Sm_{4.95}Mo_3O_{16}$
Formula weight	1252.04	1288.43
Temperature	298(2) K	298(2) K
Wavelength	0.71073 Å	0.71073 Å
Crystal system	cubic	cubic
Space group	*Pn*-3*n*	*Pn*-3*n*
Unit cell dimensions	a = 10.9959(7) Å	a = 10.8934(4) Å
	b = 10.9959(7) Å	b = 10.8934(4) Å
	c = 10.9959(7) Å	c = 10.8934(4) Å
	$\alpha = 90°$	$\alpha = 90°$
	$\beta = 90°$	$\beta = 90°$
	$\gamma = 90°$	$\gamma = 90°$
Volume	1329.5(3) $Å^3$	1292.68(14) $Å^3$
Z	4	4
Density (calculated)	6.26 mg/m^3	6.62 mg/m^3
Absorption coefficient	21.625 mm^{-1}	25.01 mm^{-1}
F(000)	2194.0	2244.0
Crystal size	0.08 × 0.06 × 0.05 mm^3	0.06 × 0.04 × 0.04 mm^3
2θ range for data collected	2.62 to 32.54°	2.64 to 35.06°
Index ranges	$-13 \le h \le 15$	$-17 \le h \le 17$
	$-16 \le k \le 16$	$-17 \le k \le 16$
	$-8 \le l \le 16$	$-27 \le l \le 17$
Reflections collected	6979	28670
Ind. reflections	416[R(int) = 0.0291]	492[R(int) = 0.0488]
Data / restraints / parameters	416 / 0 / 22	492 / 0 / 22
Goodness-of-fit on F^2	1.162	1.167
Final R indices [I>2sigma(I)]	R_1 = 0.0205	R_1 = 0.0202
	wR_2 = 0.0383	wR_2 = 0.0435
R indices (all data)	R_1 = 0.0393	R_1 = 0.0356
	wR_2 = 0.0534	wR_2 = 0.0529
Largest diff. peak and hole	0.75 and −1.04 $e^- \times Å^{-3}$	0.77 and −0.89 $e^- \times Å^{-3}$

Table 6.2 Selected interatomic distances (Å) for compounds **6.1** – **6.2**.

6.1					
Ce(1)^{9,10}–O(1)$^{1-3}$ x 4	2.3973(9)	Ce(2)–O(1)^{11} x 2	2.315(2)	Mo(1)–O(1)$^{16-18}$ x 4	1.795(2)
Ce(1)^{8}–O(2)$^{4-7}$ x 4	2.5960(19)	Ce(2)^{1}–O(2)$^{1,4,12-15}$ x 6	2.614(2)		

^{1} X, −Y+1/2, −Z+1/2 ^{2} Y, −X+1/2, Z ^{3} Y, X, −Z+1/2 ^{4} −Y+1/2, −Z+1/2, X ^{5} −Y+1/2, Z, −X+1/2
^{6} −Y+1/2, Z, −X+1/2 ^{7} −Y+1/2, −X+1/2, −Z+1/2 ^{8} Z, −X+1/2, −Y+1/2 ^{9} Y, Z, X ^{10} Z, X, Y ^{11} −X, −Y, −Z
^{12} Z−1/2, −X, Y−1/2 ^{13} −Z+1/2, X, −Y+1/2 ^{14} −X, Y−1/2, Z−1/2 ^{15} Y−1/2, Z−1/2, −X ^{16} −X, −Z+1, Y−1/2
^{17} X, −Y+3/2, −Z+1/2 ^{18} −X, Z+1/2, −Y+1

6.2					
Pr(1)^{9}–O(1)$^{4-7}$ x 4	2.574(3)	Pr(2)^{3}–O(1)$^{3,4,11-14}$ x 6	2.292(4)	Mo(1)–O(1)$^{15-17}$ x 4	1.787(3)
Pr(1)^{8,9}–O(2)$^{1-3}$ x 4	2.3814(15)	Pr(2)–O(2)^{10} x 2	2.596(3)		

^{1} X, −Y+1/2, −Z+1/2 ^{2} Y, −X+1/2, Z ^{3} Y, X, −Z+1/2 ^{4} −Z+1/2, Y, X ^{5} −Z+1/2, X, −Y+1/2
^{6} −Z+1/2, −Y+1/2, −X+1/2 ^{7} −Z+1/2, −X+1/2, Y ^{8} Z, Y, X ^{9} Y, Z, X ^{10} −X, −Y, −Z ^{11} Z−1/2, −Y, −X
^{12} −X, Z−1/2, −Y ^{13} X, −Z+1/2, Y ^{14} −Y, −X, Z−1/2 ^{15} −Y, −Z, −X ^{16} −Z, −X, −Y ^{17} −X, −Z+1, Y+1/2

Table 6.2 (cont.) Selected interatomic distances (Å) for compounds **6.3** – **6.4**.

6.3					
Nd(1)^{8}–O(1)$^{4-7}$ x 4	2.566(3)	Nd(2)^{2}–O(1)$^{4,11-15}$ x 6	2.596(3)	Mo(1)–O(1)$^{16-18}$ x 4	1.791(4)
Nd(1)^{4,9}–O(2)$^{1-3}$ x 4	2.3612(17)	Nd(2)–O(2)^{10} x 2	2.293(4)		

^{1} X, −Y+1/2, −Z+1/2 ^{2} X, Z, −Y+1/2 ^{3} Y, −X+1/2, Z ^{4} −Z+1/2, Y, X ^{5} −Z+1/2, X, −Y+1/2
^{6} −Z+1/2, −Y+1/2, −X+1/2 ^{7} −Z+1/2, −X+1/2, Y ^{8} Z, Y, −X+1/2 ^{9} −Y+1/2, X, Z ^{10} −X, −Y, −Z
^{11} −Y, −X, −Z−1/2 ^{12} Y, X, −Z+1/2 ^{13} −X, Z−1/2, −Y ^{14} X, −Z+1/2, Y ^{15} Z−1/2, −Y, −X
^{16} X, −Y+1/2 −Z+3/2 ^{17} −X, Z−1/2, −Y+1 ^{18} −X, −Z+1, Y+1/2

6.4					
Sm(1)^{9}–O(1)$^{4-7}$ x 4	2.538(3)	Sm(2)^{3}–O(1)$^{3,4,11-14}$ x 6	2.536(3)	Mo(1)–O(1)$^{15-17}$ x 4	1.795(3)
Sm(1)^{8,9}–O(2)$^{1-3}$ x 4	2.3337(14)	Sm(2)−O(2)^{10} x 2	2.268(3)		

^{1} X, −Y+1/2, −Z+1/2 ^{2} Y, −X+1/2, Z ^{3} Y, X, −Z+1/2 ^{4} −Z+1/2, Y, X ^{5} −Z+1/2, X, −Y+1/2
^{6} −Z+1/2, −Y+1/2, −X+1/2 ^{7} −Z+1/2, −X+1/2, Y ^{8} Z, Y, X ^{9} Y, Z, X ^{10} −X, −Y, −Z ^{11} Z−1/2, −Y, −X
^{12} −X, Z−1/2, −Y ^{13} X, −Z+1/2, Y ^{14} −Y, −X, Z−1/2 ^{15} −Y, −Z, −X ^{16} −Z, −X, −Y ^{17} −X, −Z+1, Y+1/2

Table 6.3 Atomic coordinates ($\times 10^4$) and equivalent isotropic displacement parameters ($Å^2 \times 10^3$) for compounds **6.1** – **6.4**. $U_{(eq)}$ is defined as one third of the trace of the orthogonalized U_{ij} tensor.

6.1					
Atom	Occupancy	*x*	*y*	*z*	U(eq)
Ce(1)	1	0.0076(1)	¼	¼	6(1)
Ce(2)	0.960(2)	0	0	0	9(1)
Mo(1)	1	0	¾	¼	8(1)
O(1)	1	0.1201(1)	0.1201(1)	0.1201(1)	7(1)
O(2)	1	0.0837(2)	0.6363(2)	0.3280(2)	13(1)

6.2					
Atom	Occupancy	*x*	*y*	*z*	U(eq)
Pr(1)	1	0.0078(1)	¼	¼	9(1)
Pr(2)	0.940(2)	0	0	0	12(1)
Mo(1)	1	0	¼	¾	12(1)
O(1)	1	0.0842(3)	0.1721(3)	0.6360(3)	16(1)
O(2)	1	0.1198(2)	0.1198(2)	0.1198(2)	10(1)
O(2)	1	0.1202(2)	0.1202(2)	0.1202(2)	12(1)

6.3					
Atom	Occupancy	*x*	*y*	*z*	U(eq)
Nd(1)	1	0.0085(1)	¼	¼	11(1)
Nd(2)	0.955(2)	0	0	0	12(1)
Mo(1)	1	0	¼	¾	12(1)
O(1)	1	0.0844(3)	0.1706(3)	0.6355(3)	17(1)
O(2)	1	0.1204(2)	0.1204(2)	0.1204(2)	12(1)

6.4					
Atom	Occupancy	*x*	*y*	*z*	U(eq)
Sm(1)	1	0.0097(1)	¼	¼	10(1)
Sm(2)	0.976(2)	0	0	0	12(1)
Mo(1)	1	0	¼	¾	11(1)
O(1)	1	0.0857(2)	0.1696(3)	0.6346(2)	16(1)
O(2)	1	0.1202(2)	0.1202(2)	0.1202(2)	12(1)

0.04°. No impurities were observed and the experimental and calculated PXRD patterns are in excellent agreement. See **Figure 6.2**.

Energy-dispersive spectroscopy (EDS).

Elemental analysis was performed on the single crystals using a TESCAN Vega-3 SBU SEM with EDS capabilities. The crystals were mounted on carbon tape and analyzed using a 20 kV accelerating voltage and an accumulation time of 1 minute. As a qualitative measure, EDS confirmed the presence of each reported element in the title compound.

UV-vis diffuse reflectance spectroscopy (UV/Vis).

UV-vis diffuse reflectance spectroscopy data of ground crystals were obtained using a PerkinElmer Lambda 35 UV-Vis scanning spectrophotometer equipped with an integrating sphere accessory in the range of 200-900 nm. Reflectance data were transformed to absorbance via the Kubelka-Munk function.[39] See **Figure 6.3**.

Calculations.

Calculations were performed with ADF2014 software using triple-zeta TZP basis set with large frozen core, scalar relativistic corrections, and BLYP functional.[40-42] Solvation energy was computed by embedding O^{2-} in the matrix of up to 40 anion-cation pairs, with full geometry optimization.

Magnetic Susceptibility.

The magnetic susceptibility was measured using a Quantum Design MPMS 3 SQUID magnetometer. The zero-field cooled magnetic susceptibility was measured as a function of temperature between 2-300 K in an applied field of 1000 Oe. The measured

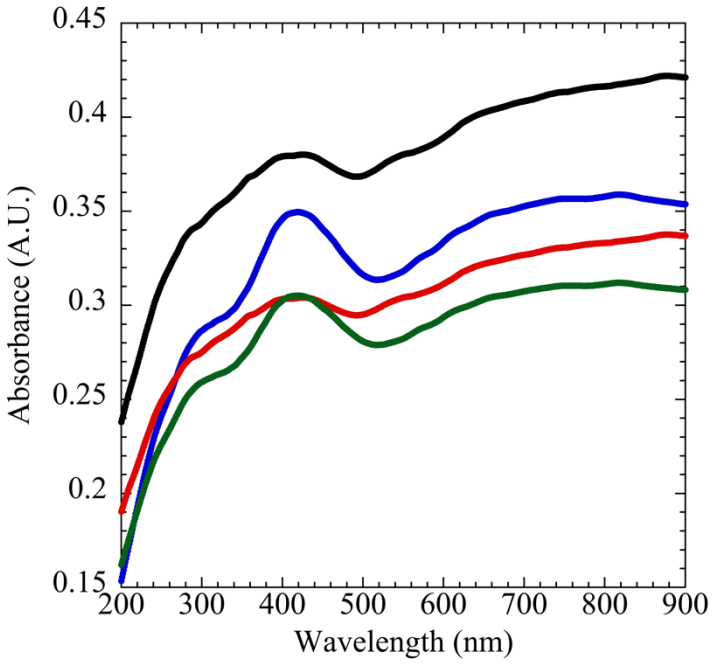

Figure 6.3 UV/Vis data for compound **6.1**, compound **6.2**, compound **6.3**, and compound **6.4** shown in blue, black, red, and green, respectively.

magnetic data were corrected for shape and radial offset effects using the method reported by Morrison et al.[43]

Results and Discussion

Synthesis.

Crystals of the title compounds were grown out of a chloride flux, which are known to be redox neutral solvents suitable for the crystal growth of reduced oxides. In this work cesium chloride allowed for the efficient dissolution of the oxides and facilitated the *in situ* reduction of dissolved Mo^{6+} to Mo^{5+}. Excluding oxidizing species from the reaction, such as water or oxygen, is crucial to promote a reducing environment. For this reason the reaction was performed in an evacuated sealed fused silica tube and all reagents except for the molybdenum powder and molybdenum oxide were dried prior to performing reactions.

In early experiments a eutectic melt of cesium chloride/sodium chloride was used to facilitate crystal growth. These reactions resulted in small cubic crystals approximately 20 μm on edge and gave poor yields, often less than 25%, with large amounts of impure powder. Changing the flux to pure cesium chloride dramatically increased the yield in excess of 65% and resulted in well faceted cubic crystals much larger in size, approximately 200 μm on edge, as well asdecreased the amount of powder side products. It was suspected that the large size of cesium cations allow for superior solvation of O^{2-} species in the melt, thereby facilitating the growth of larger single crystals and in higher yield. In the eutectic melt, a considerable amount of the far smaller Na cations are present, which are suspected to be less suitable for the solvation of O^{2-} and therefore fail

to promote crystal growth as well as Cs. Computational calculations, which support this hypothesis and the experimental observations, are discussed later.

It is of note that the molybdenum powder used in the cerium reaction provided sufficient reducing power to reduce both Mo^{6+} to Mo^{5+} as well as Ce^{4+}, from the CeO_2 starting material, to Ce^{3+}. This was not so in the case of the praseodymium reaction. Molybdenum powder, in any amount, failed to reduce Pr^{4+} to Pr^{3+} under our experimental conditions. For this reason, Pr_6O_{11} was reduced to Pr_2O_3 prior to the crystallization reaction. Attempts to prepare compounds using lanthanum or lanthanides to the right of samarium resulted in $Ln_5Mo_2O_{12}$ (*Ln* = Eu, Tb, Dy, Ho, and Er), which we have recently reported.

Structure.

The title compounds are isostructural, crystallizing in the $Nd_5Mo_3O_{16}$ fluorite-like structure type in the cubic space group *Pn*-3*n* and exhibit a three-dimensional crystal structure, shown in **Figure 6.4**, consisting of isolated MoO_4 tetrahedra that corner share with intervening lanthanide polyhedra. Mo(1) is located in a MoO_4 tetrahedron shown in **Figure 6.5** with Mo – O bond distances between 1.787(3) – 1.795(3) Å. Mo(1) shares corners with *Ln*(1) and *Ln*(2) through O(1). *Ln*(1) is located in a LnO_8 square prism shown in **Figure 6.6** with *Ln* – O bond distances between 2.3337(14) – 2.5960(19) Å. *Ln*(1) shares corners with Mo(1) through O(1) and shares edges with itself through O(2) and edges with *Ln*(2) through O(1) and O(2). *Ln*(2) is located in a LnO_8 square prism shown in **Figure 6.6** with *Ln* – O distances between 2.268(3) – 2.614(2) Å. *Ln*(2) shares corners with Mo(1) through O(1) and O(2) and shares edges with *Ln*(1) through O(1) and

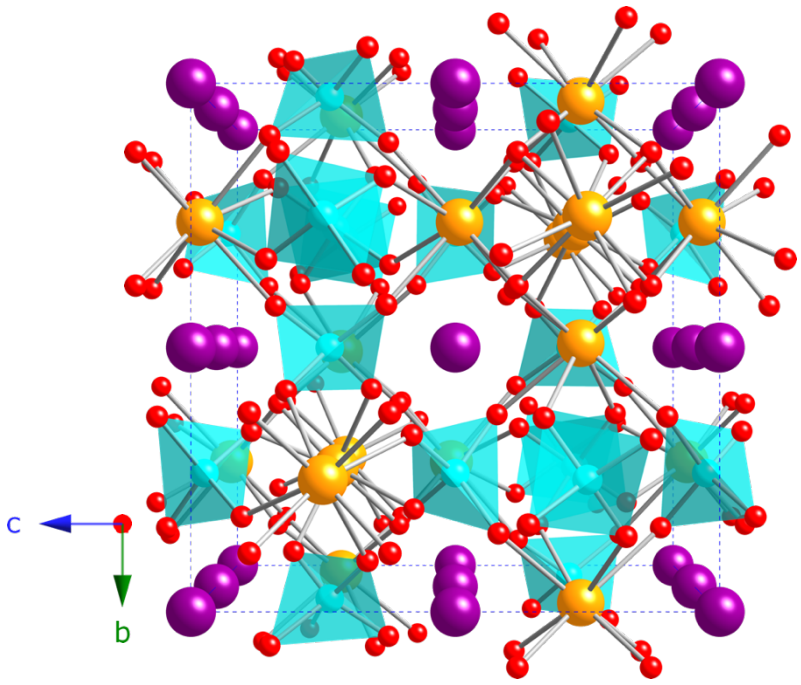

Figure 6.4 $Ln_{\sim 5}Mo_3O_{16}$ viewed down the *a* axis. *Ln*(1), *Ln*(2), Mo, and O shown in orange, purple, cyan, and red, respectively.

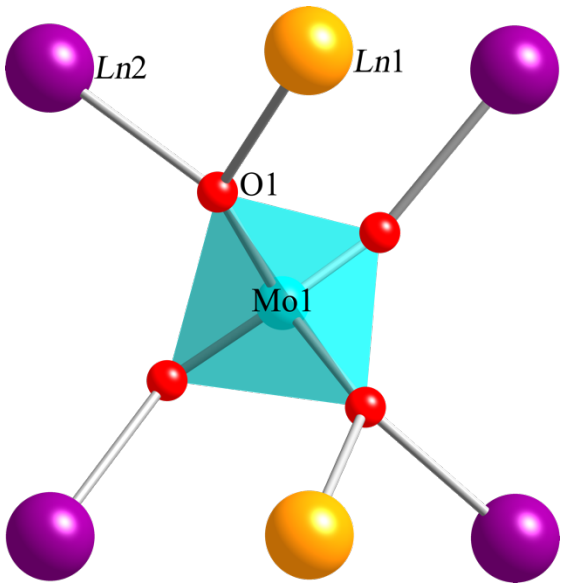

Figure 6.5 Local coordination environment of Mo(1). *Ln*(1), *Ln*(2), Mo, and O shown in orange, purple, cyan, and red, respectively.

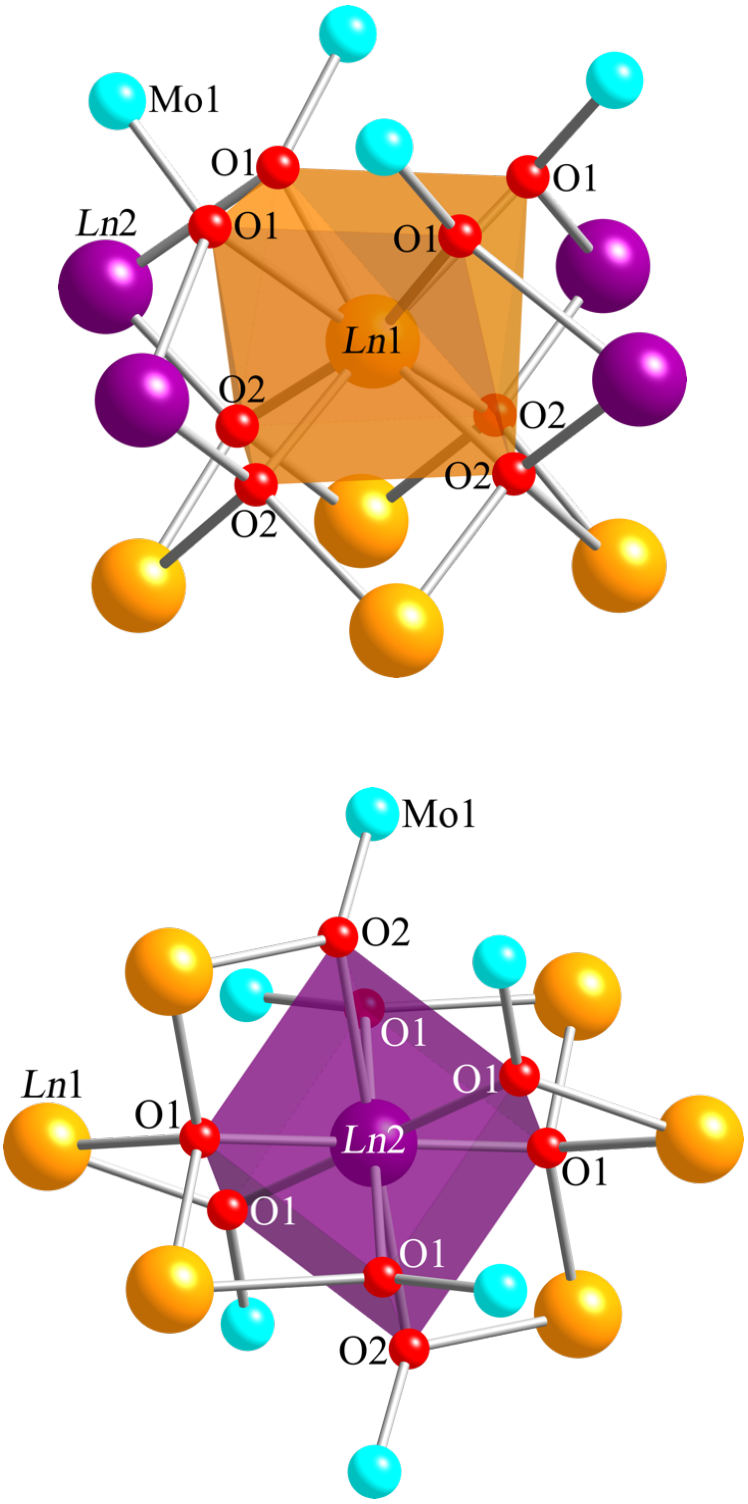

Figure 6.6 Local coordination environments of *Ln*(1) and *Ln*(2). *Ln*(1), *Ln*(2), Mo, and O shown in orange, purple, cyan, and red, respectively.

O(2). All *Ln* – O distances we report are comparable to previously reported distances for isostructural compounds.[28-30, 32]

The formal oxidation state of molybdenum in the title compounds ranges from +5.71 – +5.78. As there is only one molybdenum crystallographic site, a mixture of Mo^{5+} and Mo^{6+} must exist on this site. **Table 6.4** shows the mole fraction of Mo^{5+} and Mo^{6+} and the $\%Mo^{5+}$ present for the title compounds. A bond valence sum (BVS) analysis assuming all molybdenum is +5 gives a range of 5.50 – 5.68.[44] Using an identical treatment but assuming all molybdenum is +6 gives a range of 5.41 – 5.53.[44] These values for all compounds are shown in **Table 6.5**. These intermediate results corroborate the formal oxidation states for molybdenum in the title compounds. BVS analysis of lanthanide sites gives a range of 2.91 – 3.30, confirming the +3 oxidation of the lanthanides in each compound.

Computational study.

Modeling of Coulomb interactions, which are dominant in the interaction between the charged O^{2-} species, and the ions in the solvent melt, is likely to be relatively independent on the specific exchange-correlation functional used in the Density Functional Theory (DFT) model. The basis sets have to be flexible enough for the description of the charge distribution in the O^{2-} anion. We have used non-hybrid BLYP functional and two different basis sets: an augmented DZP and TZP sets, as defined in ADF. Unfortunately, augmented functions are not defined for Cs atoms in ADF 2014. In NaCl melt, the augmented functions affect the solvation energy of O^{2-} by about 6 kcal/mol, as we have found by computing a binding energy of O^{2-} to a NaCl molecule in

Table 6.4 Mole fraction of Mo^{5+} and Mo^{6+} and $\%Mo^{5+}$ present in compounds **6.1** – **6.4**.

Compound	Mole fraction Mo^{5+}	Mole fraction Mo^{6+}	$\%Mo^{5+}$
$Ce_{4.918(3)}Mo_3O_{16}$	0.75	2.25	25.0%
$Pr_{4.880(3)}Mo_3O_{16}$	0.64	2.36	21.3%
$Nd_{4.910(3)}Mo_3O_{16}$	0.73	2.27	24.3%
$Sm_{4.952(3)}Mo_3O_{16}$	0.86	2.14	28.7%

Table 6.5 BVS analysis of compounds **6.1** – **6.4**.

	Mo(1) BVS		*Ln* BVS	
Compound	Assuming Mo(V)	Assuming Mo(VI)	*Ln*(1)	*Ln*(2)
$Ce_{4.918(3)}Mo_3O_{16}$	5.50	5.41	3.25	3.00
$Pr_{4.880(3)}Mo_3O_{16}$	5.68	5.53	3.30	3.05
$Nd_{4.910(3)}Mo_3O_{16}$	5.59	5.47	3.15	2.91
$Sm_{4.952(3)}Mo_3O_{16}$	5.50	5.41	3.24	3.01

gas phase. The relative energy difference between NaCl and CsCl systems is likely significantly smaller, so we assume that TZP basis is sufficiently flexible.

In order to surround O^{2-} with at least two solvation shells, clusters of either 40 NaCl or 40 CsCl molecules were used in the final solvation calculations. No constraints were enforced during the geometry optimization. The cluster of 40 dimers was optimized with and without the O^{2-} anion present. Solvation energy was computed as negative energy difference between that of the optimized $M_{40}Cl_{40}O^{2-}$ (M = Na or Cs) system and energies of O^{2-} and $M_{40}Cl_{40}$ (M = Na or Cs) systems, computed separately. The solvation energy of O^{2-} in NaCl was found to be about 40kcal/mol, and to be about 50 kcal/mol in CsCl, indicating preferential solvation of O^{2-} in CsCl melts compared to the NaCl melts. These results corroborate our experimental observations and support our hypothesis that a CsCl melt allows for better solvation of O^{2-} thereby facilitating crystal growth of the title compounds.

Magnetic Susceptibility.

The unpaired *d* electrons from MoO_4 units and the unpaired *f* electrons from the lanthanide cations in **6.1** – **6.4** are expected to contribute to the magnetic moment of the compounds and can be observed in magnetic susceptibility measurements. The temperature dependencies of the magnetic susceptibilities and inverse susceptibilities of **6.1** – **6.3**, are shown in **Figure 6.7**. As the amount of Mo^{5+} is small, ranging from 21.3 – 28.7%, no magnetic coupling is expected or observed for molybdenum. As the lanthanide sites are spatially far apart, no magnetic coupling is expected or observed for the lanthanides. Down to 2K, for each compound, the data do not reveal any long range magnetic order. Above 150 K the data for **6.**1 – **6.3** follow the Curie-Weiss (C-W) law

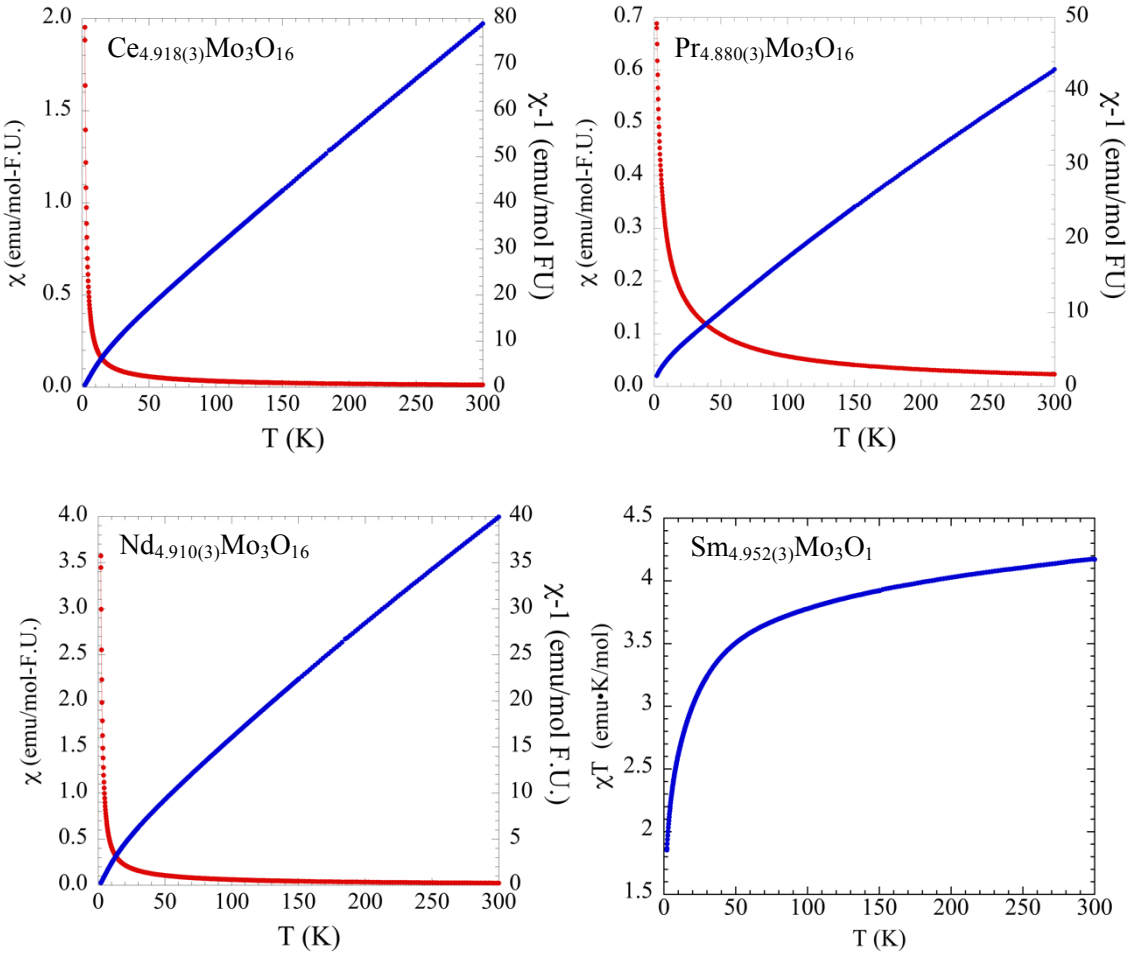

Figure 6.7 Magnetic susceptibility plots for compounds **6.1** – **6.4**. χ and $1/\chi$ are shown in red and blue, respectively. For **6.4** a χT plot is shown.

and experimental magnetic moments can be determined. It is well known that samples containing Sm^{3+} do not follow the C-W, and hence, to determine the experimental magnetic moment of **6.4** a χT vs T plot was prepared and is shown in **Figure 6.7**.[45] The magnetic moment of **6.4** at 300 K, 4.16 μ_B, is in good agreement with the theoretical 300 K value of 4.21 μ_B. The theoretical and experimental magnetic moments for **6.1** – **6.3** are collected in **Table 6.6** and are in good agreement.

Conclusion

We successfully synthesized four new reduced lanthanide molybdenum oxides, $Ce_{4.918(3)}Mo_3O_{16}$, $Pr_{4.880(3)}Mo_3O_{16}$, $Nd_{4.910(3)}Mo_3O_{16}$, and $Sm_{4.952(3)}Mo_3O_{16}$. Computational calculations support the experimentally observed result that large cesium cations are superior in their ability to solvate O^{2-} species in solution, facilitating the growth of large single crystals in high yields. As a result of the diluteness of Mo^{5+} in the title compounds, only simpleparamagnetic behavior is observed. The agreement of the experimental and theoretical magnetic moments confirms the presence and quantity of Mo^{5+} in the compounds.

Table 6.6 Magnetic data for compounds **6.1** – **6.4**. For **6.4** the calculated moment was taken from a plot of χT as the compound does not obey the C-W law.

Compound	μ_B theoretical	μ_B experimental
$Ce_{4.918(3)}Mo_3O_{16}$	5.82	5.76
$Pr_{4.880(3)}Mo_3O_{16}$	8.03	8.03
$Nd_{4.910(3)}Mo_3O_{16}$	8.26	8.15
$Sm_{4.952(3)}Mo_3O_{16}$	4.21	4.16

Acknowledgment

Financial support for this work was provided by the National Science Foundation under DMR-1301757 and is gratefully acknowledged.

References

(1) Andersson, G. *Acta. Chem. Scand.* **1954**, *8*, 1599-1606.

(2) Chen, S. C.; Wang, B.; Greenblatt, M. *Inorg. Chem.* **1993**, *32*, 4306-4310.

(3) Feger, C. R.; Ziebarth, R. P. *Chem. Mater.* **1995**, *7*, 373-378.

(4) Greenblatt, M. *Chem. Rev.* **1988**, *88*, 31-53.

(5) Greenblatt, M. *Physics and Chemistry of Materials with Low-Dimensional Structures* **1989**, *11*, 1-48.

(6) Hamasaki, T. K., H. Sekine, T. Hasem, M. Kitazawa, H. *J. Phys.: Conf. Ser.* **2009**, *150*, 042047.

(7) Hessen, B.; Sunshine, S. A.; Siegrist, T.; Fiory, A. T.; Waszczak, J. V. *Chem. Mater.* **1991**, *3*, 528-534.

(8) Hessen, B.; Sunshine, S. A.; Siegrist, T.; Jimenez, R. *Mater. Res. Bull.* **1991**, *26*, 85-90.

(9) Lancaster, T.; Baker, P. J.; Pratt, F. L.; Blundell, S. J.; Hayes, W.; Prabhakaran, D. *Phys. Rev. B: Condens. Matter. Mater. Phys.* **2012**, *85*, 184404.

(10) Mat'aš, S. O., A.; Prokeš, K. K., B. *J. Phys.: Conf. Ser.* **2010**, *251*, 012024.

(11) Morin, F. J. *Bell Syst. Tech. J.* **1958**, *37*, 1047-1084.

(12) Ok, K. M.; Chi, E. O.; Halasyamani, P. S. *Chemical Society Reviews* **2006**, *35*, 710-717.

(13) Pouchard, M.; Launay, J. C. *Mater. Res. Bull.* **1973**, *8*, 95-104.

(14) Ridgley, D.; Ward, R. *J. Am. Chem. Soc.* **1955**, *77*, 6132-6136.

(15) Serra, D. L.; Hwu, S.-J. *J. Solid State Chem.* **1992**, *101*, 32-40.

(16) Tsai, P. P.; Potenza, J. A.; Greenblatt, M. *J. Solid State Chem.* **1987**, *69*, 329-335.

(17) Van Zandt, L. L.; Honig, J. M.; Goodenough, J. B. *J. Appl. Phys.* **1968**, *39*, 594-595.

(18) Vasala, S.; Saadaoui, H.; Morenzoni, E.; Chmaissem, O.; Chan, T.-S.; Chen, J.-M.; Hsu, Y.-Y.; Yamauchi, H.; Karppinen, M. *Phys. Rev. B: Condens. Matter. Mater. Phys.* **2014**, *89*, 134419.

(19) Westman, S.; Nordmark, C. *Acta Chem. Scand.* **1960**, *14*, 465-470.

(20) Abeysinghe, D.; Smith, M. D.; Yeon, J.; Morrison, G. *Inorg. Chem.* **2016**,

(21) Abeysinghe, D.; Smith, M. D.; Yeon, J.; Morrison, G.; zur Loye, H.-C. *Cryst. Growth Des.* **2014**, *14*, 4749-4758.

(22) Abeysinghe, D.; Gerke, B.; Morrison, G.; Hsieh, C. H.; Smith, M. D.; Pöttgen, R.; Makris, T. M.; zur Loye, H.-C. *J. Sol. State Chem.* **2015**, *229*, 173-180.

(23) Cortese, A. J.; Wilkins, B.; Smith, M. D.; Yeon, J.; Morrison, G.; Tran, T. T.; Halasyamani, P. S.; zur Loye, H.-C. *Inorg. Chem.* **2015**, *54*, 4011-4020.

(24) Cortese, A. J.; Abeysinghe, D.; Wilkins, B.; Smith, M. D.; Morrison, G.; zur Loye, H.-C. *Inorg. Chem.* **2015**, *54*, 11875-11882.

(25) Cortese, A. J.; Wilkins, B.; Smith, M. D.; Morrison, G.; zur Loye, H.-C. *Solid State Sciences* **2015**, *48*, 133-140.

(26) Cortese, A. J.; Wilkins, B.; Smith, M. D.; Morrison, G.; zur Loye, H.-C. *Solid State Sciences* **2015**, *48*, 7-12.

(27) Yeon, J.; Sefat, A. S.; Tran, T. T.; Halasyamani, P. S.; zur Loye, H.-C. *Inorg. Chem.* **2013**, *52*, 6179-6186.

(28) Hubert, P. H.; Michel, P.; Thozet, A. *C. R. Seances Acad. Sci., Ser. C* **1973**, *276*, 1179-1181.

(29) Martínez-Lope, M. J.; Alonso, J. A.; Sheptyakov, D.; Pomjakushin, V. *J. Solid State Chem.* **2010**, *183*, 2974-2978.

(30) Alekseeva, O. A.; Gagor, A. B.; Pietraszko, A. P.; Sorokina, N. I.; Bolotina, N. B.; Artemov, V. V.; Kharitonova, E. P.; Voronkova, V. I. *Z. Kristallogr. - Cryst. Mater.* **2012**, *227*, 869-875.

(31) Voronkova, V. I.; Leonidov, I. A.; Kharitonova, E. P.; Belov, D. A.; Patrakeev, M. V.; Leonidova, O. N.; Kozhevnikov, V. L. *J. Alloys Compd.* **2014**, *615*, 395-400.

(32) Antipin, A. M.; Alekseeva, O. A.; Sorokina, N. I.; Kuskova, A. N.; Artemov, V. V.; Murzin, V. Y.; Kharitonava, E. P.; Orlova, E. A.; Voronkova, V. I. *Crystallogr. Rep.* **2015**, *60*, 640-648.

(33) Bugaris, D. E.; zur Loye, H.-C. *Angew. Chem. Int. Ed.* **2012**, *51*, 3780-3811.

(34) Elwell, D.; Scheel, H. J. *Crystal Growth from High Temperature Solutions*; 2011;

(35) Mahjoor, P.; Latturner, S. E. *Inorg. Chem.* **2010**, *49*, 4486-4490.

(36) Tsai, P. P.; Potenza, J. A.; Greenblatt, M. *J. Solid State Chem.* **1987**, *69*, 329-335.

(37) Mark 1: SMART Version 5.631, SAINT+ Version 6.45 and SADABS Version 2.10. Bruker Analytical X-ray Systems, Inc., Madison, Wisconsin, USA, 2003.

(38) Mark 2: *ShelXle*: a Qt graphical user interface for *SHELXL*. Hübschle, C. B., Sheldrick, G. M., Bittrich, B. *J. Appl. Cryst.* **2011**, *44*, 1281-1284.

(39) Kubelka, P.; Munk, F. *Zeit. Für Tekn. Physik* **1931**, *12*, 593.

(40) Guerra, C. F.; Snijders, J. G.; te Velde, G.; Baerends, E. J. *Theor. Chem. Acc.* **1998**, *99*, 391-403.

(41) te Velde, G.; Bickelhaupt, F. M.; Baerends, E. J.; Guerra, C. F.; van Gisbergen, S. J. A.; Snijders, J. G.; Zielger, T. *J. Comput. Chem.* **2001**, *22*, 931-967.

(42) ADF2014, SCM, Theoretical Chemistry, Vrije Universiteit, Amsterdam, The Netherlands

(43) Morrison, G.; zur Loye, H.-C. *J. Solid State Chem.* **2015**, *221*, 334-337.

(44) Brown, I. D.; Altermatt, D. *Acta Crystallogr. B* **1985**, *41*, 244-247.

(45) Blundell, S. *Magnetism in Condensed Matter*; 2001.

Chapter VII

High Temperature Salt Flux Crystal Growth of New Lanthanide Molybdenum Oxides, $LN_5Mo_2O_{12}$ *LN* = Eu, Tb, Dy, Ho, and Er. Magnetic Coupling within Mixed Valent Mo(IV/V) Rutile-like Chains*

*Adapted with permission from Cortese, A. J.; Abeysinghe, D.; Wilkins, B.; Smith, M. D.; Morrison, G.; zur Loye, H.-C. *Inorg. Chem.* **2015**, *54(24)*, 11875-11882. © 2015 American Chemical Society.

Abstract

Five new lanthanide molybdenum oxides containing mixed valent Mo(IV/V) rutile-like chains, $Ln_5Mo_2O_{12}$ *Ln* = Eu, Tb, Dy, Ho, and Er, were prepared utilizing a high temperature molten salt flux synthesis involving an *in situ* reduction utilizing metallic reducing agents. All five compounds were structurally characterized by single crystal and powder X-ray diffraction methods and were found to crystallize in the monoclinic space group *C*2/*m*. The temperature dependence of the magnetic susceptibility of these compounds was measured and $Tb_5Mo_2O_{12}$ and $Er_5Mo_2O_{12}$ were found to exhibit antiferromagnetic ordering on both molybdenum and rare earth sites, while $Eu_5Mo_2O_{12}$, $Dy_5Mo_2O_{12}$ and $Ho_5Mo_2O_{12}$ were found to exhibit antiferromagnetic ordering only on the molybdenum site. No *d-f* coupling was observed for any of the title compounds.

Introduction

Low dimensional oxides containing transition metals have attracted great interest due to their unique electronic and magnetic properties, the origin of which typically stems from the presence of isolated magnetic interactions in 2D sheets or 1D chains in the structures.[1-20] To explore the preparation of new low dimensional materials, we have focused on systems that contain reduced early transition metals, such as vanadium(IV) and molybdenum(V).[20-25] The extended *d* orbitals of such systems allow for better orbital overlap between magnetic transition metal centers and improve the chance for magnetic ordering. Furthermore, compounds containing 4*d* or 5*d* transition elements such as molybdenum, rhenium, and ruthenium can potentially exhibit direct metal to metal bonding between the 4*d* or 5*d* transition elements when unpaired electrons reside in adjacent metal centers. A number of such molybdenum containing compounds are known

and can be divided into two structural groups: those that contain isolated one dimensional infinite chains, such as MoO_2[26] and $Ln_5Mo_2O_{12}$ (Ln = Y, Gd)[27] and those that contain isolated dimers, such as $La_4Mo_2O_{11}$,[28] which contains Mo_2O_{10} octahedral dimers with an average oxidation state of +5, and La_2MoO_5,[29] which contains Mo_2O_8 square planar dimers with an average oxidation state of +4. The $Y_5Mo_2O_{12}$ structure type contains chains consisting of distorted edge-sharing $MoO_2O_{4/2}$ octahedra in which the molybdenum has an average oxidation state of +4.5; the chains are isolated from each other by rare earth polyhedra. In these chains the presence of alternating short and long metal-metal distances effectively creates $Mo(IV/V)_2O_{10}$ pairs within the chain and is indicative of direct metal to metal bonding. Each pair possesses one unpaired electron not participating in metal to metal bonding that can be involved in long range magnetic order. In the case of $Y_5Mo_2O_{12}$, these unpaired electrons order antiferromagnetically at 6K.[27]

The analogous rhenium compound, $Y_5Re_2O_{12}$[30] and a large number of analogous ruthenium compounds, $Ln_5Ru_2O_{12}$ Ln = Pr, Nd, Sm, Eu, Gd, and Tb,[31] have been obtained via highly oxidizing molten hydroxide flux methods. One of these compounds, $Tb_5Ru_2O_{12}$ was found to exhibit antiferromagnetic ordering at 7K. Torardi et al. reported no magnetic measurements for $Gd_5Mo_2O_{12}$, despite $Gd_5Mo_2O_{12}$ being an intriguing case as it possesses both unpaired *d* and *f* electrons with the potential for *d-f* coupling. Given the observed antiferromagnetic ordering of an analogous ruthenate, it is of interest to synthesize single crystals of the analogous molybdates containing additional rare earth cations, Eu, Tb, Dy, Ho, and Er, extending this body of work beyond $Y_5Mo_2O_{12}$ and $Gd_5Mo_2O_{12}$.

Traditionally oxides containing reduced molybdenum cations have been prepared via high temperature self flux methods in sealed molybdenum tubes, via electrolytic reduction of melts, or via conventional solid state methods.[7, 9, 10, 18, 27] Another method, flux crystal growth, is effective for preparing a wide variety of oxides, including ones containing reduced transition metals, and can be employed to target single crystals of complex structures containing reduced molybdenum.[24, 32-34] Using this method redox neutral fluxes and reagents are sealed in evacuated fused silica tubes to perform *in situ* reduction reactions. Alkali chlorides are attractive melt candidates for this type of flux growth as they are redox neutral, solubilize a wide variety of elements, will not attack the fused silica reaction vessel, are relatively inexpensive, and are easily separated from product crystals via sonication in water. Suitable reducing agents include metallic molybdenum and zinc powders. Often times it is beneficial to use a eutectic flux to lower the melting point and thereby lower the dwell temperature of the reaction, allowing for the growth of kinetic phases previously unattainable at higher temperatures.[23, 24, 32, 35] Herein we report the eutectic flux crystal growth and magnetic properties of a series of complex reduced molybdenum containing oxides, $Ln_5Mo_2O_{12}$ (*Ln* = Eu, Tb, Dy, Ho, and Er).

Experimental Details

Reagents.

MoO_3 (99.95%, Alfa Aesar), Mo powder ~250 mesh (99.9%, Alfa Aesar), and Zn metal 140+325 mesh (99.8%, Alfa Aesar) were used as received. Tb_4O_7 (99.9%, Alfa Aesar) was reduced to Tb_2O_3 under 4% H_2/96% N_2 at 800°C for 12 hours. Eu_2O_3 (99.9%, Alfa Aesar), Dy_2O_3 (99.9%, Alfa Aesar), Ho_2O_3 (99.9%, Alfa Aesar), and Er_2O_3 (99.9%,

Alfa Aesar) were activated in air at 1000 °C for 12 hours to drive off any hydroxides and carbonates present and stored in a vacuum desiccator. CsCl (99%, Alfa Aesar), and NaCl (Certified A.C.S., Fisher) were dried and stored in a programmable oven at 260°C.

Molten Flux Synthesis.

Synthesis of $Ln_5Mo_2O_{12}$, Ln = Tb, Dy, Ho, and Er, ***7.2-7.5***

Single crystals of $Ln_5Mo_2O_{12}$, *Ln* = Tb **7.2**, Dy **7.3**, Ho **7.4**, and Er **7.5** were grown via a molten salt flux route. 1 mmol of Ln_2O_3, *Ln* = Tb, Dy, Ho, and Er, 2 mmol MoO_3, 0.5 mmol Mo, and a 10 fold excess by weight of a eutectic mixture of CsCl and NaCl with a molar ratio of 1.85:1 were placed in a fused silica tube. The tube was evacuated to a pressure of ~ 10^{-4} torr, and flame sealed using an oxygen/methane torch. The tube was placed inside a programmable furnace and heated to 800°C at a rate of 10°C/min, held for 24 hours, cooled to 400°C at a rate of 0.1°C/min, and then cooled to room temperature by turning off the furnace. The solid flux was washed away with deionized water yielding a phase pure product in approximately 70% yield based on Ln_2O_3.

Synthesis of $Eu_5Mo_2O_{12}$, ***7.1***

A modified approach was used to synthesize **7.1**, as attempts using Mo powder as a reducing agent failed. In a typical procedure 1 mmol of Eu_2O_3, 2 mmol MoO_3, 1 mmol Zn, and 2 g of CsCl were placed in a fused silica tube, evacuated to a pressure of ~ 10^{-4} torr, and flame sealed. The tube was placed inside a programmable furnace and heated to 1000°C at a rate of 10°C/min, held for 48 hours, cooled to 550 °C at a rate of 4 °C/h, and then cooled to room temperature by turning off the furnace. This reaction mixture yielded two phases: $Eu_5Mo_2O_{12}$ and $EuMoO_4$. After washing the solid flux with deionized water,

the two phases were isolated via manual crystal picking. The yield of the desired phase was approximately 55% based on Eu_2O_3. Powder X-ray diffraction patterns (PXRD) of ground crystals demonstrates the phase purity of the picked crystals, see **Figure 7.1**.

Single Crystal X-ray Diffraction (SXRD).

Many single crystals of each phase were examined and all were found to be non-merohedral twins consisting of at least two twin domains. X-ray intensity data were collected on black needle shaped crystals at 296(2) K using either a Bruker SMART APEX diffractometer (Mo Kα radiation, λ = 0.71073 Å) or a Bruker D8 QUEST diffractometer equipped with a PHOTON 100 CMOS area detector and an Incoatec microfocus source (Mo Kα radiation, λ = 0.71073 Å). In all cases, the raw area detector data frames were reduced and corrected for absorption effects using the SAINT+ and TWINABS programs.[36] Final unit cell parameters were determined by least-squares refinement of large sets of strong reflections taken from the data sets. An initial structural model for $Er_5Mo_2O_{12}$ was obtained either with direct methods or by using the coordinates of $Er_5Mo_2O_{12}$ as the initial structural model for subsequent refinements. In all cases difference Fourier calculations and full-matrix least-squares refinement against F^2 were performed with SHELXL-2013/4 using the ShelXle interface.[37, 38] Orientation matrices, the twin law and input files for data integration were determined using the Bruker program Cell_Now.[39, 40] All compositions were found to adopt the $Y_5Mo_2O_{12}$ structure type[27] in the space group *C*2/*m*. There are three rare earth, one molybdenum and four oxygen positions. *Ln*1, *Ln*2, O3 and O4 are located on mirror planes (Wyckoff site 4*i*). *Ln*3 is located on site 2*c* with 2/*m* site symmetry. Mo1 is located on a two-fold axis (site 4*g*) and O1 and O2 are located on general positions (8*j*). All atoms were refined with

anisotropic displacement parameters. No deviation from full occupancy was observed for any of the metal atoms in each dataset, based on trial refinements of the site occupancy factors. Large calculated difference map extrema, which are heavy atom 'ripples', and some flattened oxygen atom anisotropic displacement ellipsoids reflect the non-optimum quality of single crystals of these materials. The reported atomic coordinates were standardized with Structure Tidy.

$Eu_5Mo_2O_{12}$ 7.1: The U_{ij} values of one oxygen atom (O2) became strongly oblate if refined freely. These values were therefore restrained to be approximately spherical using a SHELX ISOR instruction. The data crystal was composed of three twin domains, with refined volume fractions of 0.404(4), 0.395(4), and 0.201(4). The largest residual electron density peak and hole in the final difference map are +6.54 and -5.66 $e^-/Å^3$, located 0.24 and 0.38 Å from Eu2 and Eu1, respectively. **$Tb_5Mo_2O_{12}$ 7.2**: The data crystal was composed of two twin domains with a major fraction of 0.577(2). The largest residual electron density peak and hole in the final difference map are +5.24 and -5.17 $e^-/Å^3$, located 0.23 and 0.42 Å from Tb2 and Tb1, respectively. **$Dy_5Mo_2O_{12}$ 7.3**: The data crystal was composed of two domains with a major twin fraction of 0.812(3). The largest residual electron density peak and hole in the final difference map are +9.08 and -9.05 $e^-/Å^3$, located 0.35 and 0.53 Å from Dy2 and Dy1, respectively. **$Ho_5Mo_2O_{12}$ 7.4:** The data crystal was composed of two twin domains with a major twin fraction of 0.794(3). The largest residual electron density peak and hole in the final difference map are +6.30 and -12.34 $e^-/Å^3$, located 0.25 and 0.49 Å from Ho2 and Ho3, respectively. **$Er_5Mo_2O_{12}$ 7.5:** The data crystal was composed of two domains with a major twin domain fraction of

0.506(4). The largest residual electron density peak and hole in the final difference map are +5.07 and -3.57 $e^-/Å^3$, located 0.22 and 0.40 Å from Er2 and Er1, respectively.

Crystallographic data, atomic coordinates, and selected interatomic distances for all compounds are listed in **Tables 7.1 – 7.3**, respectively. Cambridge Crystallographic Data Centre (CCDC) numbers are as follows: compound **7.1**: # 1452135, compound **7.2**: #1452136, compound **7.3**: #1452137, compound **7.4**: #1452138, and compound **7.5**: #1452139. Inorganic Crystal Structure database numbers are as follows: compound **7.1**: #430114, compound **7.2**: #429294, compound **7.3**: #429292, compound **7.4**: #429326, and compound **7.5**, #429293.

Powder X-ray diffraction (PXRD).

Powder X-ray diffraction data were collected on a Rigaku D/Max-2100 powder X-ray diffractometer using Cu Kα radiation. The step scan covered the angular range 5-65° 2θ in steps of 0.04°. No impurities were observed for Tb, Dy, Ho and Er and the calculated and experimental PXRD patterns are in excellent agreement. One weak reflection was observed in the Eu compound that could not be matched with any known impurity. Magnetic measurements and calculations confirm the impurity does not order magnetically and present in only a small amount, see **Figure 7.1**.

Energy-Dispersive Spectroscopy (EDS).

Elemental analysis was performed on the single crystals using a TESCAN Vega-3 SBU scanning electron microscope (SEM) with EDS capabilities. The crystals were mounted on carbon tape and analyzed using a 20 mV accelerating voltage and an accumulation time of 1 minute. As a qualitative measure, EDS confirmed the presence of

Table 7.1 Crystal data and structure refinements for compounds **7.1** and **7.2**.

	7.1	**7.2**
Empirical formula	$Eu_5Mo_2O_{12}$	$Tb_5Mo_2O_{12}$
Formula weight	1143.68	1178.48
Temperature	296(2) K	296(2) K
Wavelength	0.71073 Å	0.71073 Å
Crystal system	monoclinic	monoclinic
Space group	*C*2/*m*	*C*2/*m*
Unit cell dimensions	a = 12.4754(4) Å	a = 12.3746(3) Å
	b = 5.7880(2) Å	b = 5.75232(16) Å
	c = 7.6471(3) Å	c = 7.5694(2) Å
	α = 90°	α = 90°
	β = 107.8959(11)°	β = 107.9466(7)°
	γ = 90°	γ = 90°
Volume	525.46(3) $Å^3$	512.59(2) $Å^3$
Z	2	2
Density (calculated)	7.228 mg/m^3	7.64 mg/m^3
Absorption coefficient	31.740 mm^{-1}	36.44 mm^{-1}
F(000)	990.0	1010.0
Crystal size	0.10 × 0.02 × 0.02 mm^3	0.10 × 0.02 × 0.02 mm^3
2θ range for data collected	2.80 to 32.60°	2.83 to 32.61°
Index ranges	$-18 \le h \le 18$	$-18 \le h \le 17$
	$0 \le k \le 8$	$0 \le k \le 8$
	$0 \le l \le 11$	$0 \le l \le 11$
Reflections collected	1081	1022
Ind. reflections	1081[R(int) = 0.0504]	1022[R(int) = 0.0393]
Data / restraints / parameters	1081 / 6 / 54	1022 / 0 / 53
Goodness-of-fit on F^2	1.132	1.074
Final R indices [I>2sigma(I)]	R_1 = 0.0355	R_1 = 0.0242
	wR_2 = 0.0935	wR_2 = 0.0634
R indices (all data)	R_1 = 0.0370	R_1 = 0.0255
	wR_2 = 0.0945	wR_2 = 0.0641
Largest diff. peak and hole	6.54 and −5.67 $e^- \times Å^{-3}$	5.25 and −5.18 $e^- \times Å^{-3}$

Table 7.1 (cont.) Crystal data and structure refinements for compounds **7.3** and **7.4**.

	7.3	**7.4**
Empirical formula	$Dy_5Mo_2O_{12}$	$Ho_5Mo_2O_{12}$
Formula weight	1196.38	1208.53
Temperature	296(2) K	296(2) K
Wavelength	0.71073 Å	0.71073 Å
Crystal system	monoclinic	monoclinic
Space group	*C*2/*m*	*C*2/*m*
Unit cell dimensions	a = 12.2959(14) Å	a = 12.2557(7) Å
	b = 5.7377(7) Å	b = 5.7174(3) Å
	c = 7.5300(9) Å	c = 7.4914(4) Å
	α = 90°	α = 90°
	β = 107.816(2)°	β = 107.9137(14)°
	γ = 90°	γ = 90°
Volume	505.77(10) $Å^3$	499.48(5) $Å^3$
Z	2	2
Density (calculated)	7.87 mg/m^3	8.04 mg/m^3
Absorption coefficient	38.907 mm^{-1}	41.599 mm^{-1}
F(000)	1020.0	1030.0
Crystal size	0.06 × 0.02 × 0.02 mm^3	0.06 × 0.02 × 0.02 mm^3
2θ range for data collected	2.84 to 30.48°	2.86 to 32.62°
Index ranges	$-17 \le h \le 17$	$-18 \le h \le 17$
	$-8 \le k \le 8$	$0 \le k \le 8$
	$-10 \le l \le 10$	$0 \le l \le 11$
Reflections collected	4080	995
Ind. reflections	843[R(int) = 0.0405]	995[R(int) = 0.0638]
Data / restraints / parameters	843 / 0 / 53	995 / 0 / 53
Goodness-of-fit on F^2	1.049	1.081
Final R indices [I>2sigma(I)]	R_1 = 0.0423	R_1 = 0.0432
	wR_2 = 0.0852	wR_2 = 0.1144
R indices (all data)	R_1 = 0.0533	R_1 = 0.0473
	wR_2 = 0.0904	wR_2 = 0.1170
Largest diff. peak and hole	9.08 and −9.05 $e^- \times Å^{-3}$	6.30 and −12.34 $e^- \times Å^{-3}$

Table 7.1 (cont.) Crystal data and structure refinements for compound **7.5**.

	7.5
Empirical formula	$Er_5Mo_2O_{12}$
Formula weight	1220.18
Temperature	296(2) K
Wavelength	0.71073 Å
Crystal system	monoclinic
Space group	*C*2/*m*
Unit cell dimensions	a = 12.1871(18) Å b = 5.7044(8) Å c = 7.4581(11) Å α = 90° β = 107.884(3)° γ = 90°
Volume	493.43(12) $Å^3$
Z	2
Density (calculated)	8.21 mg/m^3
Absorption coefficient	44.54 mm^{-1}
F(000)	1040.0
Crystal size	0.10 × 0.02 × 0.02 mm^3
2θ range for data collected	2.87 to 30.06°
Index ranges	$-17 \le h \le 17$ $-8 \le k \le 8$ $-10 \le l \le 10$
Reflections collected	4411
Ind. reflections	791[R(int) = 0.0452]
Data / restraints / parameters	791 / 0 / 53
Goodness-of-fit on F^2	1.072
Final R indices [I>2sigma(I)]	R_1 = 0.0367 wR_2 = 0.0877
R indices (all data)	R_1 = 0.0448 wR_2 = 0.0916
Largest diff. peak and hole	5.07 and −3.57 $e^- \times Å^{-3}$

Table 7.2 Selected interatomic distances (Å) for compounds **7.1** and **7.2**.

7.1					
Eu(1)[2]–O(2)[1,2] x 2	2.319(7)	Eu(2)–O(2)[4] x 2	2.309(10)	Eu(3)–O(3)[8] x 2	2.289(9)
Eu(1)[3]–O(4)[3]	2.360(14)	Eu(2)–O(4)	2.318(13)	Eu(3)[14]–O(2)[1,2,9,10] x 4	2.352(7)
Eu(1)[3]–O(2)[4] x 2	2.367(10)	Eu(2)[6]–O(1)[4] x 2	2.340(7)	Mo(1)–O(1)[12] x 2	1.923(6)
Eu(1)[2]–O(1)[1,2] x 2	2.490(10)	Eu(2)–O(1)[5,6] x 2	2.513(11)	Mo(1)[13]–O(3)[13] x 2	1.987(7)
Mo(1)[6,7]–O(4)[6,11] x 2	2.124(6)				

[1] –X+1/2, Y−1/2, −Z+1 [2] –X+1/2, −Y+1/2, −Z+1 [3] –X+1, −Y, −Z+1 [4] X, −Y, Z [5] –X+1/2, Y−1/2, −Z
[6] –X+1/2, −Y+1/2, −Z [7] X+1/2, Y−1/2, Z [8] −X, −Y, −Z+1 [9] X−1/2, Y−1/2, Z [10] X−1/2, −Y+1/2, Z
[11] X−1/2, Y+1/2, Z [12] −X, Y, −Z [13] −X, −Y, −Z [14] X+1/2, Y+1/2, Z

7.2					
Tb(1)[2]–O(2)[1,2] x 2	2.307(4)	Tb(2)–O(2)[3] x 2	2.298(7)	Tb(3)–O(3)[8] x 2	2.263(6)
Tb(1)–O(2)[3] x 2	2.328(7)	Tb(2)–O(4)	2.304(8)	Tb(3)[14]–O(2)[1,2,9,10] x 4	2.325(4)
Tb(1)[4]–O(4)[4]	2.337(9)	Tb(2)[6]–O(1)[3] x 2	2.316(5)	Mo(1)–O(1)[12] x 2	1.919(4)
Tb(1)[2]–O(1)[1,2] x 2	2.472(8)	Tb(2)–O(1)[5,6] x 2	2.493(8)	Mo(1)[13]–O(3)[13] x 2	1.972(5)
Mo(1)[6,7]–O(4)[6,11] x 2	2.119(4)				

[1] –X+1/2, Y−1/2, −Z+1 [2] –X+1/2, −Y+1/2, −Z+1 [3] X, −Y, Z [4] −X+1, −Y, −Z+1 [5] –X+1/2, Y−1/2, −Z
[6] –X+1/2, −Y+1/2, −Z [7] X+1/2, Y−1/2, Z [8] −X, −Y, −Z+1 [9] X−1/2, Y−1/2, Z [10] X−1/2, −Y+1/2, Z
[11] X−1/2, Y+1/2, Z [12] −X, Y, −Z [13] −X, −Y, −Z [14] X+1/2, Y+1/2, Z

Table 7.2 (cont.) Selected interatomic distances (Å) for compounds **7.3** and **7.4**.

7.3					
Dy(1)–O(2)[1] x 2	2.289(14)	Dy(2)–O(4)	2.239(18)	Dy(3)–O(3)[8] x 2	2.239(14)
Dy(1)[3]–O(2)[2,3] x 2	2.300(14)	Dy(2)–O(1)[1] x 2	2.306(13)	Dy(3)[14]–O(2)[2,3,9,10] x 4	2.321(14)
Dy(1)[4]–O(4)[4]	2.370(18)	Dy(2)–O(2)[1] x 2	2.307(13)	Mo(1)–O(1)[11] x 2	1.900(13)
Dy(1)[3]–O(1)[2,3] x 2	2.459(15)	Dy(2)[6]–O(1)[5,6] x 2	2.459(15)	Mo(1)[12]–O(3)[12] x 2	1.974(11)
Mo(1)[6,7]–O(4)[6,13] x 2	2.121(9)				

[1] X, −Y, Z [2] −X+1/2, Y−1/2, −Z+1 [3] −X+1/2, −Y+1/2, −Z+1 [4] −X+1, −Y, −Z+1 [5] −X+1/2, Y−1/2, −Z
[6] −X+1/2, −Y+1/2, −Z [7] X+1/2, Y−1/2, Z [8] −X, −Y, −Z+1 [9] X−1/2, Y−1/2, Z [10] X−1/2, −Y+1/2, Z [11] −X, Y, −Z
[12] −X, −Y, −Z [13] X−1/2, Y+1/2, Z [14] X+1/2, Y+1/2, Z

7.4					
Ho(1)[2]–O(2)[1,2] x 2	2.282(10)	Ho(2)–O(4)	2.258(17)	Ho(3)–O(3)[8] x 2	2.246(14)
Ho(1)–O(2)[3] x 2	2.304(10)	Ho(2)–O(2)[3] x 2	2.283(10)	Ho(3)[14]–O(2)[1,2,9,10] x 4	2.300(10)
Ho(1)[4]–O(4)[4]	2.332(17)	Ho(2)–O(1)[3] x 2	2.288(10)	Mo(1)–O(1)[11] x 2	1.921(10)
Ho(1)[2]–O(1)[1,2] x 2	2.443(11)	Ho(2)[6]–O(1)[5,6] x 2	2.474(11)	Mo(1)[12]–O(3)[12] x 2	1.951(11)
Mo(1)[6,7]–O(4)[13] x 2	2.119(8)				

[1] −X+1/2, Y−1/2, −Z+1 [2] −X+1/2, −Y+1/2, −Z+1 [3] X, −Y, Z [4] −X+1, −Y, −Z+1 [5] −X+1/2, Y−1/2, −Z
[6] −X+1/2, −Y+1/2, −Z [7] X+1/2, Y−1/2, Z [8] −X, −Y, −Z+1 [9] X−1/2, Y−1/2, Z [10] X−1/2, −Y+1/2, Z [11] −X, Y, −Z
[12] −X, −Y, −Z [13] X−1/2, Y+1/2, Z [14] X+1/2, Y+1/2, Z

Table 7.2 (cont.) Selected interatomic distances (Å) for compound **7.5**.

7.5					
$Er(1)^{2}$–$O(2)^{1,2}$ x 2	2.275(8)	$Er(2)$–$O(2)^{3}$ x 2	2.243(17)	$Er(3)$–$O(3)^{8}$ x 2	2.213(12)
$Er(1)$–$O(2)^{3}$ x 2	2.312(16)	Er(2)–O(4)	2.248(15)	$Er(3)^{14}$–$O(2)^{1,2,9,10}$ x 4	2.298(8)
$Er(1)^{4}$–$O(4)^{4}$	2.332(16)	$Er(2)$–$O(1)^{3}$ x 2	2.282(8)	$Mo(1)$–$O(1)^{11}$ x 2	1.909(9)
$Er(1)^{2}$–$O(1)^{1,2,}$ x 2	2.417(17)	$Er(2)^{6}$–$O(1)^{5,6}$ x 2	2.483(16)	$Mo(1)^{12}$–$O(3)^{12}$ x 2	1.963(9)
$Mo(1)^{6,7}$–$O(4)^{6,13}$ x 2	2.100(9)				

[1] −X+1/2, Y−1/2, −Z+1 [2] −X+1/2, −Y+1/2, −Z+1 [3] X, −Y, Z [4] −X+1, −Y, −Z+1 [5] −X+1/2, Y−1/2, −Z
[6] −X+1/2, −Y+1/2, −Z [7] X+1/2, Y−1/2, Z [8] −X, −Y, −Z+1 [9] X−1/2, Y−1/2, Z [10] X−1/2, −Y+1/2, Z
[11] −X, Y, −Z [12]−X, −Y, −Z [13] X−1/2, Y+1/2, Z [14] X+1/2, Y+1/2, Z

Table 7.3 Atomic coordinates ($\times 10^4$) and equivalent isotropic displacement parameters ($Å^2 \times 10^3$) for compounds **7.1** – **7.4**. $U_{(eq)}$ is defined as one third of the trace of the orthogonalized U_{ij} tensor.

7.1

Atom	*x*	*y*	*z*	U(eq)
Eu(1)	0.3081(1)	0	0.6408(1)	8(1)
Eu(2)	0.3143(1)	0	0.1741(2)	9(1)
Eu(3)	0	0	½	9(1)
Mo(1)	0	0.2180(2)	0	8(1)
O(1)	0.1611(5)	0.2533(13)	0.0813(16)	11(1)
O(2)	0.3440(6)	0.2494(13)	0.4200(16)	11(1)
O(3)	0.0015(11)	0	0.2014(13)	10(2)
O(4)	0.5009(12)	0	0.1780(14)	11(2)

7.2

Atom	*x*	*y*	*z*	U(eq)
Tb(1)	0.3072(1)	0	0.6394(1)	8(1)
Tb(2)	0.3144(1)	0	0.1751(1)	9(1)
Tb(3)	0	0	½	8(1)
Mo(1)	0	0.2181(1)	0	7(1)
O(1)	0.1621(4)	0.2541(8)	0.0817(12)	11(1)
O(2)	0.3453(4)	0.2488(8)	0.4232(12)	9(1)
O(3)	0.0004(8)	0	0.2012(9)	12(1)
O(4)	0.5016(7)	0	0.1810(9)	9(1)

7.3

Atom	*x*	*y*	*z*	U(eq)
Dy(1)	0.3070(1)	0	0.6386(2)	8(1)
Dy(2)	0.3143(1)	0	0.1744(2)	11(1)
Dy(3)	0	0	½	10(1)
Mo(1)	0	0.2183(3)	0	9(1)
O(1)	0.1614(11)	0.2530(30)	0.0835(19)	12(3)
O(2)	0.3453(12)	0.2470(20)	0.4267(19)	11(3)
O(3)	0.0013(18)	0	0.2030(20)	15(3)
O(4)	0.4977(16)	0	0.1813(19)	12(3)

7.4

Atom	*x*	*y*	*z*	U(eq)
Ho(1)	0.3065(1)	0	0.6373(1)	10(1)
Ho(2)	0.3145(1)	0	0.1749(2)	13(1)
Ho(3)	0	0	½	12(1)
Mo(1)	0	0.2185(2)	0	10(1)
O(1)	0.1637(8)	0.2553(19)	0.0844(15)	13(2)
O(2)	0.3456(8)	0.2497(19)	0.4233(14)	12(2)
O(3)	-0.0015(16)	0	0.1990(20)	17(2)
O(4)	0.5004(15)	0	0.1841(17)	12(2)

Table 7.3 (cont.) Atomic coordinates ($\times 10^4$) and equivalent isotropic displacement parameters ($Å^2 \times 10^3$) for compound **7.5**. $U_{(eq)}$ is defined as one third of the trace of the orthogonalized U_{ij} tensor.

		7.5		
Atom	*x*	*y*	*z*	U(eq)
Er(1)	0.3061(1)	0	0.6394(2)	14(1)
Er(2)	0.3146(1)	0	0.1774(2)	14(1)
Er(3)	0	0	½	14(1)
Mo(1)	0	0.2186(2)	0	13(1)
O(1)	0.1636(7)	0.2555(15)	0.0850(30)	14(2)
O(2)	0.3455(7)	0.2477(14)	0.4220(30)	15(2)
O(3)	0.0008(16)	0	0.2036(19)	19(3)
O(4)	0.4998(14)	0	0.1815(19)	14(2)

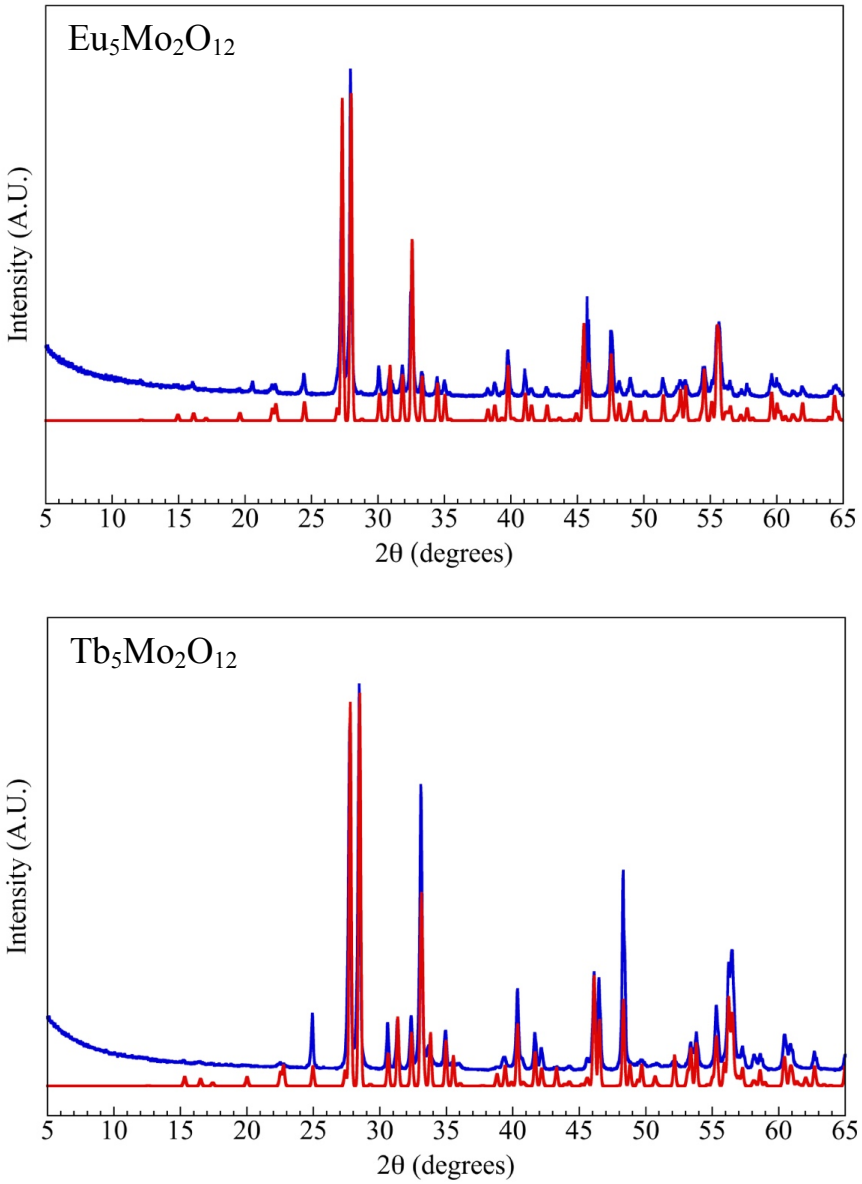

Figure 7.1 PXRD patterns of compounds **7.1** and **7.2**. Experimental diffraction is shown in blue. The calculated pattern is shown in red.

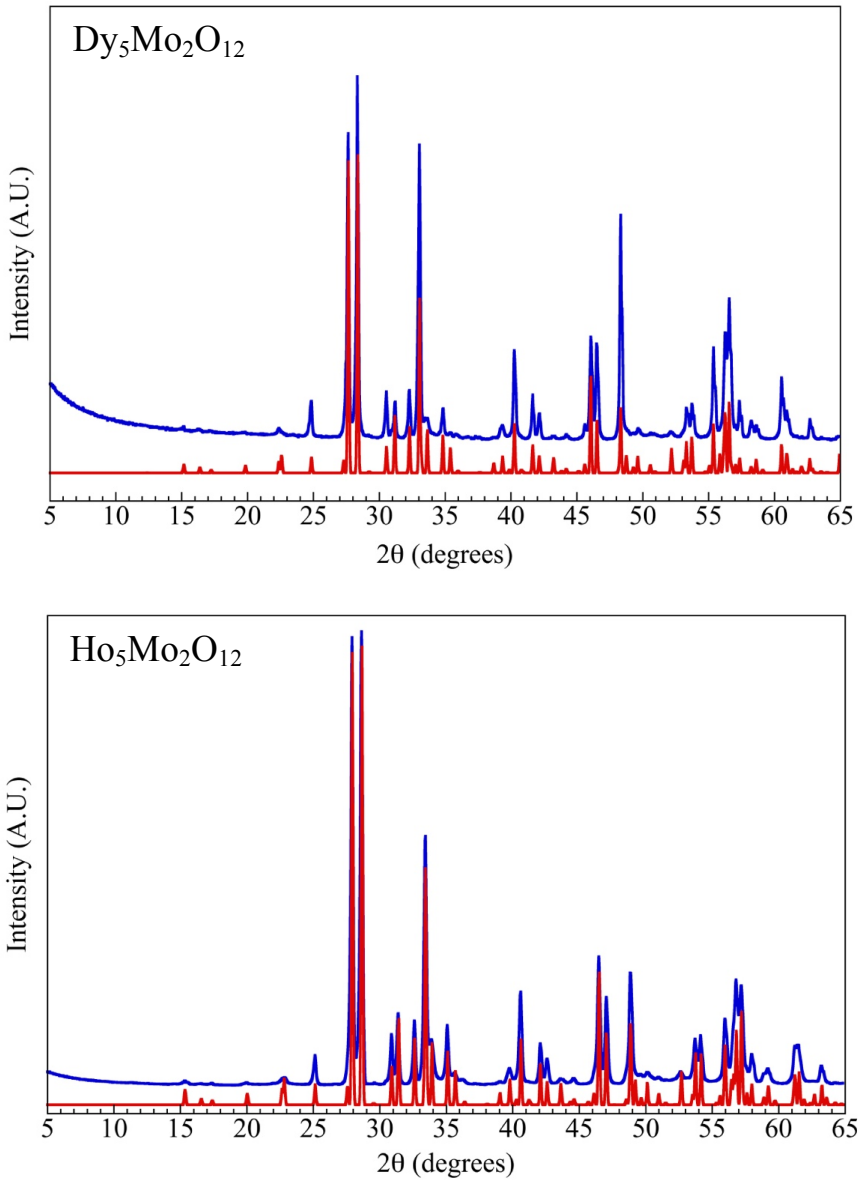

Figure 7.1 (cont.) PXRD patterns of compounds **7.3** and **7.4**. Experimental diffraction is shown in blue. The calculated pattern is shown in red.

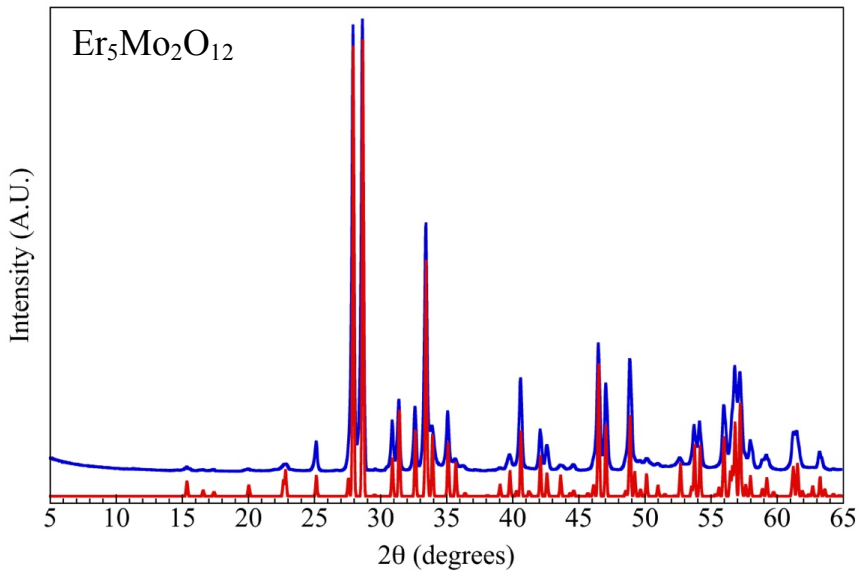

Figure 7.1 (cont.) PXRD pattern of **7.5**. Experimental diffraction is shown in blue. The calculated pattern is shown in red.

each reported element in the title compounds as well as the absence of extraneous elements, such as Zn, in the synthesis of $Eu_5Mo_2O_{12}$ **7.1**.

UV-Vis Spectroscopy.

UV-Vis diffuse reflectance spectroscopy data of ground crystals were obtained using a PerkinElmer Lambda 35 UV-Vis scanning spectrophotometer equipped with an integrating sphere accessory in the range of 200-900 nm. Reflectance data were transformed to absorbance via the Kubelka-Munk function, see **Figure 7.2**.[41]

Magnetic Susceptibility.

The magnetic susceptibility of ground crystals was measured using a Quantum Design MPSP3 SQUID magnetometer. The zero-field cooled magnetic susceptibility was measured as a function of temperature between 2-300K in an applied field of 1000 Oe. The measured magnetic moment was corrected for shape and radial offset effects using methods reports by Morrison et al.[42] which determines the correction factors by comparing the moments observed from DC and VSM scans at a single temperature, 30K.

Results and Discussion

Synthesis.

In 1985 Torardi et al.[27] reported the single crystal structures of $Y_5Mo_2O_{12}$ and $Gd_5Mo_2O_{12}$ grown via the electrolytic reduction of melts prepared from mixtures of Na_2MoO_4 or Li_2MoO_4, MoO_3, and Y_2O_3 or Gd_2O_3. While their reaction times were short, taking only approximately one hour, unidentified reduced species and MoO_2 were often observed as side products. These undesirable impurities make for difficult purification and sample work up. By comparison, molten flux single crystal growth in sealed evacuated fused silica tubes represents an attractive alternative to electrolytic reduction as

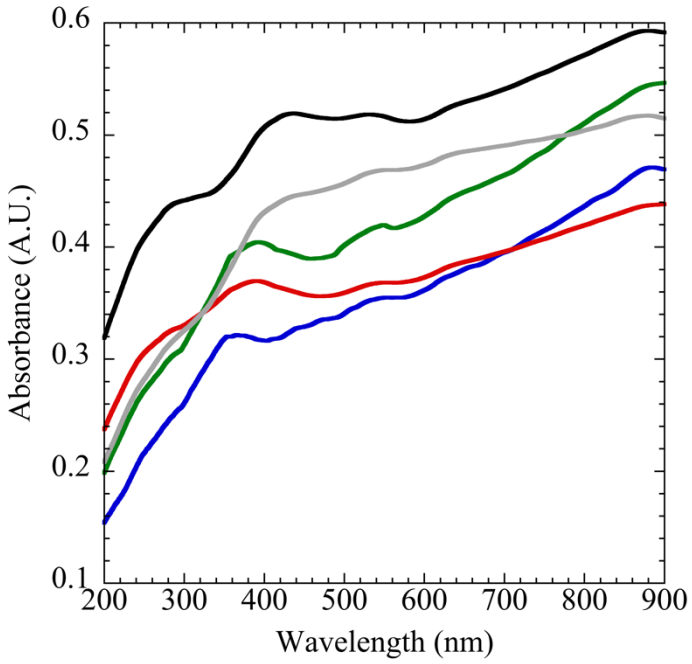

Figure 7.2. Absorbance data for compound **7.1** (gray), **7.2** (black), **7.3** (red), **7.4** (blue), and **7.5** (green).

it does not require expensive platinum foil electrodes, can be achieved at lower temperatures, and excludes air from the reaction to promote the reduction of MoO_3. Crystals of the title compounds were obtained via such a method using Ln_2O_3, *Ln* = Eu, Tb, Dy, Ho, Er; Mo or Zn powder, and a eutectic CsCl/NaCl flux.

The use of redox neutral alkali chlorides allowed for the efficient dissolution of the oxides to facilitate reduction and was easily removed via gentle sonication in water. In addition to single crystals of the title compounds, reactions containing Tb, Dy, Ho, and Er often resulted in a poorly crystalline transparent impurity phase that could easily be removed via a combination of sieving and manual crystal picking. Attempts to prepare single crystals of $Eu_5Mo_2O_{12}$ **7.1** using Mo powder as a reducing agent in any temperature regime were unsuccessful. In order to form $Eu_5Mo_2O_{12}$ single crystals, higher temperatures and Zn powder as a reducing agent were needed. Such reactions also resulted in $EuMoO_4$ single crystals that formed as an impurity phase.[32] Interestingly, this impurity phase predominantly contains Eu^{2+}, as confirmed by Mössbauer spectroscopy, and Mo^{6+}. $Eu_5Mo_2O_{12}$ **7.1**, however, contains exclusively Eu^{3+} and $Mo^{4/5+}$. Attempts to prepare analogous compounds with rare earths smaller than erbium or larger than europium were unsuccessful but did lead to other novel compositions that are currently under investigation. Single crystals of $Gd_5Mo_2O_{12}$ were previously reported by Torardi et al.[27] however we were unable to obtain them via our synthetic approach.

Structure.

The title compounds are isostructural and crystallize in the $Y_5Mo_2O_{12}$ structure type in the monoclinic space group *C*2/*m*. $Ln_5Mo_2O_{12}$ exhibits a three-dimensional crystal structure containing infinite chains of $MoO_2O_{4/2}$ edge sharing octahedra. These chains are

isolated from each other by intervening rare earth containing polyhedra. The structure contains distorted MoO_6 octahedra, distorted LnO_6 octahedra, and two crystallographically independent monocapped trigonal prismatic LnO_7 polyhedra. Mo(1) is located in a distorted MoO_6 octahedron with Mo – O bond distances between 1.900 Å – 2.124 Å. Mo(1) shares edges with itself through O(3) and O(4) forming one-dimensional chains shown in **Figure 7.3**. This edge sharing allows for better orbital overlap between molybdenum centers and enhances the possibility of unpaired electrons possessed by molybdenum to exhibit magnetic ordering. In this series of compositions, the Mo – Mo distances in the chains alternate between 3.210 Å – 3.265 Å (long) and 2.494 Å – 2.523 Å (short), which are similar to distances observed in the previously reported isostructural $Ln_5Ru_2O_{12}$ and $Ln_5Re_2O_{12}$ oxides. Mo – Mo distances for the title compounds can be found in **Table 7.4**. Mo(1) also shares edges with *Ln*(1) and *Ln*(2) through O(1) and O(4), and shares corners with *Ln*(2) and *Ln*(3) through O(1) and O(3), respectively. The local coordination environment of Mo(1) is shown in **Figure 7.4**. *Ln*(1) is located in a LnO_7 monocapped trigonal prism with *Ln* – O bond distances ranging from 2.275 Å – 2.490 Å. The local coordination environment of *Ln*(1) is shown in **Figure 7.4**. *Ln*(2) is located in a LnO_7 monocapped trigonal prism with *Ln* – O bond distances between 2.239 Å – 2.513 Å. The local coordination environment of *Ln*(2) is shown in **Figure 7.4**. *Ln*(3) is located in a LnO_6 distorted octahedron with *Ln* – O bond distances ranging from 2.213 Å – 2.352 Å. The local coordination environmental of *Ln*(3) is shown in **Figure 7.4**. All *Ln* – O distances we report are comparable to those observed in previously reported isostructural compounds. The extended $Ln_5Mo_2O_{12}$ structure, oriented along the *b* and *c* axes, is shown in **Figure 7.5**.

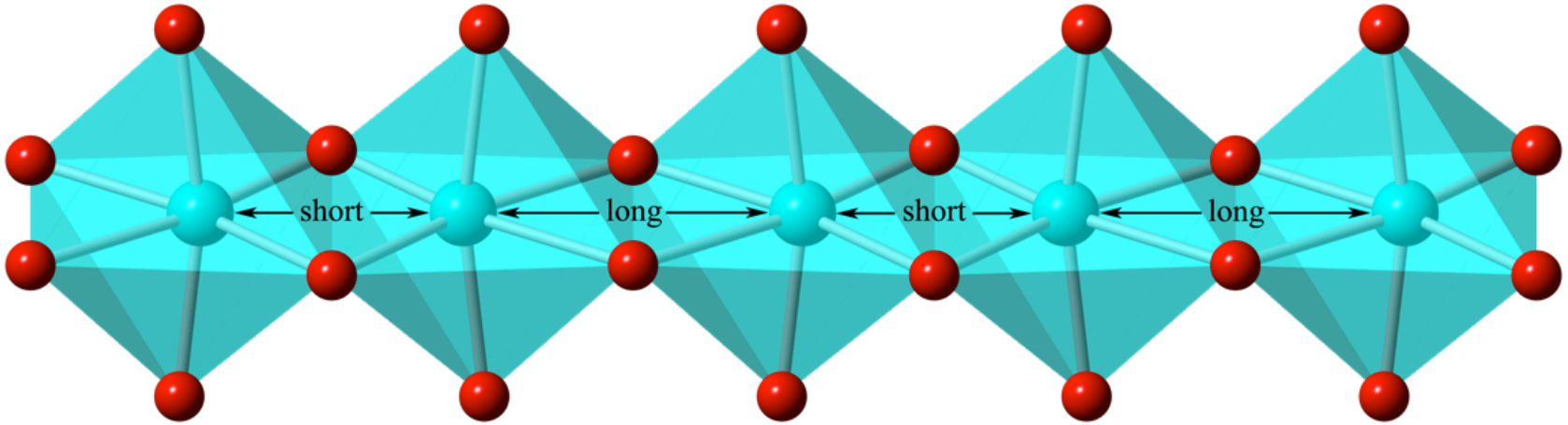

Figure 7.3 $MoO_2O_{4/2}$ 1D chains showing alternating Mo – Mo distances. Mo and O shown in cyan and red, respectively.

Table 7.4 Mo – Mo alternating distances for compounds **7.1** – **7.5**.

Compound	Short Distance (Å)	Long Distance (Å)
$Eu_5Mo_2O_{12}$	2.523	3.265
$Tb_5Mo_2O_{12}$	2.510	3.243
$Dy_5Mo_2O_{12}$	2.505	3.233
$Ho_5Mo_2O_{12}$	2.499	3.219
$Er_5Mo_2O_{12}$	2.494	3.210

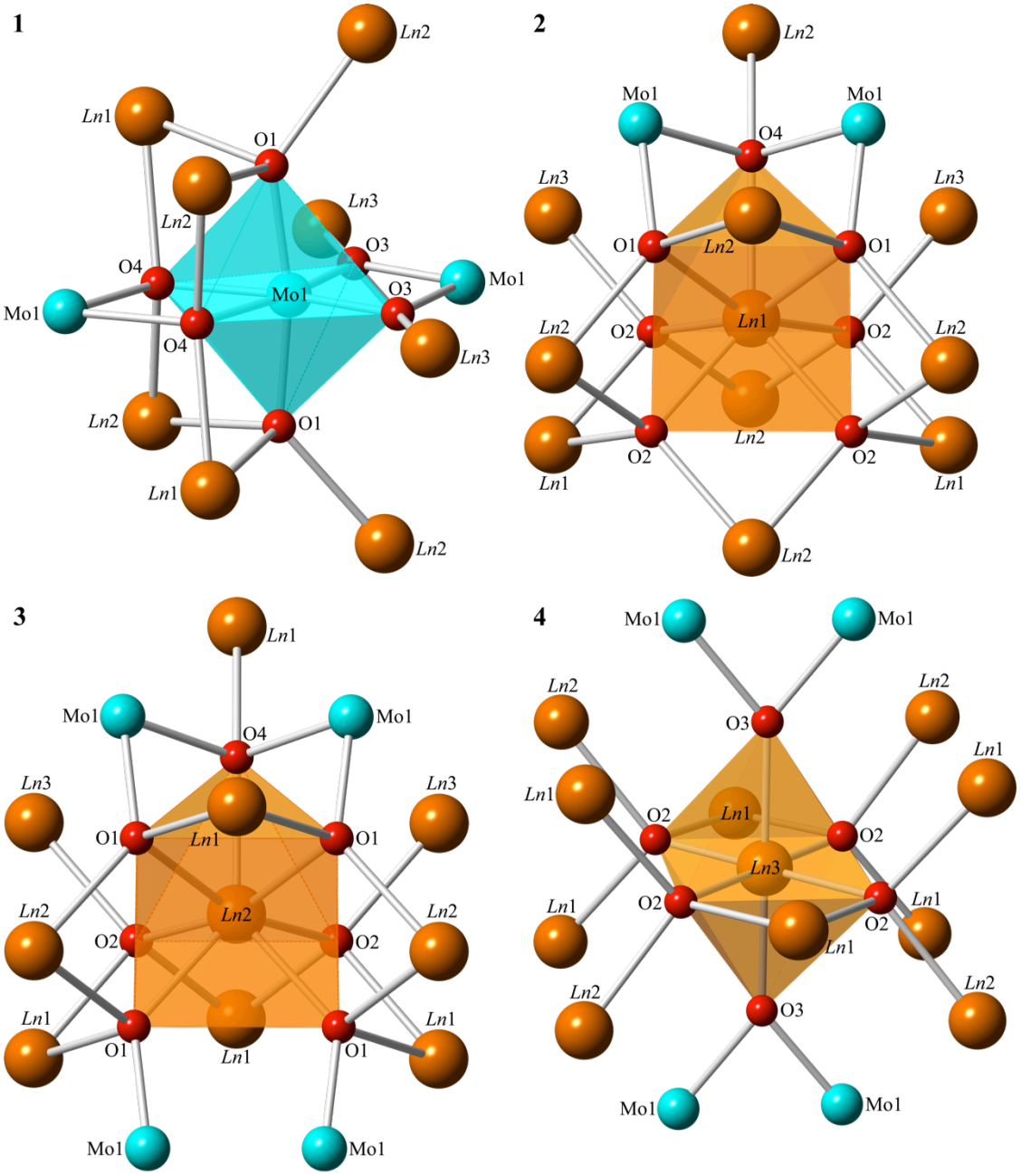

Figure 7.4 Local coordination environments of compounds **7.1** – **7.5**. Local coordination of Mo1, pane 1; local coordination of *Ln*1, pane 2; local coordination of *Ln*2, pane 3; and local coordination of *Ln*3, pane 4. *Ln*, Mo, and O shown in orange, cyan, and red, respectively.

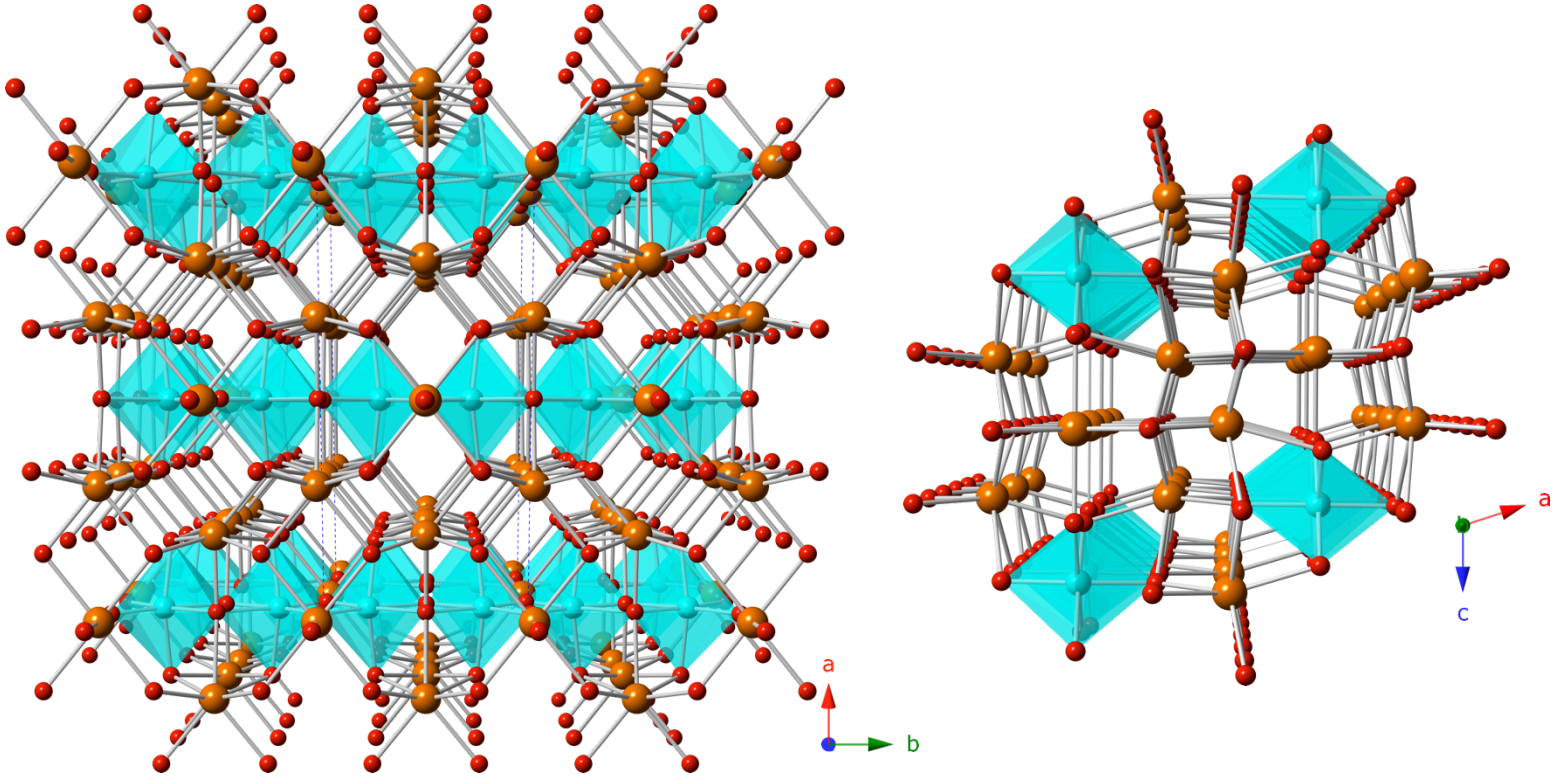

Figure 7.5 Shown left, compounds **7.1 – 7.5** viewed down the *c* axis. Shown right, compounds **7.1 – 7.5** viewed down the *b* axis. *Ln*, Mo, and O shown in orange, cyan, and red, respectively.

Only one crystallographic molybdenum site is present in the structure bearing a formal oxidation state of +4.5 with each Mo_2O_{10} unit consisting of one +4 molybdenum containing 2 unpaired electrons and one +5 molybdenum containing 1 unpaired electron. A bond valence sum (BVS) analysis of molybdenum assuming all molybdenum is +5 gives a range of 4.63 – 4.89 for the title compounds. Using an identical treatment but assuming all molybdenum is +4 gives a range of 4.38 – 4.62. These values are shown in **Table 7.5**. These intermediate results between +4 and +5 corroborate the formal oxidation state of +4.5 for molybdenum. The alternating short and long Mo – Mo distances in the infinite chains indicate the presence of direct metal to metal bonding between molybdenum. In our case one unpaired electron from a Mo(IV) center and the unpaired electron from a Mo(V) center are believed to participate in metal to metal bond formation. This leaves one remaining unpaired electron from the Mo(IV) center for participation in magnetism. Magnetic susceptibility measurements of the title compounds indicate that this remaining electron is localized.

Magnetism.

The unpaired d-electron from the Mo_2O_{10} unit and the unpaired f-electrons from the rare earth cations in $Ln_5Mo_2O_{12}$, *Ln* = Eu, Tb, Dy, Ho, and Er **7.1-7.5** are expected to contribute to the magnetic moment and can be observed in magnetic susceptibility measurements. The temperature dependencies of the magnetic susceptibilities and inverse susceptibilities of $Ln_5Mo_2O_{12}$, *Ln* = Eu, Tb, Dy, Ho, and Er **7.1-7.5** are shown in **Figure 7.6**. No differences in susceptibility between zero field cooled and field cooled measurements were observed. Above 100 K the data for Tb, Dy, Ho, and Er **7.2-7.5** follow the Curie-Weiss (C-W) law and experimental magnetic moments can be

Table 7.5 BVS of compound **7.1** – **7.5**, assuming either Mo(V) or Mo(IV).

Compound	Assuming Mo(V)	Assuming Mo(IV)
$Eu_5Mo_2O_{12}$	4.63	4.38
$Tb_5Mo_2O_{12}$	4.74	4.48
$Dy_5Mo_2O_{12}$	4.82	4.56
$Ho_5Mo_2O_{12}$	4.82	4.56
$Er_5Mo_2O_{12}$	4.89	4.62

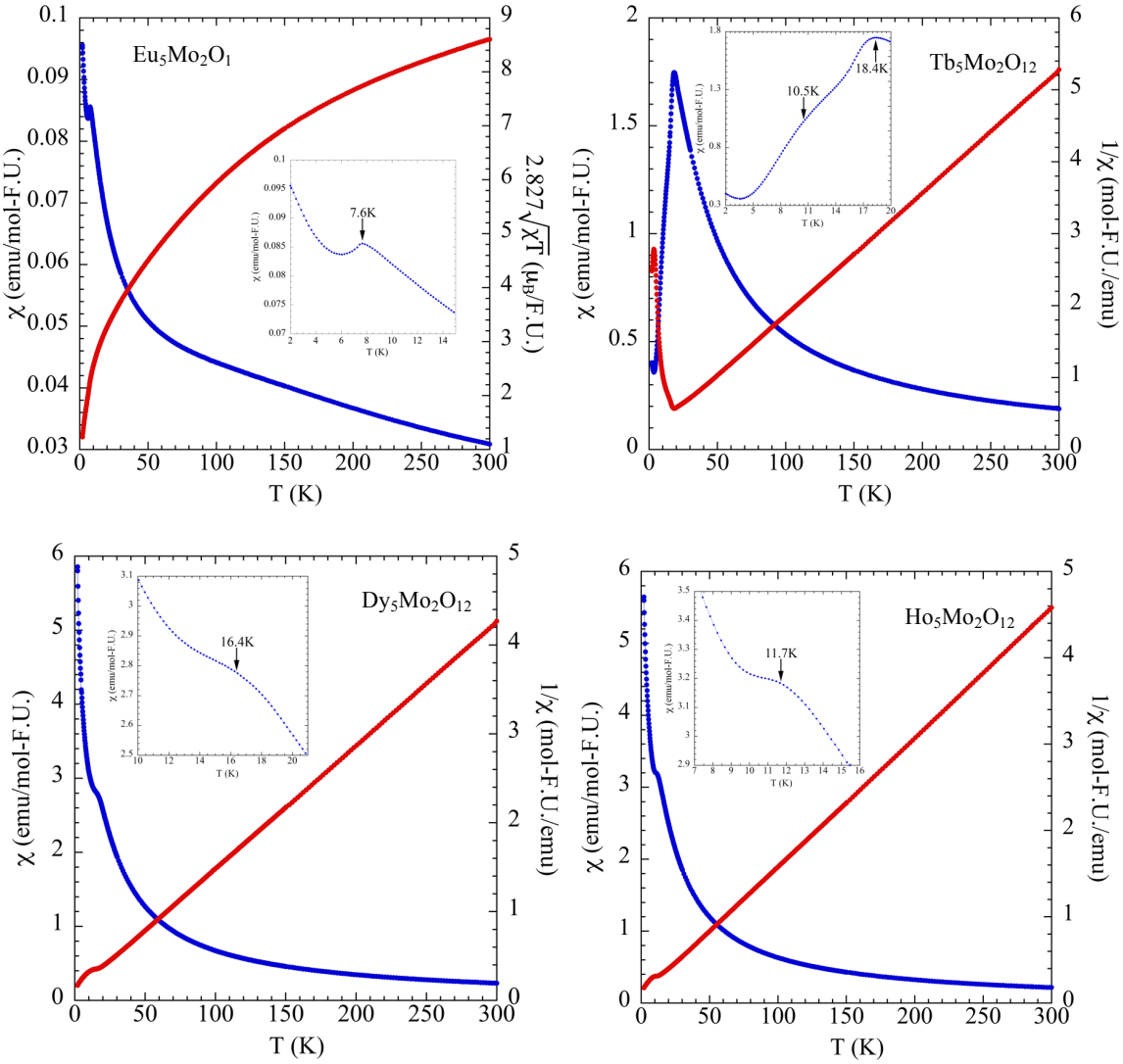

Figure 7.6. Temperature dependence of the molar magnetic susceptibility (blue), χ, and inverse susceptibility (red), 1/χ of **7.2** – **7.4**. For **7.5**, χ is shown in blue and χT is shown in red. Inset data show low temperature behavior of the susceptibility.

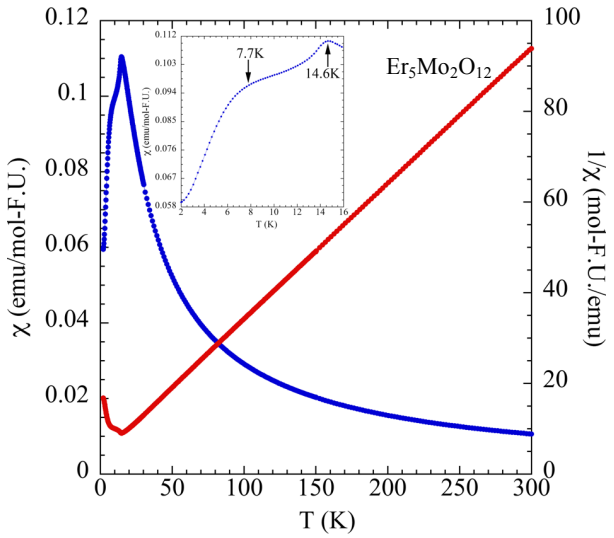

Figure 7.6. Temperature dependence of the molar magnetic susceptibility (blue), χ, and inverse susceptibility (red), $1/\chi$ of **7.5**. Inset data show low temperature behavior of the susceptibility.

determined.[37] It is well known that samples containing Eu^{3+} do not follow the C-W law,[43] and hence, to determine the experimental magnetic moment of $Eu_5Mo_2O_{12}$, **7.1** a χT vs T plot was prepared and is shown in **Figure 7.6**. The magnetic moment of $Eu_5Mo_2O_{12}$ **7.1** at 300 K, 8.60 μ_B, is in good agreement with the theoretical 300 K value of 8.29 μ_B. The theoretical and experimental magnetic moments for the Eu, Tb, Dy, Ho, and Er containing compositions are collected in **Table 7.6** and are found to be in good agreement if one unpaired electron per Mo-Mo unit is assumed. Magnetic moments calculated using three unpaired electrons do not match the observed moments, supporting that a single Mo-Mo bond exists between alternating Mo-Mo dimers. Weiss constants, Neel temperatures, and calculated and theoretical magnetic moments for all data sets can be found in **Table 7.6**.

Based on the observation of antiferromagnetic order at 6K in the isostructural $Y_5Mo_2O_{12}$, it is reasonable to expect antiferromagnetic coupling between the Mo_2O_{10} units in $Ln_5Mo_2O_{12}$, *Ln* = Eu, Tb, Dy, Ho, and Er, **7.1-7.5** as well. Since yttrium in $Y_5Mo_2O_{12}$ is non-magnetic, the observed antiferromagnetic ordering is due to the single unpaired d-electron per Mo-Mo dimer. The additional unpaired f-electrons in Eu, Tb, Dy, Ho, Er can potentially couple with the d-electron, an interaction that has been observed in $Ln_5Ru_2O_{12}$. The contribution of the rare earth cations to the total magnetic moment dwarfs the contribution of the single unpaired d-electron per Mo-Mo dimer. Hence, we would expect to see a small discontinuity from the expected antiferromagnetic ordering of the single unpaired d-electron of the Mo-Mo dimer in the magnetic data if the d- and f-electrons do not couple, and a large downturn in the magnetic data if they couple antiferromagnetically or even if just the f-electrons couple antiferromagnetically. Both

Table 7.6 Magnetic data for compounds **7.1** – **7.5**. For **7.1** a θ value cannot be determined and the calculated moment was taken from a plot of $\underline{\chi T}$ as the compound does not obey the C-W law. Calculated moments assume 1 unpaired electron per Mo_2O_{10} unit.

Compound	θ (K)	T_N (K) Mo	T_N (K) *Ln*	μ_B theoretical	μ_B experimental
$Eu_5Mo_2O_{12}$	-	7.6	-	8.29	8.60
$Tb_5Mo_2O_{12}$	-10.8	~ 10.5	18.4	21.80	21.69
$Dy_5Mo_2O_{12}$	-6.6	~ 16.4	-	23.87	23.99
$Ho_5Mo_2O_{12}$	-5.5	~ 11.7	-	23.78	23.09
$Er_5Mo_2O_{12}$	-14.5	~7.7	14.6	21.49	21.87

situations are observed. In the case of Eu, Ho, and Dy, a small kink in the susceptibility data is observed at low temperatures (7-15 K), indicating that the single unpaired d-electrons of the Mo-Mo dimers order antiferromagnetically, but that the f-electrons of the rare earths do not participate in the AF ordering. Hence, their contribution to the susceptibility continues to lower temperatures as evidenced by the continued overall increase in the susceptibility. By contrast, in the case of Er and Tb, the susceptibility data show a sharp downturn at 14.6 and 18.4 K, respectively, indicating that the rare earth f-electrons are coupling AF. Small shoulders at 10.5 and 8.5 K, in the Tb and Er data, respectively, can be ascribed to the unpaired d-electrons of the Mo-Mo dimers ordering AF. Hence it appears that while d-electron magnetic ordering and f-electron magnetic ordering is observed, the two types of electrons do not couple magnetically with each other.

Conclusion

We have successfully synthesized and characterized five new lanthanide molybdenum oxides, $Ln_5Mo_2O_{12}$ *Ln* = Eu, Tb, Dy, Ho, and Er, utilizing a molten salt flux technique. The lanthanide oxidation state in these structures is 3+ and that of the molybdenum is +4/+5. All compounds exhibit antiferromagnetic coupling between the $Mo^{4+/5+}$ ions, which is consistent with previously reported related compositions.

Acknowledgment

Financial support for this work was provided by the National Science Foundation under DMR-1301757 and is gratefully acknowledged.

References

(1) Andersson, G. *Acta. Chem. Scand.* **1954**, *8*, 1599-1606.

(2) Chen, S. C.; Wang, B.; Greenblatt, M. *Inorg. Chem.* **1993**, *32*, 4306-4310.

(3) Feger, C. R.; Ziebarth, R. P. *Chem. Mater.* **1995**, *7*, 373-378.

(4) Greenblatt, M. *Chem. Rev.* **1988**, *88*, 31-53.

(5) Greenblatt, M. *Phys. Chem. Mater. Low-Dimens. Struct.* **1989**, *11*, 1-48.

(6) Hessen, B.; Sunshine, S. A.; Siegrist, T.; Fiory, A. T.; Waszczak, J. V. *Chem. Mater.* **1991**, *3*, 528-534.

(7) Hessen, B.; Sunshine, S. A.; Siegrist, T.; Jimenez, R. *Mater. Res. Bull.* **1991**, *26*, 85-90.

(8) Morin, F. J. *Bell Syst. Tech. J.* **1958**, *37*, 1047-1084.

(9) Ok, K. M.; Chi, E. O.; Halasyamani, P. S. *Chem. Soc. Rev.* **2006**, *35*, 710-717.

(10) Pouchard, M.; Launay, J. C. *Mater. Res. Bull.* **1973**, *8*, 95-104.

(11) Ridgley, D.; Ward, R. *J. Am. Chem. Soc.* **1955**, *77*, 6132-6136.

(12) Serra, D. L.; Hwu, S.-J. *J. Solid State Chem.* **1992**, *101*, 32-40.

(13) Tsai, P. P.; Potenza, J. A.; Greenblatt, M. *J. Solid State Chem.* **1987**, *69*, 329-335.

(14) Van Zandt, L. L.; Honig, J. M.; Goodenough, J. B. *J. Appl. Phys.* **1968**, *39*, 594-595.

(15) Vasala, S.; Saadaoui H.; Morenzoni, E.; Chmaissem, O.; Chan, T.-S.; Chen, J.-M.; Hsu, Y.-Y.; Yamauchi, H.; Karppinen, M. *Phys Rev. B: Condens. Matter Mater. Phys.* **2014**, *89*, 134419/1-134419-9.

(16) Kuroe, H.; Aoki, K.; Itoh, R.; Hosaka, T.; Hasegawa, T.; Hachiuma, S.; Akaki, M.; Kuwahara, H.; Sekine, T.; Hase, M.; Oka, K.; Ito, T.; Eisaki, H. *J. Korean Phys.*

Soc. **2013**, *63*, 542-545.

(17) Lancaster, T.; Baker, P. J.; Pratt, F. L.; Blundell, S. J.; Hayes, W.; Prabhakaran, D. *Phys. Rev. B: Condens. Matter Mater. Phys.* **2012**, *85,* 184404/1-184404/4.

(18) Mat'aš, S.; Orendáčová, A.; Prokeš, K.; Klemke, B. *J. Phys.: Conf. Ser.* **2010**, *251*, 012024.

(19) Hamasaki, T.; Kuroe, H.; Sekine, T.; Hase, M.; Kitazawa, H. *J. Phys.: Conf. Ser.* **2009**, *150*, 042047.

(20) Westman, S.; Nordmark, C. *Acta Chem. Scand.* **1960**, *14*, 465-470.

(21) Abeysinghe, D.; Smith, M. D.; Yeon, J.; Morrison, G.; zur Loye, H.-C. *Cryst. Growth Des.* **2014**, *14*, 4749-4758.

(22) Abeysinghe, D.; Gerke, B.; Morrison, G.; Hsieh, C. H.; Smith, M. D.; Pöttgen, R.; Makris, T. M.; zur Loye, H.-C. *J. Solid State Chem.* **2015**, *229*, 173-180.

(23) Cortese, A. J.; Wilkins, B.; Smith, M. D.; Morrison, G.; zur Loye, H.-C. *Solid State Sci.* **2015**, *48*, 133-140.

(24) Cortese, A. J.; Wilkins, B.; Smith, M. D.; Morrison, G.; zur Loye, H.-C. *Solid State Sci.* **2015**, *48*, 7-12.

(25) Yeon, J.; Sefat, A. S.; Tran, T. T.; Halasyamani, P. S.; zur Loye, H.-C. *Inorg. Chem.* **2013**, *52*, 6179-6186.

(26) Magneli, A. *Ark. Kemi, Mineral. Geol.* **1946**, *24A*, 11.

(27) Torardi, C. C.; Fecketter, C.; McCarroll, W. H.; DiSalvo, F. J. *J. Solid State Chem.* **1985**, *60*, 332-342.

(28) Gall, P.; Gougeon, P. *Acta Crystallogr., Sect. C: Cryst. Struct. Commun.* **1992**, *48*, 1915-1917.

(29) Colabello, D. M.; Camino, F. E.; Huq, A.; Hybertsen, M.; Khalifah, P. G. *J. Am. Chem. Soc.* **2015**, *137*, 1245-1257.

(30) Chi, L.; Britten, J. F.; Greedan, J. E. *J. Solid State Chem.* **2003**, *172*, 451-457.

(31) Bharathy, M.; Gemmill, W. R.; Fox, A. H.; Darriet, J.; Smith, M. D.; Hadermann, J.; Remy, M. S.; zur Loye, H.-C. *J. Solid State Chem.* **2009**, *182*, 1164-1170.

(32) Abeysinghe, D.; Gerke, B.; Morrison, G.; Hsieh, C. H.; Smith, M. D.; Pöttgen, R.; Makris, T. M.; zur Loye, H.-C. *J. Solid State Chem.* **2015**, *229*, 173-180.

(33) Bugaris, D. E.; zur Loye, H.-C. *Angew. Chem. Int. Ed.* **2012**, *51*, 3780-3811.

(34) Elwell, D.; Scheel, H. J. *Crystal Growth from High Temperature Solutions*; 2011.

(35) Mahjoor, P.; Latturner, S. *Philos. Mag*. **2012**, *92*, 2582-2595.

(36) SMART Version 5.631, SAINT+ Version 6.45 and TWINABS Version 2012/1. Bruker Analytical X-ray Systems, Inc., Madison, Wisconsin, USA, 2014.

(37) Hübschle, C. B.; Sheldrick, G. M.; Dittrich, B. *J. Appl. Crystallogr.* **2011**, *44*, 1281-1284.

(38) Sheldrick, G. M. *Acta Crystallogr., Sect. A: Found. Crystallogr.* **2008**, *64*, 112-122.

(39) Spek, A. L. *J. Appl. Crystallogr.* **2003**, *36*, 7-13.

(40) Spek, A. L. *Acta. Crystallogr., Sect. D: Biol. Crystallogr.* **2009**, *65*, 148-155.

(41) Kubelka, P.; Munk, F. *Zeit. Für Tekn. Physik* **1931**, *12*, 593.

(42) Morrison, G.; zur Loye, H.-C. *J. Solid State Chem.* **2015**, *221*, 334-337.

(43) Blundell, S. *Magnetism in Condensed Matter*; 2001.

CHAPTER VIII

SINGLE CRYSTAL GROWTH AND CHARACTERIZATION OF THE FIRST REDUCED LANTHANUM MOLYBDENUM OXYCHLORIDE, $La_{20}Mo_{12}O_{63}Cl_4$, WITH AN UNUSUAL TRIGONAL PRISMATIC MoO_6 UNIT*

*Adapted with permission from Cortese, A. J.; Wilkins, B.; Smith, M. D.; Morrison, G.; zur Loye, H.-C. *Solid State Sci.* **2015**, *48*, 133-140. © 2015 Elsevier.

Abstract

The use of a KCl/CsCl alkali eutectic flux under reducing conditions facilitated the crystal growth of the mixed valent Mo(V)/Mo(VI) compound $La_{20}Mo_{12}O_{63}Cl_4$. $La_{20}Mo_{12}O_{63}Cl_4$ crystallizes in the noncentrosymmetric hexagonal space group *P*-62*m* with a = 10.2241(2) Å and c = 15.0768(4) Å, which represents a new structure type exhibiting a three-dimensional crystal structure containing three different molybdenum coordination environments, MoO_5 square pyramids, MoO_6 trigonal prisms, and MoO_5 trigonal bipyramids. The temperature dependence of the magnetic susceptibility was measured and $La_{20}Mo_{12}O_{63}Cl_4$ was found to be paramagnetic across the entire 2-300 K temperature range measured. Although noncentrosymmetric, $La_{20}Mo_{12}O_{63}Cl_4$ was not found to be second harmonic generation active. $La_{20}Mo_{12}O_{63}Cl_4$ was further characterized by UV/Vis spectroscopy.

Introduction

Crystal growth of complex oxides and related materials containing reduced early transition metals remains a relatively unexplored area in solid state chemistry owing to the synthetic difficulties involved in the crystal growth of reduced materials; however, it is an attractive area of research for the creation of new complex oxide materials containing unpaired *d* electrons. The presence of unpaired electrons in early transition metal cations can potentially lead to interesting electrical and magnetic properties. Known materials are predominantly limited to the simple binaries, such as VO_2, V_2O_3[1-3], TiO[4], and Ti_2O_3[5]; ternaries such as A_xNbO_3 (A=Sr, Ba)[6, 7], $Cs_{0.33}MoO_3$[8], $AMoO_3$ (A=K, Rb, Tl)[9, 10], $Ba_3M_5O_{15}$ (M=Nb, Ta) [11, 12] and SrV_4O_9[13]; and some higher order oxides such as $Ba_6Nb_{14}Si_4O_{47}$[14] and $K_2Mo_4Nb_3O_{20}$[15]. Historically, synthetic techniques used to

prepare crystals of such reduced oxides have included fused salt electrolysis, chemical vapor transport, flux, and hydrothermal methods.

The lack of materials containing reduced early transition metals has motivated us to pursue synthetic routes to prepare such oxides and to measure their physical properties. An earlier approach, a two-step mild hydrothermal method, was successful for the preparation of single crystals of hybrid materials containing transition metals in a variety of reduced oxidation states.[16-22] For the creation of new oxides we chose high temperature solution growth, a well-known method for the crystal growth of a wide variety of oxides, including some reduced ones.[17, 23, 24] The careful selection of appropriate fluxes is critical for maintaining a redox neutral melt in which to conduct the reaction. For this reason we selected alkali metal halides, which are known to solubilize a diverse array of elements. Most oxides reported in the literature have been prepared using sealed tantalum, niobium, or fused silica tubes.[11, 25-30] Our approach is based on the *in situ* reduction of Mo(VI) using Mo metal as a reducing agent, which was successful in preparing, to the best of our knowledge, the first reduced lanthanum molybdenum oxychloride. A limited number of lanthanum molybdenum oxychlorides are known including *Ln*Cl[MoO_4] *Ln* = La, Ce, Pr, Sm – Lu[31, 32], however these materials contain Mo(VI) exclusively.

To fully characterize this new structure type and the oxidation state of the molybdenum within the single crystals, a combination of single crystal X-ray diffraction, bond valence sum calculations (BVS), and magnetic susceptibility measurements were employed. Herein, we report the synthesis, crystal structure, and physical property characterization of $La_{20}Mo_{12}O_{63}Cl_4$.

Experimental Details

Reagents.

CsCl (Alfa Aesar, 99+%) and LiCl (Acros, 99%) were dried at 260°C for 24 hours before use. La_2O_3 (Alfa Aesar, 99.99%) was prefired at 1000°C for 12 hours before use. MoO_3 (Alfa Aesar, 99.95%) and Mo powder ~250 mesh (Alfa Aesar, 99.9%) were used as received.

Flux Synthesis.

Synthesis of $La_{20}Mo_{12}O_{63}Cl_4$, ***8.1***

Single crystals of **8.1** were grown out of a molten cesium chloride/lithium chloride eutectic flux. In a typical procedure, 1 mmol of La_2O_3 (prefired at 1000°C for 12 hours), 2 mmol MoO_3, 0.5 mmol Mo powder, and a 4x excess by weight of CsCl/LiCl (dried at 260°C for 24 hours) were placed into an 8'' long, ½'' diameter fused silica tube. The tube was evacuated to a pressure of 10^{-4} torr and flame sealed. The tube was heated in a programmable furnace to 800°C at a rate of 15°C/min, held for 24 hours, and then cooled to 400°C at a rate of 6°C/hr. At this point the furnace was shut off and allowed to cool to room temperature. The chloride flux was dissolved in water and the crystals were isolated via vacuum filtration yielding a phase pure product in approximately 80% yield based on La_2O_3. **Figure 8.1** shows an optical image and a scanning electron microscopy (SEM) image of representative crystals. **Figure 8.2** displays a powder X-ray diffraction pattern (PXRD) of ground crystals of **8.1** and also, for comparison, contains the calculated diffraction pattern obtained using the single crystal data, demonstrating the phase purity of the crystals.

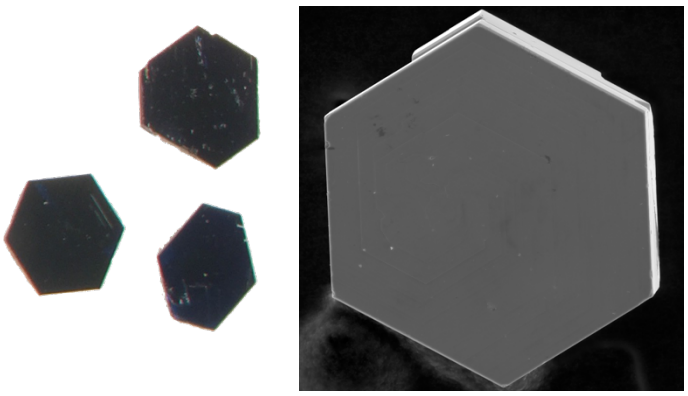

Figure 8.1 Optical image of compound **8.1** grown out of a cesium chloride/lithium chloride melt and SEM image of compound **8.1**.

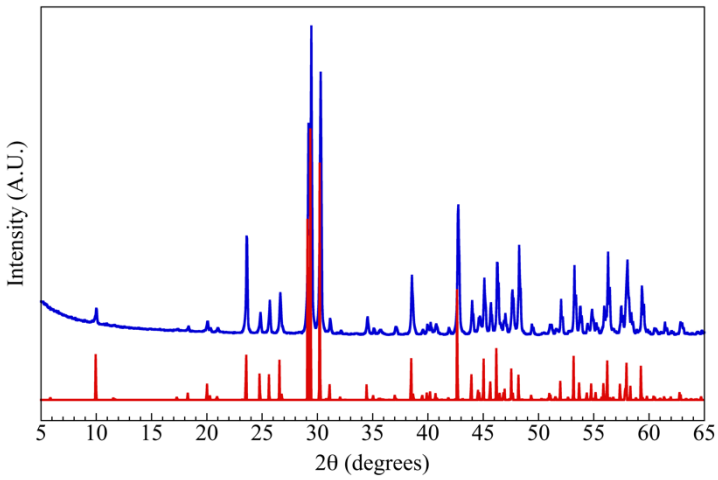

Figure 8.2 Experimental and calculated PXRD patterns for compound **8.1** demonstrating phase purity shown in blue and red, respectively.

Energy-dispersive spectroscopy (EDS).

Elemental analysis was performed on the single crystals using a TESCAN Vega-3 SBU SEM with EDS capabilities. The crystals were mounted on carbon tape and analyzed using a 20 kV accelerating voltage and an accumulation time of 1 minute. As a qualitative measure, EDS confirmed the presence of each reported element in the title compound.

Single crystal X-ray diffraction (SXRD).

X-ray intensity data from a deep blue hexagonal plate crystal were collected at 297(2) K using a Bruker SMART APEX diffractometer (Mo Kα radiation, λ = 0.71073 Å). The raw area detector data frames were reduced and corrected for absorption effects with the SAINT+ and SADABS programs. [33] Final unit cell parameters were determined by least-squares refinement of 6928 reflections from the data set. An initial structural model was obtained with direct methods. Subsequent difference Fourier calculations and full-matrix least-squares refinement against F^2 were performed with SHELXL-2014[34] using the ShelXle interface[35].

The compound crystallizes in the trigonal / hexagonal system. No systematic absences were found in the intensity data, leaving 16 possible space groups. Eventually the noncentrosymmetric group *P*-62*m* (No. 189) was confirmed by structure solution. The space group choice was checked for missed symmetry elements with the ADDSYM program, which found none.[36-39] There are 18 atomic positions in the asymmetric unit: five lanthanum atoms, three molybdenum atoms, two chlorine atoms and eight oxygen atoms. All atoms are located on special positions except for three oxygens. La(1), Mo(1), O(6) and O(7) are located on mirror planes (site 6*i*, site symmetry ..*m*). La(2) and La(3)

are located on three-fold axes (site 4*h*, site symmetry 3..). La(4) and Mo(2) are located site 3*g* with *m*2*m* site symmetry. La(5), Mo(3) and O(8) are located on site 3*f*, also with *m*2*m* site symmetry. The two chlorine atoms Cl(1) and Cl(2) are both located on site 2*e*, with 3.*m* site symmetry. O(4) and O(5) are located on the mirror planes of sites 6*k* and 6*j*, respectively, both with *m*.. site symmetry. Finally, oxygen atoms O(1), O(2), and O(3) are located on general positions (site 12*l*). All atoms were refined with anisotropic displacement parameters. No deviation from full occupancy was observed for any of the metal or chlorine atoms. The final refined absolute structure (Flack *x*) parameter determined by the Parsons quotient method is 0.006(13).[40] Final atomic coordinates were standardized with Structure Tidy.[41-43] Crystallographic data, equivalent atomic positions, and selected interatomic distances are listed in **Tables 8.1 – 8.3**. The Cambridge Crystallographic Data Centre (CCDC) number is: # 1452141. The Inorganic Crystal Structure Database (ICSD) number is: #429259.

Powder X-ray diffraction (PXRD).

PXRD data were collected on a Rigaku D/Max-2100 powder X-ray diffractometer using Cu Kα radiation. The step scan covered the angular range 5-65° 2θ in steps of 0.04°. No impurities were observed and the experimental and calculated PXRD patterns are in excellent agreement (see **Figure 8.2**).

UV-Vis diffuse reflectance spectroscopy (UV/Vis).

UV-Vis diffuse reflectance spectroscopy data of ground crystals were obtained using a PerkinElmer Lambda 35 UV-Vis scanning spectrophotometer equipped with an integrating sphere over the range of 200-900 nm. Reflectance data were transformed to absorbance via the Kubelka-Munk function.[44]

Table 8.1 Crystal data and structure refinements for compound **8.1**.

	8.1
Empirical formula	$La_{20}Mo_{12}O_{63}Cl_4$
Formula weight	5079.28
Temperature	297(2) K
Wavelength	0.71073 Å
Crystal system	hexagonal
Space group	*P*-62*m*
Unit cell dimensions	a = 10.2241(2) Å b = 10.2241(2) Å c = 15.0768(4) Å α = 90° β = 90° γ = 120°
Volume	1364.87(6) $Å^3$
Z	1
Density (calculated)	6.18 mg/m^3
Absorption coefficient	18.226 mm^{-1}
F(000)	2216.0
Crystal size	0.10 × 0.06 × 0.02 mm^3
2θ range for data collected	1.35 to 35.07°
Index ranges	$-16 \le h \le 16$ $-16 \le k \le 15$ $-24 \le l \le 22$
Reflections collected	26973
Ind. reflections	2234[R(int) = 0.0555]
Data / restraints / parameters	2234 / 0 / 97
Goodness-of-fit on F^2	1.065
Final R indices [I>2sigma(I)]	R_1 = 0.0254 wR_2 = 0.0494
R indices (all data)	R_1 = 0.0303 wR_2 = 0.0509
Largest diff. peak and hole	1.86 and −1.49 $e^- \times Å^{-3}$

Table 8.2 Selected interatomic distances (Å) for compound **8.1**.

8.1			
La(1)[7]-O(1)[1,2] x 2	2.466(4)	La(4)[3,4,22]-Cl(2)[14,15] x 2	3.1775(19)
La(1)[7]-O(2)[1,2] x 2	2.514(5)	La(5)[4]-O(3)[11,12,17,19] x 4	2.808(4)
La(1)[7]-O(3)[1,2] x 3	2.514(5)	La(5)[4]-O(5)[11,17] x 2	2.475(6)
La(1)[11,16]-O(7)[3,4] x 2	2.911(4)	La(5)-O(6)[18] x 2	2.807(7)
La(1)[2,7]-Cl(1)	3.1523(19)	La(5)[3,4]-O(8)[11,16] x 2	2.490(2)
La(2)-O(2)[5,6] x 3	2.609(4)	Mo(1)[7]-O(2)[1,2] x 2	1.919(5)
La(2)-O(3)[5,6] x 3	2.669(4)	Mo(1)[4]-O(3)[11,12] x 2	1.848(4)
La(2)[18]-O(5)[5,6] x 3	2.516(4)	Mo(1)-O(7)	1.753(6)
La(3)-O(1)[5,6] x 3	2.635(5)	Mo(2)[7]-O(1)[1,2,9,20] x 4	1.927(4)
La(3)-O(2)[5,6] x 3	2.493(4)	Mo(2)[7]-O(4)[2,9] x 2	1.909(6)
La(3)[8]-O(4)[5,6] x 3	2.507(4)	Mo(3)[7]-O(5)[2,21] x 2	1.956(6)
La(4)[4]-O(1)[10-13] x 4	2.529(4)	Mo(3)-O(6)[18] x 2	1.826(6)
La(4)[7]-O(4)[2,9] x 2	2.399(6)	Mo(3)-O(8)	1.843(8)
La(4)-O(7)[8] x 2	2.721(7)		

[1] Y, X, Z [2] −X+Y, −X, Z [3] −Y, X−Y−1, Z [4] −X+Y+1, −X+1, Z
[5] −X+Y, −X+1, Z [6] −Y+1, X−Y+1, Z [7] −Y, X−Y, Z [8] X, Y, −Z+1
[9] Y, X, −Z+1 [10] −X+1, −X+Y, −Z+1 [11] −Y+1, X−Y, Z [12] −X+1, −X+Y, Z
[13] −Y+1, X−Y, −Z+1 [14] X+1, Y, −Z+1 [15] X+1, Y, Z [16] −X+Y+1, −X, Z
[17] −X+1, −X+Y, −Z [18] X, Y, −Z [19] -Y+1, X−Y, −Z [20] -X+Y, −X, −Z+1
[21] Y, X, −Z [22] X−1, Y, Z

Table 8.3 Atomic coordinates ($\times 10^4$) and equivalent isotropic displacement parameters ($Å^2 \times 10^3$) for compound **8.1**. $U_{(eq)}$ is defined as one third of the trace of the orthogonalized U_{ij} tensor.

8.1				
Atom	*x*	*y*	*z*	U(eq)
La(1)	0.2753(1)	0	0.2731(1)	10(1)
La(2)	⅓	⅔	0.1269(1)	10(1)
La(3)	⅓	⅔	0.3808(1)	8(1)
La(4)	0.7290(1)	0	½	9(1)
La(5)	0.7298(1)	0	0	16(1)
Mo(1)	0.6189(1)	0	0.2270(1)	8(1)
Mo(2)	0.3841(1)	0	½	7(1)
Mo(3)	0.3829(1)	0	0	7(1)
Cl(1)	0	0	0.1790(3)	18(1)
Cl(2)	0	0	0.3968(2)	17(1)
O(1)	0.1368(5)	0.3809(5)	0.4133(3)	10(1)
O(2)	0.1436(5)	0.5582(5)	0.2590(2)	10(1)
O(3)	0.2240(5)	0.3745(5)	0.1627(3)	13(1)
O(4)	0.1384(6)	0.5965(6)	½	10(1)
O(5)	0.2207(7)	0.4837(7)	0	12(1)
O(6)	0.4937(7)	0	0.0950(4)	14(1)
O(7)	0.7227(6)	0	0.3196(4)	14(1)
O(8)	0.2026(8)	0	0	13(2)

Magnetic Susceptibility.

The magnetic susceptibility was measured using a Quantum Design MPMS 3 SQUID magnetometer. The zero-field cooled magnetic susceptibility was measured as a function of temperature between 2-300K in an applied field of 1000 Oe. The measured magnetic data were corrected for shape and radial offset effects using the method reported by Morrison et al.[45]

Second Harmonic Generation (SHG).

Powder SHG measurements were performed on a modified Kurtz nonlinear-optical (NLO) system using a pulsed Nd:YAG laser with a wavelength of 1064 nm. A comparison with a known SHG material was made using ground crystalline α-SiO_2. A detailed description of the equipment and methodology has been published elsewhere.[46, 47]

Results and discussion

Synthesis.

Crystals of **8.1** were grown out of a eutectic alkali metal chloride flux, which are known to be redox stable solvents suitable for the crystal growth of reduced oxides. In this work a CsCl/LiCl eutectic flux was used because of its low melting point, the long liquid range over the reaction conditions, and the low probability of incorporating either alkali metal into the product. Excluding potentially oxidizing species, such as water or oxygen, from the reaction is crucial to promote a reducing environment. For this reason the reaction was performed in an evacuated sealed fused silica tube. The hygroscopic chlorides were dried to remove water and were added to the tube immediately before sealing to minimize exposure to moisture in the atmosphere. Since lanthanum oxide is

known to absorb carbon dioxide from air at room temperature to form lanthanum carbonate, which would decompose under the reaction conditions and generate significant and unsafe pressure within the tube, the La_2O_3 was pre-fired to 1000°C overnight to ensure that only the oxide was present. At 800°C all the reactants are in solution, except for the Mo powder, which creates the reducing environment that favors the reduction of Mo(VI) to Mo(V) at the solid/liquid interface between dissolved Mo(VI) ions and Mo powder. The Mo(V) and Mo(VI) species present in solution combine with the lanthanum and chloride ions in solution during the slow cooling process to create plate crystals of **8.1** as the sole product. The PXRD pattern of the ground crystals, shown in **Figure 8.2**, is in excellent agreement with the powder pattern calculated from single crystal data, confirming phase purity of the sample. Attempts to crystallize compositions containing other rare earth elements have been unsuccessful so far. Considering that lanthanum is noticeably larger than the next smaller lanthanides it is not unreasonable to assume that the inability to crystallize products containing the smaller lanthanides is due to size effects.

Structure.

Compound **8.1** represents a new structure type exhibiting a three-dimensional crystal structure containing three different molybdenum coordination environments, MoO_5 square pyramids, MoO_6 trigonal prisms, and MoO_5 trigonal bipyramids, that are connected via edge and corner sharing lanthanum polyhedra to generate the overall structure. Molybdenum in the structure segregates into two-dimensional sheets in the *ab* plane as a function of coordination environment, with MoO_5 square pyramids, MoO_6

trigonal prisms, and MoO_5 trigonal bipyramids each forming unique sheets that stack in an ABCB fashion along the *c* axis, as shown in **Figure 8.3**.

La(1) is located in a nine coordinate LaO_8Cl irregular polyhedron, shown in **Figure 8.4**, with La–O distances ranging from 2.466 Å to 2.911 Å and a La–Cl distance of 3.1523(19) Å. La(1) shares edges with La(2) through O(2) and O(3); La(3) through O(1) and O(2); La(4) through O(1) and O(7); Mo(1) through O(2), O(3), and O(7); Mo(2) through O(1); and itself through O(7) and Cl(1). La(1) also shares a corner with La(5) through O(3). La(2) is located in a nine coordinate LaO_9 irregular polyhedron, shown in **Figure 8.4**, with La–O distances ranging from 2.516 Å – 2.991 Å. La(2) shares faces with La(3) and with itself through O(2) and O(5), respectively, forming one-dimensional infinite chains, shown in **Figure 8.5**. La(2) shares edges with La(1) through O(2) and O(3), La(5) through O(3) and O(5), and Mo(1) through O(2) and O(3). La(2) also shares a corner with Mo(3) through O(5). La(3) is located in a nine coordinate LaO_9 irregular polyhedron, shown in **Figure 8.4**, with La–O distances between 2.493 Å – 2.635 Å. La(3) shares faces with La(2) and with itself through O(2) and O(4). La(3) shares edges with La(1) through O(1) and O(2), La(4) through O(1) and O(4), and Mo(2) through O(1) and O(4). La(3) also shares a corner with Mo(1) through O(2). La(4) is located in a ten coordinate LaO_8Cl_2 irregular polyhedron, shown in 8.1 3, with La–O distances between 2.399 Å – 2.721 Å and a La–Cl distance of 3.1775(19) Å. La(4) shares edges with La(1) through O(1) and O(7), La(3) through O(1) and O(4), and Mo(2) through O(1) and O(4). La(4) also shares a corner with Mo(1) through O(7). La(5) is located in a ten coordinate LaO_{10} irregular polyhedron, shown in **Figure 8.4**, with La–O distances between 2.475 Å – 2.808 Å. La(5) shares edges with La(2) through O(3) and O(5), Mo(1) through O(3),

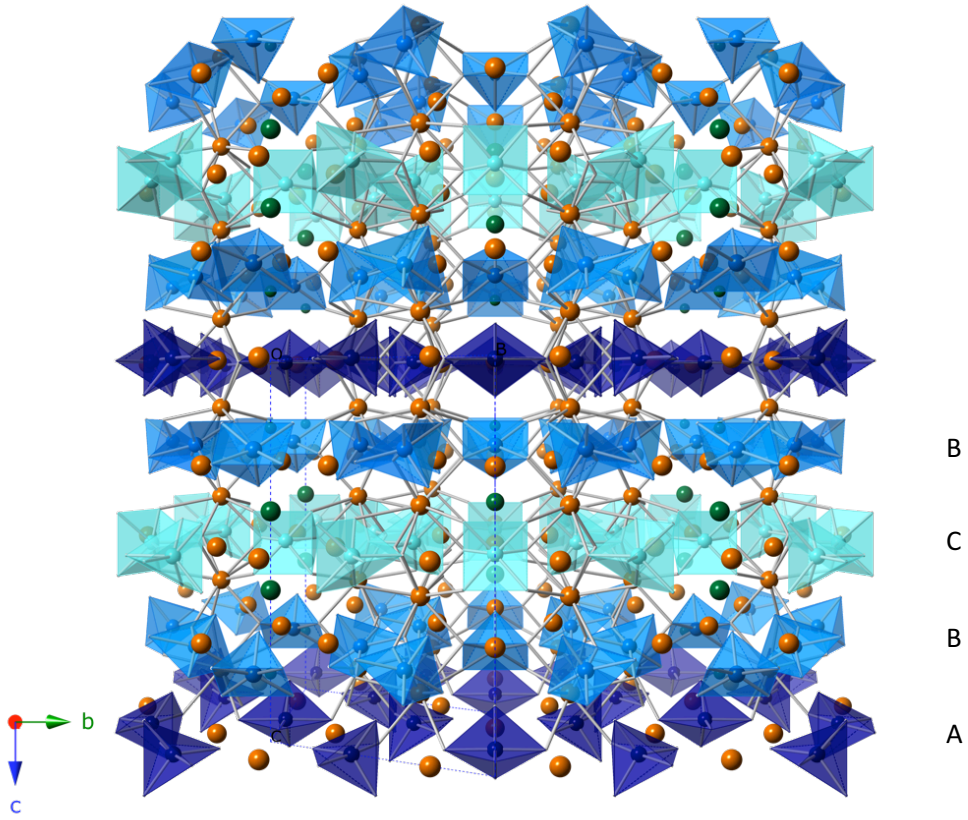

Figure 8.3 Compound **8.1** viewed down the *a* axis. Mo1, Mo2, Mo3, La, and Cl shown in aqua, cyan, navy, orange, and green, respectively. Oxygen atoms, La–Cl bonds, and select La–O bonds are omitted for clarity.

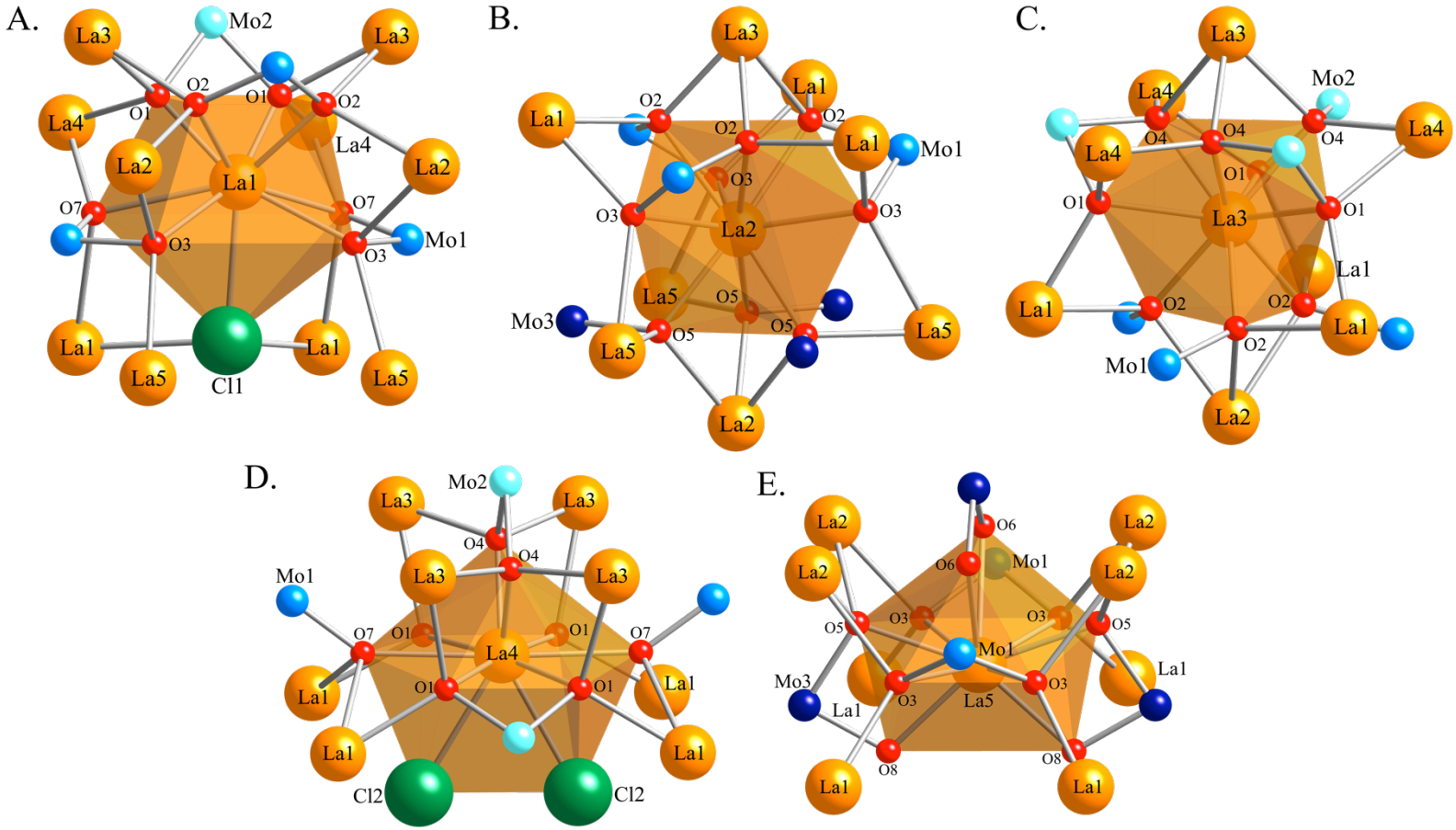

Figure 8.4 Local coordination environments of La1 – La5. La, Mo1, Mo2, Mo3, O, and Cl shown in orange, aqua, cyan, navy, red, and green, respectively. Symmetry equivalent La, O, and Cl labeled for clarity.

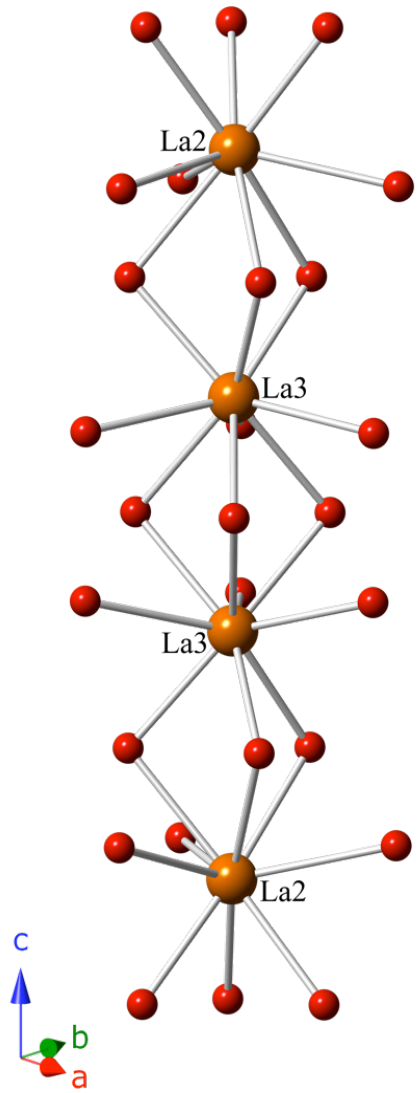

Figure 8.5 1D chains of face sharing La2 and La3 shown about the *c* axis. La and O shown in orange and red, respectively.

and Mo(3) through O(5), O(8), and O(6). La(5) also shares a corner with La(1) through O(3). Mo(1) is located in a five coordinate square pyramid, shown in **Figure 8.6**, with Mo–O distances ranging from 1.753 to 1.919 Å. These distances are consistent with other reported compounds containing square pyramidal molybdenum.[48-51] Mo(1) shares edges with La(1) through O(3), O(7), and O(2) and La(2) through O(2) and O(3). Mo(1) also shares corners with La(4) through O(7) and La(3) through O(2). Mo(2) is located in an unusual six coordinate trigonal prism, shown in **Figure 8.6**, with Mo–O distances of 1.909 Å – 1.927 Å. Few examples of trigonal prismatic molybdenum exist in the literature, where it is usually coordinated to sulfur as in MoS_2[52], coordinated to sulfur or nitrogen containing organic ligands,[53-57], or coordinated to oxygen containing organic ligands.[58, 59] The Mo–O distances in our compound are somewhat shorter than those found in other compounds containing MoO_6 trigonal prismatic coordination environments. This is likely because the trigonal prism in our compound is highly regular while known molecular compounds contain highly distorted MoO_6 trigonal prisms. To the best of our knowledge this represents the first example of an MoO_6 trigonal prism found in a three-dimensional extended structure. Mo(2) shares edges with La(1) through O(1), La(3) through O(1) and O(4), and La(4) through O(1) and O(4). Mo(3) is located in a five coordinate trigonal bipyramid, shown in **Figure 8.6**, with Mo–O distances of 1.826 Å – 1.956 Å. These distances are consistent with several known mixed valent compounds containing similar coordination environments.[51, 60, 61] Mo(3) shares edges with La(5) through O(5), O(6), and O(8). La(5) also shares a corner with La(2) through O(5). Given site multiplicities for Mo(1), Mo(2), and Mo(3) of 6, 3, and 3, no one site can be

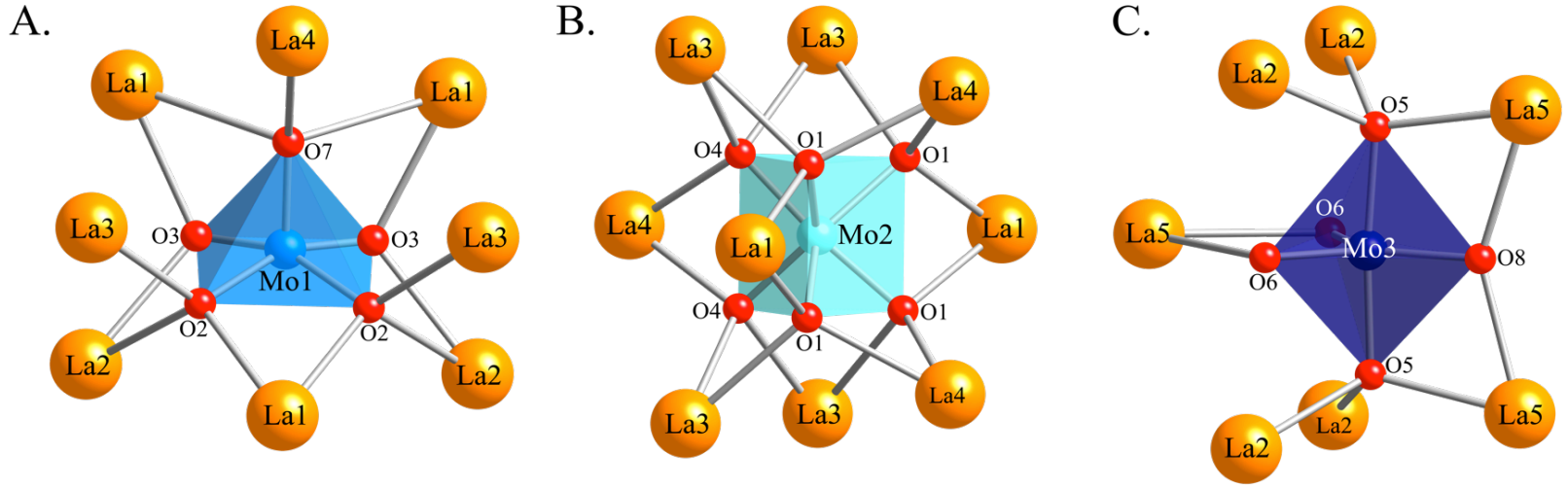

Figure 8.6. Local coordination environments of Mo1, Mo2, and Mo3. Mo1, Mo2, Mo3, La, and O shown in aqua, cyan, navy, orange, and red, respectively.

exclusively occupied by Mo(V) to satisfy charge neutrality, indicating at least one mixed valent Mo(V/VI) site. Bond valence analysis of each Mo site reveals Mo(1) = 5.79, Mo(2) = 5.77, and Mo(3) = 5.43 when all Mo is considered to be 6+ and Mo(1) = 5.36, Mo(2) = 5.34, and Mo(3) = 5.02 when all Mo is considered to be 5+. From this data we can reasonably conclude that the largest share of Mo(V) is located on Mo(3) and the largest shares of Mo(VI) are located on Mo(1) and Mo(2). Along the *c* axis La(1), La(4), La(5), Mo(1), Mo(2), and Mo(3) form chains shown in **Figure 8.7**. Mo(1), Mo(2), and Mo(3) form two-dimensional sheets in the *ab* plane and are shown in **Figures 8.8 – 8.10**.

UV-vis diffuse reflectance spectroscopy (UV/Vis).

UV-Vis absorbance data shown in **Figure 8.11** were collected using ground crystals. The absorption edge is clearly observed in the visible region, and the band gap estimated by the onset of the absorption edge is approximately 2.4 eV, indicating likely semiconducting behavior for the oxychloride. A broad absorbance ranging from 900 nm to 550 nm is observed, with a maximum at 551 nm and is consistent with the presence of Mo(V) cations in the structure, based on reports in the literature describing the UV-Vis absorption data collected on mixed Mo(VI)/Mo(V) containing compounds.[62, 63]

Magnetic Susceptibility.

The mixed valent **8.1** contains Mo(V) d^1 species that give rise to paramagnetic behavior. Measurements of the temperature dependence of the magnetic susceptibility of **8.1** measured in an applied field of 1000 Oe, shown in **Figure 8.12**, are consistent with simple paramagnetic behavior. This is not unexpected since the Mo(V) centers are isolated from each other. In **8.1** the amount of Mo(V) is around 17% and is therefore magnetically dilute, thus no magnetic coupling is expected or observed. Down to 2K, the

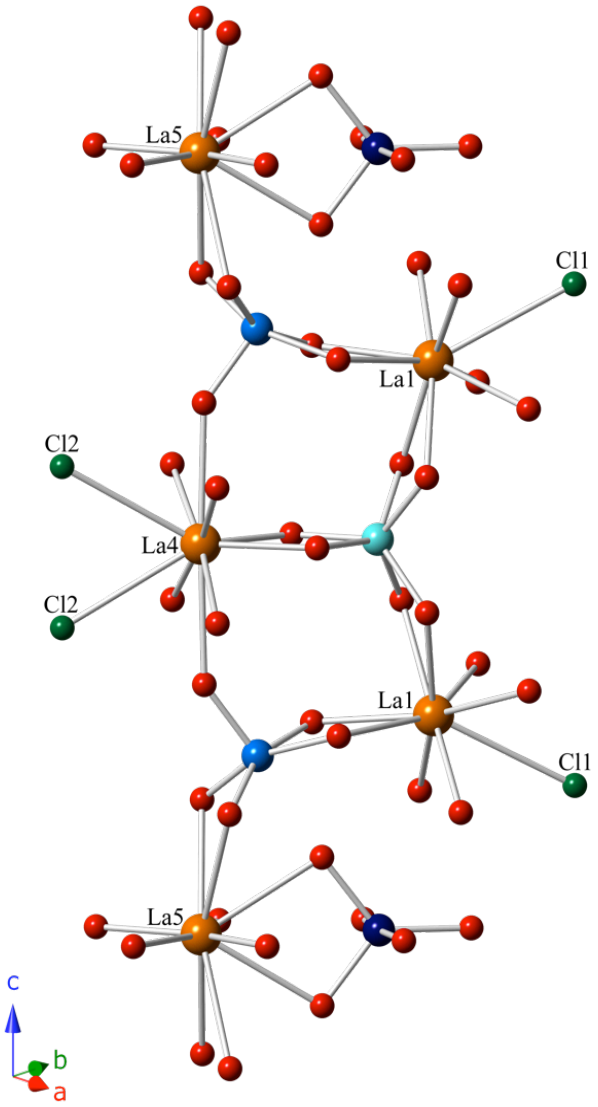

Figure 8.7 Connectivity of La1, La4, La5, Mo1, Mo2, and Mo3 shown about the *c* axis. La, Mo1, Mo2. Mo3, Cl, and O shown in orange, aqua, cyan, navy, green, and red, respectively.

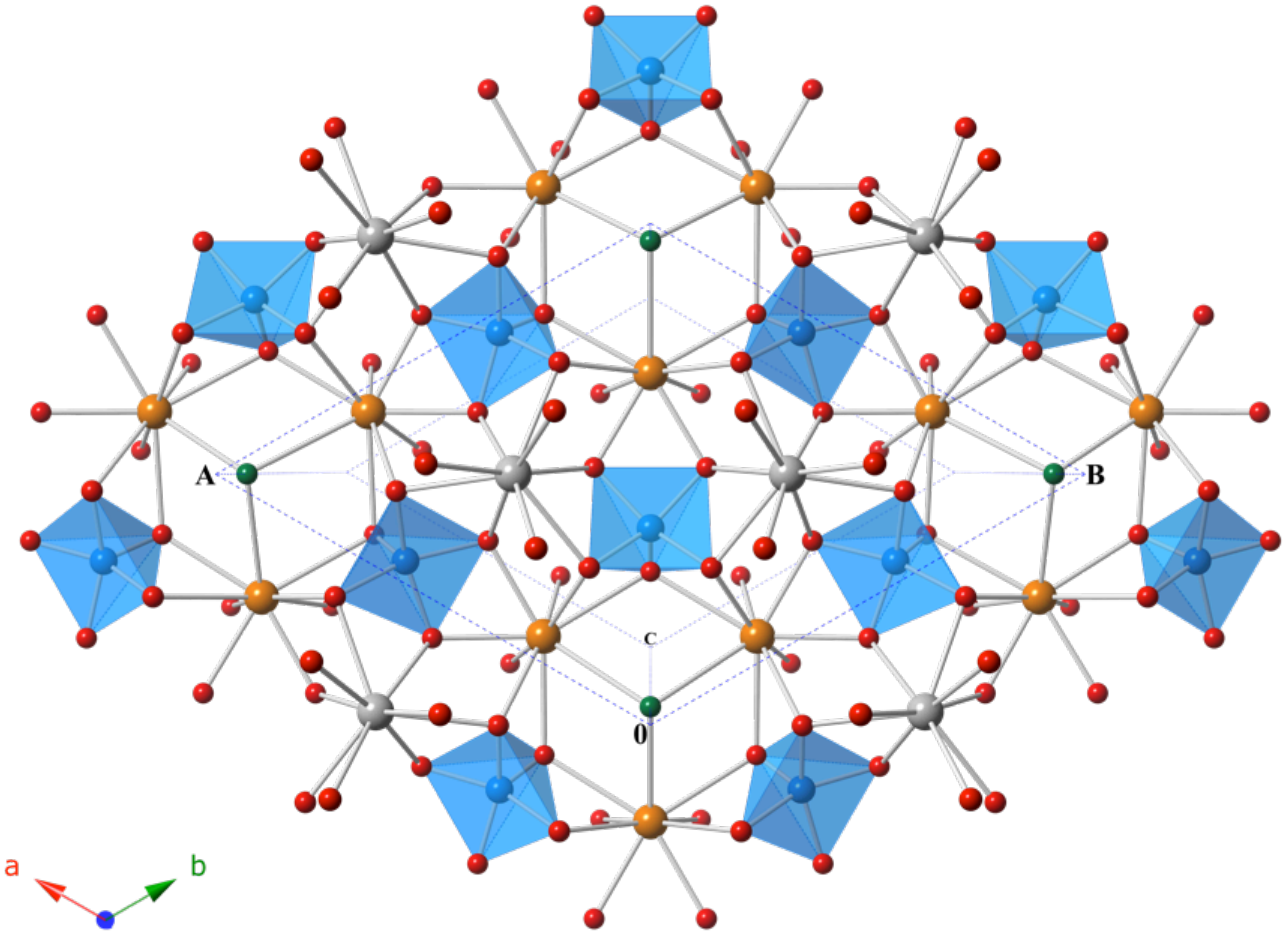

Figure 8.8 2D sheet containing Mo1 square pyramids viewed down the *c* axis. La1, La2, Mo1, Cl and O shown in orange, grey, aqua, green, and red, respectively.

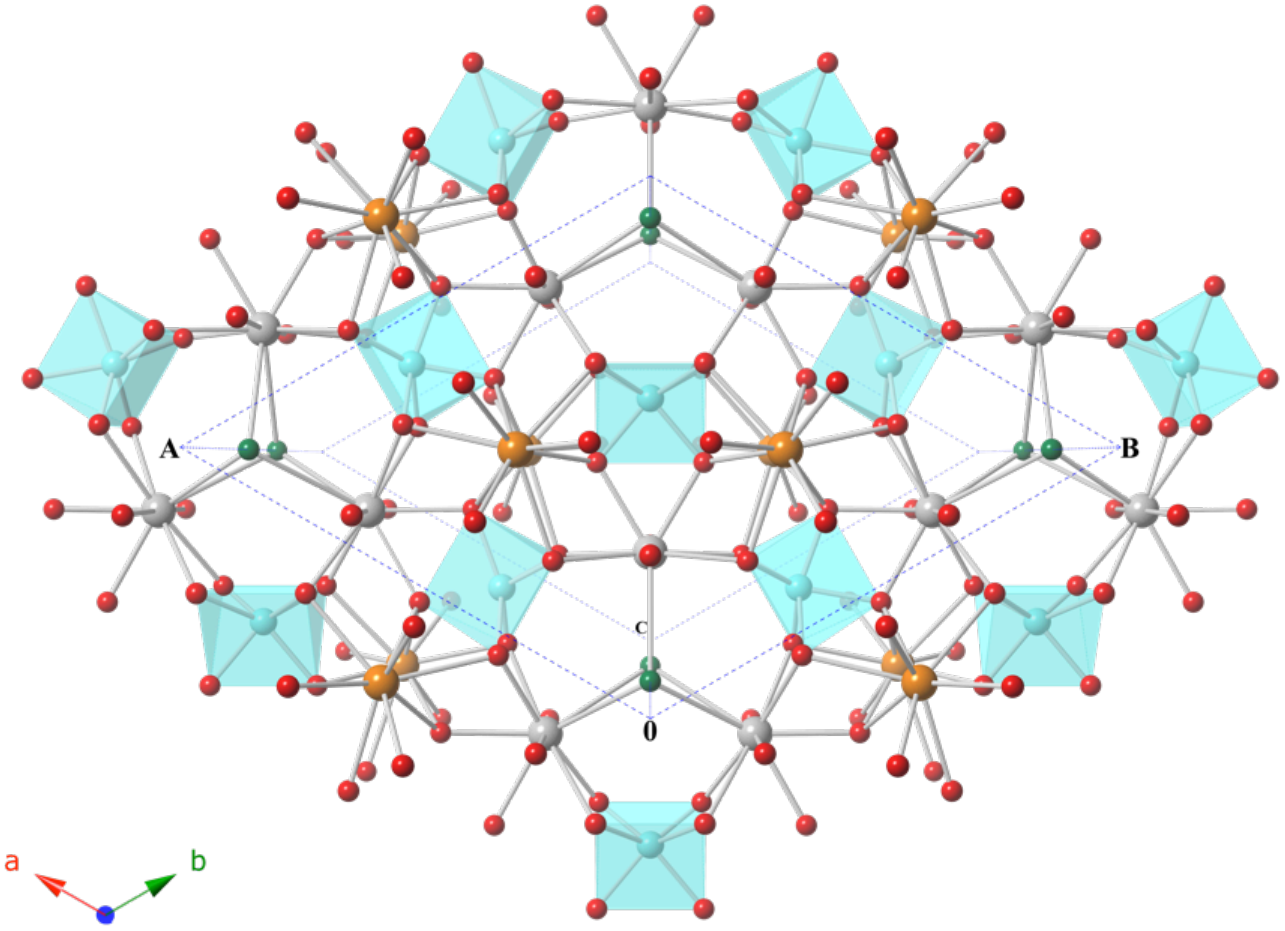

Figure 8.9 2D sheet containing Mo2 trigonal prisms viewed down the *c* axis. La3, La4, Mo2, Cl, and O shown in orange, grey, cyan, green, and red, respectively.

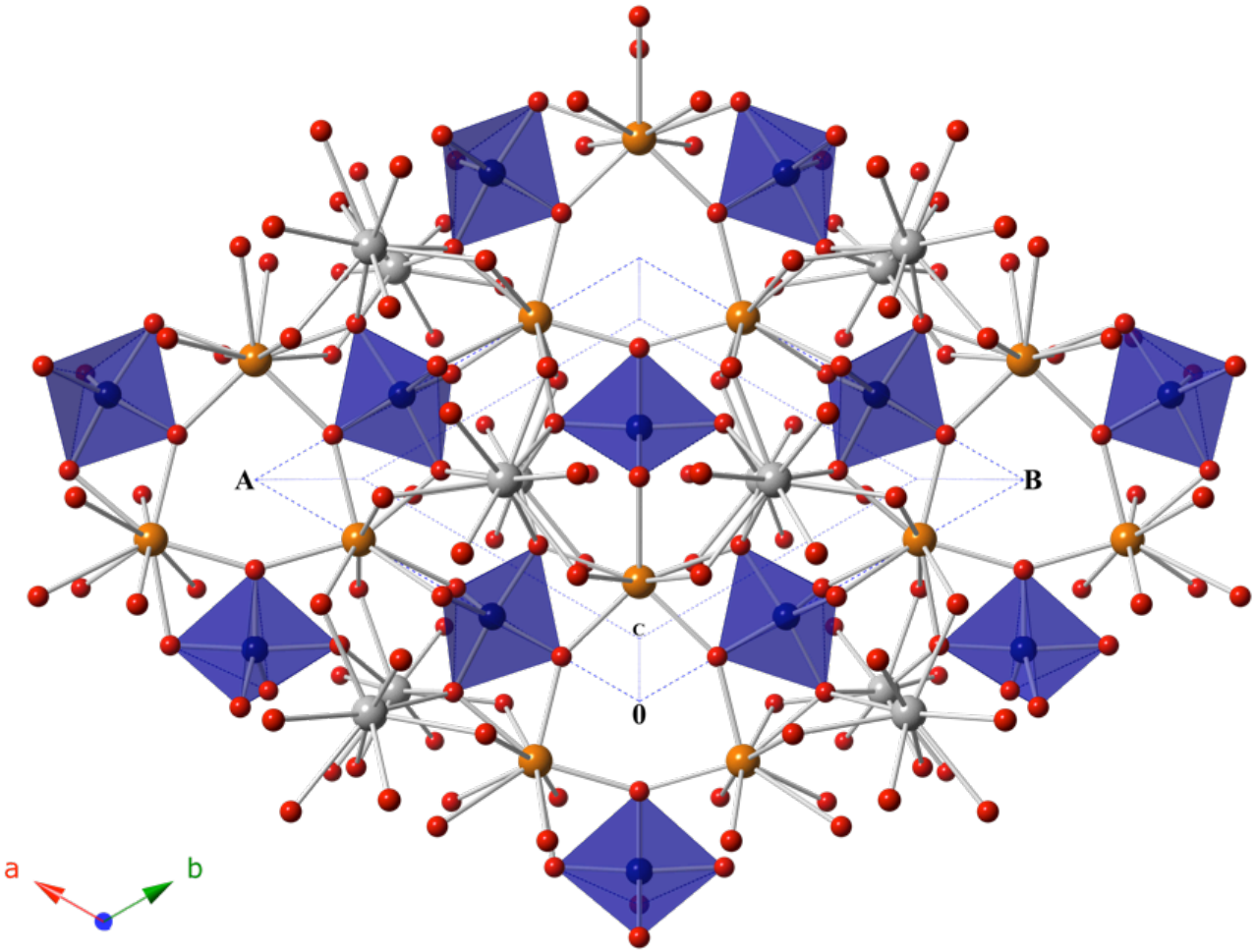

Figure 8.10 2D sheet containing Mo3 trigonal bipyramids viewed down the *c* axis. La2, La5, Mo3, and O shown in grey, orange, navy, and red, respectively.

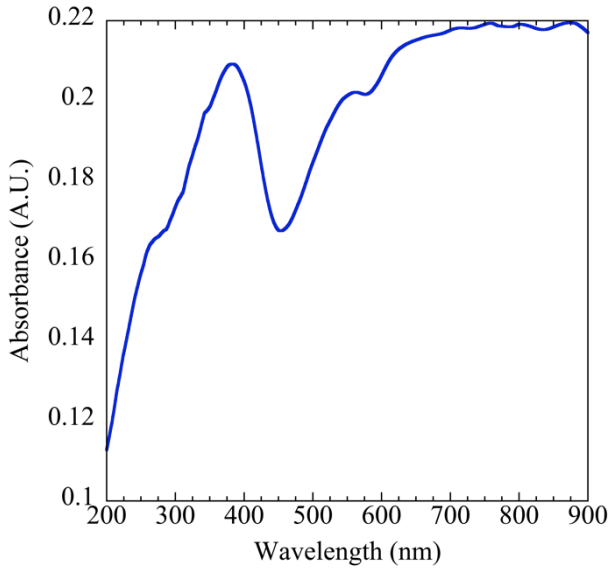

Figure 8.11 UV/Vis absorbance spectrum for compound **8.1**.

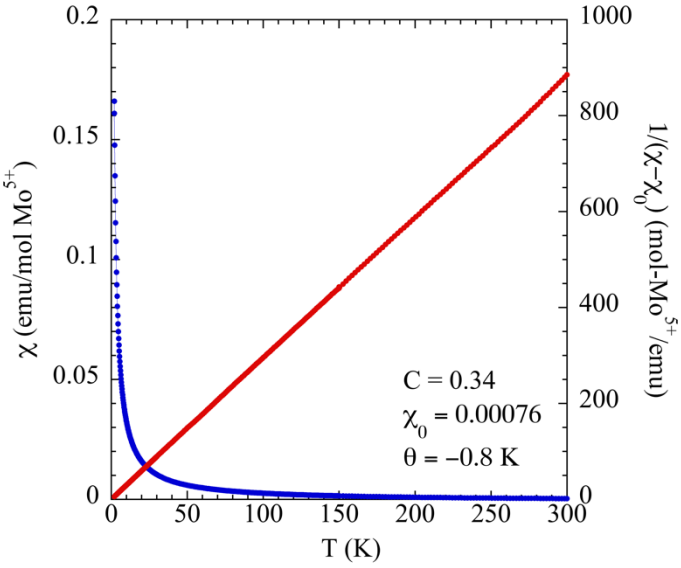

Figure 8.12 Magnetic susceptibility plot for compound **8.1**. χ and $1/\chi - \chi_o$ are shown in blue and red, respectively.

data do not reveal any long range magnetic order and follow the Curie-Weiss (C-W) law as expected for simple paramagnetic species. The magnetic moment calculated from the inverse susceptibilities is 1.68 μ_B/mol Mo(V), which is in good agreement with the expected spin only value for **8.1** of 1.73μ_B/mol Mo(V).[64]

Second Harmonic Generation (SHG).

Although **8.1** crystallizes in the noncentrosymmetric space group *P*-62*m*, no detectable SHG response was observed when measuring a ground polycrystalline sample. Given the roughly spherical geometry of the lanthanum coordination environments, the system does not have a large dipole moment and, as a consequence, does not efficiently generate an SHG response. It is known that compounds with large dipole moments typically exhibit large SHG responses.[22]

Conclusion

We successfully synthesized the new lanthanum molybdenum oxychloride $La_{20}Mo_{12}O_{63}Cl_4$ via a molten salt flux technique. The oxychloride exhibits a new structure type that was determined by single crystal X-ray diffraction. By utilizing a redox stable flux and Mo powder, we were able to reduce a fraction of the Mo(VI) in the reaction mixture to Mo(V). The average molybdenum oxidation state is +5.83 with a Mo(V) content of 16.67%. As a result of the magnetically dilute Mo(V) in the compound, only simple paramagnetic behavior is observed. The agreement of the experimental and theoretical magnetic moments confirms the presence and quantity of Mo(V) in the structure. The structure, while noncentrosymmetric, does not give rise to SHG behavior.

Acknowledgement

Financial support for this work was provided by the National Science Foundation under

DMR-1301757 and is gratefully acknowledged. Powder SHG measurements were performed at the University of Houston by T. Thao Tran of the P. Shiv Halasyamani Group and are gratefully acknowledged.

References

(1) G. Andersson. Acta. Chem. Scand. 8 (1954) 1599-1606.

(2) M. Pouchard; J. C. Launay. Mater. Res. Bull. 8 (1973) 95-104.

(3) S. Westman; C. Nordmark. Acta Chem. Scand. 14 (1960) 465-470.

(4) F. J. Morin. Bell Syst. Tech. J. 37 (1958) 1047-1084.

(5) L. L. Van Zandt; J. M. Honig; J. B. Goodenough. J. Appl. Phys. 39 (1968) 594-595.

(6) B. Hessen; S. A. Sunshine; T. Siegrist; R. Jimenez. Mater. Res. Bull. 26 (1991) 85-90.

(7) D. Ridgley; R. Ward. J. Am. Chem. Soc. 77 (23) (1955) 6132-6136.

(8) P. P. Tsai; J. A. Potenza; M. Greenblatt. J. Solid State Chem. 69 (2) (1987) 329-335.

(9) M. Greenblatt. Chem. Rev. 88 (1) (1988) 31-53.

(10) M. Greenblatt. Physics and Chemistry of Materials with Low-Dimensional Structures. 11 (1989) 1-48.

(11) C. R. Feger; R. P. Ziebarth. Chem. Mater. 7 (2) (1995) 373-378.

(12) B. Hessen; S. A. Sunshine; T. Siegrist; A. T. Fiory; J. V. Waszczak. Chem. Mater. 3 (3) (1991) 528-534.

(13) Y. Oka; T. Yao; N. Yamamoto; M. Ueda; S. Maegawa. J. Solid State Chem. 149 (2) (2000) 414-418.

(14) D. L. Serra; S.-J. Hwu. J. Solid State Chem. 101 (1) (1992) 32-40.

(15) S. C. Chen; B. Wang; M. Greenblatt. Inorg. Chem. 32 (20) (1993) 4306-4310.

(16) D. Abeysinghe; M. D. Smith; J. Yeon; G. Morrison; H.-C. zur Loye. Cryst. Growth Des. 14 (9) (2014) 4749-4758.

(17) D. E. Bugaris; H.-C. zur Loye. Angew. Chem. Int. Ed. 51 (16) (2012) 3780-3811.

(18) A. J. Cortese; B. Wilkins; M. D. Smith; J. Yeon; G. Morrison; T. T. Tran; P. S. Halasyamani; H.-C. zur Loye. Inorg. Chem. 54 (8) (2015) 4011-4020.

(19) J. Yeon; M. D. Smith; A. S. Sefat; H.-C. zur Loye. Inorg. Chem. 52 (4) (2013) 2199-2207.

(20) J. Yeon; M. D. Smith; A. S. Sefat; T. T. Tran; P. S. Halasyamani; H.-C. zur Loye. Inorg. Chem. 52 (15) (2013) 8303-8305.

(21) J. Yeon; M. D. Smith; J. Tapp; A. Moller; H.-C. zur Loye. J. Am. Chem. Soc. 136 (10) (2014) 3955-3963.

(22) J. Yeon; A. S. Sefat; T. T. Tran; P. S. Halasyamani; H.-C. zur Loye. Inorg. Chem. 52 (10) (2013) 6179-6186.

(23) D. Abeysinghe; B. Gerke; G. Morrison; C. H. Hsieh; M. D. Smith; R. Pöttgen; T. M. Makris; H.-C. zur Loye. J. Sol. State Chem. 229 (2015) 173-180.

(24) Elwell, D.; Scheel, H. J. *Crystal Growth from High Temperature Solutions*; 2011.

(25) S. J. Clarke; A. J. Fowkes; A. Harrison; R. M. Ibberson; M. J. Rosseinsky. Chem. Mater. 10 (1) (1998) 372-384.

(26) O. G. D'yachenko; S. Y. Istomin; A. M. Abakumov; E. V. Antipov. Inorg. Mater. 36 (3) (2000) 247-259.

(27) M. J. Geselbracht; L. D. Noailles; L. T. Ngo; J. H. Pikul. Chem. Mater. 16 (6) (2004) 1153-1159.

(28) S. Y. Istomin; G. Svensson; O. G. D'yachenko; W. Holm; E. V. Antipov. J. Sol. State Chem. 141 (2) (1998) 514-521.

(29) P. Mahjoor; S. E. Latturner. Inorg. Chem. 49 (10) (2010) 4486-4490.

(30) T. Siegrist; R. J. Cava; J. J. Krajewski. Mater. Res. Bull. 32 (7) (1997) 881-887.

(31) I. Hartenbach; T. Schleid; S. Strobel; P. K. Dorhout. Z. Anorg. Allg. Chem. 636 (7) (2010) 1183-1189.

(32) I. Hartenbach; S. Strobel; T. Schleid; K. W. Krämer; P. K. Dorhout. Z. Anorg. Allg. Chem. 635 (6-7) (2009) 966-975.

(33) SMART Version 5.631, SAINT+ Version 6.45 and SADABS Version 2.10. Bruker Analytical X-ray Systems, Inc., Madison, Wisconsin, USA, 2003.

(34) G. M. Sheldrick. Acta Crystallogr. A. 64 (2008) 112-122.

(35) C. B. Hübschle; G. M. Sheldrick; B. Dittrich. J. Appl. Crystallogr. 44 (Pt 6) (2011) 1281-1284.

(36) Y. Le Page. J. Appl. Crystallogr. 20 (3) (1987) 264-269.

(37) A. L. Spek. J. Appl. Crystallogr. 21 (5) (1988) 578-579.

(38) A. L. Spek. Acta. Crystallogr. Sect. A. 46 (C34) (1990).

(39) PLATON, A Multipurpose Crystallographic Tool, Utrecht University, Utrecht, The Netherlands, Spek A. L. 1998.

(40) S. Parsons; H. Flack; T. Wagner. Acta. Cryst. B69 (2013) 249-259.

(41) L. M. Gelato; E. Parthé. J. Appl. Crystallogr. 20 (1987) 139-143.

(42) S. Z. Hu; E. Parthe. Chin. J. Struct. Chem. 23 (2004) 1150-1160.

(43) E. Parthé; L. M. Gelato. Acta Crystallogr. A40 (1984) 169-183.

(44) P. Kubelka; F. Munk. Zeit. Für Tekn. Physik. 12 (1931) 593.

(45) G. Morrison; H.-C. zur Loye. J. Solid State Chem. 221 (0) (2015) 334-337.

(46) S. K. Kurtz; T. T. Perry. Journal of Applied Physics. 39 (8) (1968) 3798-3813.

(47) K. M. Ok; E. O. Chi; P. S. Halasyamani. Chemical Society Reviews. 35 (8) (2006) 710-717.

(48) E. Burkholder; A. N. Gabriel; V. Golub; C. J. O'Connor; J. A. Zubieta. J. Sol. State Chem. 178 (10) (2005) 3145-3151.

(49) B. M. Gatehouse; P. Leverett. J. Chem. Soc. A. (1968) 1398-1405.

(50) B. M. Gatehouse; C. E. Jenkins; B. K. Miskin. J. Sol. State Chem. 46 (3) (1983) 269-274.

(51) T. Hoareau; A. Leclaire; M. M. Borel; A. Grandin; B. Raveau. J. Sol. State Chem. 116 (1) (1995) 87-91.

(52) R. G. Dickinson; L. Pauling. J. Am. Chem. Soc. 45 (6) (1923) 1466-1471.

(53) D. Argyropoulos; C.-A. Mitsopoulou; D. Katakis. Inorg. Chem. 35 (19) (1996) 5549-5554.

(54) A. Cervilla; E. Llopis; A. Domenech; A. Ribera; P. Palanca; P. Gomez-Romero. Dalton Trans. 6 (1992) 1005-1008.

(55) J. R. Dilworth; J. Hyde; P. Lyford; P. Vella; K. Venkatasubramaman; J. A. Zubieta. Inorg. Chem. 18 (2) (1979) 268-274.

(56) R. F. Lang; T. D. Ju; J. C. Bryan; G. J. Kubas; C. D. Hoff. Inorg. Chim. Acta. 348 (2003) 157-164.

(57) D. Sengupta; S. Gangopadhyay; M. G. B. Drew; P. K. Gangopadhyay. Dalton Trans. 44 (3) (2015) 1323-1331.

(58) C.-M. Liu; E. Nordlander. Inorg. Chem. 43 (6) (2004) 2114-2124.

(59) C. G. Pierpont; R. M. Buchanan. J. Am. Chem. Soc. 97 (17) (1975) 4912-4917.

(60) A. Guesdon; M. M. Borel; A. Leclaire; A. Grandin; B. Raveau. J. Sol. State Chem. 109 (1) (1994) 145-151.

(61) I. Hartenbach; H. Henning; T. Schleid; T. Schustereit; S. Strobel. Z. Anorg. Allg. Chem. 639 (2) (2013) 347-353.

(62) B. Botar; A. Ellern; P. Kogerler. Dalton Trans. 41 (29) (2012) 8951-8959.

(63) R. A. Isovitsch; J. G. May; F. R. Fronczek; A. W. Maverick. Polyhedron 19 (12) (2000) 1437-1446.

(64) Blundell, S. *Magnetism in Condensed Matter*; 2001.

APPENDIX A

POLYPYRIDYL LANTHANIDE HALIDE CHELATES

A.1 $Pr_2Cl_6(phen)_4$

Crystals of compound **A.1** were grown solvothermally from supersaturated solutions of $PrCl_3$ in ethanol (EtOH) and 1,10-phenanthroline (phen). 0.5 mmol of $PrCl_3$ was placed into a nitrogen-purged septa sealed round bottom flask. 30mL of EtOH was then transferred via a nitrogen-purged syringe into the flask. The resulting solution was then transferred via syringe into a high-pressure glass tube containing 1 mmol of phen. The high-pressure vessel was sealed quickly with a Teflon cap to minimize exposure to the atmosphere, as $PrCl_3$ is extremely hygroscopic. The vessel was placed into a programmable oven which was ramped at 1 °C per minute to 180 °C, allowed to dwell for 48 hours, then allowed to cool at 0.1 °C per minute to room temperature.

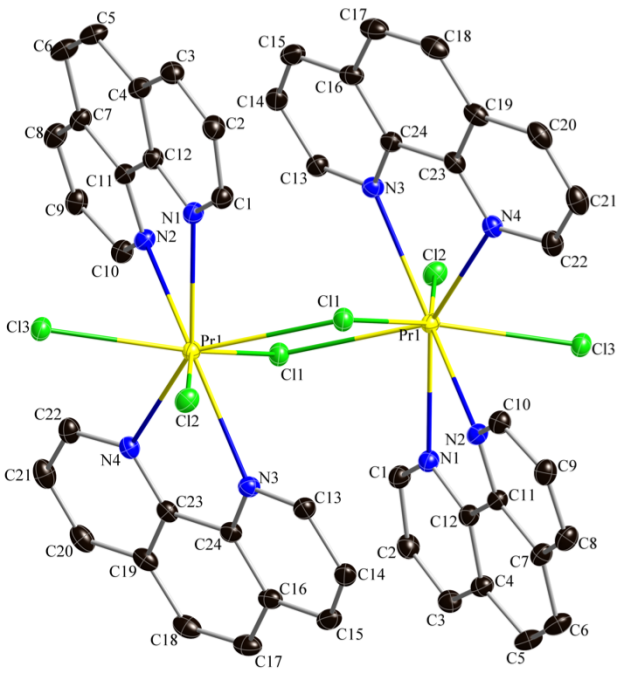

Displacement ellipsoid plot. Molecule on inversion center. Displacement ellipsoids drawn at the 50% probability level.

Crystal data and structure refinements for compound **A.1**.

	A.1
Empirical formula	$C_{48}H_{32}Cl_6N_8Pr_2$
Formula weight	1215.34
Temperature	100(2)
Wavelength	0.71073 Å
Crystal system	triclinic
Space group	*P*-1
Unit cell dimensions	a = 9.8700(4) b = 10.8789(4) c = 11.9578(5) α = 83.6570(10) β = 76.7750(10) γ = 64.5190(10)
Volume	1128.23(8)
Z	1
Density (calculated)	1.789
Absorption coefficient	2.535
F(000)	596.0
Crystal size	0.26 × 0.24 × 0.20
2θ range for data collected	3.5 to 60.1°
Index ranges	$-13 \le h \le 13$ $-15 \le k \le 15$ $-16 \le l \le 36$
Reflections collected	23469
Ind. reflections	6588[R(int) = 0.0210]
Data / restraints / parameters	6588/0/289
Goodness-of-fit on F^2	1.058
Final R indices [I>2sigma(I)]	R_1 = 0.0205 wR_2 = 0.0517
R indices (all data)	R_1 = 0.0211 wR_2 = 0.0521
Largest diff. peak and hole	1.44 and −0.52 $e^- \times Å^{-3}$

A.2 $La_2Cl_6(phen)_4$

Crystals of compound **A.2** were grown solvothermally from supersaturated solutions of $LaCl_3$ in ethanol (EtOH) and 1,10-phenanthroline (phen). 0.5 mmol of $LaCl_3$ was placed into a nitrogen-purged septa sealed round bottom flask. 30mL of EtOH was then transferred via a nitrogen-purged syringe into the flask. The resulting solution was then transferred via syringe into a high-pressure glass tube containing 1 mmol of phen. The high-pressure vessel was sealed quickly with a Teflon cap to minimize exposure to the atmosphere, as $LaCl_3$ is extremely hygroscopic. The vessel was placed into a programmable oven which was ramped at 1 °C per minute to 180 °C, allowed to dwell for 48 hours, then allowed to cool at 0.1 °C per minute to room temperature.

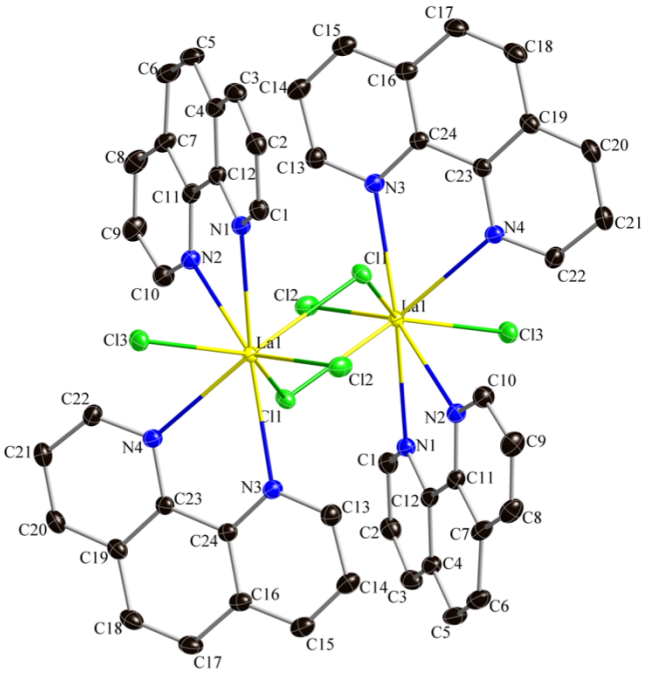

Displacement ellipsoid plot. Molecule on inversion center. Displacement ellipsoids drawn at the 50% probability level.

Crystal data and structure refinements for compound **A.2**.

	A.2
Empirical formula	$C_{48}H_{32}Cl_6N_8La_2$
Formula weight	1211.34
Temperature	100(2)
Wavelength	0.71073 Å
Crystal system	monoclinic
Space group	$P2_1/n$
Unit cell dimensions	$a = 12.0341(7)$
	$b = 14.1904(8)$
	$c = 13.4620(8)$
	$\alpha = 90.00$
	$\beta = 107.5340(10)$
	$\gamma = 90.00$
Volume	2192.1(2)
Z	2
Density (calculated)	1.835
Absorption coefficient	2.335
F(000)	1184.0
Crystal size	0.42 × 0.36 × 0.34
2θ range for data collected	3.98 to 60.22°
Index ranges	$-16 \le h \le 16$
	$-20 \le k \le 20$
	$-18 \le l \le 19$
Reflections collected	41837
Ind. reflections	6440[R(int) = 0.0292]
Data / restraints / parameters	6440/0/289
Goodness-of-fit on F^2	1.034
Final R indices [I>2sigma(I)]	$R_1 = 0.0196$
	$wR_2 = 0.0521$
R indices (all data)	$R_1 = 0.0214$
	$wR_2 = 0.0533$
Largest diff. peak and hole	0.88 and −0.43 $e^- \times Å^{-3}$

A.3 $La_2Br_6(phen)_4$

Crystals of compound **A.3** were grown solvothermally from supersaturated solutions of $LaBr_3$ in ethanol (EtOH) and 1,10-phenanthroline (phen). 0.5 mmol of $LaBr_3$ was placed into a nitrogen-purged septa sealed round bottom flask. 30mL of EtOH was then transferred via a nitrogen-purged syringe into the flask. The resulting solution was then transferred via syringe into a high-pressure glass tube containing 1 mmol of phen. The high-pressure vessel was sealed quickly with a Teflon cap to minimize exposure to the atmosphere, as $LaBr_3$ is extremely hygroscopic. The vessel was placed into a programmable oven which was ramped at 1 °C per minute to 180 °C, allowed to dwell for 48 hours, then allowed to cool at 0.1 °C per minute to room temperature. Compound **A.3** is isostructural with compound **A.2**. See the ellipsoidal plot of compound **A.2** for the crystal structure of compound **A.3**.

Crystal data and structure refinements for compound **A.3**.

	A.3
Empirical formula	$C_{48}H_{32}Br_6N_8La_2$
Formula weight	1478.10
Temperature	100(2)
Wavelength	0.71073 Å
Crystal system	monoclinic
Space group	$P2_1/n$
Unit cell dimensions	a = 12.900(3) b = 14.398(3) c = 13.905(3) α = 90.00 β = 115.004(4) γ = 90.00
Volume	2340.4(8)
Z	2
Density (calculated)	2.097
Absorption coefficient	6.967
F(000)	1400.0
Crystal size	0.18 × 0.16 × 0.15
2θ range for data collected	3.62 to 56.54°
Index ranges	−17 ≤ h ≤ 17 −19 ≤ k ≤ 19 −18 ≤ l ≤ 18
Reflections collected	26493
Ind. reflections	5796[R(int) = 0.0462]
Data / restraints / parameters	5796/0/289
Goodness-of-fit on F^2	1.026
Final R indices [I>2sigma(I)]	R_1 = 0.0298 wR_2 = 0.0682
R indices (all data)	R_1 = 0.0391 wR_2 = 0.0721
Largest diff. peak and hole	1.82 and −0.51 $e^- \times Å^{-3}$

A.4 $[LaCl_3(3478\text{-mephen})_2(EtOH)](EtOH)$

Crystals of compound **A.4** were grown solvothermally from supersaturated solutions of $LaCl_3$ in ethanol (EtOH) and 3,4,7,8-tetramethyl-1,10-phenanthroline (3478-mephen). 0.5 mmol of $LaCl_3$ was placed into a nitrogen-purged septa sealed round bottom flask. 30mL of EtOH was then transferred via a nitrogen-purged syringe into the flask. The resulting solution was then transferred via syringe into a high-pressure glass tube containing 1 mmol of 3478-mephen. The high-pressure vessel was sealed quickly with a Teflon cap to minimize exposure to the atmosphere, as $LaCl_3$ is extremely hygroscopic. The vessel was placed into a programmable oven which was ramped at 1 °C per minute to 180 °C, allowed to dwell for 48 hours, then allowed to cool at 0.1 °C per minute to room temperature.

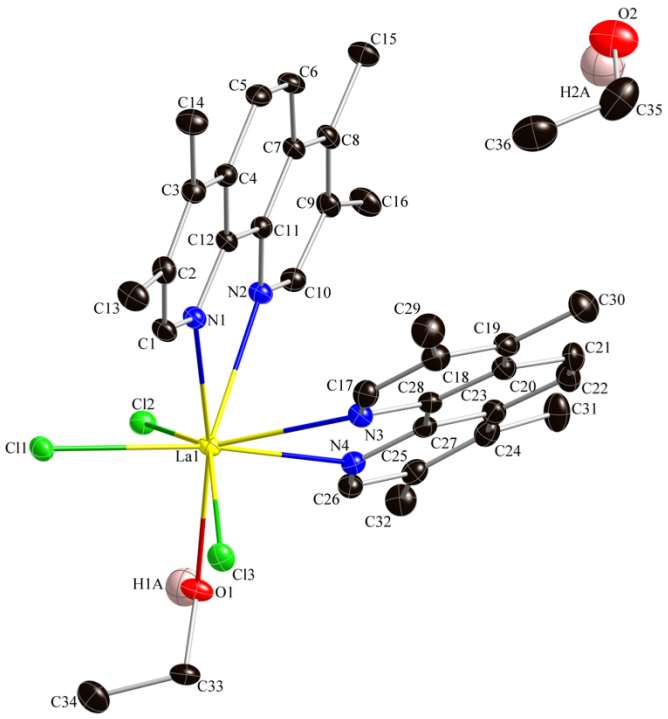

Displacement ellipsoid plot. Displacement ellipsoids drawn at the 50% probability level.

Crystal data and structure refinements for compound **A.4**.

	A.4
Empirical formula	$C_{36}H_{44}Cl_3LaN_4O_2$
Formula weight	810.01
Temperature	100(2)
Wavelength	0.71073 Å
Crystal system	triclinic
Space group	*P*-1
Unit cell dimensions	$a = 11.1377(6)$
	$b = 12.3469(6)$
	$c = 14.1038(7)$
	$\alpha = 72.0930(10)$
	$\beta = 77.0310(10)$
	$\gamma = 78.2150(10)$
Volume	1779.24(16)
Z	2
Density (calculated)	1.512
Absorption coefficient	1.463
F(000)	824.0
Crystal size	0.30 × 0.24 × 0.20
2θ range for data collected	3.08 to 55.38°
Index ranges	$-17 \le h \le 17$
	$-19 \le k \le 19$
	$-18 \le l \le 18$
Reflections collected	26091
Ind. reflections	8320[R(int) = 0.0306]
Data / restraints / parameters	8320/2/433
Goodness-of-fit on F^2	1.048
Final R indices [I>2sigma(I)]	$R_1 = 0.0247$
	$wR_2 = 0.0605$
R indices (all data)	$R_1 = 0.0268$
	$wR_2 = 0.0617$
Largest diff. peak and hole	0.89 and −0.41 $e^- \times Å^{-3}$

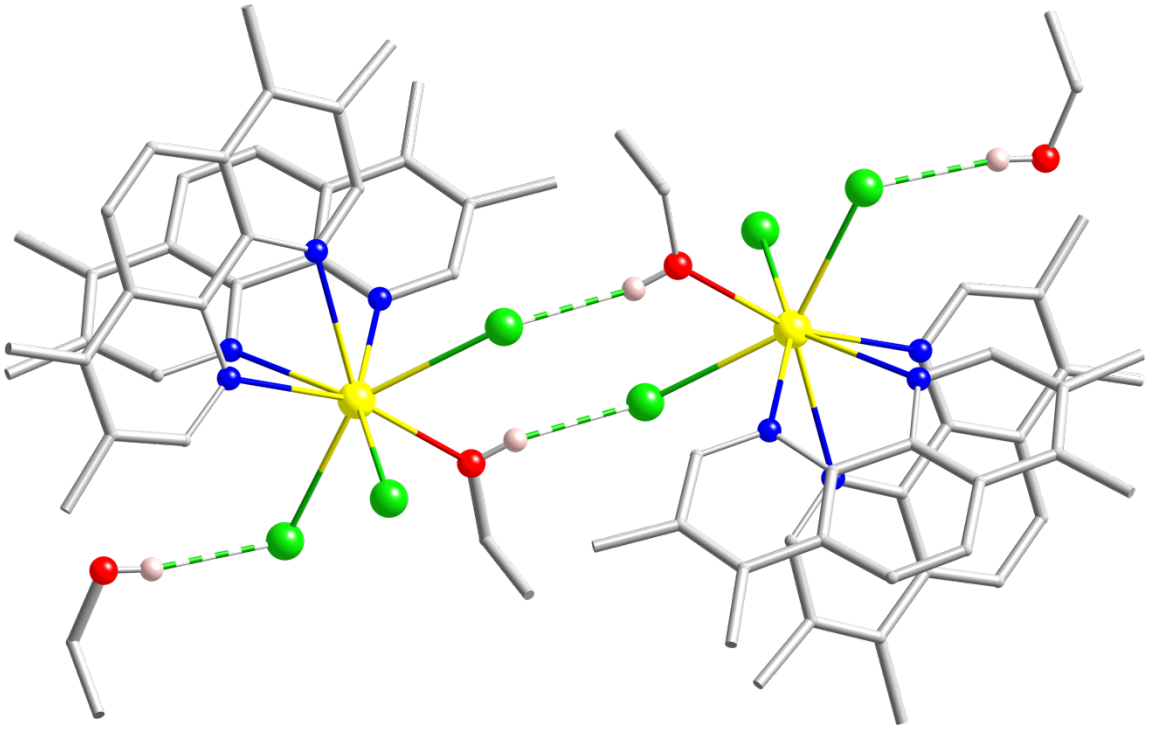

Compound **A.4** forms dimeric species through H – Cl hydrogen bonds. The non-coordinating EtOH forms a separate H – Cl hydrogen bond. La, N, Cl, O, and H shown in yellow, blue, green, red, and white, respectively. C is shown as grey stick bonds.

A.5 [$PrCl_3$(3478-mephen)$_2$(EtOH)](EtOH)

Crystals of compound **A.5** were grown solvothermally from supersaturated solutions of $PrCl_3$ in ethanol (EtOH) and 3,4,7,8-tetramethyl-1,10-phenanthroline (3478-mephen). 0.5 mmol of $PrCl_3$ was placed into a nitrogen-purged septa sealed round bottom flask. 30mL of EtOH was then transferred via a nitrogen-purged syringe into the flask. The resulting solution was then transferred via syringe into a high-pressure glass tube containing 1 mmol of 3478-mephen. The high-pressure vessel was sealed quickly with a Teflon cap to minimize exposure to the atmosphere, as $PrCl_3$ is extremely hygroscopic. The vessel was placed into a programmable oven which was ramped at 1 °C per minute to 180 °C, allowed to dwell for 48 hours, then allowed to cool at 0.1 °C per minute to room temperature. Compound **A.5** is isostructural with compound **A.4**. See the ellipsoidal plot of compound **A.4** for the crystal structure of compound **A.5**.

Crystal data and structure refinements for compound **A.5**.

	A.5
Empirical formula	$C_{36}H_{44}Cl_3PrN_4O_2$
Formula weight	812.01
Temperature	100(2)
Wavelength	0.71073 Å
Crystal system	triclinic
Space group	*P*-1
Unit cell dimensions	$a = 11.107(2)$ $b = 12.357(3)$ $c = 14.031(3)$ $\alpha = 72.417(5)$ $\beta = 76.942(5)$ $\gamma = 78.451(5)$
Volume	1770.2(7)
Z	2
Density (calculated)	1.523
Absorption coefficient	1.640
F(000)	828.0
Crystal size	0.2 × 0.06 × 0.04
2θ range for data collected	3.1 to 56.68°
Index ranges	$-14 \leq h \leq 14$ $-15 \leq k \leq 16$ $-18 \leq l \leq 18$
Reflections collected	8774
Ind. reflections	8774[R(int) = 0.0000]
Data / restraints / parameters	8774/2/432
Goodness-of-fit on F^2	1.104
Final R indices [I>2sigma(I)]	$R_1 = 0.0534$ $wR_2 = 0.1416$
R indices (all data)	$R_1 = 0.0618$ $wR_2 = 0.1473$
Largest diff. peak and hole	1.76 and −1.03 $e^- \times Å^{-3}$

A.6 $LaBr_3(3478\text{-mephen})_2(EtOH)$

Crystals of compound **A.6** were grown solvothermally from supersaturated solutions of $LaBr_3$ in ethanol (EtOH) and 3,4,7,8-tetramethyl-1,10-phenanthroline (3478-mephen). 0.5 mmol of $LaBr_3$ was placed into a nitrogen-purged septa sealed round bottom flask. 30mL of EtOH was then transferred via a nitrogen-purged syringe into the flask. The resulting solution was then transferred via syringe into a high-pressure glass tube containing 1 mmol of 3478-mephen. The high-pressure vessel was sealed quickly with a Teflon cap to minimize exposure to the atmosphere, as $LaBr_3$ is extremely hygroscopic. The vessel was placed into a programmable oven which was ramped at 1 °C per minute to 180 °C, allowed to dwell for 48 hours, then allowed to cool at 0.1 °C per minute to room temperature.

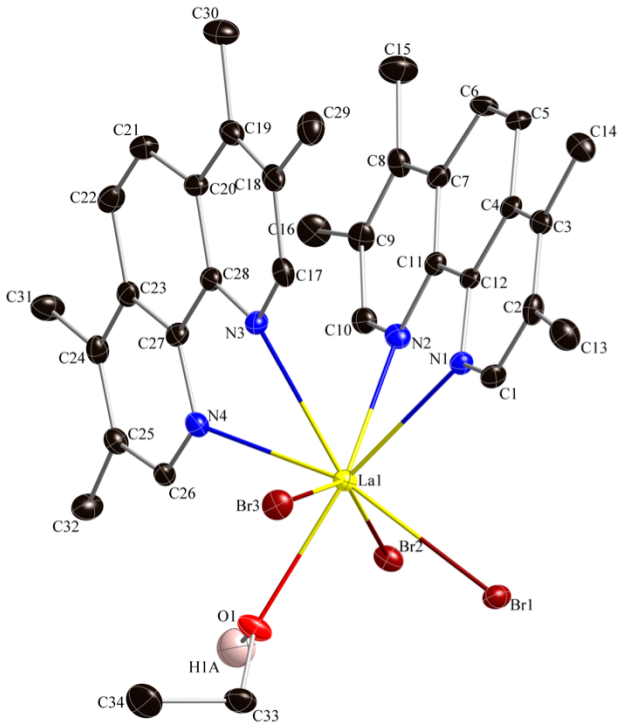

Displacement ellipsoid plot. Displacement ellipsoids drawn at the 50% probability level.

Crystal data and structure refinements for compound **A.6**.

	A.6
Empirical formula	$C_{34}H_{38}Br_3LaN_4O$
Formula weight	897.32
Temperature	100(2)
Wavelength	0.71073 Å
Crystal system	triclinic
Space group	*P*-1
Unit cell dimensions	$a = 11.310(2)$
	$b = 12.114(2)$
	$c = 15.126(3)$
	$\alpha = 110.002(4)$
	$\beta = 93.323(4)$
	$\gamma = 117.532(4)$
Volume	1667.8(6)
Z	2
Density (calculated)	1.787
Absorption coefficient	4.908
F(000)	880.0
Crystal size	0.18 × 0.16 × 0.05
2θ range for data collected	2.96 to 56.62°
Index ranges	$-15 \le h \le 15$
	$-16 \le k \le 16$
	$-20 \le l \le 20$
Reflections collected	27892
Ind. reflections	8270[R(int) = 0.0752]
Data / restraints / parameters	8270/1/401
Goodness-of-fit on F^2	0.973
Final R indices [I>2sigma(I)]	$R_1 = 0.0434$
	$wR_2 = 0.0802$
R indices (all data)	$R_1 = 0.0652$
	$wR_2 = 0.0882$
Largest diff. peak and hole	1.39 and −0.63 $e^- \times Å^{-3}$

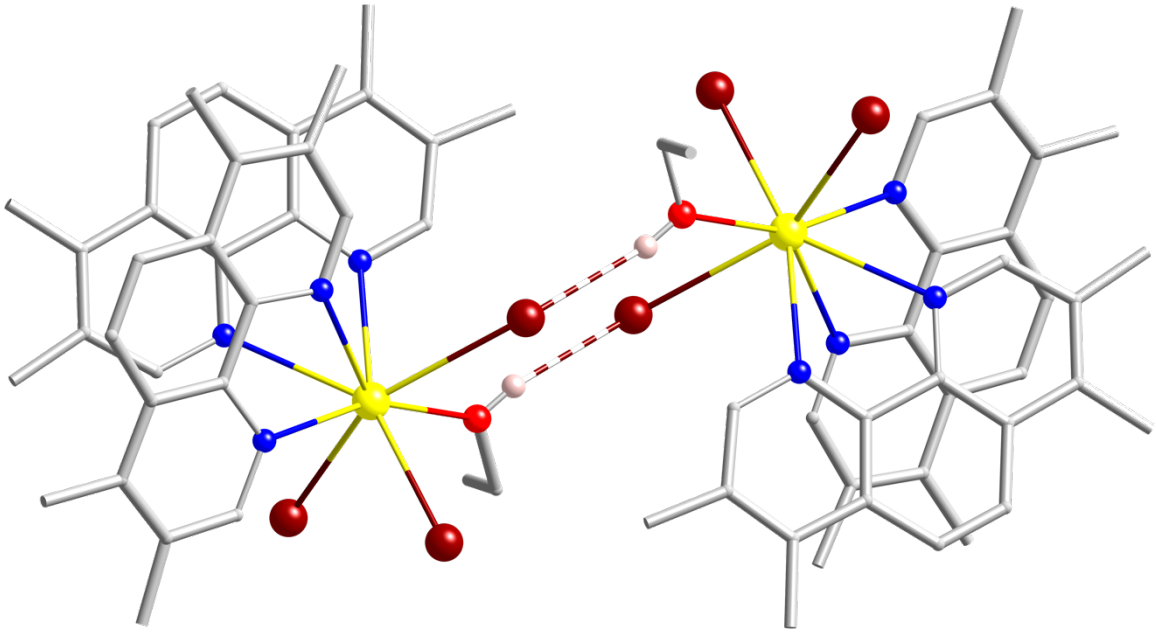

Compound **A.6** forms dimeric species through H – Br hydrogen bonds. La, N, Br, O, and H shown in yellow, blue, burgundy, red, and white, respectively. C is shown as grey stick bonds.

A.7 $[CeBr_2(3478\text{-mephen})_2(H_2O)_2]Br$

Crystals of compound **A.7** were grown solvothermally from supersaturated solutions of $CeBr_3$ in ethanol (EtOH) and 3,4,7,8-tetramethyl-1,10-phenanthroline (3478-mephen). 0.5 mmol of $CeBr_3$ was placed into a nitrogen-purged septa sealed round bottom flask. 30mL of EtOH was then transferred via a nitrogen-purged syringe into the flask. The resulting solution was then transferred via syringe into a high-pressure glass tube containing 1 mmol of 3478-mephen. The high-pressure vessel was sealed quickly with a Teflon cap to minimize exposure to the atmosphere, as $CeBr_3$ is extremely hygroscopic. The vessel was placed into a programmable oven which was ramped at 1 °C per minute to 180 °C, allowed to dwell for 48 hours, then allowed to cool at 0.1 °C per minute to room temperature.

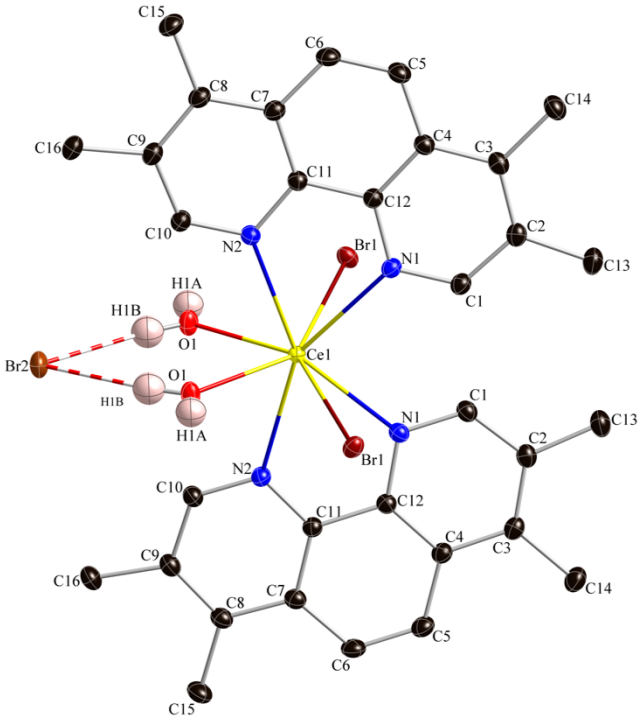

Displacement ellipsoid plot. Displacement ellipsoids drawn at the 50% probability level.

Crystal data and structure refinements for compound **A.7**.

	A.7
Empirical formula	$C_{32}H_{36}Br_3CeN_4O_2$
Formula weight	888.50
Temperature	100(2)
Wavelength	0.71073 Å
Crystal system	monoclinic
Space group	*C*2/*c*
Unit cell dimensions	a = 18.2500(12)
	b = 13.2808(9)
	c = 14.6164(10)
	α = 90.00
	β = 117.6510(10)
	γ = 90.00
Volume	3138.0(4)
Z	4
Density (calculated)	1.881
Absorption coefficient	5.307
F(000)	1740.0
Crystal size	0.4 × 0.35 × 0.3
2θ range for data collected	3.96 to 60.12°
Index ranges	$-25 \leq h \leq 25$
	$-18 \leq k \leq 18$
	$-20 \leq l \leq 20$
Reflections collected	26877
Ind. reflections	4607[R(int) = 0.0299]
Data / restraints / parameters	4607/0/203
Goodness-of-fit on F^2	1.020
Final R indices [I>2sigma(I)]	R_1 = 0.0208
	wR_2 = 0.0521
R indices (all data)	R_1 = 0.0237
	wR_2 = 0.0531
Largest diff. peak and hole	0.93 and −0.50 $e^- \times Å^{-3}$

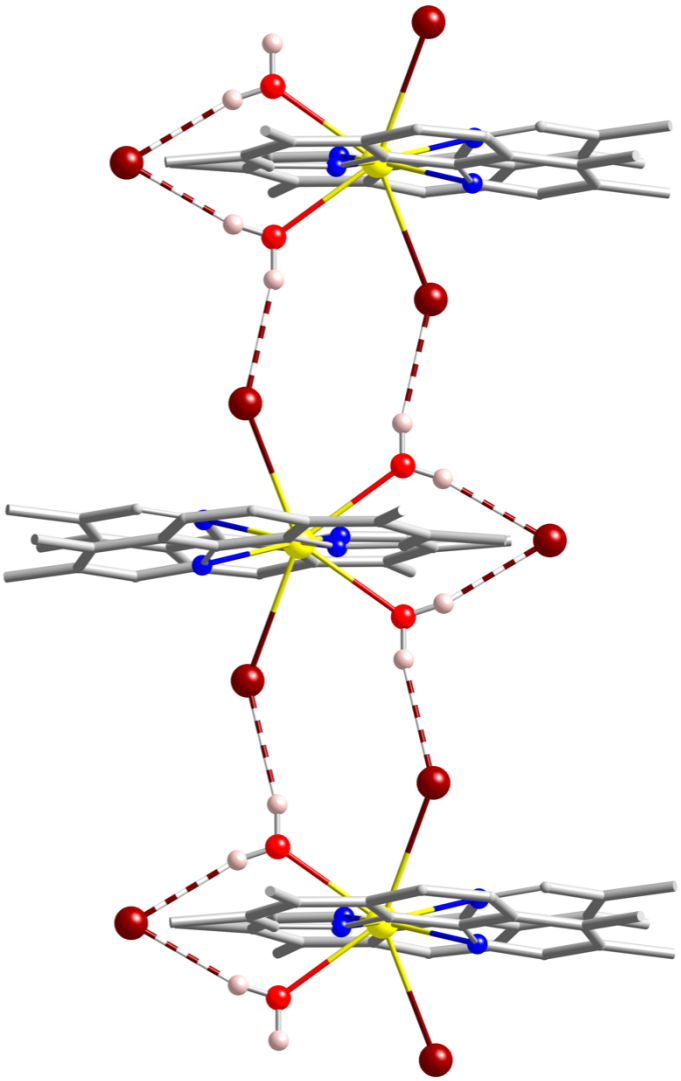

Compound **A.7** forms 1D chains through H – Br hydrogen bonds. The non-coordinating Br also forms H – Br hydrogen bonds. Ce, N, Br, O, and H shown in yellow, blue, burgundy, red, and white, respectively. C is shown as grey stick bonds.

A.8 $[Ce_2Br_2(OH)_2(3478\text{-mephen})_2(EtOH)_2]Br_2$

Crystals of compound **A.8** were grown solvothermally from supersaturated solutions of $CeBr_3$ in ethanol (EtOH) and 3,4,7,8-tetramethyl-1,10-phenanthroline (3478-mephen). 0.5 mmol of $CeBr_3$ was placed into a nitrogen-purged septa sealed round bottom flask. 30mL of EtOH was then transferred via a nitrogen-purged syringe into the flask. The resulting solution was then transferred via syringe into a high-pressure glass tube containing 1 mmol of 3478-mephen. The high-pressure vessel was sealed quickly with a Teflon cap to minimize exposure to the atmosphere, as $CeBr_3$ is extremely hygroscopic. The vessel was placed into a programmable oven which was ramped at 1 °C per minute to 180 °C, allowed to dwell for 48 hours, then allowed to cool at 0.1 °C per minute to room temperature.

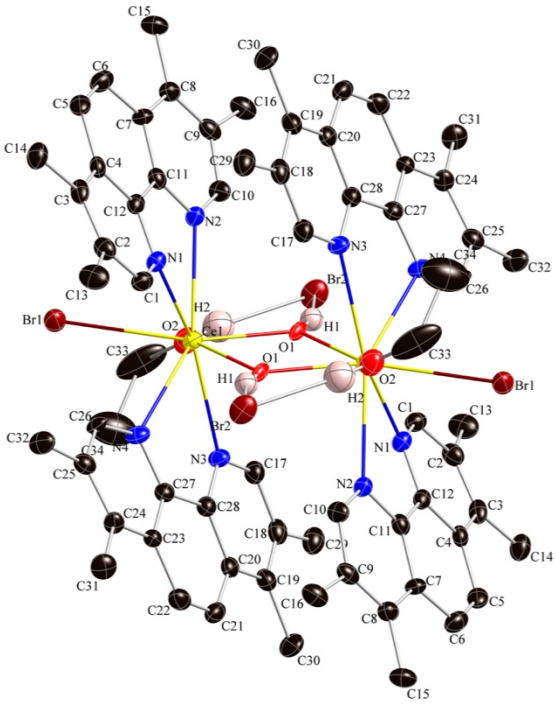

Displacement ellipsoid plot. Molecule on inversion center. Displacement ellipsoids drawn at the 50% probability level.

Crystal data and structure refinements for compound **A.8**.

	A.8
Empirical formula	$C_{68}H_{78}Br_4Ce_2N_8O_4$
Formula weight	1671.26
Temperature	100(2)
Wavelength	0.71073 Å
Crystal system	orthorhombic
Space group	*Pbca*
Unit cell dimensions	$a = 13.9087(13)$ $b = 20.8817(19)$ $c = 22.216(2)$ $\alpha = 90.00$ $\beta = 90.00$ $\gamma = 90.00$
Volume	6452.4(10)
Z	4
Density (calculated)	1.720
Absorption coefficient	3.925
F(000)	3320.0
Crystal size	0.4 × 0.35 × 0.3
2θ range for data collected	3.66 to 50.06°
Index ranges	$-16 \leq h \leq 16$ $-24 \leq k \leq 24$ $-26 \leq l \leq 26$
Reflections collected	85565
Ind. reflections	5706[R(int) = 0.1422]
Data / restraints / parameters	5706/2/403
Goodness-of-fit on F^2	1.033
Final R indices [I>2sigma(I)]	$R_1 = 0.0432$ $wR_2 = 0.0901$
R indices (all data)	$R_1 = 0.0663$ $wR_2 = 0.0995$
Largest diff. peak and hole	1.75 and −0.92 $e^- \times Å^{-3}$

A.9 [$PrBr_2$(3478-mephen)$_2$(H_2O)$_2$]Br

Crystals of compound **A.9** were grown solvothermally from supersaturated solutions of $PrBr_3$ in ethanol (EtOH) and 3,4,7,8-tetramethyl-1,10-phenanthroline (3478-mephen). 0.5 mmol of $PrBr_3$ was placed into a nitrogen-purged septa sealed round bottom flask. 30mL of EtOH was then transferred via a nitrogen-purged syringe into the flask. The resulting solution was then transferred via syringe into a high-pressure glass tube containing 1 mmol of 3478-mephen. The high-pressure vessel was sealed quickly with a Teflon cap to minimize exposure to the atmosphere, as $PrBr_3$ is extremely hygroscopic. The vessel was placed into a programmable oven which was ramped at 1 °C per minute to 180 °C, allowed to dwell for 48 hours, then allowed to cool at 0.1 °C per minute to room temperature. Compound **A.9** is isostructural with compound **A.7**. See the ellipsoidal plot of compound **A.7** for the crystal structure of compound **A.9**.

Crystal data and structure refinements for compound **A.9**.

	A.9
Empirical formula	$C_{32}H_{36}Br_3N_4O_2Pr$
Formula weight	889.29
Temperature	100(2)
Wavelength	0.71073 Å
Crystal system	monoclinic
Space group	*C*2/*c*
Unit cell dimensions	a = 18.1862(14) b = 13.2758(10) c = 14.5908(11) α = 90.00 β = 117.5640(10) γ = 90.00
Volume	3122.9(4)
Z	4
Density (calculated)	1.891
Absorption coefficient	5.435
F(000)	1744.0
Crystal size	0.34 × 0.12 × 0.1
2θ range for data collected	3.98 to 56.72°
Index ranges	$-24 \le h \le 24$ $-17 \le k \le 17$ $-19 \le l \le 19$
Reflections collected	25779
Ind. reflections	3894[R(int) = 0.0307]
Data / restraints / parameters	3894/0/203
Goodness-of-fit on F^2	1.031
Final R indices [I>2sigma(I)]	R_1 = 0.0186 wR_2 = 0.0472
R indices (all data)	R_1 = 0.0205 wR_2 = 0.0479
Largest diff. peak and hole	0.79 and −0.44 $e^- \times Å^{-3}$

A.10 $[Pr_2Br_2(OH)_2(3478\text{-mephen})_2(EtOH)_2]Br_2$

Crystals of compound **A.10** were grown solvothermally from supersaturated solutions of $PrBr_3$ in ethanol (EtOH) and 3,4,7,8-tetramethyl-1,10-phenanthroline (3478-mephen). 0.5 mmol of $PrBr_3$ was placed into a nitrogen-purged septa sealed round bottom flask. 30mL of EtOH was then transferred via a nitrogen-purged syringe into the flask. The resulting solution was then transferred via syringe into a high-pressure glass tube containing 1 mmol of 3478-mephen. The high-pressure vessel was sealed quickly with a Teflon cap to minimize exposure to the atmosphere, as $PrBr_3$ is extremely hygroscopic. The vessel was placed into a programmable oven which was ramped at 1 °C per minute to 180 °C, allowed to dwell for 48 hours, then allowed to cool at 0.1 °C per minute to room temperature. Compound **A.10** is isostructural with compound **A.8**. See the ellipsoidal plot of compound **A.8** for the crystal structure of compound **A.10**.

Crystal data and structure refinements for compound **A.10**.

	A.10
Empirical formula	$C_{68}H_{78}Br_4Pr_2N_8O_4$
Formula weight	1672.84
Temperature	100(2)
Wavelength	0.71073 Å
Crystal system	orthorhombic
Space group	*Pbca*
Unit cell dimensions	a = 13.9036(13) b = 20.853(2) c = 22.245(2) α = 90.00 β = 90.00 γ = 90.00
Volume	6449.5(11)
Z	4
Density (calculated)	1.723
Absorption coefficient	4.026
F(000)	3328.0
Crystal size	0.18 × 0.14 × 0.08
2θ range for data collected	3.66 to 56.58°
Index ranges	$-18 \leq h \leq 18$ $-27 \leq k \leq 27$ $-29 \leq l \leq 29$
Reflections collected	104995
Ind. reflections	7998[R(int) = 0.0718]
Data / restraints / parameters	7998/2/403
Goodness-of-fit on F^2	1.058
Final R indices [I>2sigma(I)]	R_1 = 0.0355 wR_2 = 0.0829
R indices (all data)	R_1 = 0.0475 wR_2 = 0.0886
Largest diff. peak and hole	1.96 and −1.14 $e^- \times Å^{-3}$

A.11 $PrBr_3(phen)_2(EtOH)$

Crystals of compound **A.11** were grown solvothermally from supersaturated solutions of $PrBr_3$ in ethanol (EtOH) and 1,10-phenanthroline (phen). 0.5 mmol of $PrBr_3$ was placed into a nitrogen-purged septa sealed round bottom flask. 30mL of EtOH was then transferred via a nitrogen-purged syringe into the flask. The resulting solution was then transferred via syringe into a high-pressure glass tube containing 1 mmol of phen. The high-pressure vessel was sealed quickly with a Teflon cap to minimize exposure to the atmosphere, as $PrBr_3$ is extremely hygroscopic. The vessel was placed into a programmable oven which was ramped at 1 °C per minute to 180 °C, allowed to dwell for 48 hours, then allowed to cool at 0.1 °C per minute to room temperature.

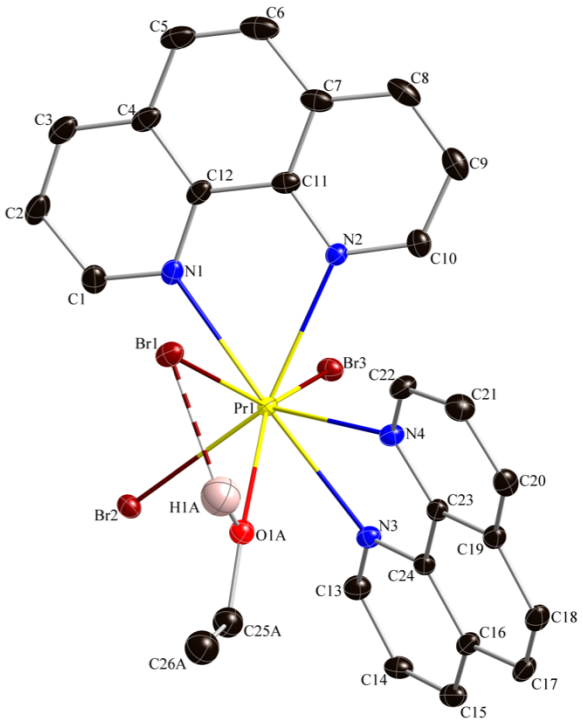

Displacement ellipsoid plot. Molecule on inversion center. Displacement ellipsoids drawn at the 50% probability level.

Crystal data and structure refinements for compound **A.11**.

	A.11
Empirical formula	$C_{26}H_{22}Br_3N_4OPr$
Formula weight	787.12
Temperature	100(2)
Wavelength	0.71073 Å
Crystal system	orthorhombic
Space group	$Pna2_1$
Unit cell dimensions	$a = 20.7928(15)$ $b = 14.3748(11)$ $c = 8.7472(6)$ $\alpha = 90.00$ $\beta = 90.00$ $\gamma = 90.00$
Volume	2614.5(3)
Z	4
Density (calculated)	2.000
Absorption coefficient	6.475
F(000)	1512.0
Crystal size	0.36 × 0.24 × 0.10
2θ range for data collected	3.44 to 56.64°
Index ranges	$-27 \leq h \leq 27$ $-19 \leq k \leq 19$ $-11 \leq l \leq 11$
Reflections collected	43269
Ind. reflections	6506[R(int) = 0.0342]
Data / restraints / parameters	6506/9/324
Goodness-of-fit on F^2	1.033
Final R indices [I>2sigma(I)]	$R_1 = 0.0172$ $wR_2 = 0.0401$
R indices (all data)	$R_1 = 0.0182$ $wR_2 = 0.0404$
Largest diff. peak and hole	0.92 and −0.36 $e^- \times Å^{-3}$

A.12 $[Pr(phen)_2(H_2O)_5]Br_3(phen)_2(H_2O)_5$

Crystals of compound **A.12** were grown solvothermally from supersaturated solutions of $CeBr_3$ in ethanol (EtOH) and 1,10-phenanthroline (phen). 0.5 mmol of $CeCl_3$ was placed into a nitrogen-purged septa sealed round bottom flask. 30mL of EtOH was then transferred via a nitrogen-purged syringe into the flask. The resulting solution was then transferred via syringe into a high-pressure glass tube containing 1 mmol of phen. The high-pressure vessel was sealed quickly with a Teflon cap to minimize exposure to the atmosphere, as $CeBr_3$ is extremely hygroscopic. The vessel was placed into a programmable oven which was ramped at 1 °C per minute to 180 °C, allowed to dwell for 48 hours, then allowed to cool at 0.1 °C per minute to room temperature.

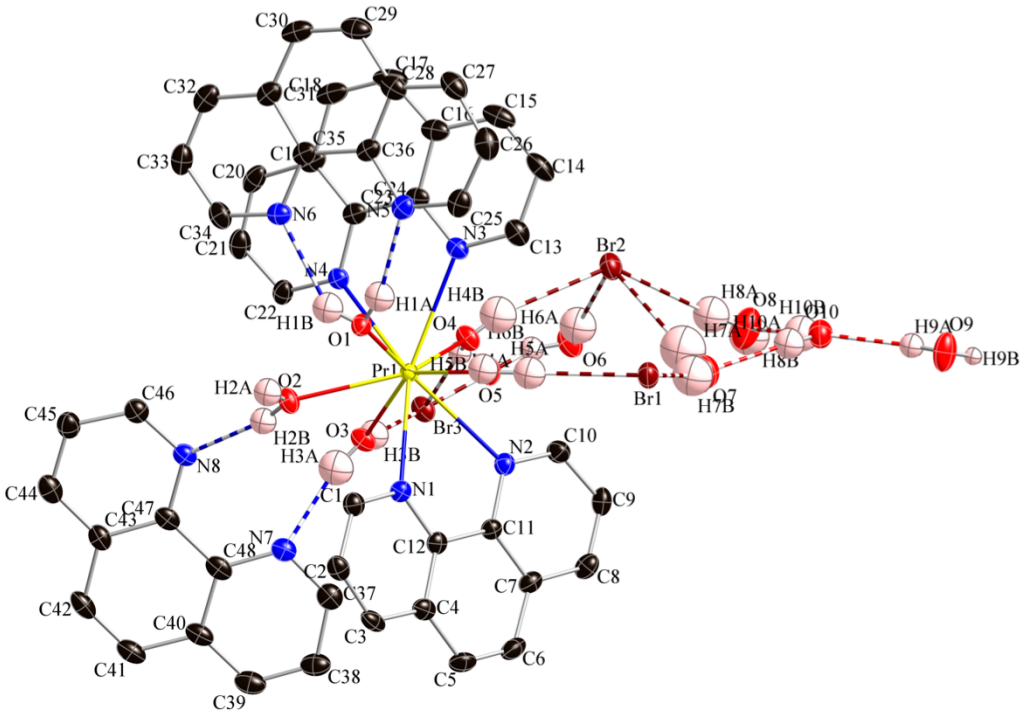

Displacement ellipsoid plot. Displacement ellipsoids drawn at the 50% probability level.

Crystal data and structure refinements for compound **A.12**.

	A.12
Empirical formula	$C_{48}H_{52}Br_3N_8O_{10}Pr$
Formula weight	1281.62
Temperature	100(2)
Wavelength	0.71073 Å
Crystal system	monoclinic
Space group	$P2_1/n$
Unit cell dimensions	$a = 10.4325(14)$
	$b = 25.883(4)$
	$c = 18.808(3)$
	$\alpha = 90.00$
	$\beta = 96.621(3)$
	$\gamma = 90.00$
Volume	5044.9(12)
Z	4
Density (calculated)	1.687
Absorption coefficient	3.407
F(000)	2560.0
Crystal size	0.22 × 0.18 × 0.08
2θ range for data collected	2.68 to 56.56°
Index ranges	$-13 \le h \le 13$
	$-34 \le k \le 34$
	$-25 \le l \le 25$
Reflections collected	84266
Ind. reflections	12490[R(int) = 0.0929]
Data / restraints / parameters	12490/190/711
Goodness-of-fit on F^2	1.018
Final R indices [I>2sigma(I)]	$R_1 = 0.0389$
	$wR_2 = 0.0805$
R indices (all data)	$R_1 = 0.0601$
	$wR_2 = 0.0892$
Largest diff. peak and hole	1.17 and −0.51 $e^- \times Å^{-3}$

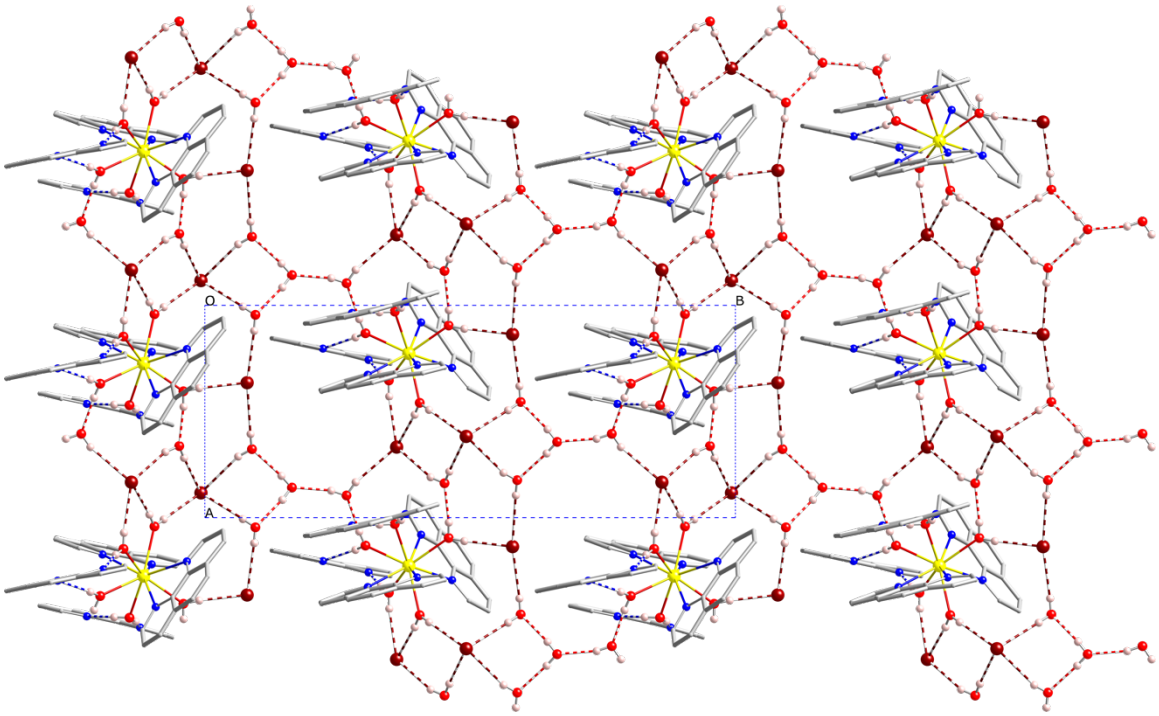

Compound **A.12** viewed down the *c* axis. 2D sheets form through an extensive H – Br and H – O hydrogen bonding network. The non-coordinating phen ligands forms H – N hydrogen bonds with coordinated water. Pr, N, Br, O, and H shown in yellow, blue, burgundy, red, and white, respectively. C is shown as grey stick bonds.

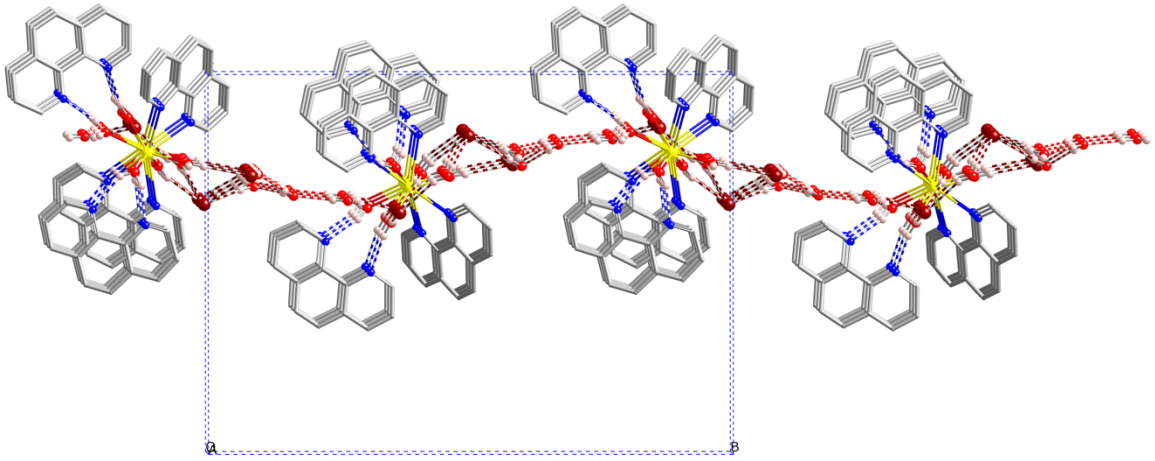

Compound **A.12** viewed down the *a* axis. Pr, N, Br, O, and H shown in yellow, blue, burgundy, red, and white, respectively. C is shown as grey stick bonds.

A.13 $CeBr_3(H_2O)(phen)_2$

Crystals of compound **A.13** were grown solvothermally from supersaturated solutions of $CeBr_3$ in ethanol (EtOH) and 1,10-phenanthroline (phen). 0.5 mmol of $CeBr_3$ was placed into a nitrogen-purged septa sealed round bottom flask. 30mL of EtOH was then transferred via a nitrogen-purged syringe into the flask. The resulting solution was then transferred via syringe into a high-pressure glass tube containing 1 mmol of phen. The high-pressure vessel was sealed quickly with a Teflon cap to minimize exposure to the atmosphere, as $CeBr_3$ is extremely hygroscopic. The vessel was placed into a programmable oven which was ramped at 1 °C per minute to 180 °C, allowed to dwell for 48 hours, then allowed to cool at 0.1 °C per minute to room temperature.

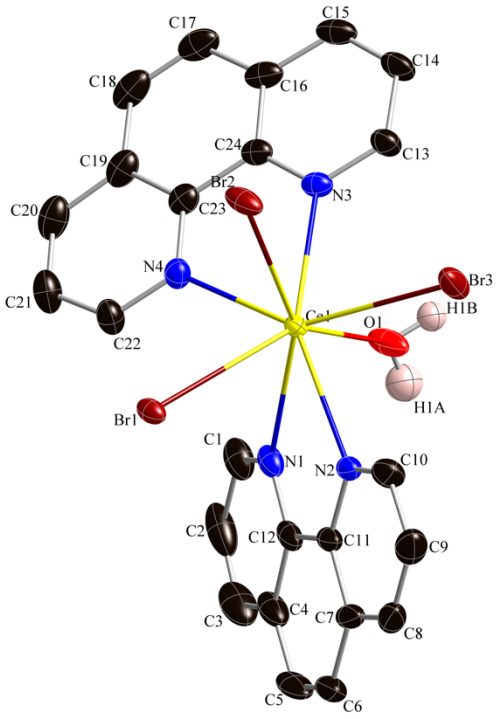

Displacement ellipsoid plot. Displacement ellipsoids drawn at the 50% probability level.

Crystal data and structure refinements for compound **A.13**.

	A.13
Empirical formula	$C_{24}H_{18}Br_3CeN_4O$
Formula weight	758.27
Temperature	100(2)
Wavelength	0.71073 Å
Crystal system	triclinic
Space group	*P*-1
Unit cell dimensions	$a = 7.2916(16)$
	$b = 10.192(2)$
	$c = 17.582(4)$
	$\alpha = 80.228(4)$
	$\beta = 79.710(4)$
	$\gamma = 70.890(4)$
Volume	1206.1(5)
Z	2
Density (calculated)	2.088
Absorption coefficient	6.881
F(000)	722.0
Crystal size	0.36 × 0.32 × 0.24
2θ range for data collected	4.26 to 56.72°
Index ranges	$-9 \le h \le 9$
	$-13 \le k \le 13$
	$-23 \le l \le 23$
Reflections collected	19829
Ind. reflections	6001[R(int) = 0.0302]
Data / restraints / parameters	6001/2/306
Goodness-of-fit on F^2	1.061
Final R indices [I>2sigma(I)]	$R_1 = 0.0330$
	$wR_2 = 0.0809$
R indices (all data)	$R_1 = 0.0383$
	$wR_2 = 0.0834$
Largest diff. peak and hole	2.78 and −2.13 $e^- \times Å^{-3}$

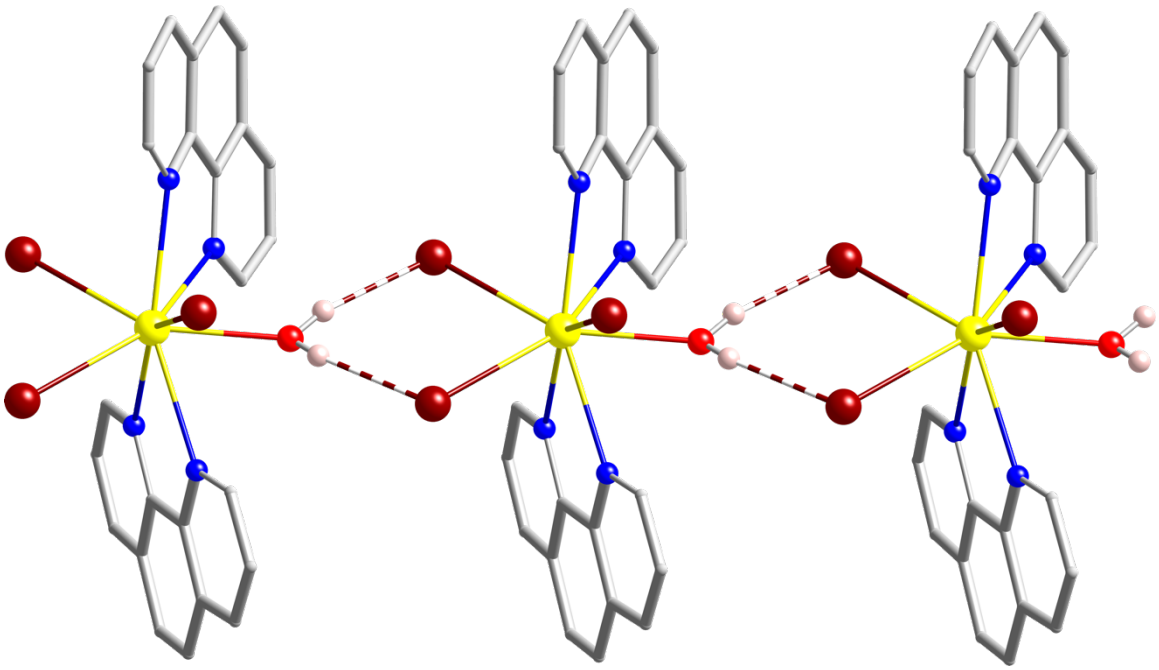

Compound **A.13** forms 1D chains through H – Br hydrogen bonds. Ce, N, Br, O, and H shown in yellow, blue, burgundy, red, and white, respectively. C is shown as grey stick bonds.

APPENDIX B

CONSIDERATIONS FOR HYDROTHERMAL REACTIONS

Oftentimes when doing a hydrothermal reaction, it is beneficial to prepare a stock solution of a reduced species that can be easily used for crystallization reactions. When preparing a stock solution of vanadium(IV) consideration needs to be given to which reagents, reaction vessel, and what source of heat/stirring will be used. Our findings show that V_2O_5, used as received, works well as a vanadium(IV) precursor. $NaVO_3$ is also an excellent vanadium(IV) precursor but must be dried ahead of time in an oven at a minimum temperature of 260 °C for 24 hours as it is deliquescent. Many organic acids will perform the reducing of V(V) to V(IV) including oxalic, tartaric, and ascorbic acid. When selecting a reaction vessel, we found that using a round bottom flask (RBF) reflux apparatus works best, with a stir bar added. In a typical procedure a ratio of 1 mmol of V(V) to 2 mmol organic reducing acid is added to 4 mL of deionized water and heated at 120°C until the solution has completely turned blue. These solutions are shelf stable for at least 6 months with no noticeable degradation. This procedure can be scaled by approximately 100x and be performed comfortably in a 500 mL RBF. Vanadium stock solution can also be prepared using a combination of concentrated sulfuric acid and zinc. These reactions never yielded any desirable crystals. After a stock solution has been prepared it can be used for complexation reactions with other metals.

It is possible to perform the reduction of vanadium(V) to vanadium(IV) and the crystallization in one step that involves an *in situ* reduction. Organic reducing acids are not suitable for this technique as they often precipitate unwanted fully oxidized side products. To prevent this problem diamines, such as ethylenediamine, can be used as powerful reducing agents. These reactions still need to occur in acidic media, and as such 85% phosphoric acid or concentrated sulfuric acid can be added to the reaction to achieve

sufficient acidity. It's important to note that extreme caution must be exercised when adding diamines to acidic solutions as much sputtering and heat evolution can occur. In a typical reaction 1 mmol of V(V) to 2 mmol of diamine to 3 mmol of acid to 2 mL of deionized water are used.

When performing a crystallization reaction there are typically two choices of reaction vessel, a thick walled pyrex tube or a polytetrafluorethylene (PTFE) autoclave. It is my experience that the PTFE autoclave walls are simply too smooth to allow for adequate nucleation of crystals. Thick walls pyrex tubes, however, are not as smooth and have comparably rough surfaces on the inner walls that allow for superior nucleation of crystals. Typically, when deciding the amount of reactants to put in a vessel a 2/3 rule is employed. Fill the vessel no more than 2/3 full with reactants. It is important to allow reaction vessels to degas before sealing with a PTFE cap. Oftentimes the acidic stock solution will react with an additional complexing reagent and effervesce. This gas must be allowed to escape the tube prior to sealing to avoid a catastrophic failure of the tube when at elevated temperatures.

There is a third reaction vessel that can be used for reactions, flame sealed evacuated pyrex tubes. In this case, the PTFE cap is swapped for a flame seal that is achieved by affixing your tube to the manifold and pulling a vacuum and then applying heat to collapse the pyrex in upon itself creating a vacuum seal. This technique is the most involved and requires that liquid reactants in the tube be frozen with liquid nitrogen prior to exposure to a vacuum. Failure to perform this step will result in your liquid reactant boiling die to heat applied and reduced atmospheric pressure experienced by the inside of the tube. This technique could potentially be a route forward in preparing

vanadium(III) and vanadium(II) materials which will only readily form in the absence of air. Whether a thick walled pyrex tube or a flame sealed tube is used, secondary containment must be employed as a failsafe to ensure reactions will not contaminate the oven in the event of a catastrophic failure of a tube. Typically our secondary containment is a thick walled, capped steel tube. These tubes should face upright in the oven during a reaction. This can be achieved by nesting the tubes in a ceramic flower pot.

When selecting a reaction coordinate you must consider the temperature at which any organic components in your reaction decompose. Even though in solution, it is no guarantee that less stable constituents will survive too high temperatures. We have found success in the 90 – 160 °C range. In a typical reaction the tube is heated at a rate of 5°C/min to the dwell temperature. Dwell times can range from 24 hours to 5 days depending on the specific reaction. In my experience no appreciable change occurs after 5 days of dwelling. After the dwell the furnace is slowly cooled to room temperature at 0.1°C/min to allow for crystallization.

When working up a reaction it is important to consider that the product may or may not be air stable and may potentially be soluble in deionized water. Therefore, extreme caution should be used with crystals that are grown hydrothermally. Crystals should not be sonicated or subjected to treatment with acid/base to remove impurities. The reaction should be carefully poured out into a prepared Buchner funnel for vacuum filtration and allowed to air dry. Oftentimes, organic solvents, such as acetone, can degrade crystals. In our experience it is best to achieve sample purity through a combination of mechanical sieving and manual crystal picking.

After a sample has been worked up, if sufficient sample exists (e.g. 100 mg), a powder X-ray diffraction pattern (PXRD) should be taken. If the resultant data does not turn up any known matches, then a crystal may be mounted on a scanning electron microscopy (SEM) stud for energy dispersive spectroscopy (EDS). It is important to note that if your crystal can potentially contain organic ligands that an accelerating voltage of 20 kV can rapidly destroy your crystal, so a shorter accumulation time should be used to prevent crystal degradation. After the constituent elements are known, the crystal may be mounted on a MitiGen tip for single crystal X-ray diffraction (SXRD) analysis. A unit cell run should be performed to determine lattice parameters. These parameters can be checked against databases to ensure the crystal is indeed a new compound. If the crystal does appear to be a new compound, several single crystals may be submitted to Mark Smith for structure solution. When a structure solution is elucidated experimental powder diffraction data should be compared with a simulated powder pattern derived from the single crystal data. If the patterns match and no impurities are observed, you may proceed with property measurements including IR, UV/Vis, fluorescence, and magnetism.

APPENDIX C

CONSIDERATIONS FOR MOLTEN FLUX REACTIONS

Molten flux reactions need to be done very carefully in order to achieve the desired result. This means careful attention must be paid to excluding water and air from reagents, flux, and the reaction vessel. Typically, this is achieved by storing common alkali and alkaline earth metal halide fluxes in an oven at a minimum of 260 °C for at least 24 hours prior to use. Reagents such as transition metal oxides should be prefired, if they can be subjected to elevated temperatures without degrading. Rare earth oxides should always be prefired at 1000 °C for 12 hours prior to use. When planning a reaction, it is essential that each reagent is dry prior to execution. Reducing agents should never be prefired, as they will simply oxidize in air to known oxides and lose their reductive power.

We've experienced great success with a variety of metallic reducing agents including calcium, zinc, molybdenum, and vanadium. Calcium and zinc offer distinct advantages over molybdenum and vanadium as they are typically in a melt state at the dwell temperature for a reaction. Vanadium and molybdenum are extremely high melting, and as a consequence the rate of reduction can be slower. It is important not to exceed 1050 °C when using zinc as a reducing agent as at that temperature a significant portion is gaseous and can exert excess pressure on the reaction vessel, potentially causing a catastrophic failure of the vessel.

When choosing a flux it is essential that it be redox neutral. This is somewhat limiting, but nevertheless we've had good success with alkali and alkaline earth metal halides. In our experience alkalis and alkaline earths with larger ionic radii often produce crystals that are superior to alkalis and alkaline earths that have smaller ionic radii (e.g CsCl vs NaCl or $BaCl_2$ vs. $CaCl_2$). Oftentimes it is beneficial to use a mixture of alkalis

or alkaline earths to reduce the melting point of the flux by creating a eutectic melt. Not only does this allow us to perform reactions that would otherwise be limited by the maximum temperature of our furnaces, but it also ensures a long liquid range of the flux to allow for the best chance at a successful crystallization.

The reaction vessel of choice for these reactions is a fused silica tube. Tubes are cut at 16 inches with a diamond wheel and then flame sealed in the center to create two 8 inch tubes, each with a sealed bottom. When filling a tube with reactants it is important that this step be done well in advance of reaction loading. In addition, the manifold should be drawing vacuum and stabilize at 10^{-4} torr before loading a tube for a reaction. Tubes should be filled around 1 inch full of reactants. The tube should quickly be attached to the manifold after reaction loading to prevent atmospheric moisture from being absorbed by the reagents. The tube must be allowed to fully degas on the manifold until a pressure of 10^{-4} is achieved again. The tube should be flame sealed with an oxygen/methane torch. Tubes should be inserted into a furnace upright or on an incline to keep the molten flux toward one end of the tube. It is not advantageous or recommended to perform reactions with a tube in a horizontal configuration.

When choosing a reaction coordinate the main consideration is the temperature at which the reaction will melt. Due to colligative properties this temperature will always be some value somewhat lower than the melting point of the flux. For this reason, the reaction should typically be slowly cooled past this point to prevent a rapid freezing of the molten flux. Since this specific temperature is not easily known, a rule of thumb is slow cool at least 100 °C below the melting point of the flux. When choosing a dwell temperature, the main consideration is that it be sufficiently higher than the melting point

of the flux, to ensure a long liquid range for crystallization to occur in. Ramp rates and slow cooling rates are similar to hydrothermal methods. Dwell times can vary from 24 hours to 1 week.

It is important to note that in our experience certain fluxes, $BaCl_2$, in particular can attack the inner walls of a fused silica tube. In some cases this has lead to new reduced early transition metal silicate materials, with the tube being the source of silicon. In our experience it did not help to include a finely divided source of silicon for subsequent reactions. It appears it must slowly be leached from the inner walls of the tube to achieve superior crystallization.

When working up a reaction the most important thing is to take extreme care to avoid getting small shards of silica in your product mixture. These are extremely hard to remove and will often show up as an impurity in your reaction. As a general rule, crystals obtained from flux reactions are far more stable than those obtained from hydrothermal reactions. This means that gentle sonication and dilute acids/bases may be used during reaction work up. When sonicating it is beneficial to select the smallest beaker that can contain your reaction. This will ensure maximum sonication of your sample, and allow for any powders adhered to the crystals to detach from the crystal surface. Often times many rounds of sonicating, decanting, vacuum filtering, and mechanical sieving are needed to completely get rid of powder from product crystals. It is important to visually monitor crystal quality during this period to ensure no degradation has taken place.

Analysis of product crystals is much the same as with crystals from a hydrothermal reaction with one major difference. When performing EDS measurements

an accumulation time of a full minute may be used as crystals from flux reactions don't often degrade when exposed to the beam.

APPENDIX D

PERMISSION TO REPRODUCE PUBLISHED MATERIALS

American Chemical Society License: Thesis/Dissertation

Chapters II and VII

This type of permission/license, instead of the standard Terms & Conditions, is sent to you because no fee is being charged for your order. Please note the following:

- Permission is granted for your request in both print and electronic formats, and translations.
- If figures and/or tables were requested, they may be adapted or used in part.
- Please print this page for your records and send a copy of it to your publisher/graduate school.
- Appropriate credit for the requested material should be given as follows: "Reprinted (adapted) with permission from (COMPLETE REFERENCE CITATION). Copyright (YEAR) American Chemical Society." Insert appropriate information in place of the capitalized words.
- One-time permission is granted only for the use specified in your request. No additional uses are granted (such as derivative works or other editions). For any other uses, please submit a new request.

Elsevier License: Personal and Scholarly Purposes

Chapters IV and VIII

Authors can use their articles, in full or in part, for a wide range of scholarly, non-commercial purposes as outlined below:

- Share copies of the article and distribute them via email to colleagues for their research use (also known as 'scholarly sharing').
- Share the article for personal use or for the author's own classroom teaching.
- Use the article at a conference, meeting or for teaching purposes.
- Allow the author's employers to use the article for other internal purposes (such as training).
- Include the article in a printed compilation of the author's works, such as collected writings and lecture notes.
- Inclusion the article in a thesis or dissertation
- Use the article in full or in part to prepare other derivative works, including expanding the article to book-length form, with each work to include full acknowledgement of the article' original publication.

These rights apply for all Elsevier authors who publish their article as either a subscription article or an open access article. In all cases we require that all Elsevier authors always include a full acknowledgement and, if appropriate, a link to the final published version hosted on Science Direct**.**